FIRST-PRINCIPLES THEORETICAL CHARACTERIZATION OF THE ELECTRONIC STRUCTURE OF IRON AND IRON OXIDE SURFACES AND THEIR INTERFACES WITH ORGANIC LAYERS

A Dissertation
Presented to
The Academic Faculty

by

Jung hyun Noh

In Partial Fulfillment
of the Requirements for the Degree
Doctor of Philosophy in the
School of Materials Science and Engineering

Georgia Institute of Technology
August 2017

FIRST-PRINCIPLES THEORETICAL CHARACTERIZATION OF THE ELECTRONIC STRUCTURE OF IRON AND IRON OXIDE SURFACES AND THEIR INTERFACES WITH ORGANIC LAYERS

Approved by:

Dr. Jean-Luc Brédas, Advisor
School of Chemistry and Biochemistry
Georgia Institute of Technology

Dr. Mark D. Losego
School of Materials Science and Engineering
Georgia Institute of Technology

Dr. Seung Soon Jang, Co-advisor
School of Materials Science and Engineering
Georgia Institute of Technology

Dr. Preet Singh
School of Materials Science and Engineering
Georgia Institute of Technology

Dr. Meilin Liu
School of Materials Science and Engineering
Georgia Institute of Technology

Date Approved: July 7, 2017

ACKNOWLEDGEMENTS

I would like to thank many individuals who I had the opportunity work with and learn from over the course of my Ph.D. studies. First and foremost, I would like to express my gratitude to my advisor, Professor Jean-Luc Brédas for providing the opportunity to study in his research group. I deeply appreciate his consistent support and encouragement, as well as scientific insight in my research over the years. His guidance truly has helped me develop the ability to critical thinking and effective communication along the way.

I would also like to thank all of the members in the Brédas group, past and present, for sharing their knowledge and experience. I'm particularly grateful to Drs. Paul Winget, Hong Li, and Veaceslav Coropceanu for their stimulating discussions and helpful feedback on my drafts and reports, Stephen Shiring for useful discussions in editing this dissertation, and Zilong Zhang for his help with workstations and clusters.

In addition, I wish to thank my collaborators in King Abdulaziz University including Professors Osman and Aziz for their new ideas and thoughtful suggestions over many conference calls, and the center for the Science and Technology of Advanced Materials and Interfaces (STAMI) for the fellowship awarded.

I'm also grateful to the members of my committee, my co-advisor, Professor Jang for much helpful guidance of my graduate study, Professor Singh for insightful advice for the corrosion project, and Professors Liu and Losego for their valuable time and suggestions.

Last, but certainly not least, I would like to thank my family and friends for their encouragement throughout my studies. Their continued love and support provided light in even the darkest of nights and gave this journey meaning. None of this would be possible without them.

TABLE OF CONTENTS

LIST OF TABLES

LIST OF FIGURES

LIST OF SYMBOLS AND ABBREVIATIONS

AFM	atomic force microscope
Alq_3	tris(8-hydroxyquinolinato)-aluminum(III)
B3LYP	Becke, Lee, Yang and Parr
BCC	Body-Centered Cubic
BOMD	Born-Oppenheimer MD
BPA	benzylphosphonic acid
CA	carboxylic acid
CBM	conduction band minimum
CHE	computational hydrogen electrode
CTR	crystal-truncation-rod x-ray diffraction
DFT	Density Functional Theory
DFT+*U*	DFT+Hubbard *U*
DOS	densities of electronic states
E_{corr}	corrosion potential
ε_d	*d* band center
E_F	Fermi level
f.u.	formula unit
Fe_3O_4	magnetite
FM	ferromagnetic
G	Gibbs free energy
GGA	generalized gradient approximation
GMR	giant magnetoresistance
GWA	GW approximation
HF	Hartree-Fock
HIS	Hybrid Interface States
HSE	Heyd, Scuseria, and Ernzerhof
i_{corr}	corrosion current densities
IPES	inverse photoelectron spectroscopies
ITO	indium tin oxide
LDA	local density approximation
LEED	low-energy electron diffraction
LSMO	$La_{0.7}Sr_{0.3}MnO_3$
MD	Molecular Dynamics
ML	monolayer
MO	molecular orbitals
MR	magnetoresistance
MRAM	magnetic random access memory

NA	nonanoic acid
NEXAFS	near edge X-ray absorption fine structure
NM	nonmagnetic
OFET	organic field effect transistors
OLED	organic light-emitting diodes
OMAR	organic magnetoresistive effect
OSC	organic semiconductors
OT	octanethiol
P (SP)	spin polarization
PA	phosphonic acid
PBE	Perdew, Burke, and Ernzerhof
PDOS	partial density of states
PES	photoelectron spectroscopy
PES	photoelectrochemical
PM-IRRAS	Polarization Modulation Infrared Reflection Absorption Spectroscopy
Q	charge
QP	quasiparticle
RSH	range-separated hybrid
SAM	self-assembled monolayer
SAPT	symmetry-adapted perturbation theory
SCLS	surface core-level shifts
STM	scanning probe microscopies
T_c	Curie temperature
TMR	tunneling magnetoresistance
UPS	ultraviolet photoelectron spectroscopy
U_{SHE}	standard hydrogen electrode
VASP	Vienna Ab initio Simulation Package
VBM	valence band maximum
vdW	van der Waals
XC	exchange-correlation
XPS	x-ray photoelectron spectroscopy
ZPE	zero-point vibrational energy
α-Fe_2O_3	hematite
α-FeOOH	goethite
γ-Fe_2O_3	maghemite
γ-FeOOH	lepidocrocite
μ	magnetic moment

SUMMARY

Organic compounds offer considerable promise in iron corrosion prevention. Attachment of organic molecules to the metal surface can alter the corrosion reactions by changing the activation barriers of the anodic and/or cathodic electrochemical reactions. Given that detailed experimental investigations of interfacial geometric and electronic structures remain challenging, computational approaches that provide quantitative structure-property descriptions of the interfacial processes can help elucidate the inhibition mechanisms of molecular modifiers with various chemical functionalities.

In this dissertation, we focus on the development of an adequate theoretical platform to investigate the surfaces and interfaces involved in metal oxidation and corrosion, taking iron as the prototypical reactive transition metal element. One of the difficulties in developing appropriate theoretical models to describe organic/inorganic heterojunctions stems from the complex nature of the exposed surfaces as a function of environmental conditions. As a first step, clean iron and iron oxide surfaces were therefore examined to determine their equilibrium surface configurations in various atmospheric and electrochemical conditions. Subsequently, self-assembled monolayers were attached to those surfaces to evaluate their physical and chemical impact on the corrosion processes. We used a theoretical approach containing quantum mechanical methods and molecular dynamic simulations in order to describe the interfacial geometric and electronic structures of iron with organic modifiers. Our findings underline that long-term stability of the monolayer film can be achieved *via* the molecular design of self-assembled monolayers and substrate pretreatment.

While in corrosion science and engineering, technologies are developed mainly to circumvent iron oxidation, it must be borne in mind that iron oxides themselves can also be of practical importance on their own, for instance, in the field of organic spintronics. In this context, the electronic and magnetic properties of interfaces between iron-based ferro-(or ferri-)magnetic electrodes and representative π-conjugated molecules have been explored. Our work underlines that not only the choice of materials but also the details of the interfacial structure, *e.g.*, substrate crystal orientation or termination and molecular adsorption geometries, have significant impact on the nature of the hybrid interface electronic states. Our results provide guidelines to tailor the spin transfer behavior at a magnetic junction in order to achieve maximum device efficiency in applications such as non-volatile magnetic random access memories and magnetic-field sensors.

CHAPTER 1. INTRODUCTION

The overarching theme of this Thesis is the fundamental understanding of surface and interface chemistry of iron-based systems. This Chapter is intended to provide an overview of iron and iron oxides in order to build a solid background prior to getting into the details in later chapters.

This Chapter begins by introducing the inherent characteristics of iron: high chemical reactivity (Section 1.2) and magnetism (Section 1.3). Regarding the former characteristic, the extensive studies have focused on elucidating corrosion processes and developing efficient prevention methods. For the latter characteristic, much attention has been drawn to the application of iron and iron oxides as an effective ferromagnetic electrode in a spintronic device. There, two independent fields of science are briefly discussed in each subsection. We then turn our focus to the surface science of metal and metal oxide (Section 1.4), followed by organic-inorganic interface physics (Section 1.5). The discussion particularly concentrates on the origin of the complex properties appearing in oxide surface and heterogeneous interface. This knowledge is central to understanding the changes in the electronic structure of the substrate that occur after surface modification with an organic layer, and we focus this Thesis on that problem.

1.1 Overview

Iron is one of the most abundant and ubiquitous elements on Earth; it is present nearly everywhere, including atmosphere, pedosphere, biosphere, hydrosphere, and lithosphere, see Figure 1.1a.[1] Among its four allotropic forms, the body-centered cubic (bcc) δ allotrope is prevalent. As a transition metal, iron exists in a wide range of oxidation states, from −2 to +6, although it forms compounds mainly in the +2 and +3 oxidation states. Once iron is exposed to oxygen-containing environments, iron oxides spontaneously form; they are widespread in nature and are readily synthesized in the laboratory. There are 16 known iron oxides in total, either in the form of oxides, hydroxides, or oxyhydroxides, being composed of Fe together with O and/or OH.[1] In most compounds, iron is in the trivalent state; three compounds, FeO, $Fe(OH)_2$ and Fe_3O_4, contain divalent Fe. In general, iron oxides consist of close-packed arrays of anions in hexagonal or cubic close packing where the interstices are partly filled with ferric or ferrous ions. The coordination of these ions is predominately octahedral ($Fe(O,OH)_6$), but can also be tetrahedral in some cases (FeO_4). Some representative crystal structures of iron oxides are given as examples in Figure 1.1b.[2]

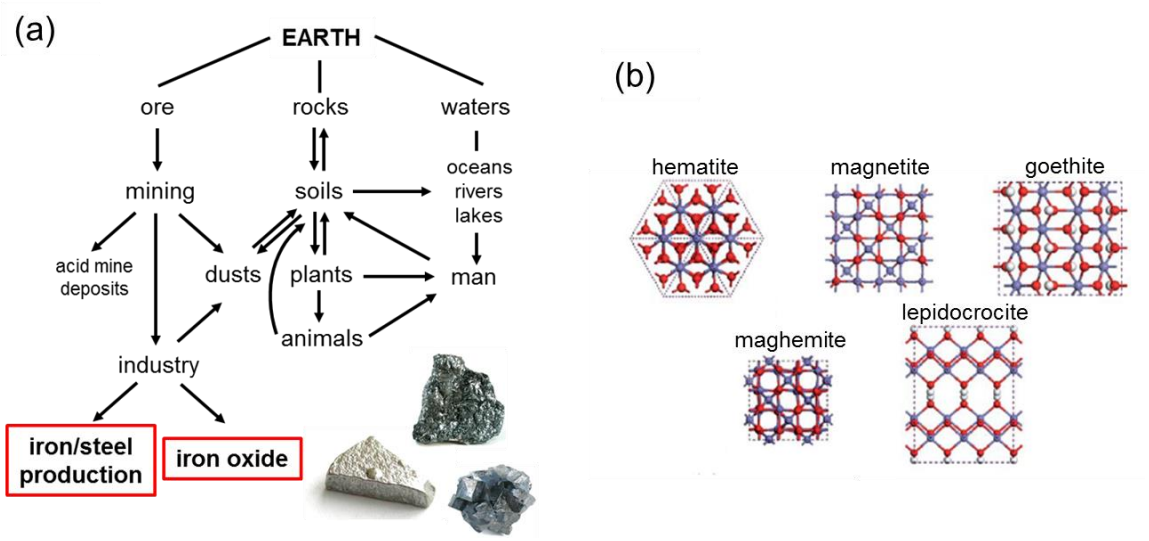

Figure 1.1 (a) Iron oxides in the global system. Modified from Ref. 1. (b) Schematic representation of the most abundant iron oxides and oxyhydroxides: hematite, magnetite, goethite, maghemite, and lepidocrocite. Reprinted with permission from Ref. 2, copyright 2013 by Royal Chemical Society.

1.2 Corrosion of iron

Iron is of greatest importance when mixed with certain other metals and carbon to form steels. However, the high reactivity of iron can be problematic in that the metal easily undergoes numerous chemical reactions when in contact with water, oxygen, and other small molecules. This occurs not only at the surface, but also near microscopic pits and cracks. This leads to the formation of new compounds which are much more porous and brittle than metallic itself iron, and the material becomes mechanically degraded over time. This process is called *corrosion*, and corrosion phenomena of iron and its associated alloys occur in a vast range of industrial fields and receive a considerable

amount of attention as corrosion-related structural failures have led to serious environmental incidents as well as tremendous economic losses over the past few decades (on the order of $300B a year in the United States alone, reported from NACE international).

1.2.1 Classification of iron corrosion

Although it can take place under a myriad of environmental conditions, there are two major classifications of iron corrosion depending on whether or not it involves water.[1]

Upon exposure to an aqueous solution made of salt, acid, and base ions, most metals including iron and steel are thermodynamically unstable; hence, they readily dissolve in water, acting as an anode in an electrochemical reaction:

$$\mathrm{Fe} \rightarrow \mathrm{Fe}^{2+} + 2\mathrm{e}^{-} \qquad E^0 = 0.44\ \mathrm{V} \tag{1.1}$$

where E^0 refers the standard equilibrium potential. The basic mechanism of this anodic reaction involves the removal of valence electrons from the iron atoms which become cations that move into the solution, building up the electric potential difference (double layer) between the metal and the solution. The half reaction for iron dissolution proceeds until equilibrium is reached.

For electrochemical corrosion to proceed, the corresponding cathodic reaction that accepts the electrons is required, which in general involves one of three major reduction

reactions. The first occurs in aerated, acid-to-neutral solutions and includes reduction of oxygen:

$$\frac{1}{4}O_2 + H^+ + e^- \rightarrow \frac{1}{2}H_2O \qquad E^0 = 1.23\ V \tag{1.2}$$

Also in aerated, alkaline solutions, oxygen is reduced as:

$$\frac{1}{2}H_2O + \frac{1}{4}O_2 + e^- \rightarrow OH^- \qquad E^0 = 0.40\ V \tag{1.3}$$

Here, the reaction produces hydroxyl ions which react directly with the Fe^{2+} ions to produce an oxide precipitate, such as ferrous hydroxide $Fe(OH)_2$.

In deaerated, acid solutions, on the other hand, protons are the oxidizing agents:

$$H^+ + e^- \rightarrow \frac{1}{2}H_2 \qquad E^0 = 0 \tag{1.4}$$

As the reaction potentials depend upon the concentration of the species in the cell, they can deviate from the standard potential, E^0.

The combined anodic and cathodic reactions form the corrosion cell, the electrochemical potential of which lies between the single potential of the two half reactions. This mixed potential is termed the *corrosion potential* (E_{corr}). The driving electromotive force for the corrosion reaction corresponds to the potential difference between the cathodic potential and the anodic potential. The corrosion rate is determined by the charge transfer across the interface between the metal and redox couples in the solution, often expressed as the current density (A/m^2). One of the familiar examples of electrochemical corrosion

is atmospheric rusting, which occurs at a particular critical humidity between 60-80% and higher.[3]

Even in a dry state, iron reacts chemically with oxygen gas in the air to form a surface film of oxide at a temperature ranging from below room temperature to near 1000 °C. This process is called thermal oxidation/corrosion. Upon adsorption of O_2 onto the iron surface, molecular oxygen is dissociated into negatively charged O atoms at the surface. As the chemisorbed O atoms cause a high electric field, the system responds to lower this field either by pulling metal ions from the metal (segregation) or pushing oxygen ions into the metal lattice (diffusion). This mass transport enables the formation of the corrosion product, which occurs at different stoichiometries such as FeO, Fe_3O_4, and Fe_2O_3. These films are only a few Å thick at room temperature, but can become much thicker at sufficiently high temperature. Here, the rate-limiting factor for growth could be diverse: ion diffusion in an oxide layer, availability of oxygen, or electronic conductivity of the film. All the basic iron oxides formed as corrosion products of iron and steel can vary under a different set of conditions but mainly consist of goethite (α-FeOOH), lepidocrocite (γ-FeOOH), magnetite (Fe_3O_4), maghemite (γ-Fe_2O_3), and hematite (α-Fe_2O_3).

The details of the charge transfer during the electrochemical corrosion are depicted in Figure 1.1. Redox reactions require electron transfer from the filled states of the metal to the empty states of the oxidized species for a cathodic reduction and from the filled states of the reduced species to the empty states in the conduction band of the metal for an anodic oxidation. This necessitates tunnelling processes between occupied and unoccupied states at the same energy level. When a metal electrode is in electrochemical

equilibrium with the redox system, *i.e.*, their difference in Fermi levels (the overpotential, η) is zero, the overlap between the occupied states of the metal and the unoccupied states of the redox system is equal to the overlap between the unoccupied states of the metal and the occupied states of the redox system (Figure 1.2a). As a consequence, the partial current densities, i_+ and i_-, have the same value with opposite sign, leading to vanishing total current density $i = i_+ + i_- = 0$. However, when the Fermi level of the redox systems, $E_{F,Redox,}$ becomes higher than the metal electrode, $E_{F,Me}$, the overlap between the unoccupied states of the metal and the occupied states of the reduced species is larger and then leads to a higher $|i_+|$ than $|i_-|$, and thus a higher anodic total current density $i > 0$ (see Figure 1.2b). If the relative energy levels are reversed, then a cathodic total current density $i < 0$ is obtained in the corrosion cell (Figure 1.2c).

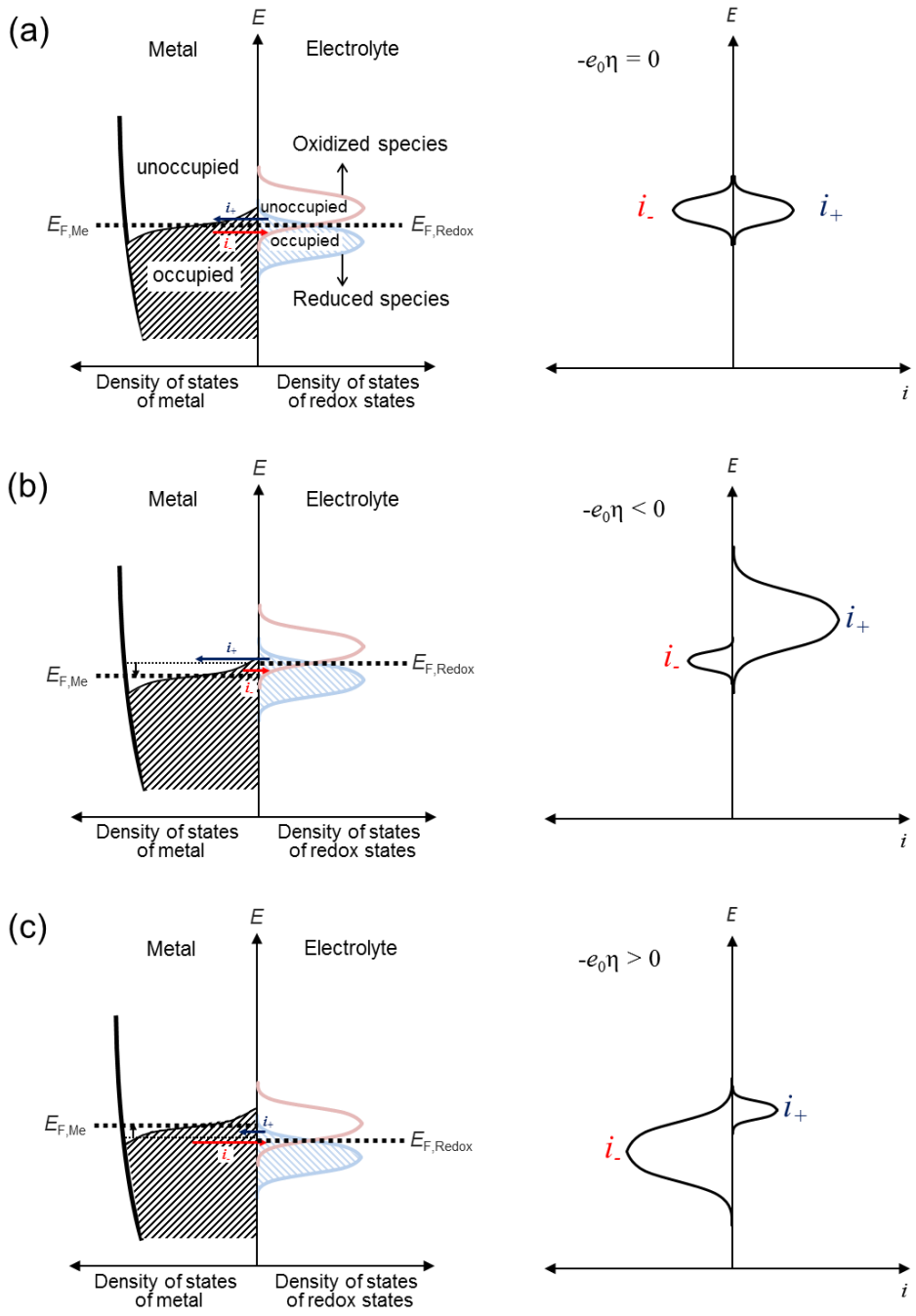

Figure 1.2 Band model for charge transfer between a metal electrode and a redox system within the electrolyte.[4]

Oxidation in dry conditions can be described by the Fromhold-Cook theory,[5] which has been demonstrated for Fe(001).[6,7] Given that the transport of electrons can proceed by tunnelling or/and thermionic emission, the electronic structure of a metal/oxide/oxygen system (see Figure 1.3) is important in terms of the oxidation process; in particular, the energy barrier (χ_0) from the metal work function (ϕ_0) to the oxide conduction band (E_C), and the energy difference (χ_L) between E_C and the O^- level in the adsorbed oxygen, are the major parameters that govern the oxidation kinetics.

Both in electrochemical and high-temperature corrosion, electron transport occurs exactly at the interface between the metal and oxidizing agents; therefore, the chemical and physical conditions of the interface play a decisive role in the redox reaction process. [4]

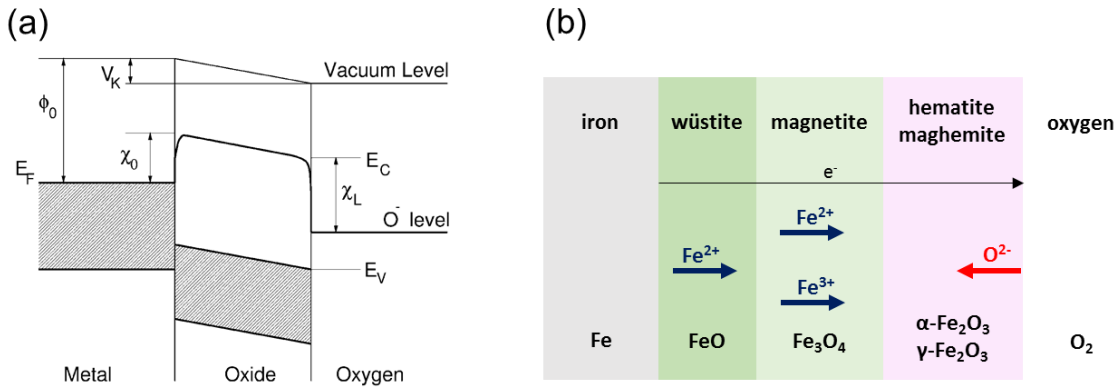

Figure 1.3 (a) Illustration of the electron-energy diagram for a metal/oxide/oxygen system (reprinted with permission from Ref. 7, copyright 2000 by American Physical Society) and (b) schematic representation of iron oxidation in an oxygen gas environment at high temperature.

1.2.2 Chemical reactivity of iron

One may ask: "Why is iron susceptible to chemical reactions while gold is not?" To understand the essential basis for the chemical reactivity of a metal, it is helpful to look at the simplest one-electron description of the quantum mechanics of atoms and molecules interacting with a metal surface, as shown in Figure 1.4a.[8,9] When an atom or a molecule is placed on a metal surface, their electronic states interact with the valence states of the surface atoms that consist of one band or several bands of states. The light-grey area in Figure 1.4a indicates the *d* band for a transition metal in the 3rd to 5th rows of the periodic table, while the dark-grey area represents the *s* or *p* state of the adsorbate. Upon bond formation at the interface, the hybridization of an adsorbate state with the *d* electrons of a surface often gives rise to bonding and antibonding states for the metal-adsorbate, just as in a simple two-state problem, due to the narrow band shape of the localized *d* states. Assuming the constant filling of the *d* band, we can expect that the band center (ε_d) is shifted up as the bandwidth decreases. Given that the antibonding states always appear above the *d* states and filling of antibonding states weaken the substrate-metal interaction, ε_d with respect to the Fermi level can be a good first indicator of the bond strength: The higher the energy of the *d* states, the higher the energy of the antibonding states, and the stronger the interfacial chemical bond.

It should be noted that the band shape, filling, and width of the *d* bands vary through the 3*d*, 4*d*, and 5*d* series, and the band center is a material-dependent parameter that can be used to predict the element's chemical reactivity with oxygen. As the *d* band centers of noble metals are typically located at low energy, for example, -3.56 eV for Au and -4.30 eV for Ag (Figure 1.4b), the corresponding antibonding oxygen 2*p*–metal *d* states are

likely to be (partially) filled, which leads to "weak chemisorption". On the other hand, when the substrate ε_d is rather high, as for transition metal including Fe (-0.92 eV), the antibonding states can be mainly empty, implying "strong chemisorption".

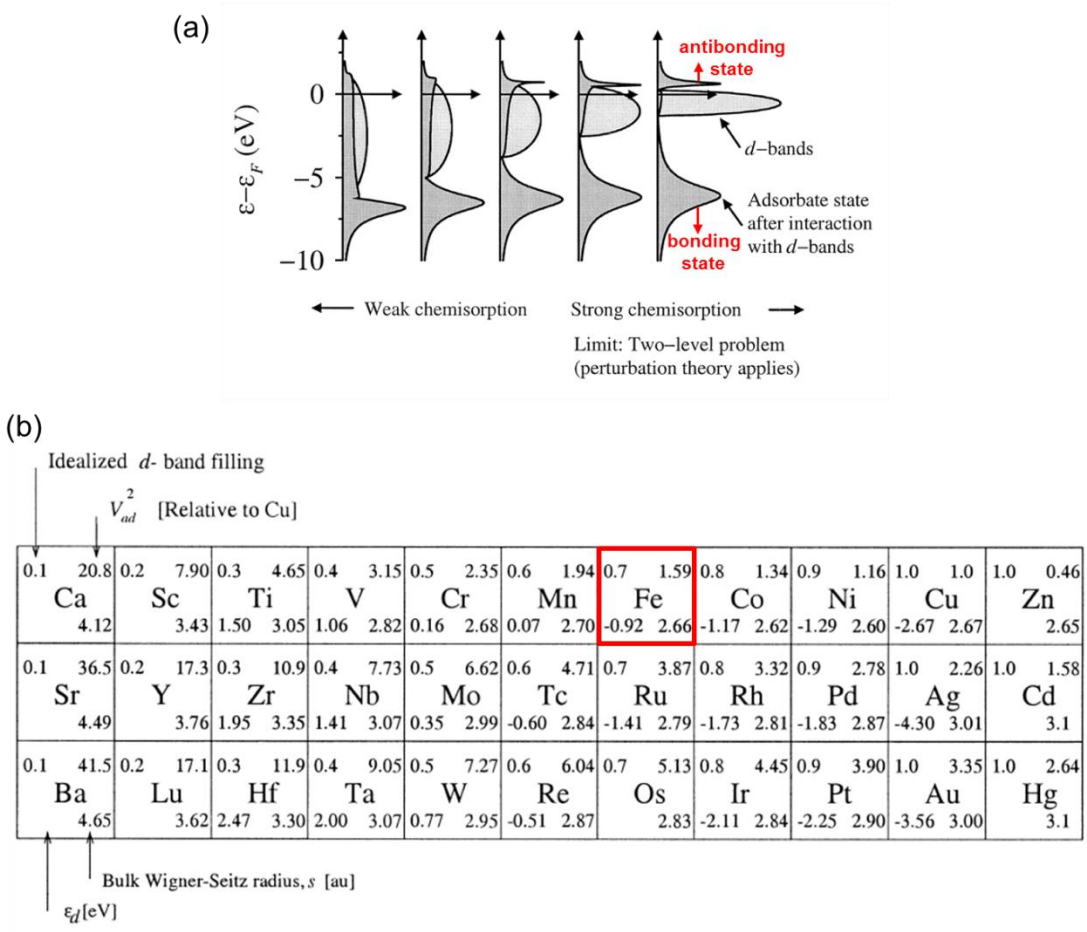

Figure 1.4 (a) Local density of states projected onto an adsorbate state interacting with the *d* bands at a surface, as calculated based on the Newns–Anderson model.[8,9] (b) Periodic table for the 3*d*, 4*d*, and 5*d* transition metals illustrating the ideal *d*-band filling (1 for complete filling), the square of the adsorbate–metal *d* coupling matrix element (V_{ad}^2), the *d* band center (ε_d), and the bulk Wigner-Seitz radius. The center of the *d* band is calculated for the most close-packed surface of each of the metals. The data are originally coming from Ref. 10 and then modified in Ref. 8 with permission, copyright 1997 and 2000 by Elsevier.

Based on the *d* band theory, it can be rationalized that a noble metal is rather chemically inert while the elements to their left in the periodic table are more chemically active. The surface reactivity can be altered by modifying the electronic structure of the substrate.

1.2.3 Corrosion prevention methods

From thermodynamics, it is inevitable that a metal, either in an elemental form or an alloy, returns to its native oxidized state, as this process is generally driven by a large free energy change. To prevent this process, a variety of strategies have focused on controlling the corrosion potential and current by altering either redox reaction. For example, cathodic protection employs either a sacrificial anode or an external power supply to decrease the potential of the metal. Conversely, anodic protection shifts the corrosion potential upward so as to maintain a protective oxide layer on the metal surface and/or reduce the overall reaction kinetics, which process is commonly referred to as passivation. The formation of a passive film provides high corrosion resistance; as an example, iron, which corrodes at half a millimeter per year in salt water, can corrode a thousand times more slowly when the surface is passivated.[3]

It is also important to note that corrosion always encompasses at least one oxidation reaction, typically in the metal substrate, and one reduction reaction involving oxygen and/or water. Since both reactions occur at the metal/solution (or gas) interface, adequate modification of the metal surface in a manner that reduces the rate of redox processes can

slow the kinetics of corrosion. Figure 1.5 shows schematic examples of the types of inhibition and their effects on the polarization curves. Inhibitors can be classified as an anodic (Figure 1.5a) and cathodic (Figure 1.5b) inhibitor. As the names imply, an anodic inhibitor reduces the rate of the anodic reaction while having less of an effect on the cathodic reaction, a cathodic inhibitor reduces the rate of the cathodic reaction while the anodic reaction is not affected. In this regard, coatings have been exploited to impede either the oxidation of the metal (anodic inhibitor) or the reduction reaction (cathodic inhibitor) by adsorbing onto the metal surface and blocking the access of corrosion agents to the surface. In general, the coating technique includes a primer coating that is applied to the metal followed by a topcoat of the physical barrier. The primer coating is chosen for good adhesion to the metal, and often contains active ingredients to further reduce the corrosion rate once the barrier has been breached over time. However, such active ingredients commonly include heavy metals, particularly hexavalent chromium, which it is desirable to eliminate when it comes to environmental and health concerns. In that respect, many anti-corrosion measures composed solely of organic materials have been explored, including active head groups like -CN, -SH, $-NH_2$, -COOH, $-PO_3H_2$, to form organic compounds, conducting polymers, and self-assembled monolayers (SAMs). The inhibitor efficiency is defined as the relative reduction in corrosion current density:

$$\eta = \frac{i_{corr}^0 - i_{corr}}{i_{corr}^0} \tag{1.5}$$

where i_{corr} and i_{corr}^0 represent the corrosion current densities at open circuit with and without the addition of an inhibitor, respectively.

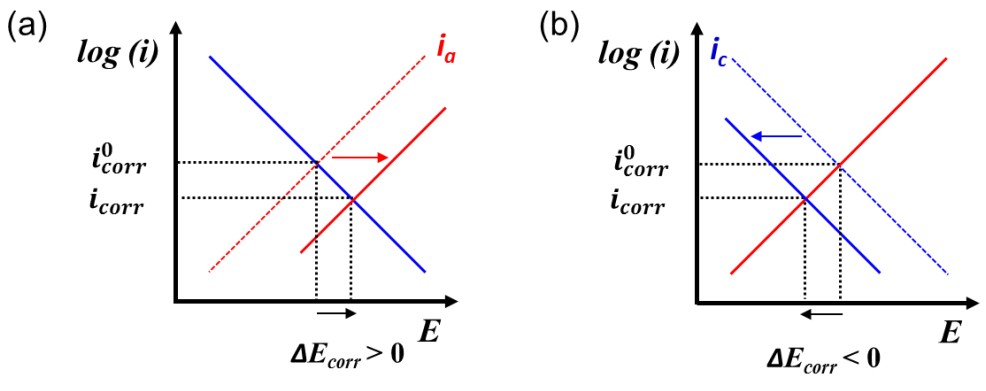

Figure 1.5 Polarization curve of a corrosion system with (a) suppression of the anodic reaction, *i.e.*, metal dissolution by increasing E_{corr} in the positive direction; and (b) inhibition of the cathodic reaction of a redox system, where E_{corr} is shifted to more negative potential.

1.3 Iron and iron oxides in spintronic applications

While methods have been developed to prevent the oxidation of iron metal in corrosion science, iron oxides themselves have practical importance in other parts of industrial applications, such as paint pigments, heterogeneous catalysts for chemical syntheses,[11,12] and energy storage devices.[13] In contrast to the featureless imperfect flakes commonly found in surface rust, iron oxides exhibit their distinctive electrical and magnetic properties when they are grown as a high-quality thin film. In particular, iron oxides have been used in all types of data storage and recording media, including magnetic disks and magnetic tape, as well as high-sensitivity biomolecular magnetic resonance imaging for medical diagnosis.

1.3.1 Magnetic structures of iron and iron oxides

The 3*d* or 4*f* transition series are known to exhibit spontaneous magnetization, *i.e.*, possess a net magnetic moment (due to unpaired electrons) in the absence of an external magnetic field. For ferromagnetic (FM) metals, the relevant density of states (DOS) mainly consists of the narrow *d*(*f*) bands, and the DOS at the Fermi level (E_F) is different for the spin-up and the spin-down directions in contrast to normal nonmagnetic (NM) metals, see the example of bcc Fe in Figure 1.6. The imbalance between the populations of spin-up and spin-down electrons at the Fermi level corresponds to the *spin polarization* (*P*):

$$P = \frac{N_\uparrow - N_\downarrow}{N_\uparrow + N_\downarrow} \tag{1.6}$$

where $N_\uparrow$ and $N_\downarrow$ are often referred to as the spin-up DOS and spin-down DOS of a FM metal at E_F, respectively. Representative *P* values for 3*d* transition FM metals are 35% for Co, 40% for Fe, and 23% for Ni.[14] Another characteristic parameter to define the material's magnetic property is the magnetic moment, a measure of the magnetism strength, *i.e.*, a magnet's tendency to align with a magnetic field. The magnetic moment originates from three intrinsic components: (i) the motion of electrons in their (atomic) orbitals (orbital magnetic moment); (ii) the spinning of an electron around its own spin axis (spin magnetic moment); and (iii) the nuclear magnetic moment due to the nuclei. Among these three, the contribution from the second component shows the most significant contribution to the net magnetic moment.

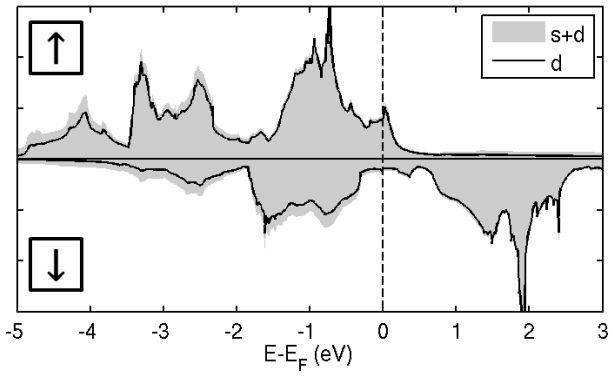

Figure 1.6 Density of states (DOS) for bulk bcc Fe (a=2.83 Å) projected to the 3*d* orbitals (line) and the sum of 4*s* and 3*d* orbitals calculated at the DFT-PBE level (gray area). The majority (spin-up) electron population at the Fermi level is larger than the minority (spin-down) electron population.

The main type of magnetic interaction between Fe ions on adjacent sites in a solid is the electrostatic exchange interaction that causes parallel or antiparallel alignment of the spins. In iron oxides, the unpaired Fe^{2+} and Fe^{3+} ions are surrounded by O^{2-} or OH^- ions, so the exchange reaction proceeds *via* the intervening ligand, which is termed *superexchange*. Superexchange interactions show a dependence on Fe-O bond length and angle: the interactions are strong for angles between 120-180°, and much weaker for an angle of 90°.[1] Therefore, various magnetic properties have been observed for different phases of iron oxides. Table 1.1 summarizes the characteristic magnetic parameters for representative iron oxides as measured by Mössbauer spectroscopy, neutron powder diffraction, and magnetometry. Owing to the inherent magnetism of iron oxides, one of their major potential applications is as spin-injecting electrode in *spintronic* devices, where the use of the electron spin in information processes is analogous to the use of the electrical charge in conventional electronics.

Table 1.1 Magnetic properties of the iron oxide.[1] [a]T_N: Néel temperature, T_C: Curie temperature, T_M: temperature of Morin transition [b]measured at room temperature.

	Magnetic structure	**Temperature[a] (K)**	**Saturation magnetization[b] (Am^2kg^{-1})**	**Anisotropy Constant (Jm^{-3})**
Goethite	antiferromagnetic	400 (T_N)	0.01-1	103
Bernalite	weakly ferromagnetic	427 (T_C)	-	-
Hematite	weakly ferromagnetic antiferromagnetic	956 (T_C) 250 (T_M)	0.3	1-6·104
Magnetite	ferrimagnetic	850 (T_C)	92-100	104-105
Maghemite	ferrimagnetic	820-986 (T_C)	60-80	105
Wüstite	antiferromagnetic	203-211 (T_N)	-	-

1.3.2 Spintronic devices

The field of spintronics dates back to 1988 with the discovery of giant magnetoresistance (GMR) reported simultaneously by Albert Fert[15] and Peter Grünberg,[16] who were awarded the 2007 Nobel Prize in Physics. The most successful spintronic device to date is a spin valve that has been already extensively exploited in the market, at the base of hard disk read/write heads. Related technologies have been currently explored in many other applications, such as non-volatile magnetic random access memory (MRAM), "racetrack" memories, magnetic-field sensors, and even quantum computing.[17]

Figure 1.7 gives a schematic representation of a basic spintronic device. This device utilizes a layered structure of thin films of a NM spacer sandwiched between FM materials that change electrical resistance depending on the relative orientations of the

magnetization of the two electrodes upon application of a magnetic field B in a specific direction.[17] Here, a spin-polarized current is injected from a spin polarizer (FM1), transported through the NM spacer, and finally detected by a second FM electrode (FM2). In order to change the magnetization direction alignment of the FM electrodes from anti-parallel to parallel and vice versa upon sweeping B, the coercive fields (B_C) of the FM electrodes, which are defined as the field necessary to completely demagnetize a magnet, should be different from each other. The coercive field is a unique material property: Co (40 mT), LSMO (5 mT), Fe_3O_4 (140 mT), and Fe (<5 mT), for example. Simply put, the higher this value, the better a magnet retains its magnetism when exposed to an opposing magnetic field. Using this configuration, the device resistance changes twice upon sweeping the field; this occurs at B_{C1} and again at B_{C2}. The typical magnetoresistance (MR) curve obtained by sweeping the applied magnetic field on spintronic devices is given at the bottom of Figure 1.7.

Among the fascinating examples of spintronic applications are giant magnetoresistance (GMR, also referred to as spin-injection magnetoresistance) and tunneling magnetoresistance (TMR). In both cases, a considerable variation of the electrical resistance can be achieved by switching the magnetization of the device's electrodes from a parallel to an antiparallel configuration, as explained above.[17]

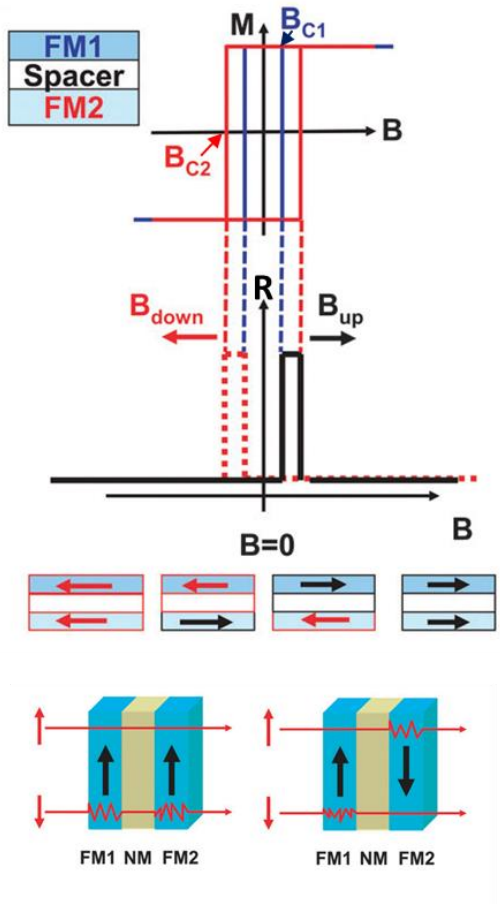

Figure 1.7 Schematic representation of a basic spintronic device illustrating the spin-dependent electron scatterings that depend on the relative alignments of the FM electrode magnetization directions upon the presence of the external magnetic field. In most cases, a charge carrier injected from the first FM experiences low resistance when it has its spin direction parallel to the magnetization direction of the second FM electrode.[23] Reprinted with permission from Ref. 23, copyright 2014 by Royal Chemical Society.

Typically, metallic spacer layers are used in GMR devices, and the spin-polarized current is injected into and transported through the NM spacer layer. During the transport from one FM electrode to the other FM electrode, the spin polarization is gradually lost by spin

flip events. This loss typically follows an exponential decay that is characterized by the spin diffusion length. If a thin layer of insulator is chosen as the spacer-layer instead of a metal, the corresponding effect is referred to as TMR, because the spin-polarized carriers tunnel through the insulating layer. This effect was originally discovered in 1975 by Jullière in Fe/GeO/Co-junctions at 4.2 K with MR ~14%.[18] With two FM electrodes, he could exploit into a device the physical concept of the spin-polarized tunnel effect and he developed a model that is now widely known as Jullière's model:

$$TMR = \frac{R_{AP}-R_P}{R_P} = \frac{I_P-I_{AP}}{I_{AP}} = \frac{2P_1P_2}{1-P_1P_2} \quad (1.6)$$

where R_{AP} (I_{AP}) and R_{AP} (I_{AP}) indicate the resistivity (current) in antiparallel and parallel alignments of the magnetization directions of two FM electrodes; P_n (n=1, 2) refers to the spin polarization of the tunnel current at the FM electrode n.

Miyazaki *et al.* measured an effect of 2.7% at room temperature, followed by 18% in junctions of iron separated by an amorphous aluminum oxide insulator.[19] Moodera *et al.* measured 11.8% in junctions with electrodes of CoFe and Co.[20] The highest effects observed to date with aluminum oxide insulators are the measurements around 70% at room temperature. Tunnelling barriers of crystalline magnesium oxide (MgO) have been under development; effects of up to 600% at room temperature and more than 1100% at 4.2 K were observed in junctions of CoFeB/MgO/CoFeB.[21] Such a high TMR is attributed to crystalline symmetry filtering of the MgO barrier.[22]

1.3.3 Organic spintronics

Typically, the materials for a NM spacer have been either NM metals or inorganic oxides (mainly Al_2O_3 and MgO), but carbon-based materials have drawn attention as promising candidates for efficient barriers in magnetic tunnel junctions as well as spin valves. The magnetoresistive effect specific to organic devices is referred to as the organic magnetoresistive effect (OMAR). As demonstrated in organic light-emitting diodes (OLEDs) and organic field-effect transistors (OFETs), organic semiconductors (OSCs) can bring flexibility, low production cost, and large-area easy processing to spintronic devices. More importantly, given that OSCs are composed mostly of light elements, *i.e.*, C, H, N, O, they have intrinsically weaker spin-orbit couplings and lower hyperfine interactions than inorganic semiconductors, which are two main causes for spins to lose their orientation. Thus, a relatively longer spin lifetime together with chemical functionality brought by molecular engineering in OSCs motivates an increasing interest in the field of *organic spintronics*.

The first report of spin transport in an organic spin valve structure was in 2002 by Dediu *et al.* using a lateral structure having two $La_{0.7}Sr_{0.3}MnO_3$ (LSMO) electrodes with sexithienyl (T_6) as a spacer.[24] A couple of years later, Xiong *et al.*[25] reported MR of -40% at 11 K in a vertical LSMO/Alq_3/Co spin valve with Alq_3 layers from 130 to 260nm thick, see Figure 1.8. A much higher tunneling magnetoresistance (TMR) up to 300% is observed for the same device architecture with a much thinner Alq_3 layer (3-10 nm).[26] However, in general, the MR responses of these prototypical devices completely

disappear above 300 K, which is attributed to the low Curie temperature (T_c) of LSMO (T_c= 370 K for bulk). Thus, new materials in which magnetism persists well above room temperature should be explored for practical operation. Although Co and Fe have very high T_c (> 1000 K), these metal electrodes are often chemically unstable with organic layers and are susceptible to a conductivity mismatch problem with OSCs. Thus, ferro- or ferrimagnetic iron oxides, typically possessing T_c > 800 K, are considered as promising candidates to replace the LSMO electrode in organic spintronic devices.

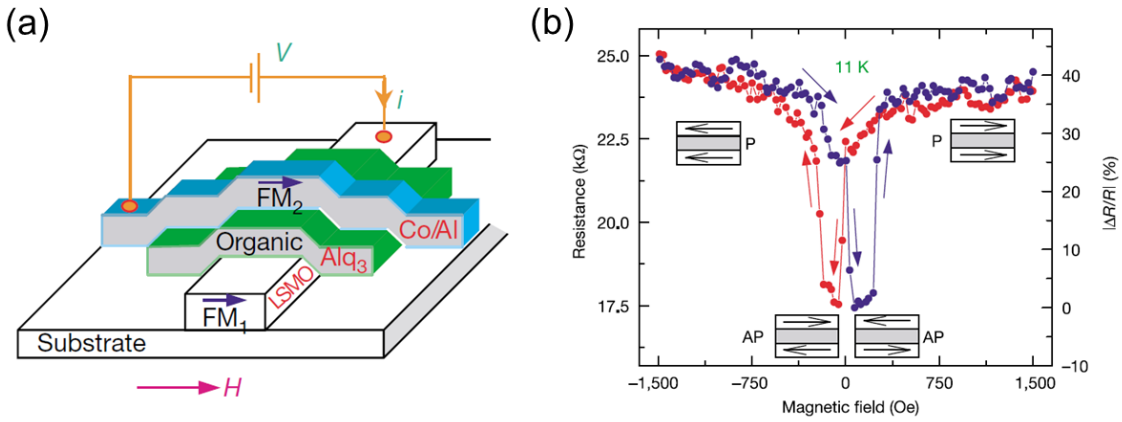

Figure 1.8 (a) Schematic structure of a vertical LSMO/Alq_3/Co OSV. (b) MR curve measured in a LSMO/Alq_3 (130 nm)/Co junction at 11 K reported by Ziong *et al.*[25] Reprinted figure with permission, copyright 2004 by Nature.

Recently, there have been intensive efforts to understand the fundamental mechanisms behind OMAR, which points to new spintronic functionalities unavailable with conventional inorganic materials. The distinctive characteristics of OMAR are understood to stem from the interface hybridization between ferromagnetic and molecular materials.[26-28]

With metallic spin filters, the spin-polarized hybridized interface states are broadened in energy with significant state densities at the Fermi level (Figure 1.9a).[27] This makes the molecule magnetic and "metallic" with a finite DOS for either one or both spin channels at E_F. The DOS mismatch for the two spin channels at E_F leads to interface spin polarization:

$$P \sim \frac{DOS_{\uparrow} - DOS_{\downarrow}}{DOS_{\uparrow} + DOS_{\downarrow}} \tag{1.7}$$

Barraud *et al.*[26] proposed a model that can explain the details of broadening and shifting of the molecular states by relating these phenomena to the molecule/FM metal interface hybridization properties.

On the other hand, in the case of resistive spin-filters, the spin-dependent hybridization gives rise to a spin splitting of the interface states above and/or below the Fermi level. However, the unavailability of states at the Fermi level creates a barrier height (φ) for charge injection into, or tunnelling through the molecule. However, since the injection current depends exponentially on the barrier height, a spin-dependent barrier height causes only one spin channel to efficiently filter through the molecule giving a large spin polarization of the current:

$$P \sim \frac{\exp(-\varphi_{\uparrow}) - \exp(-\varphi_{\downarrow})}{\exp(-\varphi_{\uparrow}) + \exp(-\varphi_{\downarrow})} \quad (1.8)$$

Typically, molecule-FM oxide junctions show the characteristic of resistive spin-filters.

Table 1.2 summarizes the difference between TMR and GMR in organic spintronic devices in terms of conduction mechanism, spacer type, reported MR value, and the relation between the electrode spin polarization and MR.

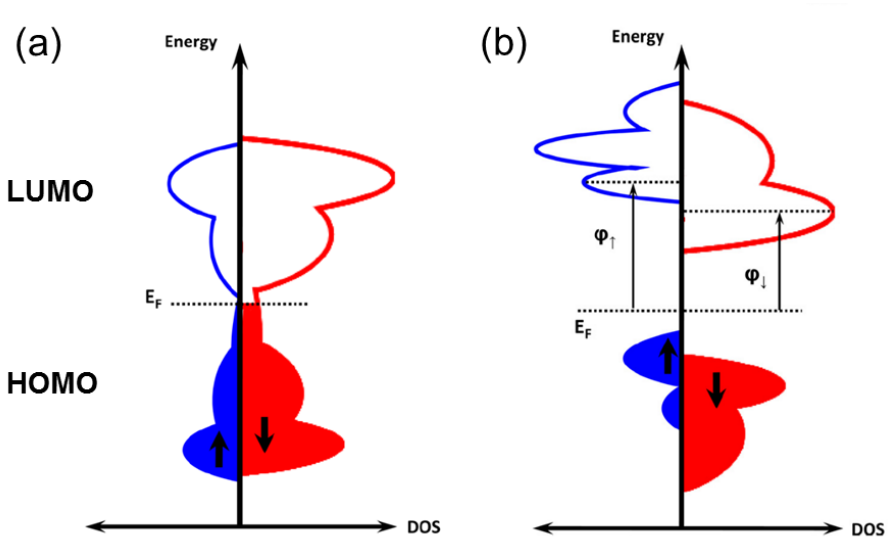

Figure 1.9 Schematic diagram of the spin-resolved local DOS of (a) metallic spin-filters and (b) resistive spin-filters, reprinted with permission from Ref. 27. Copyright 2014 by AIP Publishing.

Table 1.2 Comparison between TMR and GMR in organic spintronic devices, in terms of conduction mechanism, spacer type, reported MR value, and the relation between the electrode spin polarization and MR.

	TMR (tunnel junction)	GMR (spin valve)
Conduction	Tunnelling through a barrier	Injection +Ballistic band conduction/ Hopping via localized states
Spacer type /thickness (d)	Thin insulator d ~ a few nm	(semi)conductor d > 10nm
Reported MR(=$\Delta R/R_P$)	> 100% (low T)	often < 30% (low T) *c.f.* polymer ~ 80%
***P*(electrode) -MR relation**	Jullière model[18] Spinterface model[26]	*P* determines spin-resolved current density at interface upon injection/collection

1.4 Surface science of metal and metal oxides

Surfaces are technologically important in many fields, including catalysis, interfaces, membranes for gas separations, or semiconductor fabrication. Understanding the geometry and electronic structure of surfaces is important as many processes, such as heterogeneous catalytic activity, adhesion, and contact resistance, are critically dependent on the nature of the surface. In this regard, the control or manipulation of surface properties through physical and chemical processes is at the core of surface engineering.

1.4.1 Metal surface

Given that surfaces are created by cleaving along a given plane of the bulk material, the bond breakage upon surface truncation leads to electronic redistributions to stabilize the surface region. Unlike silicon or carbides with dangling bonds on their surfaces, metals generally do not require a drastic stabilization process such as surface reconstruction; surface relaxation often involves small variations in interlayer spacings. Among low-index surfaces, the one with the highest surface atom densities for a particular crystal structure is typically the most stable with the lowest surface energy, and thus plays an important role in actual crystals at equilibrium. For example, for bcc materials including Fe, the surface with the highest density of surface atoms is the (110) surface. When a metal surface forms, there occurs an intrinsic spilling of the electron cloud out of the surface; this results in the so-called surface dipole, whose magnitude depends on the surface plane direction and determines the work function.

1.4.2 Oxide surface

Contrary to metallic systems, whose surfaces are often well-defined, metal oxide surfaces are inherently complex systems; not only do they possess a variety of stoichiometries but also several structural phases can coexist even for one particular chemical composition.

In general, metal oxides can be classified into three different types, as shown in Figure 1.10.[29] Although Type 1 or 2 surfaces differ by the charge Q within a layer, neither of them has a net dipole moment (μ) in their repeat unit, thus, they are potentially stable. On

the contrary, Type 3 surfaces have a diverging electrostatic surface energy due to the presence of a non-zero dipole moment not only on the outer layers but also on all the repeat units throughout the material.[30] Type 3 is a so-called polar surface, which is essentially distinguished from non-polar rumpled or reconstructed surfaces that have a dipole moment confined to the surface region. Therefore, ideal polar surfaces are unstable according to classical electrostatics. In order to decrease the internal polarity perpendicular to the surface, major ionic relaxation and electron redistribution, as well as surface reconstruction are often found in of the case polar surfaces. Also, adsorption of foreign atoms or ions, coming from the residual atmosphere in the experimental set-up, or vacancy formation can occur as these processes provide for charge compensation.[30] The intrinsic defects or impurities in various forms are prevalent on metal oxide (particularly with polar oxides) surfaces, thus, controlling, characterizing, or measuring the surface configuration is among the most difficult tasks that physicists and chemists have to tackle in the field of surface science.

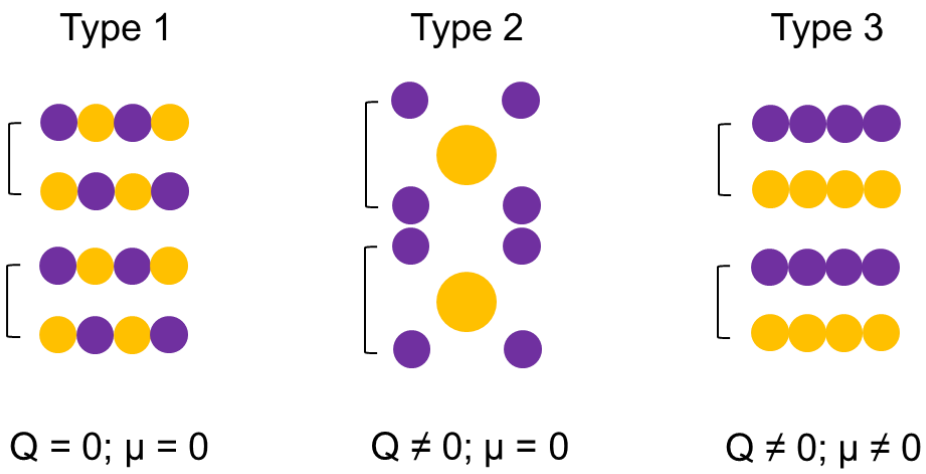

Figure 1.10 Classification of insulating surfaces according to Tasker.[29] Q and μ are the layer charge density and the dipole moment in the repeat unit perpendicular to the surface (indicated by a bracket), respectively.[30]

Experimentally, detailed information on the geometric and electronic properties of solid surfaces can be obtained from electron, ion, atom, and X-ray spectroscopies and scattering, which are performed primarily in high vacuum. These surface-sensitive experimental techniques include low-energy electron diffraction (LEED), photoelectron (UPS, XPS, XAS) and inverse photoelectron spectroscopies (IPES), scanning probe microscopies (STM), and atomic force microscope (AFM). Alongside with experimental techniques, computational approaches have been developed, in particular, first-principles calculations based on density functional theory (DFT). Since surface structures are highly affected by the sample preparation methods, a growing body of theoretical work has focused on elucidating the surface atomic configurations obtained under specific preparation conditions.[31]

1.5 Organic-inorganic interface

In many of the electronic devices based on organic materials, like OLEDs, OFETs, and photovoltaic cells, organic/inorganic heterojunctions play a critical role in the overall device performance by controlling carrier injection/collection or charge transport between different layers. Similarly, in the development of sensors, catalysts, and organic coatings, where more complex chemical reactions can take place, it is essential to understand the interactions between molecules (in the gas or liquid phase) and the metal or metal oxide substrates.

1.5.1 Interface energetics: Chemisorption and physisorption

The attachment of small molecules to oxides can occur through physisorption or chemisorption. It should be noted that there is not a sharp distinction between these two types of adsorption; by convention, it is typically accepted that the distinction occurs at a binding energy of approximately 0.5 eV per molecule (1 eV/molecule = 23.06 kcal/mol = 96.49 kJ/mol).[32]

In physisorption, the interaction is relatively weak on the order of 0.01–0.1 eV, comparable to van der Waals forces, weak coordinate bonds, or hydrogen bonds. There are typically small activation barriers for physisorption, and the dissociation energy of the modifier from the surface is low. This adsorption can be defined as bonds that can only occur at low temperatures on the surface such as the low temperature adsorption of noble

gas atoms on a metal surface. In chemisorption, new strong bonds are formed, with dissociation energies that can be orders-of-magnitude higher than physisorption, *i.e.*, on the order of 1–10 eV. Chemisorption is characterized by chemical specificity, with changes in electronic states detectable by suitable physical means, and an elementary step involving an activation energy. The resulting bonds can be either ionic or covalent, which result in a robust layer of adsorbate on the surface. Consequently, chemisorbed materials are not readily removed from the surface and require much harsher conditions for deliberate removal while physisorbed materials can easily be removed with the aid of heat or solvents. Another important aspect that accompanies the chemisorption of a material on a surface is the changes in the substrate structure due to surface relaxation or reconstruction.

1.5.2 Energy level alignment

When two materials are brought in proximity to each other, their geometric and electronic structures are altered from their isolated states due to the physical/chemical interactions at the interface. Thus, the optimal choice of materials for the given applications is, by and large, less predictable from the simple approach of considering the individual properties of each component in the system. If the system contains a heterogeneous interface between organic and inorganic materials of highly dissimilar nature, the picture is even more complex as the interface properties may greatly depart from those of the isolated elements and become more specific.

While inorganic materials usually form a continuum of states and electrons are delocalized within the bands, small molecules or oligomers have discrete energy levels that are referred to as molecular orbitals (MOs). Depending on their nature, MOs can be (1) strongly *localized* on certain functional groups or bonding regions within the molecule, or (2) *delocalized* over the entire molecule. Based on frontier molecular orbital theory, first developed by Fukui in 1952,[33] most chemical reactions can be mainly associated with the "Highest Occupied Molecular Orbital" (HOMO) and "Lowest Unoccupied Molecular Orbital" (LUMO). These orbitals can be viewed as counterparts to the valence band and conduction band of inorganic semiconductors, although their natures are quite distinct. As shown in Figure 1.11a, an isolated organic molecule normally exhibits a substantial energy gap (fundamental gap) between the electronic states defining the ionization potential (IP) and electron affinity (EA), which are responsible for hole and electron transport in OSCs, respectively.

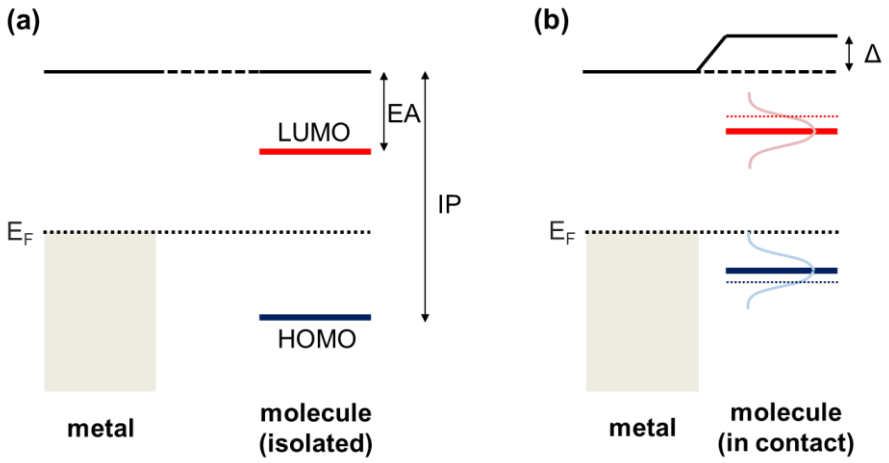

Figure 1.11 Schematic representation of the molecular energy levels when (a) a molecule is isolated from the metallic surface and (b) is brought near the metal contact. In (b), the vacuum level can shift as a result of the induced interface electrostatic dipole (Δ) and the fundamental gap reduces due to gap renormalization.

When the molecule approaches the metal surface that has a rather wide band partially filled with electrons up to the Fermi level (E_F), there are two key impacts on molecular levels: 1. An *energy level broadening* coming from hybridization of the molecular and metal electronic states; it can ranges from meV up to eV; 2. An *energy shift* of the molecular levels from their initial positions in the isolated molecule due to the combined influence of polarization / images charges (gap renormalization), pushback effects, and interfacial dipoles (Δ). Both the energy-level broadening and shift highly depend on the strength of the electronic coupling of the frontier molecular orbitals to the extended states in the metal at the interface. Therefore, vacuum evaporation of molecular films on clean metal surfaces is usually expected to yield distinctive MO interfaces that deviate from the

Schottky-Mott limit where the vacuum level alignment rule is obeyed. The variations in molecular energy levels have been measured by UPS and IPES, which probe the interfacial electronic structure of occupied and unoccupied states, respectively. It is important to note that the interfacial electronic structures of organic/inorganic hybrid junctions do depend on molecular orientations[34] and binding modes[35] as well as packing structures[36] on the surface. Despite the extensive application of experimental techniques such as XPS, AFM, Raman spectroscopy, and Fourier transform infrared spectroscopy to obtain chemical and structural information of adsorbed molecules and substrates, the direct characterization of the local electronic and geometric structures of and around the molecules remains a challenging task. For this reason, numerous theoretical studies, particularly quantum-mechanical calculations, have served to provide a deeper understanding of the interfacial processes that govern the working principle of single-molecule electronic junctions and organic electronic devices.

1.6 Thesis objectives and outlook

Our goal in this Thesis is to contribute to a fundamental understanding of the surface and interface chemistry of iron and iron oxides, based on a robust theoretical approach. Although iron corrodes easily, its oxides hold promise for applications in many industrial fields; both aspects will be addressed throughout this Thesis. We have laid the ground work in Chapter 1 by providing a brief introduction to the material properties of iron and iron oxides, along with a discussion on corrosion science and organic spintronics. These two topics will be explored in greater detail in the following chapters. These discussions

on the basic concepts of surface and interface science serve as a helpful gateway to the next chapters. The Chapters in this Thesis are essentially organized around going from simple to complex systems, beginning with a consideration of the structure and properties of bulk iron oxides, then moving to oxide surfaces, and concluding with organic-inorganic interface systems.

Chapter 2 focuses on the computational methodologies used for the evaluation of the geometric and electronic structures of iron and iron oxides under various conditions. We begin with a description of the Schrödinger equation and the approximations needed to derive the electronic-structure methods employed in this Thesis. We briefly review density functional theory (DFT), advanced DFT-based techniques (DFT+*U* and hybrid functionals), symmetry-adapted perturbation theory, and the many-body perturbation theory *GW* approximation. Next, we provide a brief review of first-principles thermodynamics that are used to determine the equilibrium surface configuration in given environmental/electrochemical conditions, such as partial pressures of oxygen and water, temperature, solution pH, and electrode potential. The last part of Chapter 2 is devoted to the basic description of *ab initio* molecular dynamics, which combines the description of bond-breaking/forming based on quantum mechanics with the inclusion of the dynamical motions of atoms and molecules.

Chapter 3 highlights work conducted to find a robust theoretical technique to describe the strongly correlated iron oxides of hematite, magnetite, and maghemite. In order to move beyond the well-known failure of conventional DFT approaches to provide accurate descriptions of the electronic structures of iron oxides, we assess the accuracy of several theoretical extensions of DFT including the Hubbard *U* correction on Fe 3*d* electrons

(DFT+*U*), the screened Heyd-Scuseria-Ernzerhof hybrid functional, and the *GW* approximation. This validation procedure has allowed us to determine appropriate computational techniques that can be applied to the materials of interest in the subsequent chapters.

Chapter 4 extends our earlier work on bulk iron oxides to surfaces of two representative iron oxide surfaces, magnetite (111) and hematite (0001). Given that the exposed surface can be very complex depending on the environment, we build a robust theoretical platform to predict the most favorable surface in gas-exposure conditions based on first-principles thermodynamics. Our focus is not only on the theoretical prediction of the relative stabilities among various surface models but also on the physical and chemical properties of the surface such as local geometries, spin polarization, and surface core-level shifts.

In Chapter 5, the modification of metal surfaces by self-assembled monolayers (SAMs) is considered in the context of iron corrosion prevention. Here, the interfacial geometric and electronic structures of iron (or iron oxide) with SAMs have been evaluated with respect to adsorption reaction energies, packing morphologies, and interface electronic structure based on quantum mechanical methods and molecular dynamics simulations. The central theme of this Chapter is to elucidate the impact that substrate characteristics as well as molecular functionalization have on corrosion inhibition efficiency.

As in Chapter 5, Chapter 6 also involves organic-inorganic interfaces, this time in the context of development of an efficient magnetic junction for organic spintronics, based on iron-based ferromagnetic electrodes. Here, the distinct electronic and magnetic

properties of interfaces between representative π-conjugated molecules and the iron surface are explored. This work is then extended to the half-metallic magnetite substrate, which can be further modified with cation vacancies and surface hydrogenation. This Chapter highlights that not only the choice of materials but also the details of interface structures, such as substrate crystal orientation or termination and molecular adsorption geometries, play a significant role in the nature of hybrid interface states.

Chapter 7 serves as an opportunity to summarize the findings reported throughout this Thesis and to put these results in context with one another. We conclude with a discussion regarding possible future directions of this research.

Appendix A provides a more detailed explanation of first-principles thermodynamics taking account of zero-point vibrational energy and entropy contribution corrections, as well as illustrating how to determine physically accessible ranges for oxygen gas and water vapor in this theoretical approach.

Appendix B addresses energy level alignment at the organic-inorganic interface with the *GW* approximation. This work, while involving the interface electronic structure, has been placed in an appendix as its focus is more related to methodological aspects. Our goal here was to employ G_0W_0 calculations to predict the energy levels of the adsorbed molecular layer on the substrate, which leads to better agreement with PES/IPES data than standard DFT. The results based on hybrid functionals and the DFT+Σ^{axc} approach are also explored to examine their prediction ability.

1.7 References

[1] Cornell, R. M.; Schwertmann, U. *The iron oxides: structure, properties, reactions, occurrences, and uses*; 2nd, completely rev. and extended ed.; Wiley-VCH: Weinheim, 2003.

[2] Guo, H. B.; Barnard, A. S. *J. Mater. Chem. A* **2013**, *1*, 27.

[3] Stampfl, C.; Ganduglia-Pirovano, M. V.; Reuter, K.; Scheffler, M. *Surf. Sci.* **2002**, *500*, 368.

[4] Marcus, P. *Corrosion mechanisms in theory and practice*; 3rd ed.; CRC Press: Boca Raton, 2012.

[5] Fromhold, A. T. *Theory of metal oxidation*; North Holland Pub. Co.; American Elsevier Pub. Co.: Amsterdam, New York, 1975.

[6] Leibbrandt, G. W. R.; Hoogers, G.; Habraken, F. H. P. M. *Phys. Rev. Lett.* **1992**, *68*, 1947.

[7] Roosendaal, S. J.; Vredenberg, A. M.; Habraken, F. H. P. M. *Phys. Rev. Lett.* **2000**, *84*, 3366.

[8] Ruban, A.; Hammer, B.; Stoltze, P.; Skriver, H. L.; Norskov, J. K. *J. Mol. Catal. A-Chem.* **1997**, *115*, 421.

[9] Hammer, B.; Norskov, J. K. *Adv. Catal.* **2000**, *45*, 71.

[10] Bassani, G. F.; Fumi, F.; Tosi, M. P.; Società italiana di fisica. *Highlights of condensed-matter theory*; North-Holland ;Sole distributor for the USA and Canada, Elsevier Science Pub. Co.: Amsterdam ; New York, 1985.

[11] Herzing, A. A.; Kiely, C. J.; Carley, A. F.; Landon, P.; Hutchings, G. J. *Science* **2008**, *321*, 1331.

[12] Hermanek, M.; Zboril, R.; Medrik, N.; Pechousek, J.; Gregor, C. *J. Am. Chem. Soc.* **2007**, *129*, 10929.

[13] Cheng, F. Y.; Liang, J.; Tao, Z. L.; Chen, J. *Adv. Mater.* **2011**, *23*, 1695.

[14] Vardeny, Z. V. *Organic spintronics*; CRC Press/Taylor & Francis: Boca Raton, 2010.

[15] Baibich, M. N.; Broto, J. M.; Fert, A.; Vandau, F. N.; Petroff, F.; Eitenne, P.; Creuzet, G.; Friederich, A.; Chazelas, J. *Phys. Rev. Lett.* **1988**, *61*, 2472.

[16] Binasch, G.; Grunberg, P.; Saurenbach, F.; Zinn, W. *Phys. Rev. B* **1989**, *39*, 4828.

[17] Galbiati, M. *Molecular Spintronics*; Springer International Publishing: Switzerland, 2016.

[18] Julliere, M. *Phys. Lett. A* **1975**, *54*, 225.

[19] Miyazaki, T.; Tezuka, N. *J. Magn. Magn. Mater.* **1995**, *139*, L231.

[20] Moodera, J. S.; Kinder, L. R.; Wong, T. M.; Meservey, R. *Phys. Rev. Lett.* **1995**, *74*, 3273.

[21] Ikeda, S.; Hayakawa, J.; Ashizawa, Y.; Lee, Y. M.; Miura, K.; Hasegawa, H.; Tsunoda, M.; Matsukura, F.; Ohno, H. *Appl. Phys. Lett.* **2008**, *93*, 082508.

[22] Butler, W. H.; Zhang, X. G.; Schulthess, T. C.; MacLaren, J. M. *Phys. Rev. B* **2001**, *63*.

[23] Sun, D. L.; Ehrenfreund, E.; Vardeny, Z. V. *Chem. Commun.* **2014**, *50*, 1781.

[24] Dediu, V.; Murgia, M.; Matacotta, F. C.; Taliani, C.; Barbanera, S. *Solid State Commun.* **2002**, *122*, 181.

[25] Xiong, Z. H.; Wu, D.; Vardeny, Z. V.; Shi, J. *Nature* **2004**, *427*, 821.

[26] Barraud, C.; Seneor, P.; Mattana, R.; Fusil, S.; Bouzehouane, K.; Deranlot, C.; Graziosi, P.; Hueso, L.; Bergenti, I.; Dediu, V.; Petroff, F.; Fert, A. *Nature Phys.* **2010**, *6*, 615.
[27] Raman, K. V. *Appl. Phys. Rev.* **2014**, *1*, 031101.
[28] Galbiati, M.; Tatay, S.; Barraud, C.; Dediu, A. V.; Petroff, F.; Mattana, R.; Seneor, P. *MRS Bull.* **2014**, *39*, 602.
[29] Tasker, P. W. *J. Phys. C Solid State* **1979**, *12*, 4977.
[30] Noguera, C. *J. Phys.-Condens. Mat.* **2000**, *12*, R367.
[31] Parkinson, G. S. *Surf. Sci. Reports* **2016**, *71*, 272.
[32] Giordano, A. J., Georgia Institute of Technology, 2014.
[33] Fukui, K.; Yonezawa, T.; Shingu, H. *J. Chem. Phys.* **1952**, *20*, 722.
[34] Duhm, S.; Heimel, G.; Salzmann, I.; Glowatzki, H.; Johnson, R. L.; Vollmer, A.; Rabe, J. P.; Koch, N. *Nature Mater.* **2008**, *7*, 326.
[35] Li, H.; Paramonov, P.; Bredas, J. L. *J. Mater. Chem.* **2010**, *20*, 2630.
[36] Raman, K. V.; Watson, S. M.; Shim, J. H.; Borchers, J. A.; Chang, J.; Moodera, J. S. *Phys. Rev. B* **2009**, *80*,195212.

CHAPTER 2. THEORETICAL METHODOLOGY

In this chapter, we review the computational methodologies used to study the geometric and electronic structures of systems consisting of iron, iron oxides, and organic molecules. We first overview density functional theory approaches with representative approximate functionals and corrections including DFT+*U*, hydrid functionals, and van der Waals (dispersion) corrections. This is followed by the description of two advanced techniques: the *GW* approximation and symmetry-adapted perturbation theory. In Section 2.2, we briefly explain the basic concepts of first-principles thermodynamics, in particular with a view on calculating oxide surface free energies as a function of temperature, partial pressure, solution pH, and electrode potential. Lastly, *ab initio* molecular dynamics is briefly described in Section 2.3.

2.1 Quantum-mechanical calculations

2.1.1 Schrödinger equation

There are many fields within the physical sciences and engineering where scientific and technological progress is initiated from understanding and controlling the electronic structures of materials systems including molecules, bulk solids, and surfaces. However, finding solutions to the fundamental equation that describes the quantum behavior of

atoms and molecules, *i.e.*, the *Schrödinger equation*, is not a trivial task since the situation we are interested in, where multiple electrons are interacting with multiple nuclei, is too complicated to be exactly solved.

In many-body (N-electron) electronic-structure calculations based on Born-Oppenheimer approximation and neglecting relativistic effects, a stationary electronic state can be described by a wavefunction, $\Psi_{elect}(\boldsymbol{r};\boldsymbol{R})$, satisfying the time-independent electronic *Schrödinger equation:*

$$\left[\sum_{i=1}^{N} -\frac{1}{2}\nabla_i^2 + \sum_{i=1}^{N} V(\boldsymbol{R}_i) + \sum_{i=1}^{N}\sum_{j<i}^{N} U(\boldsymbol{r}_i,\boldsymbol{r}_j)\right]\Psi_{elec}(\boldsymbol{r};\boldsymbol{R}) = E_{elec}(\boldsymbol{R})\Psi_{elect}(\boldsymbol{r};\boldsymbol{R}) \qquad (2.1)$$

where the three terms in brackets on the left define $-\frac{1}{2}\nabla_i^2$ as the kinetic operator for each electron; $V(\boldsymbol{R}_i)$ as the operator describing the interaction energy between each electron and the collection of atomic nuclei; and $U(\boldsymbol{r}_i,\boldsymbol{r}_j)$ as the operator describing the interaction among the electrons.[1] Solving Schrödinger's equation gives the sets of electronic total energies $E_{elec}(\boldsymbol{R})$.

For the Hamiltonian we have chosen, the electronic wave function, which is a function of each of the spatial coordinates, can be approximated to a product of individual electron spin orbitals (χ_i) expressed in a Slater determinant, which ensures the proper anti-symmetry of the wavefunction:

$$\Psi(x_1, x_2, \cdots, x_N) = \frac{1}{\sqrt{N!}}\begin{vmatrix} \chi_i(x_1) & \cdots & \chi_k(x_1) \\ \vdots & \ddots & \vdots \\ \chi_i(x_N) & \cdots & \chi_k(x_N) \end{vmatrix} \qquad (2.2)$$

By use of a Slater determinant the interchange of any two electrons, corresponding to the interchange of two rows, changes the sign of the determinant and if two electrons occupy the same spin orbital, corresponding to two columns being equal, the determinant is zero.

The total wavefunction, $\Phi(\boldsymbol{r},\boldsymbol{R})$, can be expanded in terms of the electronic wavefunctions and a set of pre-selected nuclear wavefunctions, ϕ, defined as:

$$\Phi(\boldsymbol{r},\boldsymbol{R}) = \sum_{k} \chi_k(\boldsymbol{r};\boldsymbol{R})\phi_k(\boldsymbol{R}) \tag{2.3}$$

When nonadiabatic coupling matrix elements are neglected and the wavefunction is real, the following equation can be obtained for the motion of the nuclei on a given Born-Oppenheimer potential energy surface:

$$[T_N(\boldsymbol{R}) + T''_{kk}(\boldsymbol{R}) + E_{elec}(\boldsymbol{R})]\phi_k(\boldsymbol{R}) = E\phi_k(\boldsymbol{R}) \tag{2.4}$$

This equation shows that the nuclei move in a potential field set up by the electrons. The potential energy at each point is given primarily by the expectation value of the electronic energy, $E_{elec}(\boldsymbol{R})$, with a small correction factor, $T''_{kk}(\boldsymbol{R})$, *i.e.*, diagonal Born-Oppenheimer correction.

Such a wavefunction-based method extends from the simplest Hartree-Fock (HF) method to more advanced techniques, collectively referred to as post-HF methods, such as Møller–Plesset perturbation theory, multi-configurational self-consistent field (SCF), configuration interaction (CI), coupled cluster (CC), and complete active space SCF. At the small-molecule level, obtaining the full wavefunction solutions to Schrödinger

equation can be achieved in a reasonable computational effort; however, when the systems are larger and complex, it remains challenging to efficiently apply high-level post-HF methods since the computational cost quickly becomes enormous.

2.1.2 Density functional theory (DFT)

2.1.2.1 Standard DFT with exchange-correlation functional

As a practical alternative, density functional theory (DFT) has been a phenomenally successful and widespread approach for accurately calculating and predicting various physical and chemical properties. The field of density functional theory rests on two fundamental mathematical theorems proved by Hohenberg and Kohn,[2] and the derivation of a set of equations by Kohn and Sham[3] in the mid-1960s. The first theorem states that: *The ground-state energy from Schrödinger's equation is a unique functional of the electron density*. Thus, there exists a one-to-one mapping between the ground-state wave function and the ground-state electron density, $\rho(\boldsymbol{r})$,

$$\rho(\boldsymbol{r}) = \sum_{i}^{N} |\psi_i(r)|^2 \tag{2.5}$$

which points out that the number of coordinates can shrink down from 3N to three; at the same time, the charge density contains a vast amount of the information that is actually physically observable from the direct solution of the Schrödinger equation.

Although the first Hohenberg–Kohn theorem rigorously proves that a functional of the electron density exists and can be used to solve the Schrödinger equation, the theorem

does not provide what the functional actually is. The second Hohenberg–Kohn theorem defines an important property of the functional: *The electron density that minimizes the energy of the overall functional is the true electron density corresponding to the full solution of the Schrödinger equation.* If the "true" functional form were known, then we could vary the electron density until the energy from the functional is minimized, giving us a prescription for finding the relevant electron density. This variational principle is used in practice with approximate forms of the functional.

In Kohn-Sham (KS) theory, finding the right electron density can be expressed in a way that involves solving a set of equations in which each equation only involves a single electron. The generalized expression for the ground state energy from the KS equation is formulated as:

$$E[\rho(\boldsymbol{r})] = T_s[\rho(\boldsymbol{r})] + V_{ne}[\rho(\boldsymbol{r})] + J[\rho(\boldsymbol{r})] + E_{XC}[\rho(\boldsymbol{r})] \tag{2.6}$$

where each term is defined as:

$$T_s[\rho(\boldsymbol{r})] = \sum_{i}^{N} \left\langle \psi_i \middle| -\frac{1}{2}\nabla_i^2 \middle| \psi_i \right\rangle \tag{2.7}$$

$$V_{ne}[\rho(\boldsymbol{r})] = \int \rho(\boldsymbol{r}) v(r) dr \tag{2.8}$$

$$J[\rho(r)] = \frac{1}{2}\int\int \frac{\rho(\boldsymbol{r})\,\rho(\boldsymbol{r}')}{|\boldsymbol{r}-\boldsymbol{r}'|} d\boldsymbol{r}\, d\boldsymbol{r}' \tag{2.9}$$

Here, the forms of the first three functionals are explicitly known: the electron kinetic energies ($T_s[\rho(\boldsymbol{r})]$), the Coulomb interactions between the electrons and the nuclei

($V_{ne}[\rho(\boldsymbol{r})]$), and the Coulomb interactions between pairs of electrons ($J[\rho(\boldsymbol{r})]$), Hartree term). The other term in the energy functional, $E_{XC}[\rho(\boldsymbol{r})]$, is the exchange–correlation (XC) functional, which includes all the quantum mechanical effects that are not included in the "known" terms. With the given XC potential, V_{XC}, the XC energy can be formulated as:

$$E_{XC}[\rho(\boldsymbol{r})] = \frac{\partial E_{XC}[\rho(\boldsymbol{r})]}{\partial \rho(\boldsymbol{r})} \tag{2.10}$$

To solve the KS equations, we need to define the Hartree potential, and to define the Hartree potential, we need to know the electron density. However, to find the electron density, we must know the single-electron wave functions, and to know these wave functions requires solving the KS equations. Therefore, these should be solved iteratively, which leads to the solution of the Kohn–Sham equation being self-consistent.

Initially, the exchange-correlation potential was derived from the uniform electron gas model, leading to local density approximation (LDA),[4] and its extensions including the generalized gradient approximation (GGA)[5,6] and meta-GGA.[7] To date, GGA functionals are widely used in finite and periodic calculations of both inorganic and organic crystals. Due to the missing exact exchange in these GGA parameterizations, functionals based on GGA have several drawbacks, in particular, an inability to correctly describe ground-state charge transfer and a propensity to underestimate the band gap. In some cases, for small band-gap materials, wrong occupation numbers are obtained for frontier (valence/conduction) bands, leading to the prediction of the metallic character of the system.[8] Also, these fucntionals often provide a quite poor representation of other physical properties, including equilibrium crystal structure, magnetic moments, or

vibrational spectra. In order to alleviate these issues, electron exchange and correlation interactions should be taken into account more reliably.

2.1.2.2 DFT+*U*

In general, problems of standard DFT can be traced back to the tendency of most XC functionals to over-delocalize valence electrons and to over-stabilize metallic ground states. Other inaccuracies of XC functionals include the imprecise account of the exchange interaction and the consequent incomplete cancellation of the electronic self-interaction contained in classical (density-density) Coulomb integrals.

One of the simplest models that have been formulated to rationalize (albeit in a semi-quantitative way) the physics of correlated materials, is the Hubbard model whose real-space second quantization formalism is ideally suited to describe systems with electrons localized on atomic orbitals. In its simplest, one-band incarnation, the Hubbard Hamiltonian can be written as follows:[9]

$$H_{Hub} = t \sum_{<i,j>,\sigma} (c_{i,\sigma}^{\dagger} c_{j,\sigma} + h.c.) + U \sum_{I} n_{i,\uparrow} n_{i,\downarrow} \qquad (2.11)$$

where $< i, j >$ denotes nearest-neighbor atomic sites, $c_{i,\sigma}^{\dagger}$, $c_{j,\sigma}$, $n_{i,\sigma}$ are electronic creation, annihilation and number operators for electrons of spin σ on site *i*. In virtue of strong localization, the Coulomb repulsion is only accounted for between electrons on the same atom through a term proportional to the product of the occupation numbers of atomic states on the same site, whose strength is *U* (the "Hubbard U"). When electrons

are strongly localized, their motion is described by a hopping process from one atomic site to its neighbors (first term of Eq. (2.11)) whose amplitude *t* is proportional to the dispersion (the bandwidth) of the valence electronic states and represents the single-particle term of the total energy.

In DFT+*U* method,[10] the Hubbard Hamiltonian is used to describe strongly correlated electronic states (typically, localized *d* or *f* orbitals), while the rest of valence electrons are treated at the standard level of approximation, which can be achieved with the following general functional form:

$$E^{DFT+U}[\rho(\boldsymbol{r}), \{n_{Ilm\sigma}\}] = E^{DFT}[\rho(\boldsymbol{r})] + E_{Hub}[\{n_{Ilm\sigma}\}] - E^{dc}[\{N_{Il\sigma}\}] \quad (2.12)$$

where E^{DFT} is the DFT energy of the system based on the total electron density, $\rho(\boldsymbol{r})$, $E_{Hub}$is the term that contains electron-electron interactions as modeled in the Hubbard Hamiltonian (Equation 2.11), *i.e.*, the on-site energy, and E^{dc} is a double-counting term that corrects for the fact that on-site interactions are included in both $E^{DFT}$and E_{Hub}. $n_{Ilm\sigma}$ corresponds to the number of electrons with spin σ; angular momentum, l; and magnetic quantum number, m that are localized on atom I.[11]

Throughout the Thesis, we will focus on the DFT+*U* formalism developed by Dudarev *et al.*[12] where the spherically average Coulomb and exchange interactions between electrons of angular momentum *l* that are localized on the same *I*, U_{Il} and J_{Il}, respectively, are used to provide a HF-like treatment of the on-site interaction energies:

$$E^{DFT+U}[\rho(\boldsymbol{r}), \{n_{Ilm\sigma}\}] = E^{DFT}[\rho(\boldsymbol{r})] + \sum_{I,l,m,\sigma} \frac{(U_{Il} - J_{Il})}{2}(n_{Ilm\sigma} - n_{Ilm\sigma}^2) \quad (2.13)$$

2.1.2.3 Hybrid functionals

Alternatively, a portion of Hartree-Fock exact exchange (E_X^{HF}) can be integrated into standard DFT functionals to overcome the local nature of LDA and GGA, which is the basis for the so-called *hybrid functionals*. There are various types of hybrid functionals that have been developed with a different mixing of local and nonlocal exchange and number of parameters. In this Chapter, we will focus on a few representative functionals: B3LYP, PBE0, HSE, and long-range corrected functionals.

The Becke, Lee, Yang, and Parr (B3LYP) hybrid functional[13] is one of the most widely used functionals in quantum chemistry calculations. This functional can be formulated as:

$$E_X^{B3LYP} = 0.80E_X^{LSDA} + 0.20E_X^{HF} + 0.72\Delta E_X^{B88} \tag{2.14}$$

$$E_C^{B3LYP} = 0.19E_C^{VWN} + 0.81E_C^{LYP} \tag{2.15}$$

where the numerical parameters are determined by fitting to experimental data.

Another commonly used parameterization scheme is based on the addition of the HF exchange to the PBE functional (PBE0),[14] which is defined as:

$$E_{XC}^{PBE0} = \frac{1}{4}E_X^{HF} + \frac{3}{4}E_X^{PBE} + E_C^{PBE} \tag{2.16}$$

Another commonly used parameterization scheme is based on the addition of the HF exchange to the PBE functional (PBE0),[14] which is defined as:

$$E_{XC}^{PBE0} = \frac{1}{4}E_X^{HF} + \frac{3}{4}E_X^{PBE} + E_C^{PBE} \tag{2.16}$$

Hybrid functionals often give reasonably accurate predictions of band gaps and lead to more accurate total energies and geometries. However, such functionals are computationally more demanding because of the slow decay of the HF exchange, and become intractable for extended systems.[15] Thus, short-range functionals, such as the screened range-separated hybrid functional[16,17] proposed by Heyd, Scuseria, and Ernzerhof (HSE) seem to be an effective alternative to standard hybrid functionals.

In range-separated hybrid functionals (RSH), the spatial decay of the HF exchange interaction is accelerated by substitution of the full 1/r Coulomb potential with a screened one. The functional separates the exchange energy into short-range (SR) and long-range (LR) components:

$$\frac{1}{r_{12}} = \frac{[1 - \mathrm{erf}(\omega r_{12})]}{r_{12}} + \frac{\mathrm{erf}(\omega r_{12})}{r_{12}} \tag{2.17}$$

where r_{12} indicates interelectronic distance and ω represents an adjustable parameter that defines the partitioning between the SR and LR.

In HSE, the SR exchange contains both HF and PBE terms while the LR exchange interactions consist only of PBE exchange. The correlation part is PBE in all regions. The resulting functional can be written as:

$$E_{xc}^{HSE} = \alpha E_x^{HF,SR}(\omega) + (1-\alpha)E_x^{PBE,SR}(\omega) + E_x^{PBE,LR}(\omega) + E_c^{PBE} \tag{2.18}$$

For HSE, the value α = 0.25 is the usual portion of HF exchange used (it was chosen from perturbation theory). One variation is the so-called HSE06 functional using a = 0.25 and ω = 0.11 bohr^{-1}, as it can give accurate predictions of enthalpies of formation, ionization potentials, and electron affinities for molecules, as well as lattice constants and band gaps of solids in general.[18]

More recently, it has been suggested that further improvement can be obtained by the generalization of the RSH scheme: combining a fraction of SR HF exchange that would improve the description of the localized orbitals, with LR HF exchange that is essential for gap prediction.[19] Here, the Coulomb operator can be partitioned as:

$$\frac{1}{r_{12}} = \frac{1 - [\alpha + \beta \operatorname{erf}(\omega r_{12})]}{r_{12}} + \frac{\alpha + \beta \operatorname{erf}(\omega r_{12})}{r_{12}} \tag{2.19}$$

where α corresponds to the HF exchange mixing contribution over the whole range by a factor of α, and β allows the DFT counterpart to be included over the whole range by a factor of $1 - (\alpha + \beta)$ with range separation parameter ω. In many cases, $\alpha + \beta$ is fixed to 1 to guarantee that full HF exchange is obtained asymptotically.[20]

Janak's theorem states that the energy of the highest occupied molecular orbital (HOMO) or energy of the valence band should be mathematically equal to the vertical ionization potential (IP) of the system; this exact condition should be obeyed for any stable ionic state of the system. Thus, one can seek to reach the optimal value of ω via satisfaction of the above condition by minimizing the following target function for the N-electron system:[21]

$$J^2 = [\varepsilon_H(N + i) - IP(N + i)]^2 \tag{2.20}$$

where $\varepsilon_H(N+i)$ is the HOMO eigenvalue of the $(N+i)$-electron system. By applying this non-empirical "tuning" procedure, excellent agreement was obtained between calculations and experiment for ground and excited states for a variety of systems.[22,23]

2.1.2.4 Dispersion correction

To unravel the structural and electronic properties of organic molecule-surface systems in this study, we carried out van der Waals (vdW)-corrected DFT calculations. When vdW interactions play a crucial role in adsorption processes, LDA, GGA, and hybrid functionals fail to describe the adsorption of molecules on metals since these functionals are fundamentally unable to describe the non-local character of the correlation effects responsible for the attractive vdW forces. This often leads to a substantial overestimation of adsorption heights and an underestimation of binding energies, especially for weakly interacting molecules.[24] It should be noted that although the vdW correction does not directly modify the calculated charge density, it can play a critical role on the interface electronic structures by changing the equilibrium distances and configurations between the adsorbate and substrate, through the variational process.

In this Thesis, we have chosen the semiclassical DFT-D3 method developed by Grimme coupled with the Becke-Johnson damping method where dispersion is taken into account as the sum of atomic pairwise contributions.[25] In the D3 method, the R^{-6}-dependent dispersion coefficient ($C_{6,i,j}$) changes as a function of the atom coordination number in such a way that the local geometry of each atomic species i (j) can be adequately

reflected in the dispersion description. This allows one to distinguish among the different hybridization states of atoms in molecules.

2.1.3 *GW* approximation (GWA)

To overcome the limitations of DFT-based approaches, the *GW* approximation (GWA) can be a promising solution in order to model the charge/spin transport by considering the scattering of quasiparticles (QPs). Since GWA, originally formulated by Hedin,[26] uses the many-body Green's function to solve the quasiparticle equations, with a perturbative expansion for the self-energy operator, it can calculate accurate QP energy gaps close to the experimental values. Despite its complexity and high computational cost, GWA is becoming increasingly accessible through high-performance computing systems and exploited to calculate the QP energy gaps in molecules,[27] organic crystals,[22] and transition metal oxides.[28] Hence, a much better understanding of organic/inorganic interfaces and related device performance can be achieved via the accurate prediction of the interface electronic structure with GWA.

In GWA with a plane-wave basis set, the quasiparticle energy ($E_{n\boldsymbol{k}}$) for the *n*th band with the Bloch-vector **k** is determined perturbatively based on the DFT results:[28]

$$\left(-\frac{1}{2}\Delta^2 + V_{ext}(\boldsymbol{r}) + V_H(\boldsymbol{r})\right)\psi_{n\mathbf{k}}(\boldsymbol{r}) + \int \Sigma(\boldsymbol{r}, \boldsymbol{r}', \omega)\psi_{n\mathbf{k}}(\boldsymbol{r}')d\boldsymbol{r}' = E_{n\boldsymbol{k}}\psi_{n\mathbf{k}}(\boldsymbol{r}) \quad (2.21)$$

where $-\frac{1}{2}\Delta^2$ corresponds to the kinetic energy operator; $V_{ext}(\boldsymbol{r})$, to the ionic potential; $V_H(\boldsymbol{r})$, to the Hartree potential; and $\Sigma(\boldsymbol{r}, \boldsymbol{r}', \omega)$, to the non-local and energy-dependent self-energy operator which is described as:

$$\Sigma(r, r', \omega) = \frac{i}{4\pi}\int_{-\infty}^{\infty} e^{i\omega'\delta} G(\boldsymbol{r}, \boldsymbol{r}', \omega + \omega') W(\boldsymbol{r}, \boldsymbol{r}', \omega') d\omega' \tag{2.22}$$

Here, *G* denotes the Green's function; *W*, the screened Coulomb interaction; and δ, an infinitesimal. Since the Green's function is the inverse of the Hamiltonian:

$$G^{-1} = (\omega - H) \tag{2.23}$$

And the Green's function of a KS Hamiltonian at frequency ω is given by:

$$G(\boldsymbol{r}, \boldsymbol{r}', \omega) = \sum_n \frac{\psi_n(\boldsymbol{r})\psi_n^*(\boldsymbol{r}')}{\omega - \epsilon_n + i\eta sgn(\epsilon_n - \mu)} \tag{2.24}$$

The Green's function $G(\boldsymbol{r}, \boldsymbol{r}', t - t')$ describes the propagation of a particle from $(\boldsymbol{r}, t)$ to $(\boldsymbol{r}', t)$, *i.e.*, provided we have particle at position $\boldsymbol{r}$ at time t, $G(\boldsymbol{r}, \boldsymbol{r}', t - t')$ is the probability of finding it at position $\boldsymbol{r}'$ at time t'. The self-energy Σ is made up of all Feynman diagrams with one in- and one out-going propagator line, and the two first-order diagrams represent the Hartree and exchange interactions.

In the present implementation of VASP,[29] the *GW* approximation is applied perturbatively to the DFT wavefunctions and one-electron energy. This leads to several different *GW* approaches depending on whether these quantities in *G* and *W* operators are self-consistently iterated or not. The most basic level is G_0W_0, which corrects the initial DFT eigenvalues using only a one-shot perturbation. In typical main-group

semiconductors or oxides such as Si or MgO, it was found that G_0W_0 calculations considerably improve the band gap in comparison to DFT results, although substantial underestimations still remain.[30] *GW* calculations with higher self-consistency level are divided into two groups. One is the eigenvalue-only updated approach such as GW_0 or *GW* calculations. In the other approach, called QPGW_0 or QP*GW* calculations, QP wavefunctions, as well as eigenvalues, are updated. The difference between QPGW_0 and QP*GW* (or GW_0 and *GW*) is whether the self-consistency in the eigenvalues is considered only in *G* (QPGW_0 and GW_0) or both *G* and *W* (QP*GW* and *GW*).

2.1.4 Symmetry-adapted perturbation theory (SAPT)[31,32]

Non-covalent interactions are responsible, for instance, for the structures of organic molecular crystals, provide a significant contribution to the secondary and tertiary structures of biological macromolecules such as proteins, or dictate the interactions between DNA base pairs. These non-covalent interactions (E_{int}) can be evaluated using a supramolecular approach as follows:

$$E_{int} = E_{complex} - E_A - E_B \tag{2.25}$$

where $E_{complex}$ represents the total energy of the complex (*A*+*B*) while E_A and E_B indicate the energies of the isolated subsystems *A* and *B*, respectively.

One of the efficient methods to decompose this interaction energy is to rely on perturbation theory, specifically the so-called symmetry-adapted perturbation theory

(SAPT). SAPT calculations decompose the noncovalent interactions into four physical components:

$$E_{int} = E_{exch} + E_{elec} + E_{ind} + E_{disp} \tag{2.26}$$

corresponding to the interaction energy contribution from exchange repulsion, electrostatics, induction, and dispersion, respectively.

Among these four terms, the main repulsive interaction originates from the *exchange* interaction as a consequence of the Pauli exclusion principle, *i.e.*, no two electrons can occupy the same quantum state/region of space. Exchange repulsion limits wavefunction overlap between electrons, hence avoids physical proximity between atoms or molecules. This repulsive interaction can be overcome by the other types of interactions: electrostatics, induction (or polarization), and dispersion. The *electrostatics* terms describes the interaction among permanent multipoles on each molecule, *e.g.*, dipole-dipole, quadrupole-quadrupole, dipole-quadrupole. If an excess charge is present on one molecule, interactions such as monopole-dipole can occur. *Dispersion*, as we briefly discussed in Section 2.1.2.4, leads to an attractive force in the interaction of atoms or molecules; this term comes from the instantaneous charge fluctuations (induced dipoles) in electron density when the atoms/molecules start interacting. For interacting nonpolar molecules, the dispersion energy is the dominant attractive component and is purely due to electron correlation. Since DFT cannot completely describe such dynamic correlation effects, it cannot capture the dispersion correctly. The smallest noncovalent interaction tends to be *induction*, which basically comes from the electronic relaxation of one molecule in response to the presence of another.

Since SAPT methods are based on perturbation theory, they differ in the sophistication of their treatment of electron-electron correlation. For instance, the simplest SAPT method, SAPT0, treats the monomers at the HF level and adds explicit dispersion terms emerging from second-order perturbation theory to the electrostatics, exchange, and induction terms inherited from the HF dimer treatment, while SAPT2 adds terms for electrostatics, exchange, and induction up to second-order with respect to intra-monomer electron correlation.[33]

2.2 First principles thermodynamics based on DFT

As illustrated in Chapter 1, the oxide surfaces are not only structurally complicated but also highly affected by the sample preparation procedures. In this context, a growing body of theoretical work has focused on elucidating the surface atomic configurations obtained under specific preparation conditions. In particular, many efforts have been made to extend DFT calculations, which in most cases refer to the zero-temperature and zero-pressure properties of a given set of atoms, in order to describe systems in contact with a chemical reservoir, such as surfaces in thermodynamic equilibrium with an atmosphere of variable composition. For this purpose, it is necessary to rely on thermodynamics and introduce the chemical potentials of the atomic constituents in the theory. In this Section, taking hematite (α-Fe_2O_3) as an example, we will briefly describe the method used to calculate the surface Gibbs free energies of the metal oxide in oxygen- or/and water-exposing conditions as well as electrochemical conditions.

For a surface exposed to a given environment with multiple gas-phase species at partial pressures $\{p_i\}$ at temperature T, the surface energy, $\gamma(T, \{p_i\})$ can be defined as:

$$\gamma(T, \{p_i\}) = \frac{1}{2A}\left[G(T, \{p_i\}, N_i) - \sum_i n_i \mu_i(T, p_i)\right] \tag{2.27}$$

where $G(T, N_i)$ stands for the Gibbs free energy of a solid with two equivalent surfaces of area A; n_i and $\mu_i(T, p_i)$ are the atom number and chemical potential of each species i constituting the total system.

If we consider the hematite surface in contact with a gas phase containing oxygen and hydrogen, primarily in the molecular forms of O_2 and H_2O, the surface Gibbs free energy can be expressed as:

$$\gamma\left(T, p_{O_2}, p_{H_2O}\right) = \frac{1}{2A}\left[G_{slab} - n_{Fe_2O_3} g_{Fe_2O_3}^{bulk} - n_{O_2}\mu_{O_2}\left(T, p_{O_2}\right) - n_{H_2O}\mu_{H_2O}\left(T, p_{H_2O}\right)\right] \tag{2.28}$$

where G_{slab} denotes the free energy of the symmetric slab with two equivalent surfaces of area A; $g_{bulk}^{Fe_2O_3}$, the free energy of a bulk hematite per formula unit; and n_i, μ_i, and p_i, the number, chemical potential, and partial pressure, respectively for component i in the given slab.

Considering the reasonable assumptions described in Appendix A, we can derive the surface energy (γ), expressed as a linear function of the chemical potentials of the two gas reservoirs, μ_{O_2} and μ_{H_2O}, which are determined on the basis of temperature and their partial pressures:

$$\gamma(T, p_{O_2}, p_{H_2O}) = \frac{1}{2A}\left[G_{slab} - \frac{1}{2}N_{Fe}g_{bulk}^{Fe_2O_3} - \left(\frac{1}{2}N_O - \frac{3}{4}N_{Fe} - \frac{1}{4}N_H\right)\mu_{O_2}(T, p_{O_2}) - \frac{1}{2}N_H\mu_{H_2O}(T, p_{H_2O})\right]$$

(2.29)

To map the predominant domains of hydroxylated/hydrated hematite in an aqueous solution, the computational hydrogen electrode (CHE) model has been adopted to avoid the explicit treatment of solvated protons.[34] In this approach, the total chemical potential of the proton-electron pair can be expressed as a function of a potential relative to the standard hydrogen electrode (U_{SHE}) and pH:

$$\mu(H^+) + \mu(e^-) = \frac{1}{2}\mu_{H_2}^{\circ} - eU_{SHE} - k_BT\ln 10 \times \text{pH} \quad (2.30)$$

where $\mu_{H_2}^{\circ}$ denotes the chemical potential of hydrogen gas in the standard state.

Taking the proton-electron pair and liquid water as the main reservoirs leading to hydration/hydroxylation of oxide surfaces in aqueous solution, the surface energy can be calculated as:

$$\gamma(T) = \frac{1}{2A}\left[G_{slab} - n_{Fe_2O_3}g_{Fe_2O_3}^{bulk} - n_{(H^+ + e^-)}(\mu(H^+) + \mu(e^-)) - n_{H_2O(l)}\mu_{H_2O(l)}(T)\right]$$

(2.31)

where $\mu_{H_2O}(l)$ indicates the chemical potential of liquid water in standard condition.

Using Equations 2.30 and 2.31, we can build a surface Pourbaix diagram for hematite where the relative stability among different surface configurations are plotted as a

function of the electrode potential and the solution pH[35] in a water-based reference state[36]:

$$\gamma(U_{SHE}, \mathrm{pH}) = \frac{1}{2A}\Big[G_{slab} - \frac{1}{2}N_{Fe}g_{bulk}^{Fe_2O_3} - \Big(N_O - \frac{3}{2}N_{Fe}\Big)\mu_{H_2O}(l) - \Big(\frac{3}{2}N_{Fe} - N_O + \frac{1}{2}N_H\Big)\mu_{H_2}^{\circ} + (3N_{Fe} - 2N_O + N_H)(eU_{SHE} + k_BT\ln 10 \times \mathrm{pH})\Big] \quad (2.32)$$

Here, $\mu_{H_2O}(l)$ is set to the chemical potential of saturated water vapor at 300 K.

The free energy is considered as the total energy obtained from the DFT calculations, corrected for zero-point vibrational energy (ZPE) and entropy contributions (TS) for the adsorbates and gas (liquid) molecules. The details of these energy corrections entering the surface free energies are given in Appendix A.

2.3 *Ab initio* molecular dynamics

Ab initio methods can be used to generate the forces needed for a molecular dynamics (MD) simulation. This can be done either by: (i) fitting an empirical potential using the results from ab initio calculations; or (ii) generating the forces directly from electronic structure calculations as the MD trajectory evolves.

In order to produce analytical potentials, accurate descriptions of interactions between all involved types of atoms are necessary. However, even when the best fixed potential can be generated, classical MD simulations still have inherent limitations. If the system includes many different atom types, there must be numerous interactions to be parametrized, which is extremely time-consuming. In this case, it is highly likely that

some of the chemical processes may not be foreseen, thus, they cannot take place during the simulations. Also, changes in electronic structure, *e.g.*, bonding pattern, are generally not accounted for. Thus, for the modelling of many phenomena, quantum mechanical simulations are irreplaceable, which led to the development of *ab initio* MD.

There are three major approaches for combining electronic structure calculations with molecular dynamics: Born-Oppenheimer MD (BOMD), Ehrenfest MD (EMD), and Car-Parrinello MD (CPMD). Here, we mainly focus on BO MD as it is the method employed for the work presented in this Thesis.

As discussed in Section 2.1.1, the total wavefunction can be obtained from the time-independent electronic Schrödinger equation under the assumption of nuclei in fixed positions. In the Born-Oppenheimer approximation, the time-dependent Schrödinger equation can be expressed as follows:[37]

$$\left[-\sum_{I}\frac{\hbar^2}{2M_I}\nabla_I^2 + E_k(\{\boldsymbol{R}_I\})\right]\chi_k = i\hbar\frac{\partial}{\partial t}\chi_k \tag{2.33}$$

where the first and second terms on the left refer to the kinetic energy of nuclei and total electronic energy of electronic state *k* for the nuclei set at $\{\boldsymbol{R}_I\}$.

By approximating the nuclei as classical point particles, the wavefunction χ_k at time t can be written in terms of an amplitude factor A_k and a phase S_k:

$$\chi_k(\{\boldsymbol{R}_I\};t) = A_k(\{\boldsymbol{R}_I\};t)\exp\left[\frac{iS_k(\{\boldsymbol{R}_I\};t)}{\hbar}\right] \tag{2.34}$$

Since the momenta of the nuclei ($\boldsymbol{P}_I$) are defined as a derivative of S_k, the Newtonian equations of motion can be written as:

$$\frac{d\boldsymbol{P}_I}{dt} = M_I\ddot{\boldsymbol{R}}_I = -\nabla_I E_k \tag{2.35}$$

The nuclei move according to classical mechanics in an effective potential, which is given by the Born-Oppenheimer potential energy surface E_k while E_k is obtained by solving the time-independent electronic Schrödinger equation for the k^{th} state at the given nuclear configuration $\{\boldsymbol{R}_I(t)\}$. Because the forces are directly obtained from the Born-Oppenheimer total energy, E_k, this approach is often referred to as Born-Oppenheimer molecular dynamics. Since the electronic state is obtained from the time-independent Schrödinger equation, the time dependence of the electronic system is dictated by the motion of the nuclei, therefore, BOMD highly depends on the ground electronic state reached at each time step.

2.4 Software

All quantum mechanics, molecular mechanics, and molecular dynamics methods used for the calculations reported in the subsequent Chapters, have been employed as implemented in the following codes: Vienna Ab initio Simulation Package[29] (VASP, 5.3.5 and 5.4.1), Quantum ESPRESSO[38] (5.4.0), Gaussian 09[39] (revisions C.01 and D.01), PSI4 beta-5, and ADF[40] (2016.102).

2.5 References

[1] Szabo, A.; Ostlund, N. S. *Modern quantum chemistry : introduction to advanced electronic structure theory*; Dover Publications: Mineola, N.Y., 1996.

[2] Hohenberg, P.; Kohn, W. *Phys. Rev. B* **1964**, *136*, B864.

[3] Kohn, W.; Sham, L. J. *Phys. Rev.* **1965**, *140*, 1133.

[4] Perdew, J. P.; Zunger, A. *Phys. Rev. B* **1981**, *23*, 5048.

[5] Perdew, J. P.; Burke, K.; Ernzerhof, M. *Phys. Rev. Lett.* **1996**, *77*, 3865.

[6] Perdew, J. P.; Burke, K.; Ernzerhof, M. *Phys. Rev. Lett.* **1997**, *78*, 1396.

[7] Sun, J. W.; Marsman, M.; Csonka, G. I.; Ruzsinszky, A.; Hao, P.; Kim, Y. S.; Kresse, G.; Perdew, J. P. *Phys. Rev. B* **2011**, *84*.

[8] Giovannetti, G.; Kumar, S.; van den Brink, J.; Picozzi, S. *Phys. Rev. Lett.* **2009**, *103*, 037601.

[9] Cococcioni, M. The LDA+U Approach: A Simple Hubbard Correction for Correlated Ground States; Verlag des Forschungszentrum: Jülich, 2012; Vol. 2.

[10] Anisimov, V. I.; Poteryaev, A. I.; Korotin, M. A.; Anokhin, A. O.; Kotliar, G. *J. Phys.-Condens. Mat.* **1997**, *9*, 7359.

[11] Mosey, N. J.; Liao, P.; Carter, E. A. *J. Chem. Phys.* **2008**, *129*.

[12] Dudarev, S. L.; Botton, G. A.; Savrasov, S. Y.; Humphreys, C. J.; Sutton, A. P. *Phys. Rev. B* **1998**, *57*, 1505.

[13] Becke, A. D. *J. Chem. Phys.* **1993**, *98*, 1372.

[14] Adamo, C.; Barone, V. *J. Chem. Phys.* **1999**, *110*, 6158.

[15] Heyd, J.; Scuseria, G. E. *J. Chem. Phys.* **2004**, *121*, 1187.

[16] Heyd, J.; Scuseria, G. E.; Ernzerhof, M. *J. Chem. Phys.* **2003**, *118*, 8207.

[17] Heyd, J.; Scuseria, G. E.; Ernzerhof, M. *J. Chem. Phys.* **2006**, *124*, 219906.

[18] Krukau, A. V.; Vydrov, O. A.; Izmaylov, A. F.; Scuseria, G. E. *J. Chem. Phys.* **2006**, *125*, 224106.

[19] Yanai, T.; Tew, D. P.; Handy, N. C. *Chem. Phys. Lett.* **2004**, *393*, 51.

[20] Rohrdanz, M. A.; Herbert, J. M. *J. Chem. Phys.* **2008**, *129*.

[21] Refaely-Abramson, S.; Sharifzadeh, S.; Govind, N.; Autschbach, J.; Neaton, J. B.; Baer, R.; Kronik, L. *Phys. Rev. Lett.* **2012**, *109*.

[22] Refaely-Abramson, S.; Sharifzadeh, S.; Jain, M.; Baer, R.; Neaton, J. B.; Kronik, L. *Phys. Rev. B* **2013**, *88*.

[23] Sun, H. T.; Zhong, C.; Bredas, J. L. *J. Chem. Theory Comput.* **2015**, *11*, 3851.

[24] Grimme, S. *Wires Comput. Mol. Sci.* **2011**, *1*, 211.

[25] Grimme, S.; Antony, J.; Ehrlich, S.; Krieg, H. *J. Chem. Phys.* **2010**, *132*.

[26] Hedin, L. *Phys. Rev.* **1965**, *139*, A796.

[27] Koval, P.; Foerster, D.; Sanchez-Portal, D. *Phys. Rev. B* **2014**, *89*.

[28] Shishkin, M.; Kresse, G. *Phys. Rev. B* **2007**, *75*.

[29] Kresse, G.; Furthmuller, J. *Phys. Rev. B* **1996**, *54*, 11169.

[30] Shishkin, M.; Kresse, G. *Phys. Rev. B* **2006**, *74*, 035101.
[31] Szalewicz, K. *Wires Comput. Mol. Sci.* **2012**, *2*, 254.
[32] Sutton, C.; Risko, C.; Bredas, J. L. *Chem. Mater.* **2016**, *28*, 3.
[33] Parker, T. M.; Burns, L. A.; Parrish, R. M.; Ryno, A. G.; Sherrill, C. D. *J. Chem. Phys.* **2014**, *140*.
[34] Peterson, A. A.; Abild-Pedersen, F.; Studt, F.; Rossmeisl, J.; Norskov, J. K. *Energ. Environ. Sci.* **2010**, *3*, 1311.
[35] Bajdich, M.; Garcia-Mota, M.; Vojvodic, A.; Norskov, J. K.; Bell, A. T. *J. Am Chem. Soc.* **2013**, *135*, 13521.
[36] Zeng, Z. H.; Chan, M. K. Y.; Zhao, Z. J.; Kubal, J.; Fan, D. X.; Greeley, J. *J. Phys. Chem. C* **2015**, *119*, 18177.
[37] Marx, D.; Hutter, J. Ab Initio Molecular Dynamics: Basic Theory and Advanced Methods; Cambridge University Press, 2009.
[38] Giannozzi, P.; Baroni, S.; Bonini, N.; Calandra, M.; Car, R.; Cavazzoni, C.; Ceresoli, D.; Chiarotti, G. L.; Cococcioni, M.; Dabo, I.; Dal Corso, A.; de Gironcoli, S.; Fabris, S.; Fratesi, G.; Gebauer, R.; Gerstmann, U.; Gougoussis, C.; Kokalj, A.; Lazzeri, M.; Martin-Samos, L.; Marzari, N.; Mauri, F.; Mazzarello, R.; Paolini, S.; Pasquarello, A.; Paulatto, L.; Sbraccia, C.; Scandolo, S.; Sclauzero, G.; Seitsonen, A. P.; Smogunov, A.; Umari, P.; Wentzcovitch, R. M. *J. Phys.-Condens. Mat.* **2009**, *21*.
[39] Frisch, M. J. *e. a.*, Gaussian, Inc., Wallingford CT 2016.
[40] te Velde, G.; Bickelhaupt, F. M.; Baerends, E. J.; Guerra, C. F.; Van Gisbergen, S. J. A.; Snijders, J. G.; Ziegler, T. *J. Comput. Chem*. **2001**, *22*, 931.

CHAPTER 3. BULK PROPERTIES OF IRON OXIDES

A first step in determining a robust theoretical technique to describe complex systems consisting of surfaces and interfaces is to find the level of calculations that would ideally reproduce the geometric and electronic structure of the bulk materials. While standard density of functional theory (DFT) calculations provide overall a reasonable description of the structural parameters and magnetic ground state of iron oxides, they usually fail to provide an accurate determination of the electronic structure of iron oxides even in a qualitative manner.[1-3] These limitations mainly arise from strong correlation effects amongst Fe 3*d* electrons leading to a small splitting of the *d* bands. Thus, in Section 3.2, we take bulk hematite (α-Fe_2O_3) as a benchmark material to assess the accuracy of several theoretical extensions of DFT in describing its electronic properties. The methods of interest include the Hubbard *U* correction on Fe 3*d* electrons (DFT+*U*), the screened Heyd-Scuseria-Ernzerhof (HSE) hybrid functional, and the *GW* Approximations (GWA) of varying degrees of self-consistency. The technical schemes validated for hematite are further applied to calculations for bulk magnetite (Fe_3O_4, Section 3.3) and maghemite (γ-Fe_2O_3, Section 3.4), in order to obtain the geometric and electronic structures for the ground state of each mineral. This work can provide baseline intrinsic properties of related materials which allow a direct comparison to the surface and interface structures appearing in the following sections: hematite (chapters 4 and 5), magnetite (chapters 4 and 6), maghemite (chapter 5).

3.1 Computational details

All calculations have been performed using spin-polarized DFT as implemented in the Vienna ab initio simulation package (VASP).[4,5] The ionic potentials are described by the PAW pseudopotential[6] with valence configurations of $3d^7 4s^1$ and $2s^2 2p^4$ for the Fe and O atoms, respectively. The energy cutoff for a plane-wave basis set was set to 450 eV for maghemite and 550 eV for hematite and magnetite. The Brillouin zone (BZ) integration was performed by using a finite-temperature Gaussian smearing function with $\sigma = 0.05$ eV. Grids consisting of 9×9×9, 7×7×7, and 6×6×2 Γ-centered **k**-points are used in the BZ integration of the unit cell calculations of hematite, magnetite, and maghemite, respectively. Geometries were optimized with a quasi-Newton or/and conjugate-gradient algorithm until the Hellmann-Feynman forces were lower than 0.01 eV/Å and energy convergence within 10^{-5} eV/atom. The local densities of states (DOS) were calculated by projecting the Kohn-Sham (KS) wave functions onto atom-centered spherical harmonic functions within each atom's Wigner-Seitz radius. The exchange-correlation (XC) contribution to the DFT energy was calculated using the generalized gradient approximation (GGA) exchange-correlation functional of Perdew, Burke, and Ernzerhof (PBE).[7]

In this work, we exploited the DFT+Hubbard *U* (DFT+*U*) approach[8] with a U_{eff} = 4 eV value for the Fe 3*d* electrons in the simplified rotationally invariant formulation of Dudarev *et al.*[9] where the on-site Coulomb parameter, *U*, and exchange parameter, *J*, are combined into a single parameter, $U_{eff} \equiv U - J$. Although it has been demonstrated that

the DFT+*U* method can provide remarkable improvement in describing correlated phenomena in transition metal oxides without a massive increase in computational cost, one of the major drawbacks stems from the fact that it contains *d*-electron specific empirical parameters that are typically pre-set to give reasonable agreement with experimental values (most of the time, the electronic band gap). One proposed alternative is a hybrid functional where a portion of non-local exact exchange HF functional (E_{xx}) is included. Among various types of hybrid functionals, the screened HSE06 functional (25% E_{xx} in the short range with a screening parameter ω = 0.11 bohr^{-1}) was chosen as it has been shown to accurately predict enthalpies of formation, ionization potentials, and electron affinities for molecules as well as lattice constants and band gaps of ionic crystals in general.[10] Considering the fact that the optimal amount of HF exchange can be system-dependent for hybrid functionals,[11] we also present results obtained using a reduced value of a = 0.15, referred as HSE(15%). All range-separated calculations were performed using a 450 eV cutoff on the basis of geometries optimized with PBE+*U* while the **k**-point grid is reduced by half to speed up the calculations.

For the *GW* calculations for bulk hematite and magnetite, we took the initial guess of QP energies and wave function from the PBE calculations in order to completely exclude any of numerical inputs derived from experiments. In this context, GWA can be viewed as a perturbation theory improvement of DFT via consideration of the excited states. The electronic density and wave functions were calculated for a rhombohedral hematite structure at the G_0W_0 level with an increasing number of unoccupied bands per atom, n_{unocc}= 9.4, 22.2, 47.8, and 99, which corresponds to including unoccupied levels up to 47, 94, 148, and 250 eV, respectively, above the valence band maximum (VBM). Since

the difference in calculated quasi-particle (QP) band gaps are less than 0.1 eV between n_{unocc}= 9.4 and n_{unocc}= 99, here, we present the results from G_0W_0, GW_0, GW, scQPGW_0, and scQPGW calculations performed with n_{unocc}= 22.2. For magnetite, the total number of 512 bands is used with 320 of them empty to include unoccupied levels up to ~30 eV above VBM for the scQPGW_0 calculation. Γ-centered **k**-point meshes of 4×4×4 and 2×2×2 were used for the rhombohedral hematite and cubic magnetite unit cells, respectively, yielding a sampling of ~ 0.05 $Å^{-1}$ (note that the QP band gap at the GW level changes by < 0.02 eV upon k-mesh reduction). Energy cutoff for the number of G-vectors representing the response function is chosen as 276 eV, and a sampling of 50 frequency points is taken for the dielectric function.

3.2 Hematite (α-Fe_2O_3)

3.2.1 Introduction

Hematite crystallizes in a corundum structure (space group $R\bar{3}c$) with lattice constants a=5.035 Å and c=13.747 Å at atmospheric pressure,[12] as shown in Figure 3.1. Here, the oxygen anions are hexagonally close-packed (hcp) on the (0001) plane while the Fe cations fill two-thirds of the octahedral sites between hcp oxygen layers. The primitive cell of α-Fe_2O_3 contains four Fe atoms ordered along [111] with a short axis between pairs of Fe centers (type A) and a longer axis separating the pairs (type B). All iron atoms have an equivalent octahedral environment and the octahedra consist of a Fe atom in the center and an O atom at each vertex. This layered geometry yields a very dense structure (5.26 g/cm^3) exhibiting a high polarizability and a high refractive index and also

generates complex interactions with photons and electrons. These attributes of hematite must be properly understood when considering its application as a semiconductor for solar radiation-based water splitting.

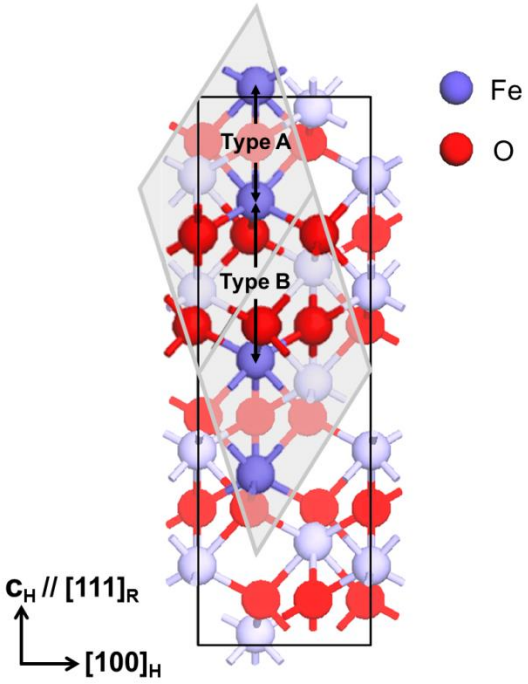

Figure 3.1 Crystal structure of hematite (α-Fe_2O_3) in the hexagonal unit cell (black box) and rhombohedral primitive cell (white box). Iron and oxygen atoms are colored in blue and red, respectively. In a primitive unit cell, four Fe atoms are aligned along $[111]_R$ and two distinguishable Fe-Fe pairs exist: one in the same close-packing layer (type A) while the other separated by an interlayer with a longer distance (type B).

Below the Néel temperature (T_N = 963 K), α-Fe_2O_3 is known as an antiferromagnet with weak ferromagnetic interactions. Possible antiferromagnetic configurations include: (↑↓↓↑), (↑↓↑↓), (↑↑↓↓) along the [111] direction in a rhombohedral primitive cell (see

Figure 3.1); the (↑↓↓↑) configuration, *i.e.*, antiferromagnetic ordering where the magnetic moments of the Fe^{3+} ions are ferromagnetically coupled within each double iron layer along $[111]_R$, *i.e.*, $[0001]_H$ but opposed to the adjacent double layer, has been proposed to be the most favorable ordering. The Fe atoms center within a distorted octahedral local environment that produces a high-spin crystal field splitting into their 3*d* levels, which leads to a high spin magnetic moment of ~ 4.6-4.9 μ_B per atom in experiments.[13] Experimentally, hematite has been shown to exhibit significant variations in band gap energy, depending on sample preparation and measurement techniques: a thermal band gap of 2 eV,[14] an optical gap between 1.9 and 2.2 eV (or 650–560 nm),[15] and a band gap of ~2.6±0.4 eV as measured with PES and IPES.[16]

3.2.2 Optimized crystal structure

The primitive rhombohedral cell of hematite (2 formula units (f.u.)/unit cell) optimized at the PBE+*U* level has a lattice constant of 5.477 Å with an angle of 55.146°, which in a hexagonal representation can be written as a=5.066 Å, c=13.879 Å. The calculated lattice parameters are in a good agreement with the experimental values[12] with an overestimation of less than 2% while PBE slightly underestimates the lattice parameter in a hexagonal plane direction. Each Fe atom is surrounded by six O atoms in a distorted octahedral geometry, where half of the Fe-O bond lengths are shortened. The local geometries are reasonably predicted with PBE+*U* to give values similar to the experimental measurements although the longer Fe-Fe distance (4.05 Å) and Fe-O bond length (2.12 Å) are longer due to the expanded lattice vectors in the unit cell. As

mentioned earlier, standard DFT calculations provide overall a reasonable description of the structural parameters and magnetic ground state of iron oxides but usually fail to provide an accurate determination of the electronic structure of iron oxides.[1-3] The magnetic moments of the Fe atoms and (indirect) band gap energy are 3.61 μ_B and 0.54 eV, which are too small compared to the experimental values, 4.6-4.6-4.9 μ_B[13] and 2 eV,[14] respectively. The lower magnetic moment predicted by PBE than the other two functionals comes from the artificial over-delocalization of the electron density caused by the electron self-interaction error in standard DFT.

Table 3.1 Calculated and experimental values of structural parameters, band gap, and spin magnetic moment related to ferric ions in hematite. The results of HSE (12%) calculations for hematite are taken from Ref. 17. The magnetic moments are obtained from the integration of the spin density inside PAW spheres for the Fe cation.

		PBE	**PBE+*U***	**HSE(12%)[17]**	**expt.[12]**
lattice constant (Å)	a	5.006	5.066	5.067	5.035
	c	13.878	13.879	13.882	13.747
atomic distance (Å)	Fe-Fe	2.94, 4.00	2.89, 4.05	2.94, 4.00	2.88, 3.98
	Fe-O	1.93, 2.14	1.97, 2.12	1.95, 2.06	1.99, 2.06
band gap (eV)		0.54	2.11	1.95	1.9-2.6[15,16]
μ (μ_B/Fe)		3.53	4.15	4.16	4.6-4.9[13]

3.2.3 Electronic structures

3.2.3.1 DFT+*U* method and hybrid functionals

Figure 3.2a presents the band structure and orbital-projected density of states (PDOS) derived from PBE for a hexagonal hematite unit cell. Not only is the band gap underestimated compared to the experimental data, but the valence band character is also incorrectly described as a Mott-Hubbard insulator, contradicting the experimental photoemission spectra.[18] PBE inaccurately positions 3*d* orbitals and has the valence-band edge Fe 3*d* dominated. However, soft-X-ray (O K-edge) absorption and emission spectra[19] indicate that α-Fe_2O_3 is more like a charge transfer (CT) insulator, which indicates an O 2*p* dominant character at the top of the valence band. These limitations arise from the strong correlation effects amongst Fe 3*d* electrons, leading to a small splitting of the *d* bands. In many cases, this can be corrected by introduction of an on-site Coulomb repulsion at the *d* electron sites. Thus, we utilized the PBE+*U* (U_{eff} = 4 eV) approach to modifying the intra-atomic Coulomb interaction among strongly correlated Fe 3*d* electrons. The inclusion of an on-site Coulomb potential successfully produces a CT-type semiconductor by identifying the top of the valence band as O 2*p* states rather than Fe 3*d* (Figure 3.2b). Since the shape of the valence band is also affected by U_{eff}, the hole effective mass accordingly varies from 0.715 m_h^* to 0.903 m_h^* at the VBM.

Another scheme to overcome the shortcomings of standard PBE is to use a hybrid functional with a fractional amount of exact exchange. In particular, the range-separated hybrid functional HSE06 could be an optimum choice for the solid where the slowly decaying long-range part of the HF exchange interaction is replaced by the corresponding

part of the PBE density functional. This approach has been shown to accurately predict enthalpies of formation, ionization potentials, and electron affinities for molecules as well as lattice constants and band gaps of solids in general; however, the computational cost is much higher than for standard DFT calculations. Based on an optimal amount of HF exchange, 15%, used in previous studies,[2] we calculated the Fe_3O_4 band structure; the results along the K-M directions are shown in Figure 3.2b. The tuned HSE06 results confirm the validity of using PBE+*U* to describe the electronic structure of hematite. For the hematite and magnetite surfaces, we also found that PBE+*U* (U_{eff} = 4 eV) can provide relative surface stabilities and electronic structures comparable to HSE(15%).[20]

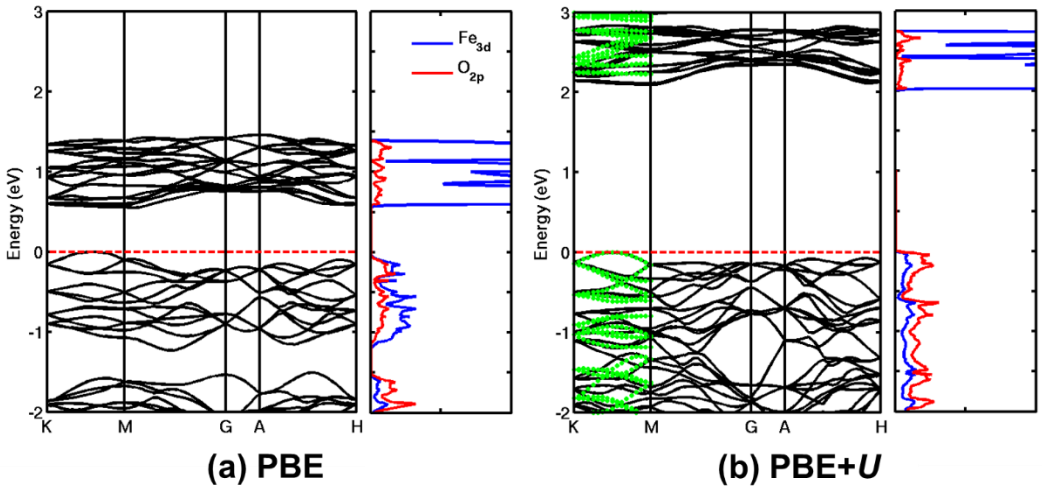

Figure 3.2 Band structure and orbital-projected density of states (PDOS) calculated with (a) PBE and (b) PBE+*U* (U_{eff} = 4 eV). The Fermi level is indicated by a horizontal dashed red line. The HSE(15%) results are represented by green dotted lines in (b).

3.2.3.2 *GW* approximation

Recently, the many-body perturbation theory within the GWA has begun to be widely used as it provides the quasiparticle (QP) band structure in a non-empirical fashion. In GWA, the evaluation of the self-energy, $\Sigma = iGW$ where G is the Green's function and W is the screened Coulomb interaction, requires starting eigenvalues and wavefunctions. If these are kept fixed at the initially provided DFT-derived values, the method is called the single-shot (or non-consistent) G_0W_0. One can also impose self-consistency in G and/or W with or without QP wavefunctions being updated. If only eigenvalues are being corrected to QP energies during iterations, the schemes are referred to as GW_0 and GW, while QP wavefunctions are computed and updated at each step in scQPGW_0 and scQPGW by applying a Hermitian approximation to Σ.

QP band gap values for different levels of the GWA (using the PBE-derived KS wave functions as starting points) are summarized and compared with the ones from DFT-based methods in Table 3.2. With the single-shot correction of the PBE eigenvalues, the band gap value improves from 0.68 eV to 1.22 eV although it still underestimates the experimental values of ~ 2 eV. For the energy-only corrected *GW* methods, the QP band gap increases in the order of $G_0W_0 < GW_0 < GW$; it reaches at 1.74 eV with the *GW* approach. This is partly due to the adjustment in dielectric constant from DFT during the iteration in *W*, as demonstrated in other semiconductors.[21] The band gap widening is largely attributed to the upshift of conduction bands with some downshifts of the valence bands.

Table 3.2 Calculated Fe magnetic moments and eigenvalue gaps (DFT) or QP band gaps (GWA) at different levels of calculation based on the PBE+*U*-optimized geometry. The values were obtained after 6 iterations for GW_0, *GW*, scQPGW_0, and scQP*GW* schemes.

	μ (μ_B/Fe)	**band gap (eV)**	**VBM Fe 3*d* (%)**
PBE	3.56	0.68	64
PBE+*U* (U_{eff}= 4 eV)	4.15	2.11	32
HSE(15%)	3.96	2.32	39
PBE G_0W_0	3.56	1.22	64
PBE GW_0	3.56	1.51	64
PBE *GW*	3.56	1.74	64
PBE scQPGW_0	3.94	1.93	43
PBE scQP*GW*	4.15	3.18	33
expt.	4.6-4.9[13]	2.0-2.2, 2.6[15,16]	CT insulator[19]

The QP energies obtained in *GW* present a much better agreement with the experimental gap, which seems to resolve the problem of bandgap underestimation in conventional DFT. However, it should be noted that the nature of the VBM is basically the same as the one derived from PBE, *i.e.*, Fe 3*d* dominated, as the wavefunctions are not updated at this level of theory. Therefore, we need to apply a self-consistent GWA to obtain the corrected wavefunctions and further examine whether this can mitigate the underbinding issue of the Fe *d* levels in PBE. Figure 3.3 gives the PDOS calculated at three levels of self-consistency: G_0W_0, scQPGW_0, and scQP*GW*. It is found that conventional DFT calculations typically provides too shallow *d* levels, roughly a few eV above the experimental measurements, leading to band gap shrinkage due to *p*-*d* repulsion from a strong hybridization of *d* bands with oxygen *p* levels. Since GWA does not suffer from the strong self-interaction of *d* electrons, these *d* levels are located at a higher binding

energy, hence produce a mixed Fe 3*d* and O 2*p* character at the VBM, and correctly predict hematite as a CT or intermediate insulator.

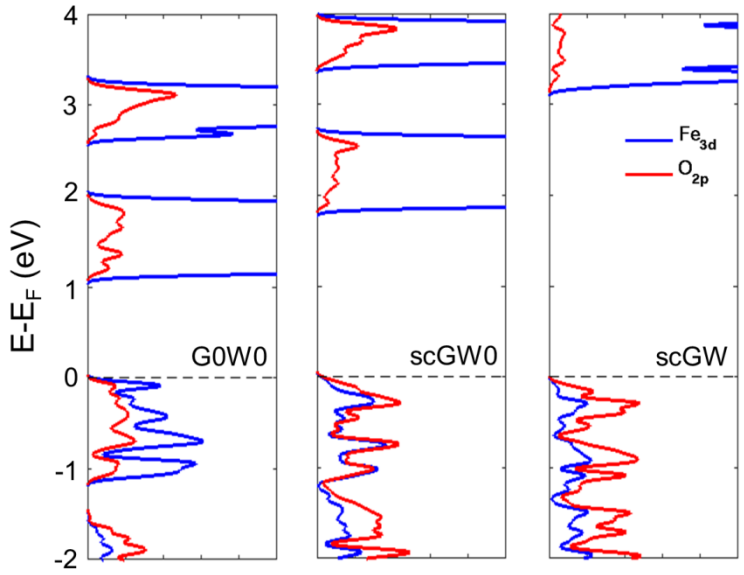

Figure 3.3 Calculated PDOS of hematite in the G_0W_0, scQPG_0W_0, and scQP*GW* approaches. Blue and red lines represent Fe_{oct} 3*d* and O 2*p* states, respectively. The valence band maximum is set to the zero of energy, indicated by a dashed line.

However, in scQP*GW*, the perturbation widens the gaps to too large an extent, *ca.* 3.2 eV. The large QP energy gap in sc*GW* has been commonly found in other systems and has been attributed to a neglect of the lattice polarization contribution to the screening of the electron-electron interactions, which always leads to band gap lowering.[21] To partially remedy the tendency for sc*GW* to overestimate band gaps, the scQPGW_0 approach has

been proposed. In scQPGW_0, the dielectric matrix is set to that determined from a random phase approximation (RPA) evaluation based on the KS wavefunctions before the *GW* iteration. Errors from RPA and DFT basically cancel each other, thereby producing macroscopic optical dielectric constants close to the experimental values. If the eigenvalues are updated with *W* iterations at the QP levels, the dielectric response is underestimated, resulting in the overestimation of the band gap.

Overall, among the various GWA techniques, scQPGW_0 shows the best agreement with experiment for hematite. The prediction based on scQPGW_0 agrees well with the PBE+*U* and HSE(15%) results; however, it should be noted that scQPGW_0 does not require any parameter to be calibrated to experimental data beforehand, as is the case in the two DFT-based methods.

3.3 Magnetite (Fe_3O_4)

3.3.1 Introduction

Magnetite has a cubic inverse spinel structure (space group $Fd\bar{3}m$) at room temperature with 8 f.u. in the conventional unit cell as shown in Figure 3.4. Its chemical formula, often written as $[Fe^{3+}]_A\ [Fe^{3+},Fe^{2+}]_B\ O_4$, indicates that the tetrahedral sites denoted as A are occupied by ferric ions while the octahedral sites denoted as B contain an equal number of ferric and ferrous ions. In magnetite, the tetrahedral and octahedral sites form two magnetic sublattices with the spin moments on the A sublattice antiparallel to those on the B sublattice. The proposed electronic structure of the octahedral Fe^{2+} cations

corresponds to a situation where an extra electron resides in the lowest unoccupied t_{2g} orbital located at the Fermi level, as illustrated in Figure 3.5. Such an occupation then would give rise to 100% spin-polarized charge carriers, a situation highly desirable for spintronic applications. [22,23]

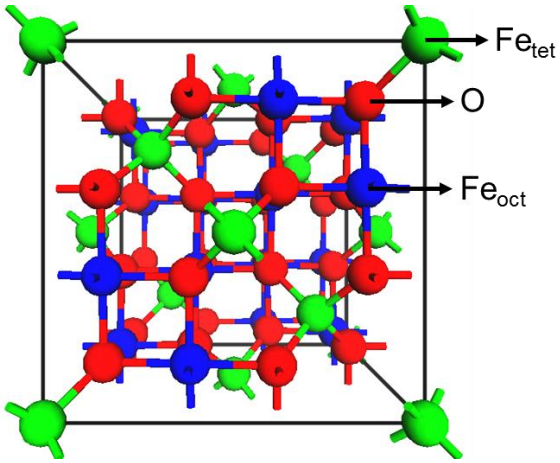

Figure 3.4 Crystal structure of magnetite (Fe_3O_4) in its cubic $Fd\bar{3}m$ phase. Tetrahedral-site Fe atoms (8/unit cell) and octahedral-site Fe atoms (16/unit cell) are colored in green and blue, respectively, and oxygen atoms (32/unit cell) in red.

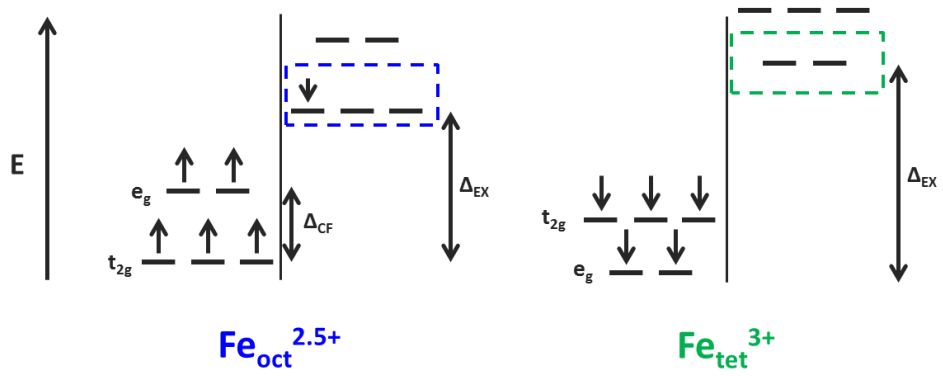

Figure 3.5 Proposed electronic structures of magnetite where excess electrons in the octahedral cations reside in the lowest unoccupied t_{2g} orbital located at the Fermi level. Such an occupation would give rise to 100% spin-polarized charge carriers.

Magnetite displays an electrical conductivity as high as 2×10^2 S/cm in the thermodynamic standard state; however, it undergoes a Verwey phase transition[24] with a clear opening of the optical gap, ~0.14 eV at 121 K,[25] a temperature below which the electronic conductivity abruptly decreases by two orders of magnitude. This quasi metal-to-insulator transition has been explained by restricted electron hopping between Fe^{2+} and Fe^{3+} ions in the octahedrally coordinated positions due to charge ordering below the transition temperature.[26,27] In addition to the increase in electrical resistivity and changes in magnetization and heat capacity, this transition is also accompanied by a structural distortion from the room temperature cubic system; orthorhombic,[28] monoclinic,[29] and triclinic[30] unit cells have been observed at low temperatures.

Although magnetite has been extensively investigated in past decades, most of the studies have focused on the low-temperature monoclinic *Cc* phase (*i.e.*, on the charge-ordered structure below the Verwey transition temperature), while there are only a few reports on

the high-temperature cubic $Fd\bar{3}m$ phase. However, it is the structure at ambient temperature that is relevant in the actual operating conditions for many of the applications of magnetite[31]; therefore, a detailed understanding of the physical and chemical nature of the cubic system is clearly needed.

3.3.2 Optimized crystal structure

The Fe_3O_4 unit cell containing 24 Fe and 32 O atoms was fully relaxed at the PBE and PBE+*U* levels *while preserving cubic symmetry*. As presented in Table 3.3, the PBE lattice constant is 8.387 Å, nearly identical to the experimental value, 8.396 Å[31]; PBE+*U* slightly overestimates the experimental value by 1% (8.488 Å). In addition to the minor difference in lattice constant, the bond lengths between Fe and surrounding O atoms are calculated to be longer by 0.02-0.03 Å upon consideration of on-site Coulomb interactions among Fe 3*d* electrons, which effectively decreases the charge density in the Fe-O bonds. In terms of the energy of formation per O atom, *i.e.*, equating the internal energy to the Gibbs free energy, the PBE+*U* calculations result in a value much closer to the experimental free energy of formation, of -3.12 eV vs. -2.89 eV per O atom at low temperature[32] than PBE, which underestimates the value by 20%.

Table 3.3 Lattice constant, interatomic distances and energy of formation (per O) of cubic Fe_3O_4 calculated using PBE and PBE+*U*. The experimental lattice constant and Gibbs free energy of formation is listed for comparison.

	PBE	PBE+*U*	expt.
lattice constant (Å)	8.387	8.488	8.396[31]
d(Fe_{tet}-O) (Å)	1.88	1.90	1.88
d(Fe_{oct}-O) (Å)	2.06	2.09	2.06
ΔE_f(eV)	-2.31	-3.12	-2.89[a](-2.91[b])[32]

[a] $\Delta G_f(0\mathrm{K})$ [b] $\Delta G_f(298\mathrm{K})$

3.3.3 Electronic and magnetic structure

3.3.3.1 DFT, DFT+*U*, hybrid, and scGW_0 calculation

In cubic-phase magnetite at room temperature, electron hopping occurs between the Fe^{2+} and Fe^{3+} sites of the mixed-valence octahedral plane, resulting in an average oxidation level of $Fe^{2.5+}$ per occupied site and a magnetic moment of 4 μ_B per Fe_3O_4 formula unit. While both PBE and PBE+*U* (U_{eff} = 4 eV) calculations provide the same net magnetic moment of 4 μ_B/f.u., the descriptions of the local magnetic moments and Bader charges for the Fe_{oct}, Fe_{tet}, and O atoms vary with the consideration of the effective Coulomb interaction, as shown in Table 3.4. The magnetic moment of the tetrahedral Fe atom is calculated with PBE to be 3.47 μ_B, which is significantly smaller than the experimentally measured value of 3.82 μ_B.[33] This indicates a strong hybridization among the 3*d* orbitals of Fe_{tet} with the surrounding oxygen atoms. Adding the modified Coulomb repulsion, U_{eff}, in the PBE+*U* calculations improves the agreement with experimental data. For instance, the magnetic moment and electron charge are increased by 0.6 μ_B and 0.18|e|, respectively, at the PBE+*U* level compared to the values obtained in PBE. Similar trends

are obtained for Fe_{oct}: the magnetic moment is 0.4 μ_B lower with PBE than PBE+*U* and atomic charges are smaller by 0.12|e|. Partial inclusion of exact exchange in HSE06 functionals also improve the spin magnetic moments of Fe_{tet}; however, HSE06 leads to a localization of the Fe 3*d* electrons in octahedral positions, and significant reduction of magnetic moments in Fe_{oct} atoms where the values range from 3.49 to 4.37 μ_B; this is in contrast with the PBE and PBE+*U* results that are more uniform, the maximum difference being 0.03 μ_B. This issue will be further discussed in section 3.3.3.2.

Table 3.4 Magnetic moment, μ, and Bader charge, q, of each element in bulk Fe_3O_4, calculated using PBE, PBE+*U*, HSE06, HSE(15%), and scGW_0. The HSE06, HSE(15%), and scGW_0 calculations are based on the PBE+*U*-optimized geometry. The minimum and maximum values of the magnetic moment are tabulated for the four Fe_{oct} ions.

	Fe_{oct}		Fe_{tet}		O	
	μ (μ_B)	q (|e|)	μ (μ_B)	q (|e|)	μ (μ_B)	q (|e|)
PBE	3.55-3.58	+1.60	3.47	+1.68	0.08	-1.22
PBE+*U*	3.96-3.98	+1.72	4.09	+1.86	0.08	-1.22
HSE06	3.49-4.37	+1.82	4.06	+1.99	0.03	-1.40
HSE(15%)	3.82-3.85	+1.71	3.92	+1.89	0.06	-1.33
scGW_0	3.84	+1.56	3.92	+1.72	0.06	-1.20

The partial density of states (PDOS) projected on the Fe_{oct}, Fe_{tet}, and O sites were obtained from the PBE and PBE+*U* calculations for the $Fd\bar{3}m$ unit cell as shown in Figure 3.6. For consistency between the metallic and semiconducting systems, the Fermi energy (E_f) is (artificially) taken here as the highest occupied energy level of the system.

Both the PBE and PBE+U results indicate that cubic Fe_3O_4 is a half-metallic oxide where the majority spin band exhibits insulating or semiconducting behavior whereas the minority spin band shows metallic behavior. However, the specific details of the electronic structure are significantly different when using the two methodologies. In the PBE-derived electronic structure, the majority spin band structure has a direct band gap of 0.6 eV at the Γ point in. The majority spin valence band maximum consists of Fe 3d e_g orbitals and O 2p orbitals in nearly equal proportions, while the conduction bands are mainly comprised of 3d states from tetrahedral Fe atoms. Localized 3d states of the Fe_{oct} atoms are present between -2.5 eV and -3.8 eV and delocalized oxygen 2p orbitals appear well below E_f. In the minority spin band structure, the results show that the t_{2g} states from Fe_{oct} ions dominate the DOS around E_f, which is consistent with previous studies.[34] The PBE functional locates the valence band at low binding energy, resulting in the majority valence band and the minority conduction band virtually overlapping some 0.3 eV below the Fermi energy. The PDOS does not replicate the observation of band discontinuities at the Fe 3p → 3d resonance photon energy for the high-lying Fe 3d-derived bands.[35]

On the other hand, PBE+U describes the semiconducting nature in the majority spin state of Fe_3O_4 with an increased band gap, 2.1 eV. At the valence band maximum, the contribution of O 2p orbitals increases from 51% to 82% and there is no longer a localized Fe_{oct} 3d band below the hybridized states. This is attributed to the fact that the Fe 3d states originally lying close to Fermi level are now shifted to higher binding energy due to on-site Coulomb interaction among Fe 3d electrons. In contrast to the results from PBE, PBE+U shows the valence band extending from 2 to 9 eV, which is consistent with

the presence of O 2*p*-derived states in the 3-8 eV range and Fe 3*d*-derived states at 4 eV below E_f in a photoemission study.[36] The minority spin structure obtained from PBE+*U* has a large gap of 1.9 eV between Fe_{oct} 3*d* t_{2g} states and O 2*p* hybridized states at Γ, which gives rise to an overall band discontinuity between the majority and minority spin channels from -0.3 eV to -1.1 eV. These results show nearly 100% spin polarization, which is in reasonable agreement with previous calculations [22] and spin-polarized photoemission experiments.[37,38]

To put our results in a broader perspective, we also performed HSE(15%) and scQPGW_0 calculations that partly correct for the self-interaction error. As we have seen for hematite in Section 3.2, these two schemes present electronic structures very similar to PBE+*U* near the Fermi level, while the Fe 3*d* states are located at lower binding energy in the -5 to -4 eV region.

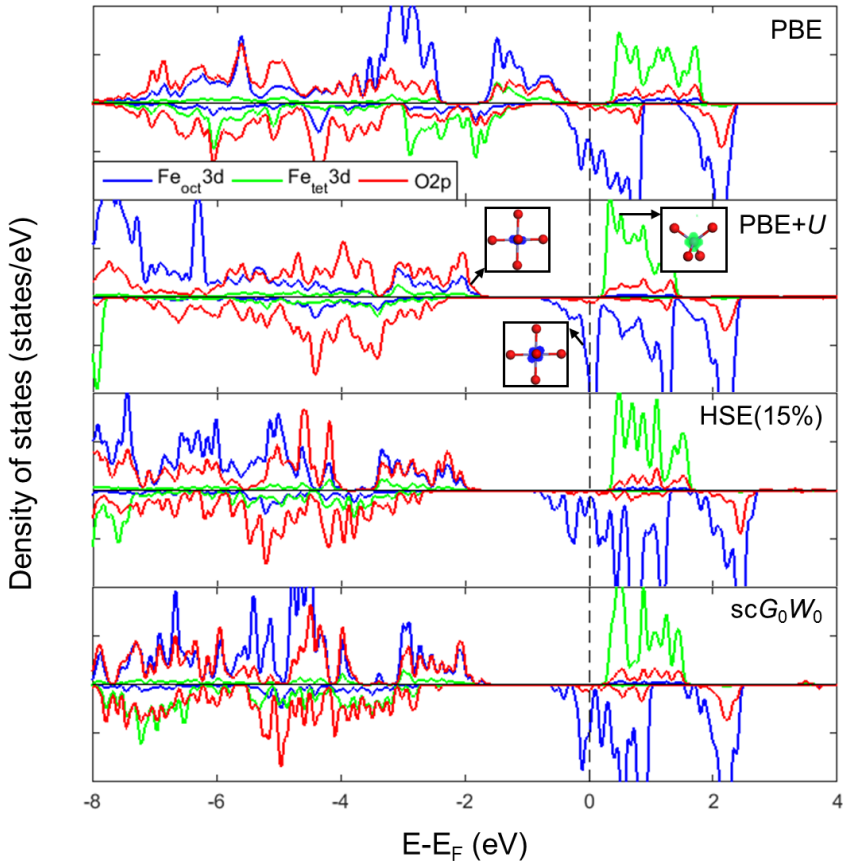

Figure 3.6 PDOS of bulk Fe_3O_4 with PBE, PBE+U, HSE(15%) and scQPGW_0. The blue, green, and red lines represent surface Fe_{oct} 3d, Fe_{tet} 3d, and O 2p states, respectively. The Fermi level is indicated by a dashed line. The partial charge density at the valence band maximum or conduction band minimum (as indicated by an arrow), as obtained at the PBE+U level, is shown in the inset.

3.3.3.2 Exact exchange and charge ordering

We note that while the PBE+U functional produces a stable structure in the cubic point group, previous optimizations at the hybrid-DFT (B3LYP) level lead to a structure with no symmetry.[39] Thus, here, we used the optimized PBE+U structure for these hydrid

functional calculations, which is similar in spirit to earlier studies where the lattice parameters were fixed at the experimental values. As presented in Table 3.4, a wide range of magnetic moments are calculated for Fe_{oct} with E_{xx} = 25% in the short range, which implies a possible charge ordering within a bulk crystal. In order to confirm this charge ordering with HSE06, the PDOS of Fe_{oct} ions from two octahedral sites (with fractional coordinates given in parentheses: Fe_{oct}-1 (0.625, 0.625, 0.625) and Fe_{oct}-2 (0.625, 0.125, 0.125)) are plotted in Figure 3.7a. It is found that the electronic structures of Fe_{oct}-1 and Fe_{oct}-2 are quite different: there is no state at E_f for Fe_{oct}-1 (Fe^{3+}) while a distinctive peak appears below E_f for Fe_{oct}-2 (Fe^{2+}). The HSE06 calculation (with 25% exact exchange) fails to describe the observed room-temperature symmetrical charge distribution over Fe_{oct} atoms in a unit cell in spite of the symmetry constraints imposed on the cubic structure. This PDOS is similar to the one obtained from Fe_3O_4 in a lower symmetry $P2/C$ unit cell in the work of Rowan *et al.*[39] Distortions of Fe B site octahedra can be caused by symmetry breaking due to charge ordering,[39] which can also be characterized by disproportionation of magnetic moments between Fe_{oct} atoms and opening of a *d*-*d* optical band gap.[25] We expect that these geometric distortions would occur, leading to the instability of the cubic Fe_3O_4 phase in the HSE06 functional. When using a smaller fraction of Hartree-Fock exchange, 15%, in the short range, the same electronic structure for two Fe_{oct} atoms in different positions is retained, as shown in Figure 3.7b. The magnetic moments and atomic charges from this electronic structure are similar to the PBE+*U* values although the magnetic moments of the Fe atoms are slightly smaller.

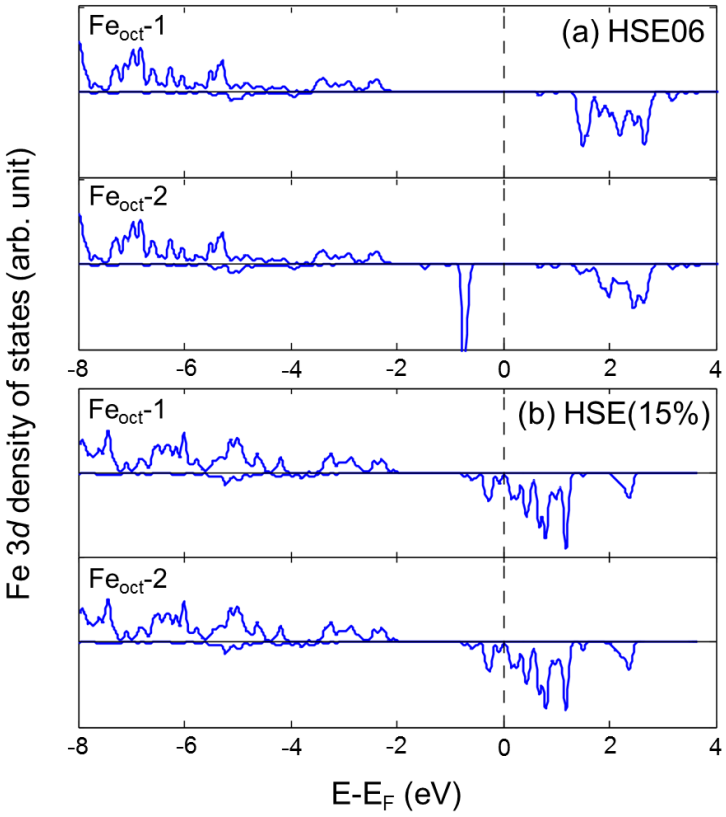

Figure 3.7 Density of states for Fe_{oct} atoms in two different positions: Fe_{oct}-1 (0.625, 0.625, 0.625) and Fe_{oct}-2 (0.625, 0.125, 0.125) in the cubic $Fd\bar{3}m$ phase using the (a) HSE06 and (b) HSE(15%) functionals.

3.4 Maghemite (γ-Fe_2O_3)

3.4.1 Introduction

The oxidation of magnetite, which occurs at a relatively low temperature near 50 °C, leads to maghemite (γ-Fe_2O_3). From a crystallographic point of view, maghemite has a spinel structure often written as $[Fe^{3+}]_A[Fe^{3+}_{5/3},V_{Fe,1/3}]_BO_4$ where the tetrahedral sites are denoted as A and the octahedral sites as B. These octahedral sites contain a number of cationic vacancies, V_{Fe}. We recall that magnetite (Fe_3O_4) is a ferrimagnet that has also a spinel structure with a chemical formula $[Fe^{3+}]_A[Fe^{3+},Fe^{2+}]_BO_4$, where the octahedral sites are filled with an equal number of ferric and ferrous ions. The structural similarities between the maghemite and magnetite crystals are demonstrated by the rapid adsorption of oxygen on magnetite surfaces and subsequent cation migration, leading to the formation of a maghemite coating.[40-46] However, maghemite has optical and electrical characteristics rather different from magnetite. One of the main advantages of working with maghemite over magnetite is its chemical stability, which results in maghemite being the second most stable polymorph of iron oxides following hematite. Since this material can be obtained as particles of different morphologies over a wide range of sizes from a few nm to microns, it attracts a great deal of interest in the field of nanoparticles for various technological applications such as ferrofluids, refrigeration systems, medical imaging, drug targeting, catalysis, and superparamagnetism.[47] Apart from the applications based on its magnetic properties, maghemite is a very interesting solid from a fundamental perspective as it contains cation vacancies inside the structure, which can be distributed with different degrees of ordering that impact its structural and magnetic properties.

Since not only the number of vacancies but also their ordering impact the lattice constants and, therefore, the physical properties of the structure, there have been intensive studies for several decades to elucidate the nature and degree of iron vacancy distributions in the octahedral sites within a maghemite crystal. Initially, it was suggested that four vacancies are randomly distributed amongst sixteen possible sites, preserving the cubic $Fd\bar{3}m$ symmetry; however, more recent studies have identified a higher degree of ordering, for example, corresponding to space group $P4_332$ where two types of octahedral sites exist: one with multiplicity 12 and the other 4. If maghemite possesses this symmetry, Fe vacancies are constrained to Wyckoff 4b sites, but with some level of disorder as the 4b sites have fractional (1/3) iron occupancies.[48] There is also evidence for a spinel tetragonal superstructure with c/a ~ 3 where the Fe atoms are completely ordered. Based on neutron diffraction studies[49] and synchrotron x-ray powder diffraction data,[50] the ordered maghemite structure is believed to have the tetragonal $P4_12_12$ space group with a=8.437 Å and c=25.042 Å. Figure 3.8 shows the ordered vacancy sites (spheres colored in white) for the $P4_12_12$ structure, which corresponds to the spinel cubic cell tripled along the c axis. This fully ordered structure with tetragonal space group $P4_12_12$ has been theoretically investigated by Grau-Crespo *et al.*[51] and these authors confirmed the thermodynamic stability of $P4_12_12$ over other partially disordered cubic spinel structures. According to their calculations based on the Born model, the suggested cationic configuration gives rise to a minimal Coulombic repulsion among Fe^{3+} cations. Therefore, we can expect that vacancy ordering can either change the symmetry of the spinel phase (cubic $Fd\bar{3}m$ to tetragonal $P4_12_12$) or appear without any distortion of cubic cell (cubic $Fd\bar{3}m$ to cubic $P4_332$).

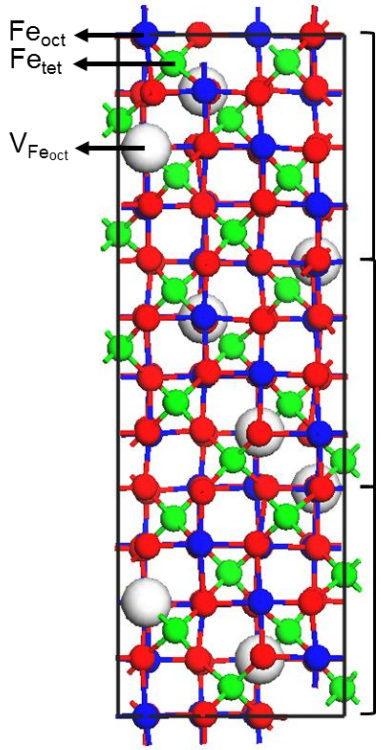

Figure 3.8 Crystal structure of maghemite (γ-Fe_2O_3) in its tetragonal space group $P4_12_12$ phase. Tetrahedral-site and octahedral-site Fe atoms are colored in green and blue, respectively, and oxygen atoms are in red. The cationic vacancies at octahedral sites are indicated by white spheres.

3.4.2 Optimized crystal structure

The lattice constant of maghemite in the $P4_12_12$ phase (a=8.340 Å[52]) is well-reproduced in PBE (8.344 Å), while PBE+*U* (8.405 Å) slightly overestimates the value by 0.065 Å. Such an overestimation is what we have observed in the hematite and magnetite crystal structures optimized with PBE+*U*. However, one of the important structural parameters

for maghemite, the ratio of c/a, 2.99, is consistent among PBE, PBE+*U* and experiment. Experimentally, the lattice constant in *a* direction of tetragonal maghemite decreases by ~ 0.7% compared to cubic magnetite. The value is estimated slightly lower in PBE, 0.5%, but higher in PBE+*U*, 1.0 %. Overall, the differences in geometric descriptions between PBE and PBE+*U* are not significant; however, from a practical standpoint, it is highly recommended to use a consistent level of calculations when comparing the structural data from one mineral to another in order to minimize the error coming from subtle variations in methodological treatments.

In tetragonal $P4_12_12$ maghemite, Fe-centered octahedra and tetrahedra undergo a geometric distortion from those in cubic $Fd\bar{3}m$ magnetite due to the presence of Fe_{oct} vacancies. Figure 3.9a shows the pair-wise radial distribution function of the Fe-O bond lengths within a maghemite unit cell that contains 32 f.u. For comparison, the bond lengths of Fe_{tet}-O and Fe_{oct}-O in a perfect magnetite crystal, 1.90 Å and 2.09 Å, are also indicated. At first glance, the bond distances between Fe and O are either shortened or elongated regardless of Fe position types: Fe_{tet}-O bond distances distribute in the range of 1.86-1.95 Å and Fe_{oct}-O in the range 2.02-2.17 Å. On right side of Figure 3.9a, examples of local geometries around 4-fold Fe_{tet} and 6-fold Fe_{oct} sampled from the optimized maghemite unit cell are presented. Indeed, for a Fe-centered tetrahedron, two of four Fe-O bonds are shortened to ~1.86 Å while the other becomes longer, ~1.93 Å. Six Fe_{oct}-O bonds in an Fe-centered octahedron show similar relaxation patterns: one bond becomes elongated by 0.06 Å, another remains unchanged, and the other four have shorter bonds by up to ~0.15 Å. Alternatively, we can also view these geometric alterations from an oxygen perspective. In the absence of cation vacancies, oxygen atoms are coordinated by

three Fe_{oct} and one Fe_{tet} atoms (see Figure 3.9d). When one third of Fe_{oct} atoms are removed from a unit cell, structural distortions appear. The oxygen atoms which are directly connected to the vacancy sites (Figure 3.9c) more strongly bind to the neighboring three Fe atoms to maintain local charge neutrality, which leads to Fe being more oxidized. On the other hand, near oxygen sites which preserve the full four-fold coordination, the Fe_{tet}-O bond length increases with Fe_{oct}-O bonds being either shorter or longer. Given that the details of the geometric structure differ markedly from magnetite, we can expect maghemite to display distinctive physical and chemical properties.

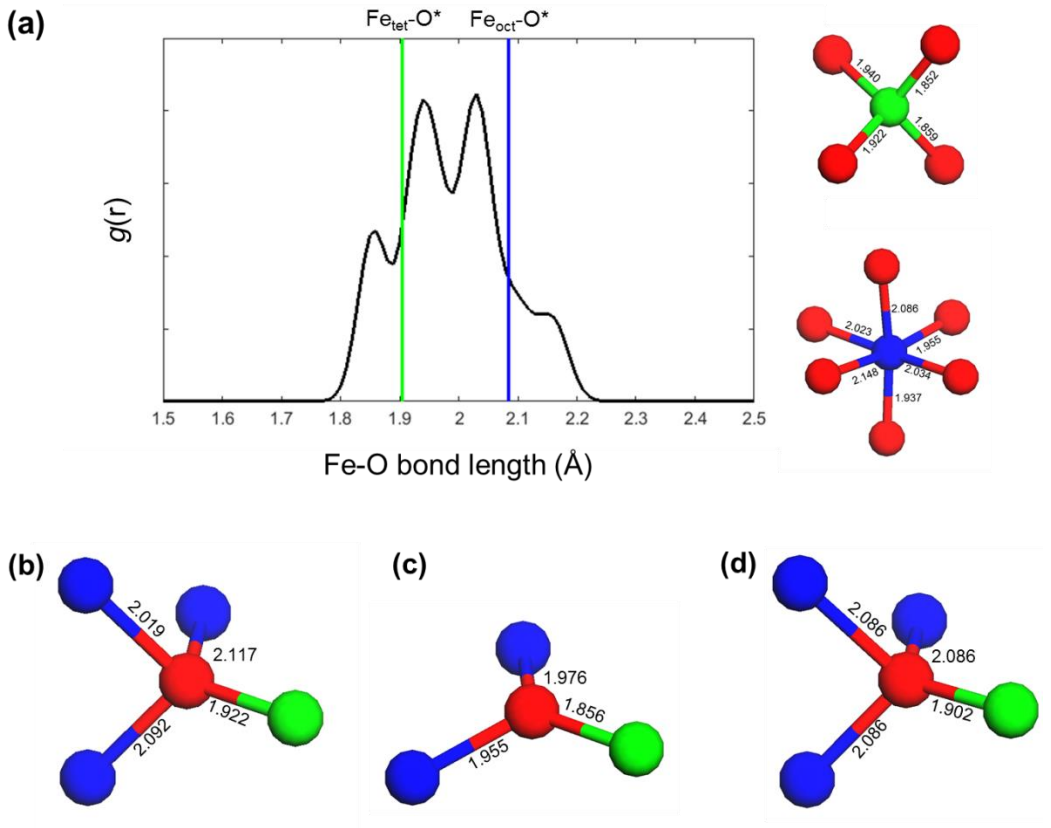

Figure 3.9 (a) Pair-wise radial distribution function, *g*(r), of Fe-O bond lengths in a tetragonal unit cell optimized with PBE+*U*. The RDF was constructed with a sampling of 0.005 Å interval, then broadened with a Gaussian distribution function of σ = 0.025 Å. Fe-O_{tet}^{*} and Fe-O_{oct}^{*} represent the bond distances in cubic magnetite. The inset images indicate Fe tetrahedron and octahedron randomly taken from the optimized unit cell. Two types of oxygen-centered tetrahedra present in maghemite are given in (b) and (c); the perfect O-Fe tetrahedron in bulk magnetite is also given in (d). Fe_{tet} atoms and Fe_{oct} atoms are colored in green and blue, and oxygen atoms in red. All numerical values in the geometric structures are in Å.

Figure 3.10 illustrates the distribution of Bader charges and Fe magnetic moments in a maghemite unit cell of $[Fe_{24}]_A[Fe_{40}]_BO_{96}$ calculated with PBE, PBE+*U*, and HSE(15%). The mean values for these physical parameters are also presented in Table 3.5. In a way

similar to the other iron oxides discussed earlier in this chapter, PBE tends to delocalize its electron density, which leads to the least ionic state in the solid, hence, underestimation of the Fe spin magnetic moments. At the PBE level, the magnetic moment is 3.71 μ_B for the octahedral Fe ions and 3.44 μ_B for the tetrahedral cations in an antiparallel direction, values that are much lower than the neutron diffraction data of 4.41 μ_B and 4.18 μ_B, respectively.[52] The results becomes closer to the experiment values at the PBE+*U* and HSE(15%) levels: PBE+*U* gives 4.18 $\mu_B$for octahedral sites and 4.08 μ_B for tetrahedral sites while HSE(15%) presents slightly lower values.[52] Overall, the calculated net magnetic moment of a tetragonal unit cell is ~ 2.47 μ_B/f.u., which indicates that all iron cations are now in a high-spin state. Compared to bulk magnetite, the lower content of Fe atoms in octahedral sites of maghemite results in electronic redistribution in such a way that all Fe_{oct} atoms are in a higher oxidation state. This accompanies a reduction in the magnetic moments of Fe_{oct}.

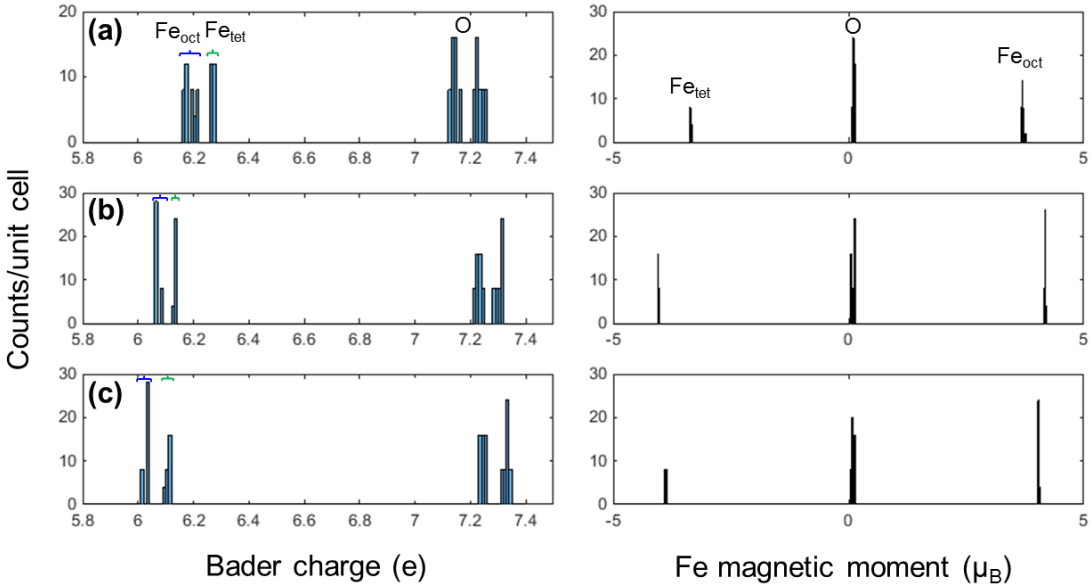

Figure 3.10 Distribution of Bader charges (left) and Fe magnetic moments (right) within the maghemite tetragonal $P4_12_12$ unit cell calculated with (a) PBE, (b) PBE+*U*, and (c) HSE(15%) with a sampling interval of 0.01.

Table 3.5 Mean values of magnetic moment μ and atomic charge, q, of each element in bulk maghemite calculated using PBE, PBE+*U*, and HSE(15%). HSE(15%) results are obtained at the PBE+*U*-optimized geometry. The corresponding values calculated for magnetite at the PBE+*U* level are given as a reference.

	Fe_{oct}		Fe_{tet}		O	
	μ (μ_B)	q (|e|)	μ (μ_B)	q (|e|)	μ (μ_B)	q (|e|)
PBE	3.71	+1.81	3.44	+1.73	0.11	-1.19
PBE+*U*	4.18	+1.93	4.05	+1.86	0.09	-1.27
HSE(15%)	4.04	+1.96	3.89	+1.99	0.11	-1.29
Fe_3O_4(PBE+*U*)	3.97	+1.72	4.09	+1.86	0.08	-1.22

3.4.3 Electronic and magnetic structure

Figure 3.11 shows the PDOS and electronic band structure of bulk maghemite. It should be pointed out that the DOS near the Fermi level is not symmetric due to its ferromagnetic ordering. The top of the valence band that consists of Fe 3*d* and O 2*p* hybridized states is higher in energy for majority spin electrons while the bottom of the conduction band is lower for minority spin electrons. The calculated electronic structure for tetragonal γ-Fe_2O_3 is similar to that of Fe_3O_4 albeit without a half-metallic character. When it comes to functionals, the PBE eigenvalue gap at the Γ point is calculated to be 0.90 eV for the spin-up bands and 0.37 eV for the spin-down bands. Again, this is far below the experimental value: for maghemite nanoparticles (22 nm), a band gap of 2.17–2.18 eV was estimated from the onset of the absorption edge in UV-visible diffused reflectance spectra.[53] This value is increased either by introducing a Hubbard *U* or partly including exact exchange in the short range: 2.34 eV (2.01 eV) and 2.58 eV (2.09 eV) for the spin majority (minority) channel, respectively.

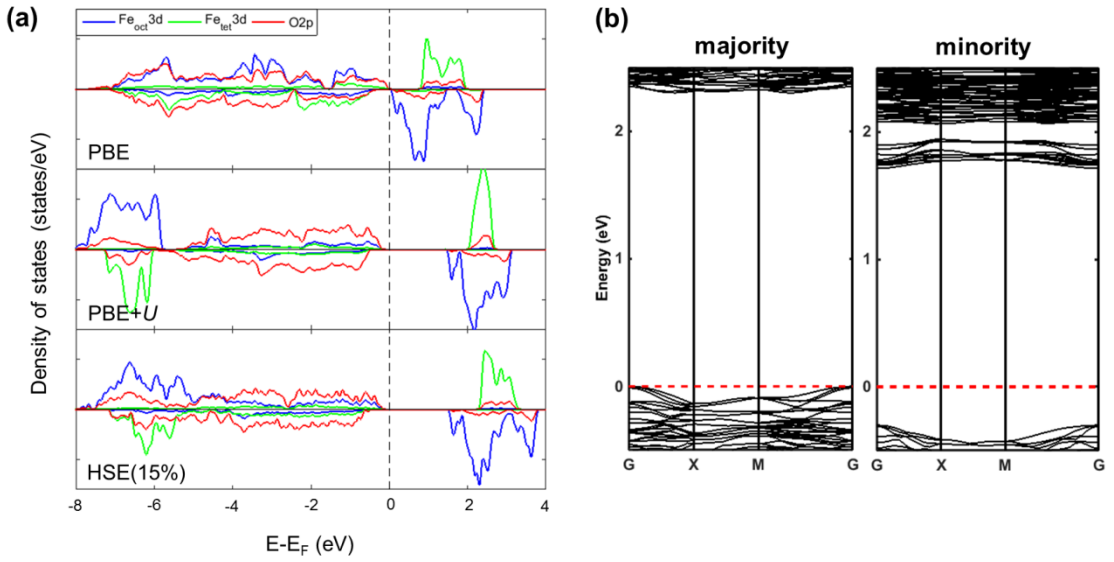

Figure 3.21 (a) PDOS and (b) electronic band structure of γ-Fe_2O_3 in a $P4_12_12$ unit cell. The blue, green, and red lines represent surface Fe_{oct} 3*d*, Fe_{tet} 3*d*, and O 2*p* states. The valence band maximum is set to zero energy and indicated with a dashed line.

3.5 Conclusions

In this Chapter, we have assessed the bulk properties of three different iron oxide phases: hematite (α-Fe_2O_3), magnetite (Fe_3O_4), and maghemite (γ-Fe_2O_3) from first-principles electronic-structure calculations. Although this class of materials shares similar crystal structures where Fe cations occupy octahedrally and/or tetrahedrally coordinated interstices in a close-packed oxygen anion lattice, interestingly, it has been shown that they present distinctive physical and chemical properties. The central point of this Chapter is not only to provide detailed descriptions of the geometric and electronic

structures of bulk iron oxides but also to determine the level of calculations that can correctly predict the physical observables.

The major findings presented in this Chapter can be summarized as follows:

- Although conventional DFT calculations can produce structural parameters close to experimental data, they fail to describe the electronic structures of iron oxides both quantitatively and qualitatively.
- Overall, a Hubbard *U* correction or the partial inclusion of exact exchange (E_{xx}) in hybrid functionals can alleviate this problem but the parameters should be carefully chosen by tuning U_{eff} or E_{xx} to experimentally obtained physical values.
- By taking hematite as an example, we also considered many-body quasi-particle (QP) techniques which do not require any empirical input. Amongst different levels of self-consistency based on PBE-derived KS wave functions, scQPGW_0 has been shown to yield a reasonable QP energy gap and to describe the material as a charge transfer or intermediate insulator.
- For magnetite, the amount of E_{xx} has a significant impact on the electronic structure: HSE with E_{xx} = 25%, *i.e.*, HSE06, predicts highly localized states for Fe_{oct} and introduces a spin minority gap at the Fermi level, while HSE with E_{xx} = 15% successfully reproduces the half-metallic character of cubic magnetite expected at room temperature. Thus, HSE06 may not be applicable to describe the room-temperature properties of surfaces and interfaces required to optimize devices and magnetite-catalyzed reactions.
- We confirmed that PBE+*U* (U_{eff} = 4 eV) and HSE(15%) can be applied to describe maghemite, which to date has been less studied than the other oxides.

The variations in the oxidation state of Fe_{oct} in tetragonal $P4_12_12$ maghemite results in geometric distortions from the magnetite crystal structure. The electronic band structure is predicted to be ferrimagnetic nature with an energy gap of ~ 2 eV, in good agreement with experiment.

3.6 References

[1] Rollmann, G.; Rohrbach, A.; Entel, P.; Hafner, J. *Phys. Rev. B* **2004**, *69*, 165107.
[2] Noh, J.; Osman, O. I.; Aziz, S. G.; Winget, P.; Bredas, J. L. *Sci. Technol. Adv. Mater.* **2014**, *15*, 044202.
[3] Tunega, D. *J. Phys. Chem. C* **2012**, *116*, 6703.
[4] Kresse, G.; Furthmuller, J. *Comp. Mater. Sci.* **1996**, *6*, 15.
[5] Kresse, G.; Furthmuller, J. *Phys. Rev. B* **1996**, *54*, 11169.
[6] Blochl, P. E. *Phys. Rev. B* **1994**, *50*, 17953.
[7] Perdew, J. P.; Burke, K.; Ernzerhof, M. *Phys. Rev. Lett.* **1997**, *78*, 1396.
[8] Anisimov, V. I.; Zaanen, J.; Andersen, O. K. *Phys. Rev. B* **1991**, *44*, 943.
[9] Dudarev, S. L.; Botton, G. A.; Savrasov, S. Y.; Humphreys, C. J.; Sutton, A. P. *Phys. Rev. B* **1998**, *57*, 1505.
[10] Krukau, A. V.; Vydrov, O. A.; Izmaylov, A. F.; Scuseria, G. E. *J. Chem. Phys.* **2006**, *125*, 224106.
[11] Franchini, C.; Podloucky, R.; Paier, J.; Marsman, M.; Kresse, G. *Phys. Rev. B* **2007**, *75*, 195128.
[12] Finger, L. W.; Hazen, R. M. *J. Appl. Phys.* **1980**, *51*, 5362.
[13] Coey, J. M. D.; Sawatzky, G. A. *J. Phys. Part C Solid* **1971**, *4*, 2386.
[14] Mochizuki, S. *Phys. Status Solidi A* **1977**, *41*, 591.
[15] Merchant, P.; Collins, R.; Kershaw, R.; Dwight, K.; Wold, A. *J. Solid State Chem.* **1979**, *27*, 307.
[16] Zimmermann, R.; Steiner, P.; Claessen, R.; Reinert, F.; Hufner, S.; Blaha, P.; Dufek, P. *J. Phys-Condens Mat.* **1999**, *11*, 1657.
[17] Pozun, Z. D.; Henkelman, G. *J. Chem. Phys.* **2011**, *134*.
[18] Fujimori, A.; Saeki, M.; Kimizuka, N.; Taniguchi, M.; Suga, S. *Phys. Rev. B* **1986**, *34*, 7318.
[19] Ma, Y.; Johnson, P. D.; Wassdahl, N.; Guo, J.; Skytt, P.; Nordgren, J.; Kevan, S. D.; Rubensson, J. E.; Boske, T.; Eberhardt, W. *Phys. Rev. B* **1993**, *48*, 2109.
[20] Noh, J.; Osman, O. I.; Aziz, S. G.; Winget, P.; Bredas, J. L. *Chem. Mater.* **2015**, *27*, 5856.
[21] Botti, S.; Marques, M. A. L. *Phys. Rev. Lett.* **2013**, *110*, 226404.
[22] Zhang, Z.; Satpathy, S. *Phys. Rev. B* **1991**, *44*, 13319.
[23] Jordan, K.; Cazacu, A.; Manai, G.; Ceballos, S. F.; Murphy, S.; Shvets, I. V. *Phys. Rev. B* **2006**, *74*, 085416.
[24] Verwey, E. J. W. *Nature* **1939**, *144*, 327.
[25] Park, S. K.; Ishikawa, T.; Tokura, Y. *Phys. Rev. B* **1998**, *58*, 3717.
[26] Senn, M. S.; Loa, I.; Wright, J. P.; Attfield, J. P. *Phys. Rev. B* **2012**, *85*, 125119.
[27] Senn, M. S.; Wright, J. P.; Attfield, J. P. *Nature* **2012**, *481*, 173.
[28] Mizoguchi, M. *J. Phys. Soc. Japan* **1978**, *44*, 1501.
[29] Wright, J. P.; Attfield, J. P.; Radaelli, P. G. *Phys. Rev. B* **2002**, *66*.
[30] Miyamoto, Y.; Shindo, M. *J. Phy. Soc. Japan* **1993**, *62*, 1423.
[31] Cornell, R. M.; Schwertmann, U. *The iron oxides : structure, properties, reactions, occurrences, and uses*; 2nd, completely rev. and extended ed.; Wiley-VCH: Weinheim, 2003.

[32] Chase, M. W.; National Institute of Standards and Technology (U.S.) *NIST-JANAF thermochemical tables*; 4th ed.; American Chemical Society;American Institute of Physics for the National Institute of Standards and Technology: Washington, DC, New York, 1998.
[33] Rakhecha, V. C.; Murthy, N. S. S. *J. Phys. C Solid State* **1978**, *11*, 4389.
[34] Zhu, L.; Yao, K. L.; Liu, Z. L. *Phys. Rev. B* **2006**, *74*, 035409.
[35] Cai, Y. Q.; Ritter, M.; Weiss, W.; Bradshaw, A. M. *Phys. Rev. B* **1998**, *58*, 5043.
[36] Lad, R. J.; Henrich, V. E. *Phys. Rev. B* **1989**, *39*, 13478.
[37] Fonin, M.; Dedkov, Y. S.; Pentcheva, R.; Rudiger, U.; Guntherodt, G. *J. Phys-Condens Mat.* **2007**, *19*, 315217.
[38] Wang, W.; Mariot, J. M.; Richter, M. C.; Heckmann, O.; Ndiaye, W.; De Padova, P.; Taleb-Ibrahimi, A.; Le Fevre, P.; Bertran, F.; Bondino, F.; Magnano, E.; Krempasky, J.; Blaha, P.; Cacho, C.; Parmigiani, F.; Hricovini, K. *Phys. Rev. B* **2013**, *87*.
[39] Rowan, A. D.; Patterson, C. H.; Gasparov, L. V. *Phys. Rev. B* **2009**, *79*.
[40] Frison, R.; Cernuto, G.; Cervellino, A.; Zaharko, O.; Colonna, G. M.; Guagliardi, A.; Masciocchi, N. *Chem. Mater.* **2013**, *25*, 4820.
[41] Kaur, M.; McCloy, J. S.; Qiang, Y. *J. Appl. Phys.* **2013**, *113*, 17D715.
[42] Kumar, N.; Auffan, M.; Gattacceca, J.; Rose, J.; Olivi, L.; Borschneck, D.; Kvapil, P.; Jublot, M.; Kaifas, D.; Malleret, L.; Doumenq, P.; Bottero, J.-Y. *Environ. Sci. Tech.* **2014**, *48*, 13888.
[43] Santoyo Salazar, J.; Perez, L.; de Abril, O.; Truong Phuoc, L.; Ihiawakrim, D.; Vazquez, M.; Greneche, J.-M.; Begin-Colin, S.; Pourroy, G. *Chem. Mater.* **2011**, *23*, 1379.
[44] Vaz, C. A. F.; Balan, A.; Nolting, F.; Kleibert, A. *Phys. Chem. Chem. Phys.* **2014**, *16*, 26624.
[45] Wang, C.; Baer, D. R.; Amonette, J. E.; Engelhard, M. H.; Antony, J.; Qiang, Y. *J. Am. Chem. Soc.* **2009**, *131*, 8824.
[46] Yao, Y.; Hu, Y.; Scott, R. W. J. *J. Phys. Chem. C* **2014**, *118*, 22317.
[47] *Surface and Colloid Science*; Matijevic, E.; Borkovec, M., Eds.; Springer US, 2004; Vol. 17.
[48] Rai, B. *Molecular Modeling for the Design of Novel Performance Chemicals and Materials* **2012**, Xi.
[49] Shmakov, A. N.; Kryukova, G. N.; Tsybulya, S. V.; Chuvilin, A. L.; Solovyeva, L. P. *J. Appl. Crystallogr.* **1995**, *28*, 141.
[50] Jorgensen, J. E.; Mosegaard, L.; Thomsen, L. E.; Jensen, T. R.; Hanson, J. C. *J. Solid State Chem.* **2007**, *180*, 180.
[51] Grau-Crespo, R.; Al-Baitai, A. Y.; Saadoune, I.; De Leeuw, N. H. *J Phys-Condens. Mat.* **2010**, *22*.
[52] Greaves, C. *J. Solid State Chem.* **1983**, *49*, 325.
[53] Apte, S. K.; Naik, S. D.; Sonawane, R. S.; Kale, B. B. *J. Am. Ceram. Soc.* **2007**, *90*, 412.

CHAPTER 4. MODELING OF OXIDE SURFACES IN VARIOUS ENVIRONMENTAL CONDITIONS

The primary objective of this Thesis is to understand how iron-based substrates can be surface-modified with organic layers and to characterize theoretically the inorganic-organic interfacial geometric and electronic structures. However, reaching an understanding of the basic physics and chemistry of molecular adsorption on iron and iron oxide surfaces requires first to build a thorough understanding of the atomic and electronic structure of the clean surfaces: to know what has happened upon organic-layer deposition, we need to know where we started.

This Chapter attempts to address a theoretical description of iron oxide surfaces; these are in fact not uniquely defined by their orientation since different terminations with distinct chemical compositions can be exposed at the surface. Computational approaches involving so-called "first-principles thermodynamics" based on density functional theory (DFT), have been used to describe systems in contact with a chemical reservoir, such as surfaces in thermodynamic equilibrium with an atmosphere of variable compositions, as illustrated in Chapter 2.

The first half of the Chapter (section 4.2) is devoted to magnetite as an example to explain how to consider an oxide structure from a surface point of view. The initial focus is on the theoretical prediction of the most favorable surface configuration of Fe_3O_4

(111), which can vary as a function of temperature and oxygen partial pressure. We further discuss surface stabilization mechanisms at work on Fe_3O_4 (111) polar surfaces, such as interlayer relaxation effects, change of covalency in the surface layers, and partial filling of surface states to assess their actual efficiency in cancelling polarity, which eventually determines the surface characteristics. Also, we compare the electronic and magnetic properties associated with various surface configurations of Fe_3O_4 (111), which is required regarding its potential application as a spin-injecting electrode in spintronic devices.

In the last section (section 4.3), we extend this thermodynamic approach to determine the surface stoichiometry of iron oxide surfaces exposed to atmospheric conditions including multiple gas components: oxygen and water vapor; here, we take hematite as an example. Since a major promising application of hematite is its development as a catalytic electrode material for photoelectrochemical (PEC) water splitting systems,[1,2] it is important to investigate the exact nature of the hematite surface, where chemical species can possibly bind through electrostatics, charge transfer, or hydrogen bonding. For α-Fe_2O_3 (0001), which corresponds to the preferential growth direction,[3] we determine the most favorable surface domains in water exposure conditions and further examine the surface models in terms of how the surface core-level shifts and local geometries are modified by hydroxylation and hydration.

4.1 Computational details

First-principles calculations have been performed using spin-polarized DFT as implemented in the Vienna ab initio simulation package (VASP).[4,5] The ionic potentials are described by the PAW pseudopotential[6] with valence configurations of $3d^7 4s^1$ and $2s^2 2p^4$ for the Fe and O atoms, respectively. The energy cutoff for the plane-wave basis set was set to 550 eV. We exploited the DFT+Hubbard *U* (DFT+*U*) approach[7] to describe the intra-atomic Coulomb interaction among strongly correlated Fe 3*d* electrons. This approach describes the band gap and magnetic moments of iron oxides with good accuracy when combined with the generalized gradient approximation (GGA) exchange-correlation functional of Perdew, Burke, and Ernzerhof (PBE).[8] In this work, we applied U_{eff} = 4 eV to the Fe 3*d* electrons in the simplified rotationally invariant formulation of Dudarev *et al.*[9] where the on-site Coulomb parameter, *U*, and exchange parameter, *J*, are combined into a single parameter, $U_{eff} \equiv U - J$.

A well-established tool to investigate the electronic structure of surfaces and interfaces at the DFT level is the repeated slab approach that allows one to take easy account of the two-dimensional periodic character of such systems. The surface is modeled using a symmetric slab with a (1×1) unit cell based on the optimized bulk crystal structures obtained in Chapter 3. The slabs contain ~ 20 atomic layers with a vacuum region of approximately 20 Å separating the slabs. In order to maintain bulk behavior below the surface, the central layers were kept fixed at the bulk crystal positions while the outermost six atomic layers on both sides of the slab were allowed to relax. A ferrimagnetic ordering, where the sign of the Fe_{oct} atoms are antiparallel to those of the Fe_{tet} atoms, was taken as the initial magnetic configuration and allowed to relax for all the

surface models of Fe_3O_4 (111). Similarly, the bulk antiferromagnetic ordering, *i.e.*, (↑↑↓↓) along the [111] direction, was used for the hematite slabs. For Brillouin-zone integrations, 7×7×1 **k**-point meshes are used for the unit cell of (1×1) Fe_3O_4 (111) and α-Fe_2O_3 (0001). The van der Waals (vdW) interactions from dynamic correlations between fluctuating charge distributions were approximated using Grimme's D3 method.[10] Geometries were optimized with a quasi-Newton or/and conjugate-gradient algorithm until the Hellmann-Feynman forces were lower than 0.01 eV/Å and energy convergence within 10^{-5} eV/atom. A Gaussian-smearing approach for the orbital occupancies with σ = 0.05 eV was used during the geometry optimizations.

In the electronic-structure analyses, the densities of electronic states (DOS) were evaluated using the tetrahedron method with Blöchl corrections.[11] The oxidation state of surface Fe atoms was obtained from a Bader charge analysis.[12] The surface states of Fe_3O_4 (111) are investigated using *pseudo*-STM images obtained from the Tersoff-Hamann method[13] where the tunneling current in an STM experiment is assumed to be proportional to the local density of states integrated from the Fermi level to the bias.[14] The O1s surface core-level shifts (SCLS) of hematite slabs were calculated in the final-state approximation using the approach of Köhler *et al.* as implemented in VASP.[15] The SCLS values were also calculated by an alternative approach based on the Slater-Janak transition-state theorem,[16,17] which essentially gives the same results as the former method.

4.2 Fe_3O_4 (111) surfaces in an oxygen environment

4.2.1 Surface models examined

The magnetite crystal contains layers of either only iron cations or oxygen anions along the [111] direction with the stacking sequence: O_1-Fe_{oct1}-O_2-Fe_{tet2}-Fe_{oct2}-Fe_{tet1}, as displayed in Figure 4.1; this leads to six unique atomic planes, where we follow the conventional notations to refer to each of the six bulk terminations.[18] The four iron terminations can present two different Fe sublayers; one is a dense monolayer (3/4ML) with all octahedrally coordinated Fe atoms (Fe_{oct1}) on the same plane, while the other sublayer contains three distinct low-density monolayers (1/4ML) involving both octahedrally and tetrahedrally coordinated Fe atoms (Fe_{tet2}-Fe_{oct2}-Fe_{tet1}). Those two iron sublayers are alternating between nearly close-packed oxygen stacking layers (1ML) that present a slight buckling. As the number and charge of the iron and oxygen ions on the surface differ, Fe_3O_4 (111) can be classified as a type-3 polar surface in the Tasker classification scheme,[19] with diverging electrostatic surface energy due to the presence of a non-zero dipole moment on all the repeat units throughout the material. In order to decrease the internal polarity perpendicular to the surface, major ionic relaxation and electron redistribution, as well as surface reconstruction, are expected;[20] in spite of multiple studies involving various surface science techniques and computational approaches, the atomistic details of the Fe_3O_4 (111) surface are still a matter of debate as the exposed surface depends strongly on the preparation conditions and chemical environment. As the spin-polarization, resistivity, and Verwey transition are dependent on the exact stoichiometry of thin films, development of an atomic-level description is vital.

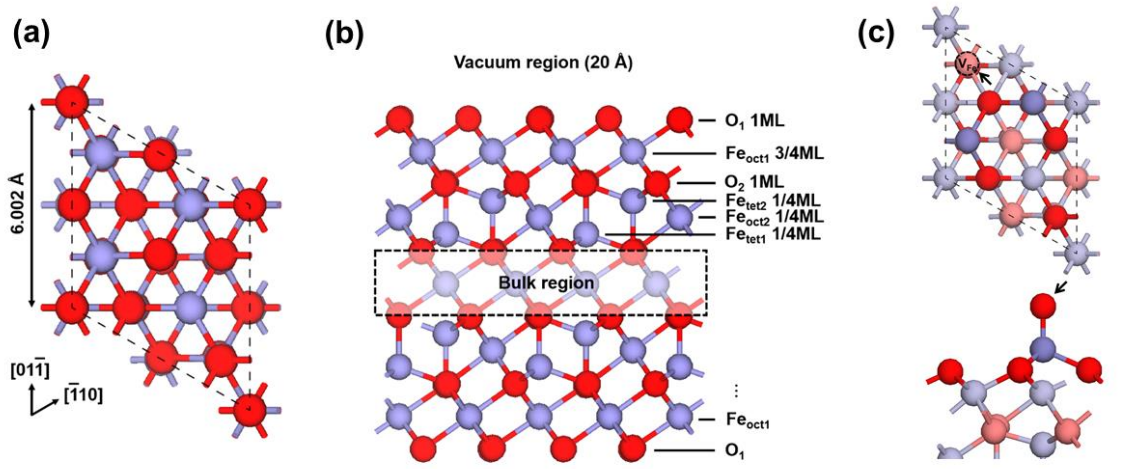

Figure 4.1 (a) Top view and (b) side view of the symmetric Fe_3O_4 (111) slab model. The stacking sequence, labeled O_1-Fe_{oct1}-O_2-Fe_{tet2}-Fe_{oct2}-Fe_{tet1}, is shown in panel (b). Fe atoms are colored blue, and oxygen ions are colored red. (c) Top view of the Fe_{oct1} termination with one Fe vacancy. The vacant site is indicated by an arrow (top). Side view of the Fe_{tet1} termination with ferryl group formation upon attachment of an additional oxygen atom on the surface, indicated with an arrow. Fe atoms are colored blue, and oxygen ions are colored red.

At this stage, it is useful to recall a number of previous observations regarding magnetite surfaces. Scanning tunneling microscopy (STM) study of Fe_3O_4 (111) annealed at 1173 K in 2×10^{-7} mbar O_2 reported a coexisting surface termination composed of a hexagonal array of 6.1 Å and a honeycomb pattern separated by 3.6 Å.[21] The authors assigned the second pattern to termination to 2/4 ML of Fe atoms, which is predicted to be more stable than the former, 3/4 ML capped by an O atom. In a later paper, the same authors reexamined the surface structure of single crystal UHV-prepared Fe_3O_4 (111) and concluded that the surface mainly consists of Fe_{tet1}, Fe_{oct2}, and ferryl terminations.[22] Full-potential density functional theory calculations by Zhu *et al.*[23] show that the Fe_{oct2}

termination is energetically more favorable using a local density approximation (LDA)+*U* approach; their results are consistent with those from *ab initio* periodic Hartree-Fock (HF) calculations,[24] although HF bulk band-structure calculations fail to reproduce the known antiferromagnetic alignment of magnetic moments within the tetrahedral and octahedral sublattices.[25] STM and low-energy electron diffraction (LEED) intensity analysis at 1000 K in a 10^{-6} mbar atmosphere indicates the Fe_3O_4 (111) surface forms an unreconstructed bulk termination that exposes ¼ ML Fe_{tet1} atoms over a close-packed oxygen layer, with protrusions arranged in a hexagonal lattice with a 6 Å periodicity.[26,27] Both Paul *et al.*[28] and Shimizu *et al.*[29] report that the Fe_{tet1} termination is routinely observed in naturally grown single crystals at room temperature whereas Fe_{oct2} appears only when the sample is prepared under oxygen-poor conditions, for instance, when exposed to UHV for a long period of time. This supports the results of GGA+*U* calculations by Grillo *et al.*[30] and Kiejna *et al.*,[31] which indicates that the two surfaces have comparable thermodynamic stabilities at this limit. Another type of coexistence of surface terminations has been observed by Berdunov *et al.*[32] Here, the regular Fe_{tet1} termination consists of the superstructure with an oxygen-rich surface for crystalline Fe_3O_4 (111) possibly with oxygen vacancies after annealing in an oxygen partial pressure of 10^{-6} mbar at 950 K and subsequently cooling to room temperature.

An alternative to bulk termination reconstruction is the existence of defects, *e.g.*, vacancies or adatoms, on the surface. Lennie *et al.*[21] have proposed that the irregular texture observed in their STM images points to the presence of defects in the surface layer. One of the possible defects is an iron vacancy formed on Fe_{oct1} termination to stabilize the surface polarity. In the Fe_{oct1} surface, a single V_{Fe} is expected to be more

stabilizing than two cationic vacancies as its surface charge (+5) from the remaining octahedral ions is closer to half the absolute value of the subsurface charge (-4), which fulfills the condition for the cancellation of the macroscopic dipole moments according to classical electrostatics.[20] Ferric iron vacancies have also been observed on Fe_{tet1}-terminated epitaxial Fe_3O_4 (111) films grown on Pt (111) substrates in a 10^{-6} mbar oxygen partial pressure,[27] as having inhomogeneities caused by FeO_x agglomerates[33] and FeO_{1-x} overlayers[27,28] on the surface. In order to evaluate the impact of defects, in addition to four bulk terminations in the [111] direction (Fe_{tet1}, Fe_{oct1}, Fe_{oct2}, and O_1), we have chosen to study single cationic vacancies formed at the octahedrally coordinated iron layer (Fe_{oct1}) on the surface. Iron vacancies in octahedral sites are exceptionally noteworthy as they are associated with the oxidation redox cycles of magnetite(100)[34] in contrast to oxygen vacancies in other metal oxides.[35] We have also considered oxygen vacancies in the close-packed oxygen layer as proposed in earlier STM studies.[32] Other possible surface modifications are attachments of foreign atoms or ions from the residual atmosphere due to experimental conditions. Several STM studies have observed adsorbates above the atomic layer.[28,33] Importantly, high-resolution STM measurements show there is a distinctive step of 1.2±0.1Å above the regular Fe_{tet1} terminated surface, suggesting that surface iron atoms may be capped by a single oxygen atom at the atop position.[22] A similar termination, with a hydroxyl group on top of the surface terminating cations, has been proposed after water exposure.[29,36] The STM results indicate that dissociative water adsorption to form surface hydroxyls takes place on a termination of Fe_3O_4 (111) thought to contain a 1/4 monolayer of Fe^{3+} ions on top of a close-packed oxygen monolayer.[37] To evaluate this class of defects, we have modified the Fe_{tet1}

termination with two adsorbates, an oxygen atom and a hydroxyl group. Thus, in total, we will consider four defect-containing surface terminations; (i) iron vacancy in Fe_{oct1} (V_{Fe}, bottom panel of Figure 4.1c); (ii) oxygen vacancy in O_1 (V_O); (iii) oxygen adatom on Fe_{tet1} (ferryl, top panel of Figure 4.1c); and (iv) hydroxyl adsorbate on the Fe_{tet1} termination.

4.2.2 Surface energetics and structural relaxation

Using the computational approach described in Chapter 2, we have evaluated the relative stabilities of the surface models. The results are plotted as a function of oxygen partial pressure in Figure 4.2a for the PBE+*U* functional. Previous theoretical studies containing only bulk terminations have concluded that the Fe_{tet1} termination has the lowest surface energy in the oxygen-rich regime, while the Fe_{oct2} and Fe_{oct1} surfaces are competitive in the oxygen-poor regime.[30,31,38,39] The defect-containing surfaces that we examine here are viable in comparison to the bulk-like terminations. For example, as both the V_O and ferryl-terminated surfaces are within 100 meV/Å^2 (1.60 J/m^2) of the Fe_{tet1} surface near the oxygen-rich limit, specific sample preparation methods or environmental conditions may lead to the observation of these oxygen-rich surfaces. The ferryl termination is more stable than the formally oxygen-terminated surfaces over most of the pressure range. Experimental observations by Berdunov *et al.*[32] point to the presence of such oxygen-terminated surfaces, which are higher in surface energy than the defect-containing surfaces. This is in agreement with the large binding energy of an oxygen atom located in a bridge position between Fe_{tet1} and Fe_{oct2} atoms as calculated by Santos-Carballal *et al.*[39]

We note that there is a well-known overbinding problem[40] in small molecules within DFT (and DFT+*U*), which can lead to an inaccurate energy for molecular oxygen. If we replace the calculated binding energy of oxygen gas with the experimental value, 5.23 eV[41] ($E_{B,exp.}$), the chemical potential limit can be rewritten as $\mu_{O_2,exp} = E_{B,exp.} + 2\mu_{O,DFT}$. This equates to shifting the oxygen-rich limit to a more positive value by 0.4 eV, shown as the rightmost vertical line in Figure 4.2a. This is smaller than the 1.36 eV shift determined by differences in experimental and calculated formation energies over a series of oxides, which was used previously.[42] At this extreme, the ferryl termination becomes isoenergetic with the Fe_{tet1} termination.

In the oxygen-poor limit, the Fe_{oct2} termination is shown to be more stable than the Fe_{tet1} termination, as suggested before.[21,28,29] The Fe_{oct1} termination becomes more energetically favored than the Fe_{oct2} termination only at extremely low oxygen chemical potentials, beyond the estimated oxygen-poor limit, because of the higher density of Fe ions on the Fe_{oct1} surface. However, missing Fe atoms on this termination, labeled as V_{Fe}, moderately stabilize the surface, leading to competitive surface energies with the Fe_{oct2} termination over the entire range of oxygen chemical potentials.

The modified surfaces presented above are high in defect density, with one defect or adlayer in each unit cell. The stability of the ferryl surface with a lower defect coverage on the Fe_{tet1} termination ($\Theta = 1/4$) is shown in Figure 4.2b. This approach has previously been used to study mixed terminations of hematite surfaces.[43] The resulting mixed surface is nearly equal in energy to the Fe_{tet1} termination over much of the potential range, and the point at which it becomes lower in energy shifts further toward

lower oxygen chemical potentials. In a macroscopic surface, these defects may be present, even if higher in energy in a small unit cell. Given the stringent requirements for spin-injection and -detection in devices, contributions from these slightly higher-energy surfaces may determine the overall operational success of a device.

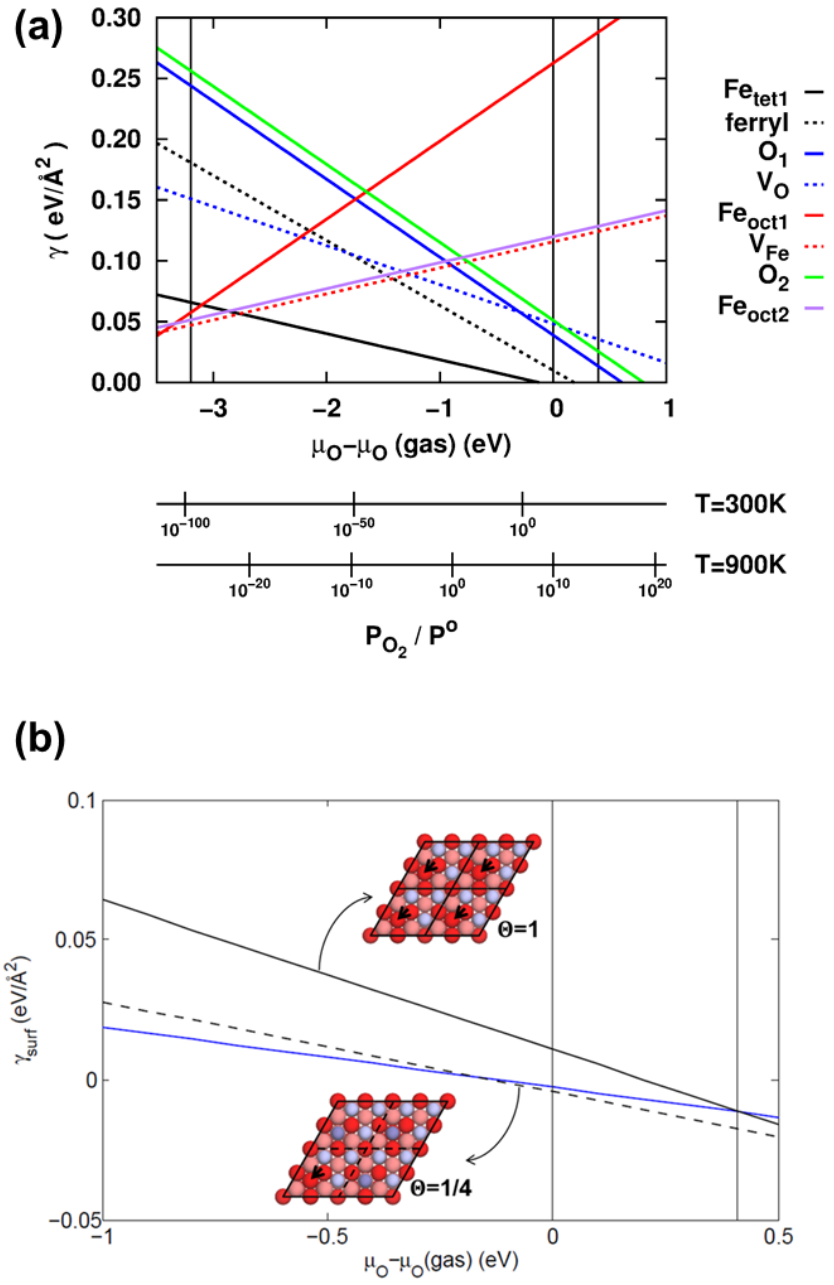

Figure 4.2 (a) PBE+*U* derived surface energies of the different terminations plotted against the oxygen chemical potential. The vertical black lines indicate the allowed range of the chemical potential. The bottom two horizontal axes indicate corresponding oxygen pressure in log scale at 300 K and 900 K, respectively (p° = 1 bar). (b) Surface free energy change as a function of the oxygen chemical potential for two different ferryl concentrations on the surface: 25% (dotted black) and 100%. (solid black) The blue line indicates Fe_{tet1} termination. The arrows in inset images correspond to the positions where oxygen adatoms are attached.

As described above, (111) surfaces created from cleavage of bulk cubic magnetite are unstable as two inequivalent layers of opposite charge densities alternate perpendicular to the surface. A high dipole moment, 29.5 D, is estimated within the repeat unit of six distinct layers when using formal charges and the bulk interlayer spacing.[20] One pattern of stabilization of these surfaces is through significant changes in the nuclear positions of the atoms comprising the surface layers.

The interlayer relaxations are determined mostly by a response to the large dipole moments of alternating polar layers in the surface layers. The relaxations between adjacent layers (ij) of the outmost six layers as a percentage (Δ_{ij}) of the bulk interlayer distance are shown in Figure 4.3 for terminations based on (a) Fe_{tet1}, (b) O_1, and (c) Fe_{oct1}. For instance, in the Fe_{tet1} termination, the surface Fe_{tet1} atom shows a strong inward relaxation and the interlayer spacing between the surface layer and subsurface layer decreases by 37%. Further reduction in polarity is achieved by a 22% compression in the O_1- Fe_{oct1} distance, which fully stabilizes the surface as there are progressively smaller changes in geometries for the rest of the slab. The overall relaxation of the Fe_{tet1} termination is consistent with a previous LEED analysis.[26] For the ferryl and hydroxyl surfaces, the surface Fe_{tet} atom retains its bulk-like tetrahedral coordination by binding to the oxygen adatom; also, the electrostatic attraction of a surface Fe ion to the oxygen atoms in the sublayer is balanced by the adatom. The newly formed Fe=O and Fe-O bonds are estimated to be 1.62 Å and 1.77 Å, which are consistent with the 1.5 Å-height adsorbates reported in STM studies.[33] Hence, the Fe_{tet1}-O_1 distance decreases by 17% and 9% for the ferryl and hydroxyl surfaces. However, the relaxations in the next layers in the

slab are now in the opposite direction than in the Fe_{tet1} slab, with the Fe_{oct1}-O_2 distance being compressed and the O_2-Fe_{tet2} distance slightly expanding.

There are only moderate changes in interlayer spacing in the O_1 surface, and these are smaller in the V_O surface due to the reduced surface charge. The introduction of a Fe vacancy in the Fe_{oct1} termination (V_{Fe}), shown in 3c, changes the local geometries at the surface, although in a different fashion from the bulk Fe_{oct1} termination. In the V_{Fe} termination, one of the four oxygen atoms in the subsurface ends up migrating above the iron surface due to the vacated volume and a strong electrostatic attraction between two outermost layers. As a consequence, the surface Fe_{oct1} atoms bind more strongly to the surrounding oxygen atoms with a reduced bond length, 1.88 Å, compared to the bond in the Fe_{oct1} termination, 1.93 Å. Moreover, the three remaining oxygen atoms in the O_2 layer now interact more with the underneath iron layers, Fe_{tet2} and Fe_{oct2}, since the protruding oxygen exclusively forms ionic bonds with the two Fe atoms on the surface.

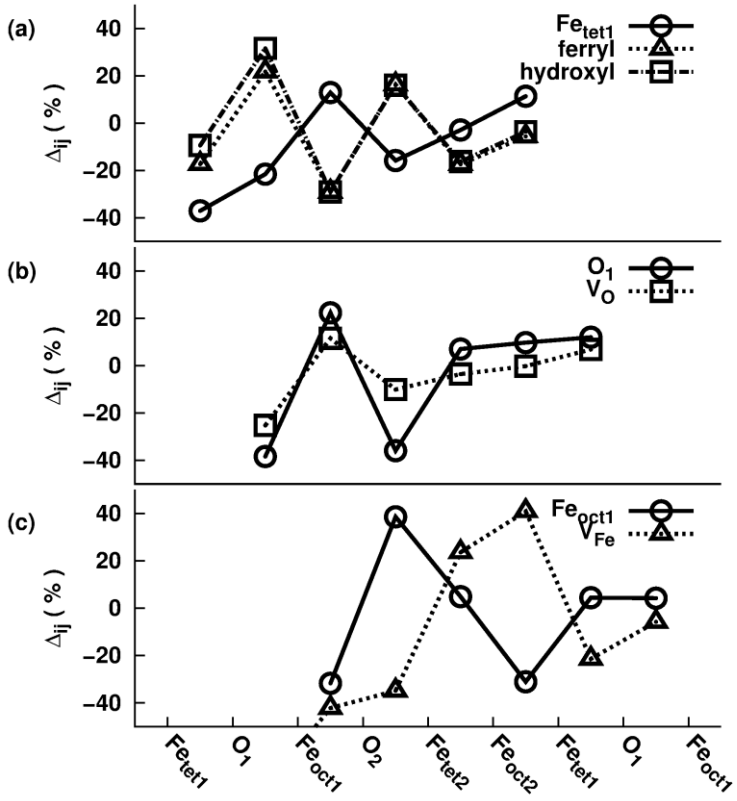

Figure 4.3 Surface relaxations in the outmost six layers given as a percentage (Δ_{ij}) of the bulk interlayer distances between two adjacent surface planes (i) and (j) projected onto the c axis for the seven terminations of Fe_3O_4 (111). Terminations based on (a) Fe_{tet1}, (b) O_1, and (c) Fe_{oct1} are shown in separate panels. The bulk interlayer distances between Fe_{oct1}-O, Fe_{tet}-O, and Fe_{tet}-Fe_{oct2} are 1.19 Å, 0.64 Å, and 0.61Å, respectively.

4.2.3 Surface electronic structure and chemistry

Since the surfaces are created by cleaving ionic bonds, significant charge redistribution occurs due to the appearance of dangling bonds. In this study, the density of states (DOS), Bader charge, net magnetic moment, and work function are calculated to describe

the related stabilization mechanism upon surface cleavage and change in surface chemistry.

4.2.3.1 Density of states

The DOS projected on Fe_{oct}, Fe_{tet}, and O atoms for near-surface (3-4) layers of each termination are displayed in Figure 4.4. The electronic structure of bulk Fe_3O_4 in a cubic $Fd\bar{3}m$ phase can be described as a half-metallic oxide, which is consistent with the crystal-field splitting explanation for octahedral Fe ions that the five *d* levels separate into three degenerate t_{2g} levels and two degenerate e_g levels.[44] The PDOS for the central layers of the slab retain this electronic structure.

The PDOS for the surface layers in the Fe_{tet1} termination, plotted in Figure 4.4a, show that the minority (spin-down) Fe t_{2g} states from the octahedral sites are no longer present at or near the Fermi level and there appears a surface state related to tetrahedral-site iron in the middle of the majority spin (spin-up) gap. The partial charge density for this state is shown in Figure 4.4, and demonstrates that the 3*d* orbitals in the direction of reduced coordination, *i.e.*, the [111] direction, are more stabilized and now lie below the Fermi level. In general, surface truncation of iron-terminated surfaces promotes a further splitting within Fe_{tet1} e_g and t_{2g} orbitals at the surface as the symmetry is lowered because of missing apical oxygen.[45] Since the Fe_{tet1} termination has a positively charged surface, the top Fe_{tet1} layer obtains more electrons through electronic redistribution to reduce the polarity, with the bottom of the conduction band becoming occupied. The ferryl termination, where the Fe_{tet1} surface has an additional oxygen atom bound to the exposed iron atom, shows a different DOS with respect to the Fe_{tet1} surface; the ferryl group

comprises a set of states near the Fermi level and the surface state related to tetrahedral-site iron no longer appears in the spin-up gap (the PDOS of adsorbate oxygen is colored in magenta in Figure 4.4). In the hydroxyl termination, these hybridized states are stabilized and now located in the same region as the surface oxygen atoms.

In the Fe_{oct1} termination with a vacancy, V_{Fe}, there are no longer octahedral states observed around the Fermi energy in contrast to Fe_{oct2} although the two models have the same Fe coverage over the oxygen sublayer, *i.e.*, ½ ML. Instead, the electrons are redistributed over the surface in a fashion similar to the Fe_{oct1} termination. In both cases, the Fe 3*d* states on octahedral sites are shifted to lower energy, leading to a reduction of these Fe atoms to stabilize the positively charged outmost layer. The occupied Fe 3*d* minority spin states (between -1 eV and -0.5 eV) are more populated in the bulk-terminated Fe_{oct1} surface. Despite overall similarity in the PDOS between Fe_{oct1} and V_{Fe}, the states just below the Fermi level (marked with arrows c and d in Figure 4.4) are qualitatively different. In the Fe_{oct1} surface, the charge is delocalized over the first layer of the surface, whereas the iron vacancy leads to the state becoming more localized on each Fe atom on the surface.

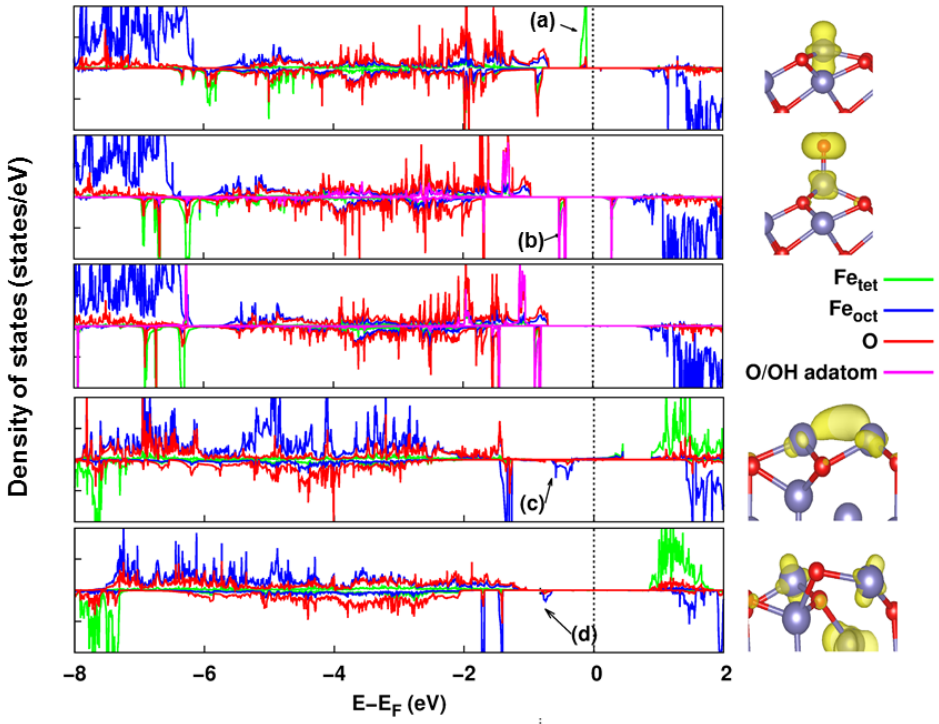

Figure 4.4 Electronic densities of states of bulk phase and the near-surface (3-4) layers of the surfaces: $Fe_{tet1,}$ ferryl, hydroxyl, $Fe_{oct1,}$ and V_{Fe} termination from PBE+*U* calculations from -8 eV to +2 eV with respect to the Fermi level. The 2*p* orbitals of adsorbate oxygen are colored in magenta, which can be distinguishable from the regular oxygen colored in red. The Fermi level (= zero of energy, see text) is indicated by a dashed line. Partial charge densities of the surface states for (a) Fe_{tet1}, (b) ferryl, (c) Fe_{oct1}, and (d) V_{Fe} termination. The states marked with short arrows in PDOS are taken into account for the calculations.

4.2.3.2 Bader charge and net magnetic moment

The ionic and electronic relaxations described above can also be understood through changes in Bader charge and magnetic moment on each of the atoms when going from

bulk to the surface, as presented in Table 4.1. The atomic charges for the bulk cubic system show that all the equivalent octahedral ions with a formal oxidation state of +2.5 have a Bader charge of +1.72 |e| and the tetrahedral ferric sites, a charge of +1.86 |e|. The oxygen ions each have a charge of -1.33 |e|. In general, the charges of both Fe and O tend to decrease in absolute values compared to the bulk due to reduced coordination of surface atoms and electronic redistribution. We present the results of four terminations in Table 4.1. The hydroxyl surface has a similar charge and spin distribution as the ferryl surface. As for the surface relaxations and DOS, there is little difference between the O_1 and V_O terminations.

Table 4.1 Average change in atomic charge and magnetization (per atom) in the top layers for four terminations. All the values listed represent the changes from the values for the equivalent atoms in the bulk system. Net magnetic moment for bulk Fe_{oct}, Fe_{tet}, and O atom are 3.96-3.98, 4.09, and 0.03 μ_B, respectively. The experimental magnetic moment for bulk Fe_{tet} is 3.82 μ_B.46 [a]Values from the PW91+*U* (U_{eff} = 3.61 eV) calculations of ref. 31.

Fe_{tet1}			**ferryl**		
layer	Δq (e)	Δμ (μ_B)	layer	Δq (e)	Δμ (μ_B)
			O	-0.66	-0.12
Fe_{tet1}	+0.41	-0.54(-0.53[a])	**Fe_{tet1}**	-0.04	-0.83
O_1	-0.07	+0.22	**O_1**	-0.10	+0.21
Fe_{oct1}	-0.19	+0.22	**Fe_{oct1}**	-0.20	+0.22
O_2	-0.04	+0.04	**O_2**	-0.04	+0.04
Fe_{oct1}			**V_{Fe}**		
layer	Δq (e)	Δμ (μ_B)	layer	Δq (e)	Δμ (μ_B)
Fe_{oct1}	+0.60	-0.46	**Fe_{oct1}**	+0.35	-0.37
O_2	+0.03	-0.01	**O_2**	-0.03	-0.05
Fe_{tet2}	+0.02	-0.04	**Fe_{tet2}**	+0.05	-0.04
Fe_{oct2}	+0.24	-0.30	**Fe_{oct2}**	+0.25	-0.33

Due to the dangling bonds, the top layer in the Fe_{tet1} termination gains 0.41 electrons, as anticipated from the change in the DOS that the originally unoccupied conduction band of the spin-up channel is slightly shifted below the Fermi level. The oxygen ions in the second layer also help reduce the surface dipole by losing 0.07 electrons and thus being less negative, which contributes to further stabilization. Meanwhile, each of the three iron ions in the third layer becomes more positive by 0.19 |e|, which alleviates the overall negatively charged nature of the surface and subsurface. In the ferryl termination, *i.e.*, when adding an atop oxygen to the exposed Fe_{tet1} atom, the charge on the Fe_{tet1} atoms remain close to the bulk value. Just as in the Fe_{tet1} surface, there is an increase in positive charge character for Fe_{oct1} in the third layer.

In the Fe_{oct1} and V_{Fe} terminations, there are essentially more electrons residing on the topmost layer than in the bulk system. These electrons reduce the positive charge on the iron atoms on the surface, although the O_2 sublayer preserves its bulk charge state. Notably, in the V_{Fe} termination, the cationic vacancy brings about a lesser electron gain to the remaining two surface Fe_{oct1} atoms.

The variations in the magnetic moment of the surface atoms are consistent with the changes in atomic charge, especially for the metal-terminated surfaces. For the ferryl group, there is a decrease in magnetic moment of -0.83 μ_B for the Fe_{tet1} atom despite a negligible variation in atomic charge, 0.04 e; this is the result of combined effects due to depopulation of the originally occupied spin-up Fe_{tet} 3*d* orbitals in the valence band and population of the previously unoccupied spin-down Fe_{tet} 3*d* orbitals, which is related to

bonding with the atop oxygen atom. In the top two iron layers of Fe_{oct2} termination, the Fe_{oct} atoms gain electron density in the bulk unoccupied minority spin (spin-down) bands, which leads to a magnetic moment decrease. This is also the case for the Fe_{tet1}, Fe_{oct1}, and V_{Fe} terminations; this result is reasonable as the Fe 3*d* orbitals in the minority spin states are now more partially occupied while the majority bands stay fully occupied.

4.2.3.3 Work function

The work function is one of the critical surface parameters which could be illustrative of the charge distribution over the surface of a material. The work function, Φ, of a surface in the DFT-slab framework is defined as:

$$\Phi = E_{vac} - E_f \tag{4.1}$$

where E_{vac} is the plane-averaged electrostatic potential energy of an electron in the vacuum region away from the slab surface at the distance where the potential energy has reached its asymptotic value, and E_f denotes the Fermi energy of the total system.

Table 4.2 collects the work functions for each surface. The calculated work function of 5.76 eV for the model Fe_{tet1} termination is 0.24 eV higher than the experimentally measured value, 5.52 eV, for the same surface.[18] The value that we calculate for the Fe_{tet1} surface is 0.28 eV higher than the values from PW91+*U* (U_{eff} = 3.61 eV) calculations in ref. [31] and 0.15 eV and 0.75 eV lower than the O_1 and Fe_{oct2} value, respectively. The other three iron-terminated surfaces have lower work functions by up to 2.61 eV whereas the oxygen-terminated surfaces, ferryl and O_1, show a narrow range (within 0.33 eV) of work functions. Thus, there is a large difference between the calculated work functions of the

iron- and oxygen-terminated surfaces, which can be explained on the basis of simple electrostatics: Magnetite has a dipole moment in the [111] direction generated by alternating cation layers and anion layers; when the termination ends with a negatively charged layer, the corresponding potential increases at the surface, which gives rise to a relatively high vacuum level, while positively top charged layers give rise to the opposite effect.

Table 4.2 Work function calculated for the eight surface terminations. [a]Value from the PW91+*U* (U_{eff} = 3.61 eV) calculations of ref. 31.

Surface	Termination	Work function (eV)
Fe_{oct1}	$^3/_4$ML Fe_{oct}	3.91
V_{Fe}	$^2/_4$ML Fe_{oct}	4.03
Fe_{oct2}	$^2/_4$ML (Fe_{oct}+Fe_{tet})	3.15 (3.90)[a]
Fe_{tet1}	$^1/_4$ML Fe_{tet}	5.76 (5.48)[a]
hydroxyl	$^1/_4$ML Fe_{tet}+OH	5.80
ferryl	$^1/_4$ML Fe_{tet}+O	7.61
V_O	$^3/_4$ML O	7.33
O_1	1ML O	7.94 (8.09)[a]
Exp.[18]	$^1/_4$ML Fe_{tet}	5.52

The work function decreases by 2.6 eV upon an increase in iron density over the oxygen layer from 1/4 ML (Fe_{tet1}) to 2/4 ML (Fe_{oct2}). When introducing a Fe cation vacancy on the Fe_{oct1} termination, the work function increases by +0.11 eV compared to the bulk-terminated Fe_{oct1} surface (3.91 eV). This small change in work function between Fe_{oct1} and V_{Fe} can be attributed to the charge states of the Fe_{oct} atoms becoming more positive,

from +1.12 |e| to +1.37 |e|, in the presence of the defect. The work function for Fe_{oct2} is also smaller than the work function of the V_{Fe} termination with exactly the same iron coverage at the surface. Given that the exposed surface cations of Fe_{oct2} (+1.33 |e|) are as positive as in the V_{Fe} surface, the oxygen atom above the V_{Fe} surface plays a substantial role in determining the work function difference of 0.88 eV between the two surfaces.

In the ferryl termination, the negatively charged oxygen atoms on the top of the Fe atoms bring about a substantial increase of 1.85 eV in work function compared to the bulk-terminated Fe_{tet1} surface. Despite having a significantly less dense oxygen layer, the work function of the ferryl termination then is comparable to that of the oxygen-terminated surfaces, O_1 and V_O. An explanation for this behavior is the bond dipole formed between iron and oxygen, which leads to a large dipole component in the direction perpendicular to the surface. In the bulk oxygen terminations, the Fe-O bonds are aligned at an angle to the surface, reducing the component perpendicular to the surface. Thus, the atop oxygen on Fe_{tet1} plays a significant role in considerably increasing the work function despite having a smaller negative charge than the oxygen atoms on other terminations. This impact is diminished by the additional hydrogen in the hydroxyl group. Finally, we note that while there is some quantitative variation depending on the choice of methodology, *e.g.*, the work function varies up to 1.53 eV for the O_1 surface between PBE and HSE(15%), however, the overall trends upon terminations are similar compared to the results from PBE+*U*.

4.2.3.4 Surface chemistry

As a consequence of atomic displacements and charge redistributions, the surfaces can have quite different chemistries compared to those predicted from the bulk properties; in addition, defect-modified surfaces can be different than bulk-terminated surfaces. An example is depicted in Figure 4.5, which illustrates the electrostatic potential profile measured at 1.3 Å, a typical bonding distance, above the surface atoms for the Fe_{oct1} and V_{Fe} terminations. Here, the octahedral Fe positions are distinguishable because of their lower potential, displayed in blue. Combined with the Bader charge analysis, it is clear that Fe_{oct1} and V_{Fe} are markedly different surfaces given the fact that in the latter the positive charge near the iron atoms is intensified and the oxygen protrusion contains a slight negative charge, in comparison to the bulk-truncated surface. Thus, it is important to emphasize that the mode of chemisorption of an organic layer, for instance, the binding of a phosphonic acid as was done on the (La,Sr)MnO_3 (LSMO) surface,[47] could be significantly different on a vacancy-containing surface compared to a bulk termination. This change in the mode of chemisorption is expected to have a significant influence on the performance of SAM-based magnetic tunnel junctions.

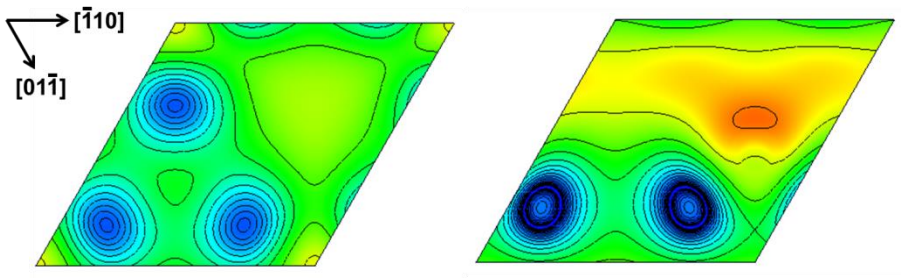

Figure 4.5 Planar electrostatic potential plot evaluated at 1.3 Å above the Fe_{oct1} atoms for the Fe_{oct1} (left) and V_{Fe} (right) terminations. The potential is illustrated in the reverse rainbow spectrum: lower potential in the blue region and higher potential in the red region.

The surface state of Fe_{tet1} and the defect-containing surfaces with adsorbed oxygen or hydroxyl group are investigated using *pseudo*-STM images, as shown in Figure 4.6. The three calculated STM images taken at a positive bias (+2V) are very much alike; they clearly show a hexagonal lattice of protrusions, which is the characteristic morphology of a single-atom terminated Fe_3O_4 (111) film. Therefore, it is rather difficult to distinguish among them with STM images alone. Nonetheless, there is one noticeable feature of the regular termination for which the close-packed oxygen layer underneath (O_1) is apparent in the image together with the top Fe_{tet1} layer. This could be explained by the very small interlayer spacing, 0.41 Å, between surface and subsurface. In addition, weakly hybridized Fe_{tet} 3*d*-O 2*p* states in the spin minority channel seen in Figure 4.4 can also be assigned to O_1 contributions within the given energy range, $[E_f, E_f + 2\ \text{eV}]$. On the other hand, more bright protrusions corresponding to atop-positioned oxygen or hydrogen atoms at the position of Fe_{tet1} can be found in the modified surfaces.

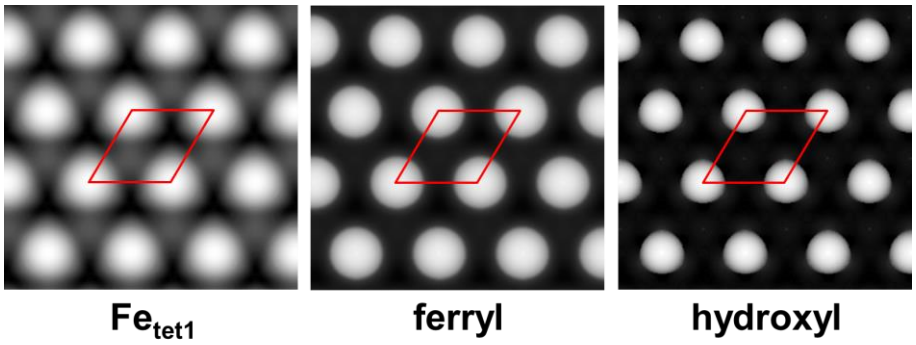

Figure 4.6 Calculated STM images for Fe_{tet1}, ferryl, and hydroxyl terminations with a simulated bias voltage of +2 V in a constant current mode. The hexagonal cell (in red) corresponds to a (1×1) unit cell with a 6 Å periodicity.

4.2.4 Surface spin polarization near the Fermi level

The spin polarization at the surface is a major factor determining the spin-injection and -collection efficiency of an electrode. The spin polarization ratio at the Fermi level can be defined as $P(E_f) = (n_\uparrow - n_\downarrow)/(n_\uparrow + n_\downarrow)$ where $n_\uparrow$ and $n_\downarrow$ are the densities at E_f of the majority and minority spins, respectively. Dedkov *et al.*[48] measured $P(E_f)$ to be -80±5% at room temperature near the surface of epitaxial Fe_3O_4 (111) films on Fe (110) using spin-resolved photoemission spectroscopy. They attributed the high spin polarization to the bulk Fe_3O_4 with a small reduction from the ideal value, -100%, due to the excitation of spin waves at the surface. They suggest a half-metallic state for Fe_3O_4 even after high oxygen exposure by finding a 0.45 eV gap for the spin-up electrons below E_f. The half-metallic state of Fe_3O_4 is retained even after high oxygen exposure as the spin-down electrons retain a high density-of-states near E_f contrary to spin-up electrons. In contrast to those results, Pratt *et al.*[49] reported the opposite spin polarity using the naturally-grown

single crystal annealed under $<10^{-8}$ bar at 550 °C and proposed P(E_f) of >20% measured using a spin-polarized metastable helium beam [He(2^3S)] under magnetic fields up to 4 T at 298K. To reconcile these data, the authors assigned the difference to the penetration depth of their probe beams, which is much lower in the latter study than in UV photoemission where the octahedrally coordinated Fe layers below the surface can contribute to the cumulative spin polarization.

In order to reveal the origin of these seemingly contradictory experimental results for the spin polarization, we have investigated the spin polarization of the Fe_{tet1} termination along the slab thickness. In Figure 4.7, we use the plane-averaged spin density in the energy range from E_f-0.5 eV to E_f to present the spin polarization at each layer (a) and also the cumulative polarization as a function of the probe penetration depth (b).

As predicted from the partial DOS of top layers of Fe_{tet1} in Figure 4.4, the surface spin polarization begins with nearly +100%, shown in Figure 4.7a, which is due to the positively polarized surface Fe_{tet1} cations. The positive polarization decreases until the fifth layer beneath the surface where the spin polarization changes its sign. At ~ 6 Å, the spin polarization reaches the bulk spin polarization of -100%. It is only in the second Fe_{oct1} layer (the fifth overall) where the Fe_3O_4 (111) begins to show the intrinsic magnetic property found in a bulk phase, while the t_{2g} level of near-surface octahedral Fe atoms is far above the Fermi level.

Strong surface states from the Fe_{tet1} surface layer dominate near the Fermi level, and the cumulative polarization remains positive for large penetration depths. It is only at depths around 8 Å where the cumulative value becomes negative; consequently, a negative net

spin polarization can be achieved below this depth. This quantitative evaluation of layer-resolved spin polarity confirms the significance of the penetration depth of probe beams when analyzing a Fe_3O_4 (111) film, as described by Pratt *et al.*[49]

When evaluating the functional dependence of the layer-resolved spin polarization, the hybrid calculation presents a pattern similar to PBE+*U*, while PBE does not reach a -100% spin polarization even in the deeper region. The latter result is expected given the poor description of the bulk electronic structure found in our previous study.[44]

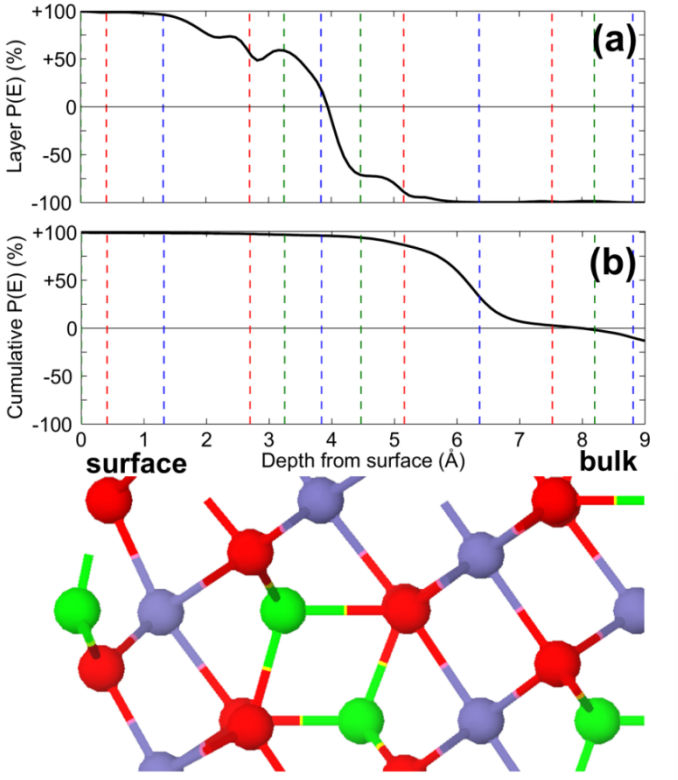

Figure 4.7 (a) Spin polarization over the range from E_f-0.5 eV to E_f for each layer comprising a Fe_{tet1} termination using plane-averaged spin density. The dotted line indicates the position of the first top six layers with different colors for each atom-type: Fe_{tet} (green), O (red), Fe_{oct} (blue). (b) Accumulated spin polarization at a certain depth of the given slab.

Nonetheless, the positive spin polarization reported by Pratt *et al.* is dramatically lower than our calculated value, +100% just below the Fermi level if we consider a shallow penetration depth of the beam. Another possible explanation for such variance in spin polarization can be assigned to the surface defects or coexistence of different terminations with the regular surface since superstructures with several different surface types have been frequently observed in previous STM experiments.[28,29]

In Figure 4.8, the spin polarizations, P(E), calculated for the top six layers, *i.e.*, one repeat unit (corresponding to approximately 4.8 Å from the surface), are plotted for the eight terminations. As seen above, the DOS have distinctive features depending on the surface termination; these features are directly reflected in the surface spin polarization. The Fe_{tet1} termination, panel a, shows a positive spin polarization below and negative above the Fermi level. In contrast, the ferryl termination presents a negative spin polarization on both sides of the Fermi energy; as seen in the DOS, the negative spin polarity at E_f originates from Fe 3*d*-O 2*p* hybridized orbitals of the newly formed Fe=O. The negative spin polarization below the Fermi level is no longer evident in the hydroxyl termination, as the spin-down states associated with the adatom are no longer in the spin-up gap. The defect structure of the Fe_{tet1} termination could significantly decrease the positive value of P(E) near E_f, as expected from the bulk electronic structure. As the magnitude and polarization of the PDOS of the Fe_{oct1} and V_{Fe} terminations are similar, P(E) presents a similar profile in the region of the Fermi level. In the Fe_{oct1} surface, the polarization ratio becomes positive slightly above the Fermi level, which is not seen in the V_{Fe} surface. The

O_1 and V_O terminations have nearly +100% spin polarization from -0.5 eV to +0.5 eV and -0.5 eV to +0.15 eV, respectively.

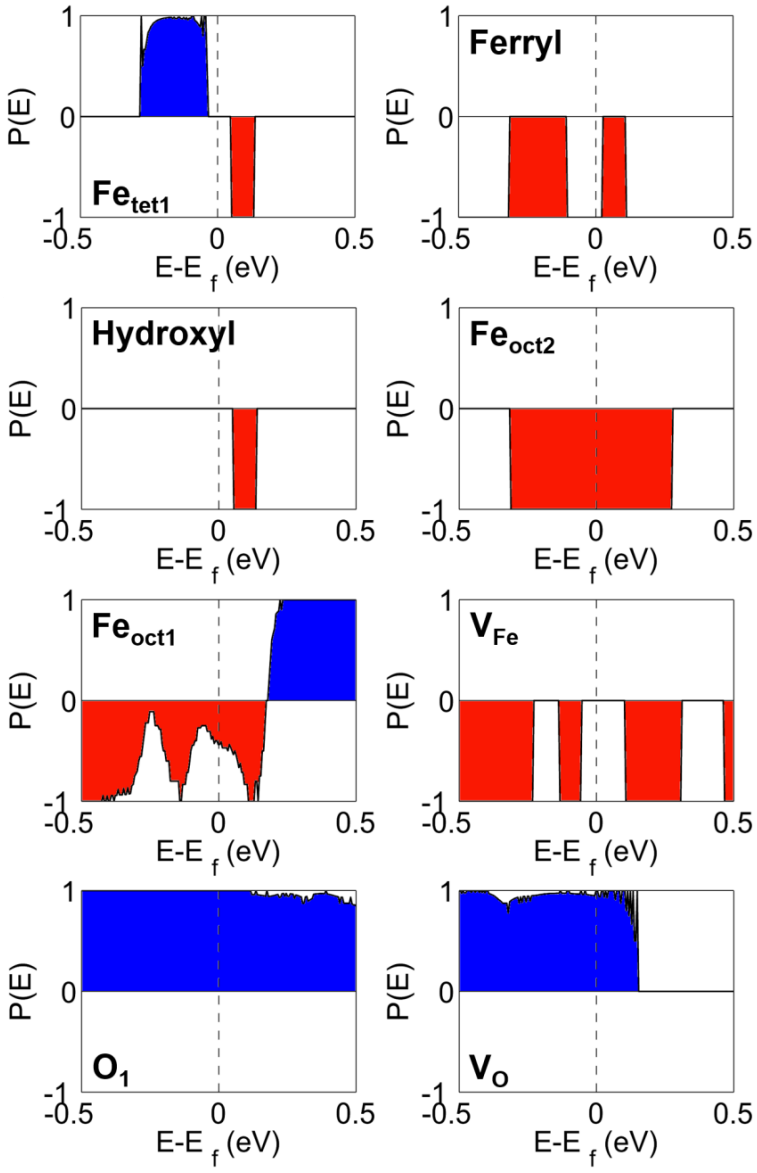

Figure 4.8 Spin polarization as a function of energy, P(E), calculated for eight terminations within [E_f-0.5 eV, E_f+0.5 eV]. The vertical dotted lines indicate the Fermi level. The blue regions correspond to positive spin polarization while the red ones indicate negative spin polarization.

4.3 α-Fe_2O_3 (0001) surfaces in a water environment

4.3.1 Surface models examined

The layer stacking sequence along the c axis, [0001], of hematite is –(Fe-O_3-Fe)–, where the subscript 3 denotes three oxygen atoms per layer in a (1×1) hexagonal unit cell. Therefore, α-Fe_2O_3 (0001) can have three different bulk-truncated surfaces: single Fe (for which the conventional notation is 1Fe), double Fe (2Fe), or oxygen (O_3) termination,[50] see Figure 4.9. Two inherent defects found in synthetic hematite are oxygen and iron vacancies,[51] although V_{Fe} concentrations are predicted to be rather small.[52] Over the past few years, extensive studies on α-Fe_2O_3 (0001) indicate that the most dominant surface configuration of α-Fe_2O_3 (0001) is a single Fe termination,[53-55] while the coexistence of oxygen-terminated and ferryl surface structures have been observed at high oxygen pressure.[50, 56] On the other hand, partial reduction of the surface layer to other iron oxide phases, *e.g.*, Fe_3O_4 (111)[57] or $Fe_{1-x}O$ (111),[58] can appear under highly reducing conditions.

When exposed to water vapor, molecular and dissociative water adsorptions are expected on α-Fe_2O_3 (0001).[59,60] Previous theoretical studies predicted that dissociation of a water molecule is energetically favorable[61] and hydroxylation could be spontaneous even on a defect-free surface.[62-64] In a combined crystal truncation rod diffraction (CTR) and DFT study,[63] Trainor *et al.* investigated the structure of the hydroxylated hematite (0001) surface at room temperature in near water-saturated atmosphere. The authors assigned the dominant surface stoichiometry to two different moieties: a fully hydroxylated 1Fe

termination and a hydroxylated oxygen termination, with a ratio of 4:6, consistent with later CTR results by Tanwar *et al.*[65] Via *in situ* X-ray photoelectron spectroscopy (XPS) investigations at ambient pressure,[66] Yamamoto *et al.* found that, at very lower water vapor pressure, $3x10^{-8}$ Torr at 295 K, hydroxylation first occurs at the top surface of 1Fe-terminated α-Fe_2O_3 (0001), followed by molecular adsorption on the hydroxylated surface at higher relative humidity. With liquid water present at the surface, the *in situ* high-resolution specular X-ray reflectivity (XR) measurement of Catalano showed the presence of a single domain of hydroxylated oxygen termination on the hematite (0001) surface.[67] This result agrees with an earlier proposition from classical atomistic potential simulations[68] where the fully hydrated Fe-terminated surface is prone to lose $Fe(OH)_3$ resulting in the hydroxylated O-terminated surface. However, previous STM studies by Eggleston *et al.*[69] suggested that hematite is more or less inert *vs.* dissolution even in a highly acidic aqueous solution.

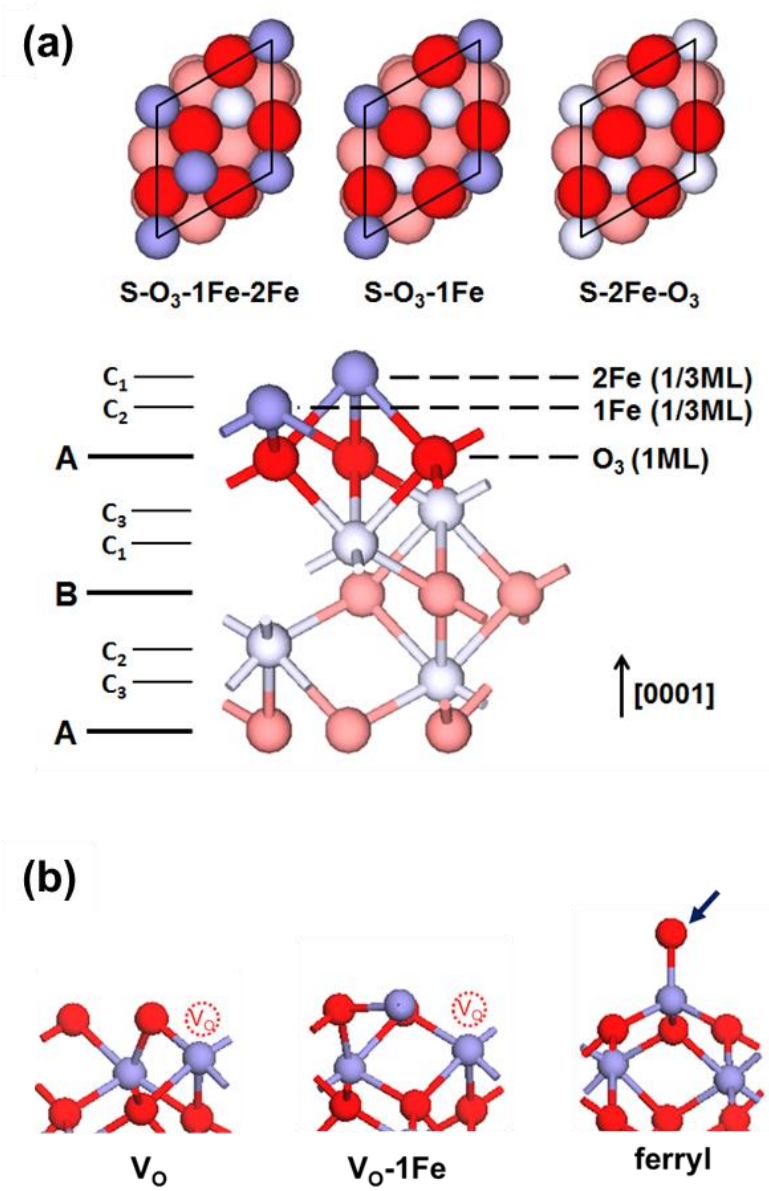

Figure 4.9 (a) Top view of three possible terminations and packing structures of α-Fe_2O_3 (0001) with the (1×1) hexagonal unit cell. Atoms below the top three layers are brightly colored. Anions are arranged in the alternating A, B planar packing structures whereas cations are in C arrangement. The numeral subscript indicates the occupation of iron in the different sites of the C layer. 1ML refers to the complete occupancy of a close-packed layer. (b) Three point defects considered in this work - single oxygen vacancy at the top layer of O_3; a single oxygen vacancy at the subsurface oxygen layer of 1Fe; and (iii) an oxygen atom capping the 1Fe surface.

Here, with regard to hydration/hydroxylation, we have examined the three bulk-truncated surfaces (O_3, 1Fe, and 2Fe) and three defect-containing surfaces corresponding to: (i) a single oxygen vacancy at the top layer of O_3 (V_O); (ii) a single oxygen vacancy at the subsurface oxygen layer of 1Fe (V_O-1Fe); and (iii) an oxygen atom capping the 1Fe surface (ferryl). The hydroxylation includes two different types of OH species that can appear on the iron oxide: (i) a hydroxyl group binding to a surface Fe atom (denoted OH); and (ii) a lattice hydroxyl formed by the attachment of a hydrogen atom to the lattice oxygen (denoted O_3H). We use 'S' to refer to the remaining atomic layers that retain the bulk unit-cell stacking sequence. Several surface configurations with non-dissociative molecular adsorption of H_2O are also considered; they are denoted by '/H_2O'. As an example, the notation S-O_3H-1Fe-(OH)/H_2O refers to the 1Fe termination covered by chemical products resulting from one dissociative H_2O adsorption and one H_2O molecular adsorption. The hydroxyl surfaces studied here are tabulated in Table 4.3.

Table 4.3 Depiction of the models for the hydroxylated surfaces of clean and defect-containing α-Fe_2O_3 (0001) investigated in the current work. (OH) and O_3H indicate a hydroxyl adsorbate on a Fe atom and a hydrogenated surface O atom, respectively. S represents the atomic layers that retain the bulk stacking sequence.

Termination	Hydroxylated surface
O_3	S-2Fe-O_3
	S-2Fe-O_3H_n (n=1,2,3)
V_O	S-2Fe-O_2
	S-2Fe-O_2H_n (n=1,2)
1Fe	S-O_3-1Fe
	S-O_3H_n-1Fe (n=1,2,3)
	S-O_3-1Fe-$(OH)_n$ (n=1,2,3)
	S-O_3H_n -1Fe-$(OH)_n$ (n=1,2,3)
ferryl	S-O_3-1Fe-O
	S-O_3H-1Fe-O(OH)
V_O-1Fe	S-O_2-1Fe
	S-O_2H_n-1Fe-$(OH)_n$ (n=1,2)
2Fe	S-O_3-1Fe-2Fe
	S-O_3H_n-1Fe-2Fe (n=1,2,3)
	S-O_3H_n-1Fe-2Fe-$(OH)_n$ (n=1,2,3)

4.3.2 Water adsorption and dissociation

4.3.2.1 Reaction energetics of H_2O adsorption on an hydroxylated surface at finite temperature

On the 1Fe termination, there is only one cationic site per unit cell, although three oxygen atoms, emulating the crystal close-packed atomic layer, may be accommodated. The hydration energy at 300 K, ΔG_{hyd}, can be calculated from the reaction energy between initial reactants and final product upon water adsorption:

$$S\text{-}O_3\text{-}1Fe\text{-}(H_2O)_{x-1} + H_2O \rightarrow S\text{-}O_3\text{-}1Fe\text{-}(H_2O)_x \quad (4.2)$$

where x varies between 1 and 3. The energy of hydration for the first water molecule is -0.53 eV, with dissociation of the water further stabilizing the surface by -0.25 eV. These reaction energies are comparable to the values predicted from a Buckingham potential model, -0.46 eV and -0.79 eV for molecular and dissociative adsorption of water, respectively.[70] In the optimized S-O_3-1Fe/H_2O structure, the water molecule appears to adsorb on the surface in a tilted fashion where the oxygen forms a chemical bond of 2.16 Å with the undercoordinated ferric ion on the surface, while one of the water H atoms binds to the subsurface oxygens via hydrogen bonds. The Fe-O distance is slightly longer than the value from molecular dynamics simulations, 2.03 Å,[71] but close to the experimentally reported bond length, 2.11 Å.[63,65] The tilted adsorption geometry is consistent with the one obtained from an earlier PBE+*U* calculation,[61] but differs from the on-top configuration of water in the PBE calculation of Yin *et al.*,[64] where there is no hydrogen bonding to the lattice oxygen. Given that the energy barrier for the dissociation of the first water molecule is predicted to be very small, [61] the molecule is more likely to dissociate after its adsorption on S-O_3-1Fe to form surface hydroxyls.

In Table 4.4, the relative energetics of one, two, and three water molecules on the 1Fe termination are compared with respect to the bulk-truncated surface. Here, zero-point vibrational energies (ZPE) and entropic contributions (TS) at T= 300 K are taken into account to estimate the hydration energetics. While ZPE corrections only change the reaction energies by *ca.* 0.10 eV, the entropy difference between isolated and adsorbed H_2O has a major impact on the overall relative energetics upon hydration. We assigned the saturation point of vapor water to the initial condition of water at 300 K, where the chemical potential of a water molecule in a liquid phase is the same as in a gas phase.

The kinetic energy barriers for attachment of additional H_2O to surface 1Fe are calculated to be negligible; however, the magnitude of ΔG_{hyd} becomes smaller with each subsequent addition, -0.33 eV for the second water molecule and -0.08 eV for the third molecule. In contrast to the first molecule, dissociation is not spontaneous for the second and third water as there is only one exposed iron atom of limited valence on the surface. There are a number of different minima with slightly different local geometries of water and hydroxyls in a higher energy range of ~0.10-0.15 eV with the same surface chemical composition. These numerical variances can be attributed to the formation of hydrogen bonds of the surface-molecule and molecule-molecule types, which are estimated to be between 0.15-0.25 eV with the PW91 functional.[72] Since the differences in other observable quantities, *e.g.*, DOS and magnetic moments, do not significantly change despite the variation in energies, here we only present the results for the structures with the lowest energy.

Table 4.4 ZPE corrections and entropic energy contributions at T= 300 K for the hydration energies, ΔG_{hyd} on S-O_3-1Fe. ΔE^a and ΔE^b refer to the obtained energies calculated with the PBE+*U* and PBE+*U*+D3 functionals, respectively. The standard molar entropy of water in the initial state is taken from the NIST-JANAF table in water saturation condition, *i. e.*, p_{H_2O}= 0.035 bar.

	Adsorption type	Reaction energies (eV)			
		ΔE^a	ΔE^b	ΔE^b+ΔZPE	ΔE^b+ΔZPE-TΔS
n=1	O_3-1Fe/H_2O	-0.89	-1.10	-1.00	-0.53
	O_3H-1Fe-OH	-1.07	-1.27	-1.26	-0.77
n=2	O_3H-1Fe-OH/H_2O	-0.72	-0.98	-0.78	-0.33
n=3	O_3H-1Fe-OH/2H_2O	-0.37	-0.77	-0.61	-0.08

4.3.2.2 Equilibrium surface diagram in ambient conditions

Figure 4.10a displays the most stable surfaces of the various hydroxylated/hydrated Fe_2O_3 (0001) configurations as a function of μ_O and μ_{H_2O}. Over a vast swath, the 1Fe surface (dark green) is the most favorable arrangement; however, nine other surfaces can become energetically the most stable within the chemical potential space. Based on the temperature dependence of the chemical potentials of water and oxygen in the gas phase given in the JANAF-NIST table,[73] we can convert the chemical potentials to experimentally measurable thermodynamic variables, *i.e.*, temperature and pressure. To provide a more intuitive understanding, the derived (T,*p*) phase diagrams are illustrated in Figure 4.10b.

Within the physically accessible regime, the transition from the 1Fe surface to the dissociated water surface, S-O_3H-1Fe-(OH), occurs at μ_{H_2O} = -1.26 eV (this corresponds to the boundary between the green and magenta areas in Figure 4.10a). This transition point is slightly lower than the threshold p_{H_2O} derived from earlier PES experiments where the hydroxylation of hematite occurs between ~10^{-8}-10^{-4} Torr at room temperature, *i.e.*, $\mu_{H_2O} \approx$ -1.13-0.90 eV.[59,66] Conventionally, the vapor pressure dependence of hydroxylation on oxide surfaces is estimated based on the relative stability between the oxides and corresponding (oxy)hydroxides in bulk phases. However, this approach gives too high a threshold pressure for hematite hydroxylation: five orders of magnitude higher than the experimentally reported value, *i.e.*, μ_{H_2O} ~ -0.60 eV.[74] This underlines that the DFT-derived surface phase diagram can more accurately predict the onset partial pressure

for hydroxylation on the hematite surface since it considers the construction of intermediate phases on the surface, which occurs during the transformation into (oxy)hydroxide.

When the partial pressure of water increases, there occurs a second transition at μ_{H_2O} = -0.78 eV where a second water molecule attaches to the surface to form the water-hydroxyl mixed phase (S-O_3H-1Fe-(OH)/H_2O). Just below the saturation limit of water vapor, a transition from S-O_3H-1Fe-(OH)/H_2O to S-O_3H-1Fe-(OH)/2H_2O occurs at μ_{H_2O} = -0.61 eV. In contrast to the first molecule, molecular dissociation is not spontaneous for the second and third water uptakes, as there is only one exposed iron atom of low coordination on the surface (per surface unit cell).

In the case of the double iron termination (2Fe), hydroxylation can stabilize the surface upon H_2O exposure. A single hydroxyl group adsorbed on the surface in a bidentate mode, S-O_3-1Fe-2Fe-(OH) (cyan in Figure 4.10a), is more favorable than the clean surface in the low μ_{H_2O} region, while S-O_3H_2-1Fe-2Fe-$(OH)_2$ becomes stabilized near the water saturation point. The optimized S-O_3H_2-1Fe-2Fe-$(OH)_2$ configuration shows surface geometries similar to those observed in another corundum structure, Cr_2O_3 (0001), where two surface Cr ions are bound to OH/H_2O species at atop sites.[75] However, it should be noted that hydroxylated 2Fe surfaces become as stable as the hydroxylated 1Fe or O_3 termination below μ_O ~ -2.6 eV, which is attainable only in extreme conditions, *e.g.*, p_{O_2} = 10^{-15} mbar at 900 K. On the other hand, the difference between the calculated surface energies of the S-2Fe-O_3H_3 and S-O_3H-1Fe-(OH)/2H_2O is relatively small (~ 20 meV/Å^2) in ambient conditions, as presented in Figure 4.10c. Thus, the hydroxylated S-

2Fe-O_3 configuration could be competitive with hydroxylated S-O_3-1Fe and become present on the surface. Indeed, S-2Fe-O_3H_3 is one of two hypothesized configurations from an STM experiment in aqueous media[69] and CTR studies at 298 K in near water-saturated atmosphere.[63,65]

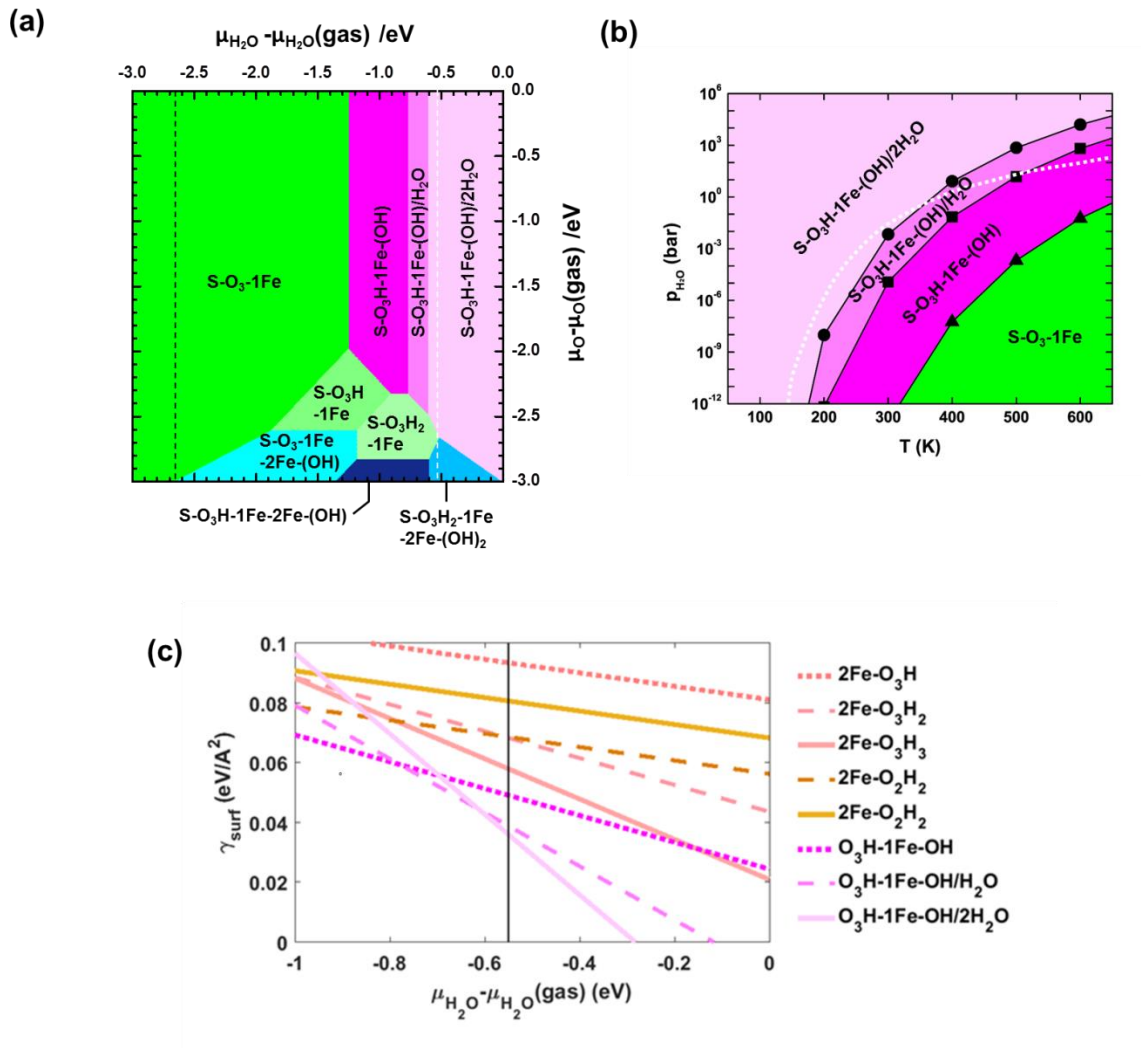

Figure 4.10 (a) Equilibrium phase diagram of hydroxylated terminations as a function of μ(O_2) and μ(H_2O). Two black vertical lines indicate the physically possible range of water molecules. The lower limit is set to -2.65 eV at the experimental critical temperature, T_c= 647 K in the UHV condition. (10^{-9} mbar) The upper limit corresponds to -0.51 eV, the highest chemical potential of water in a vapor phase based on the saturation point, *i.e.*, μ_{H_2O} (*g*) = μ_{H_2O} (*l*) at 200 K, 3.32×10^{-3} mbar. (b) Calculated (*T*,*p*) phase diagram of different surface terminations. The saturation point of water vapor is denoted as a white dotted line. (c) Calculated surface energies of key 1Fe- and O_3 terminations as a function of water chemical potential in the oxygen-rich condition. The black vertical line corresponds to the water saturation limit at 300 K.

Since the defect-containing surface domains are energetically less favorable than the 1Fe termination, they are predicted to appear on the α-Fe_2O_3 (0001) surface only in an irregular manner. However, surface defects are often regarded as the most active sites for water hydroxylation on oxides;[74] therefore, they still can play a significant role in the hydroxylation at the initial stage of water exposure despite their limited presence on the surface. From a thermodynamic standpoint, the instance where the clean and hydroxylated surfaces have the same surface energy can be related to the threshold μ_{H_2O} value for the 1st water dissociation. In Table 4.5, the calculated transition points for S-O_3-1Fe and three defect-containing surfaces (V_O, V_O-1Fe, and ferryl) are presented with respect to the water chemical potential. (We recall that since the chemical potential is a function of partial pressure and temperature, the larger negative chemical potential indicates the condition of lower water partial pressure at a given temperature). Interestingly, low thresholds are predicted when oxygen vacancies occur in the first oxygen layer of the 1Fe- and O_3-terminations compared to the perfect 1Fe surface, whereas the ferryl group does not exhibit any significant chemical reactivity for hydroxylation. In particular, V_O at the subsurface of the 1Fe termination significantly favors hydroxylation, either with the water oxygen occupying the vacant lattice oxygen site (S-O_3H_2-1Fe) or attaching on 1Fe to form a surface hydroxyl group (S-O_2H-1Fe-(OH)). Therefore, the water dissociation at very low H_2O pressure is more likely to take place near oxygen vacancies than on defect-free hematite. This is consistent with earlier UPS measurements where an α-Fe_2O_3 (0001) surface that contains a high density of oxygen vacancies produced by ion bombardment, shows higher H_2O chemisorption

reactivity at much lower water pressure than a corresponding annealed sample that has fewer defects.[60]

Table 4.5 Calculated transition μ_{H_2O} for the first hydroxylation on defect-free and defect-containing 1Fe-terminated surfaces. The values correspond to the conditions where clean and hydroxylated surfaces have the same surface energy.

clean surface	hydroxylated surface	1st transition μ_{H_2O} (eV)
S-O_3-1Fe (1Fe)	S-O_3H-Fe-OH	-1.26
S-2Fe-O_2 (V_O)	S-2Fe-O_3H_2	-1.47
S-O_2-1Fe (V_O-1Fe)	S-O_3H_2-1Fe	-2.17
	S-O_2H-1Fe-(OH)	-2.03
S-O_3-1Fe-O (ferryl)	S-O_3-1Fe-$(OH)_2$	-0.95
	S-O_3H-1Fe-O(OH)	-0.66

4.3.3 O1s surface core level shift

An experimental measurement sensitive to surface hydroxylation is the O1s core level shift (CLS). Each of the various types of oxygen species near the surface region has different chemical environments, thus shows distinctive CLS trends relative to the lattice oxygen. When hematite crystals are exposed to water vapor, a new feature appears at ~1.5-2.2 eV from the oxygen lattice peak, which is attributed to surface hydroxyl groups.[59] Yamamoto and co-workers[66] reported in their *in situ* XPS measurements that the peak shift for OH appears at +1.58 eV (higher binding energy) in the early stage of water vapor exposure, and then gradually decreases to +0.97 eV as the water partial

pressure increases. At the same time, an additional peak begins to grow at +3.25 eV, which can be assigned to adsorbed water molecules on the surface.

Figure 4.11 displays the calculated O1s CLS for the hydrated 1Fe-terminated surfaces. The oxygen species can be classified into four types: (i) subsurface lattice oxygen (O_{S-1}); (ii) subsurface hydroxylated oxygen ($O_{S-1}H$); (iii) surface hydroxyl $(OH)_{ad}$; and (iv) adsorbed water $(H_2O)_{ad}$ on the surface Fe site. On the clean 1Fe-terminated surface, the O_{S-1} atoms show a peak shift at -0.87 eV compared to the bulk reference, which becomes less negative upon water adsorption. When the subsurface lattice oxygen takes a hydrogen fragment after water dissociation, $O_{S-1}H$ shows a positive shift, the magnitude of which is sensitive to the local geometric configuration. For the hydroxylated S-O_3H-1Fe-(OH) structure, protonation of the lattice oxygen leads to a CLS of +1.94 eV. Increasing the number of water molecules on the surface leads to a smaller CLS for the $O_{S-1}H$ atoms, ~1 eV, as there are significant hydrogen bonding interactions among adsorbates on the surface. When a partially negatively charged oxygen in $(OH)_{ad}$ or water approaches an H atom of $O_{S-1}H$, a hydrogen bond forms, leading to a slight elongation of the lattice hydroxyl bond, which serves as an H-bond donor. The lower binding energies predicted for the subsurface lattice oxygen in more saturated conditions can be therefore attributed to the weaker covalent bonding character within O_{S-1}-H. Such a dependence of the core-level binding energies on the H-bond network has also been proposed for Pt (111),[76,77] hydrogen-passivated RuO_2 (110),[78] hydroxylated MgO (100),[79] and liquid water.[80] The same trend is predicted for the adsorbed hydroxyl groups and water molecules. At low coverage, $(OH)_{ad}$ is predicted to have a higher binding energy (CLS = +1.21 eV) while additional water molecules or surface hydroxyls have a CLS in the range

of ~0.33-0.97 eV. The largest CLS is calculated for a molecularly adsorbed H_2O on S-O_3H-1Fe and S-O_3H-1Fe-(OH), +3.72 and +3.96 eV, respectively; the overall CLS becomes somewhat smaller, ca. +3 eV in fully saturated conditions. Thus, overall, our calculations confirm that the decrease in the O1s CLS observed via XPS near the saturation limit can be ascribed to a more hydroxyl-rich surface at high water partial pressure.

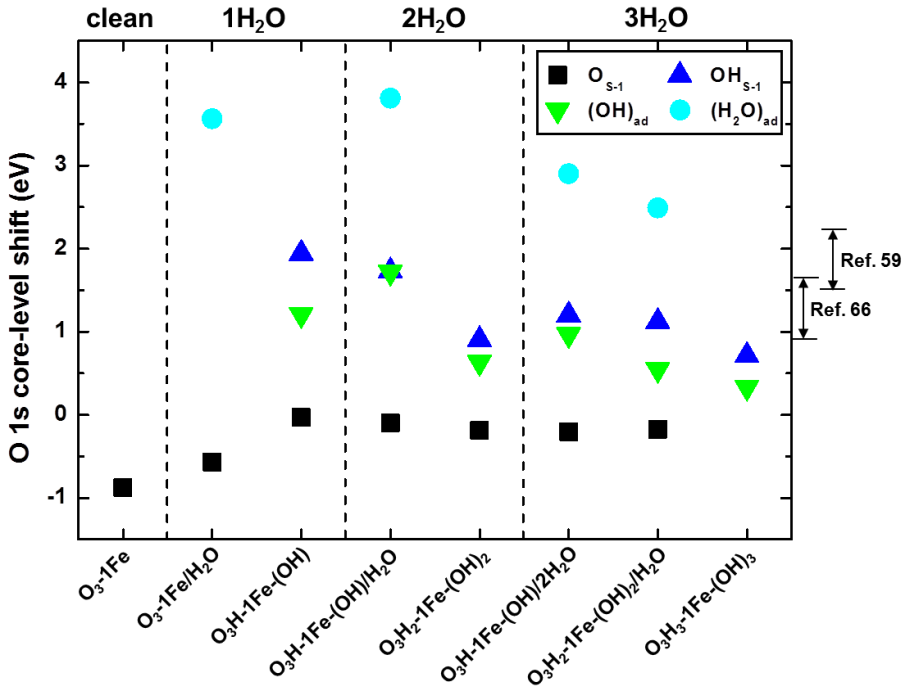

Figure 4.11 Calculated O1s core-level shifts for different surfaces of hydrated/hydroxylated hematite. The reference binding energy is taken from an oxygen atom in the center of the slab. O_{S-1}, $O_{S-1}H$, $(OH)_{ad}$ and $(H_2O)_{ad}$ are defined in the text. When the system contains multiple numbers of oxygen atoms of the same type on the surface, their average CLS values are presented. For the sake of comparison, the O1s core-level shifts obtained from the application of the Slater-Janak transition-state theorem are also calculated; the results are nearly identical.

4.3.4 Near-surface local geometries and interlayer relaxation

Table 4.6 presents the bond distances between Fe and O near the surface upon hydroxylation. When going to more water-saturated surfaces where the 1Fe atoms recover their six-fold coordination, the Fe-O bond lengths regain their bulk values: three short bonds (1.97 Å) and three long bonds (2.12 Å); the same occurs for the magnetic moment and oxidation state of the surface ferric ion. The variations in Fe-O bond lengths near the surface as a function of surface stoichiometry occur in the range of 1.8 Å ± 0.1 Å and 2.18 ± 0.1 Å; these values agree with the iron–water oxygen radial distribution functions from two CTR studies. [63, 65] Compared to the clean surface, the bond distances between the sub-surface lattice oxygens and surface irons increase by ~0.13-0.35 Å for the fully hydroxylated/hydrated structures. In particular, S-O_3H_3-1Fe-$(OH)_3$ has only long bonds of 2.14 Å between the surface 1Fe and three O_{S-1}(H) atoms; the hydroxylation of the lattice oxygen thus considerably weakens the surface-subsurface interactions. The implication is that fully hydroxylated 1Fe atoms are prone to dissociation from the surface via dynamical perturbations; on the other hand, on partially hydroxylated surfaces, the O_{S-1}-1Fe short bond(s) can still prevent 1Fe complete dissociation. These results underline that reaching a significant degree of hydroxylation of the subsurface lattice oxygens of the 1Fe termination can be a major factor in determining whether iron dissolution occurs at the surface and consequently leads to the appearance of the O_3 termination over the hematite surface.

Table 4.6 Calculated geometric parameters of the surface Fe atoms including their coordination number (CN) and bond lengths to adjacent oxygen atoms corresponding to different species. Averaged bond lengths are taken for multiple bonds of the same type (the number of each bond type is given in parentheses).

surface		CN	bond length (Å)			
			$O_{S\text{-}1}$-1Fe	$O_{S\text{-}1}$H-1Fe	1Fe-(OH)	1Fe-(H_2O)
clean	S-O_3-1Fe	3	1.81(3)			
1H_2O	S-O_3-1Fe/H_2O	4	1.84(3)			2.16
	S-O_3H-1Fe-(OH)	4	1.86(2)	1.99	1.85	
2H_2O	S-O_3H-1Fe-(OH)/H_2O	5	1.86(2)	2.03	2.00	2.31
	S-O_3H_2-1Fe-$(OH)_2$	5	1.85	2.13(2)	1.93(2)	
3H_2O	S-O_3H-1Fe-(OH)/2H_2O	6	1.92(2)	2.15	1.99	2.19(2)
	S-O_3H_2-1Fe-$(OH)_2$/H_2O	6	1.94	2.16(2)	1.95(2)	2.16
	S-O_3H_3-1Fe-$(OH)_3$	6		2.14(3)	1.94(3)	
bulk		6	1.97(3), 2.12(3)			

In Figure 4.12, the changes in interlayer distances for fully hydroxylated surfaces of 1Fe-terminated hematite (0001) are presented together with those derived from surface-sensitive X-ray diffraction methods.[63,65] In our calculations, the structural domain proposed in previous CTR analyses, S-O_3H_3-1Fe-$(OH)_3$, is in fact found to be less stable than two models of the same stoichiometry: S-O_3H-1Fe-(OH)/2H_2O and S-O_3H_2-1Fe-$(OH)_2$/H_2O. These surfaces differ in the positions of the hydrogen atoms, which cannot be accurately assessed at the X-ray diffraction level.[65,71] For the 1Fe-terminated configurations with three adsorbed water molecules, S-O_3H-1Fe-(OH)/2H_2O has the lowest surface energy at the water-rich limit; it also shows the best quantitative fit to the estimated interlayer relaxations from the CTR analysis by Trainor *et al.*[63] In the case of

the hydroxylated 1Fe termination, the distance between the surface oxygen and 1Fe layer experiences a contraction of -26% compared to the bulk O_3-1Fe distance, which is fully consistent with the CTR data, -24%. This decrease can be attributed to the stronger attraction of the under-coordinated surface oxygen toward 1Fe in the subsurface compared to the crystal. Upon molecular adsorption, the strong compression of the topmost interlayer (1Fe-O_3, -68%) of the clean surface reverses and shows an expansion of 30% with respect to the bulk layer spacing.

Another surface moiety suggested from CTR[63,65] and X-ray reflectivity[67] (aqueous) analyses is the hydroxylated oxygen termination (S-2Fe-O_3H_3). Both qualitatively and quantitatively, the calculated values for interlayer relaxations are in good agreement with experiments, as depicted in Figure 4.12b. The fully hydroxylated oxygen termination shows an outward expansion of +25% in the O_3-2Fe interlayer spacing, consistent with the experimentally measured values, +23% and +33%, from CTR and X-ray reflectivity measurements, respectively.

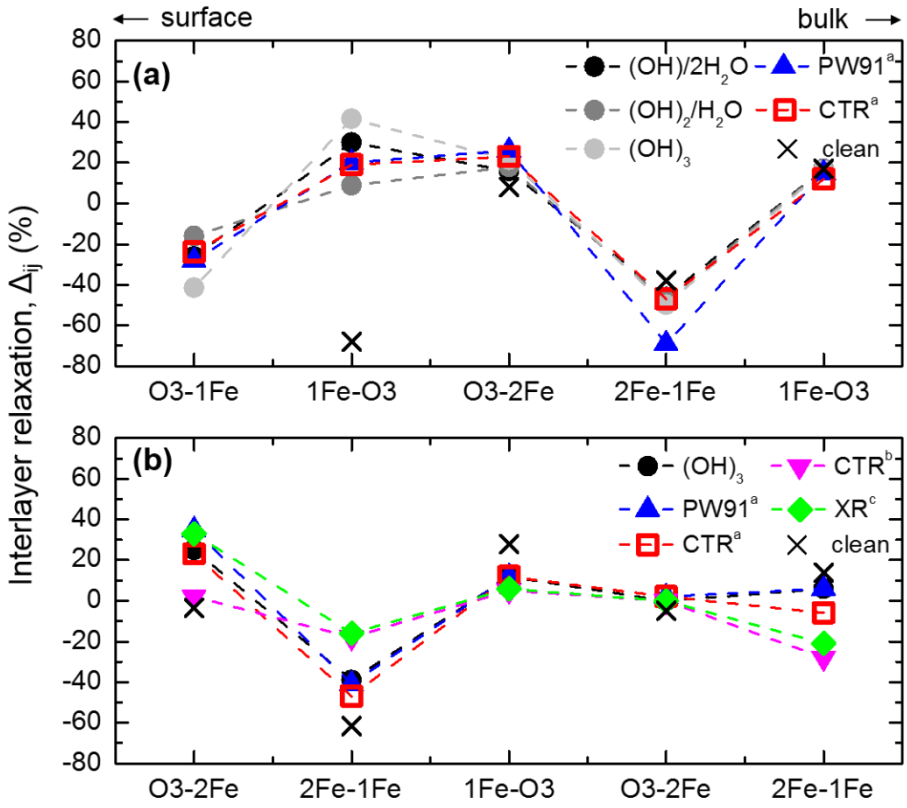

Figure 4.12 Variations in near-surface interlayer distances for: (a) the fully hydroxylated 1Fe termination (S-O_3H_x-1Fe-O_3H_y); and (b) the hydroxylated O_3 termination (S-2Fe-O_3H_3) of Fe_2O_3 (0001). The relaxations of the layer spacing are given as a percentage of the bulk interlayer Fe-O (0.87 Å) and Fe-Fe distances (0.58 Å) projected onto the c axis. The PBE+*U* data (black squares) are compared to data taken from CTR/DFT[a] (Ref. 63), CTR[b] (Ref. 65), and X-ray reflectivity[c] (Ref. 67) measurements.

4.3.5 Surface electronic structures

The impact of adsorbates on the hematite electronic structure is examined through analysis of the partial density of states (PDOS) as presented in Figure 4.13. For S-O_3-1Fe/H_2O, the $1b_1$ orbital of water, mainly consisting of oxygen lone-pair character,

broadens from -1 eV to -5 eV upon chemisorption due to the interaction with surface 1Fe 3*d* states at the upper valence band. A more discrete peak derived from $3a_1$ states of mixed bonding and nonbonding character appears at higher binding energy near -5.5 eV. In a similar manner, the first hydroxylation also leads to more dispersive (OH) 1π states (in the range from the Fermi level to -2 eV) while the 2σ orbital appears as a discrete level at ca. -5 eV. It should be noted that the 1Fe surface states introduced at the bottom of the conduction band upon surface cleavage disappear after the first hydroxylation whereas they are still preserved for the molecular adsorption in S-O_3-1Fe/H_2O. This implies that hydroxylation leads to a more effective oxidation of the surface 1Fe ion A than molecular adsorption. Bader charge analysis predicts a stronger positive character on the surface iron in S-O_3H-1Fe-OH than S-O_3-1Fe/H_2O by +0.04 |e|, which is consistent with the 0.3 Å shorter chemical bond between surface 1Fe and adsorbate oxygen in 1Fe-(OH) than 1Fe-(H_2O).

As the coverage of water/hydroxyl over the surface increases to S-O_3H-1Fe-(OH)/H_2O and S-O_3H_2-1Fe-$(OH)_2$, the O2*p* orbitals from the adsorbates show the largest admixture over a wide energy range with the valence bands consisting of oxide O2*p*-Fe3*d* hybridized states, leading to similar DOS to those of bulk hematite. In S-O_3H-1Fe-(OH)/2H_2O and S-O_3H_2-1Fe-$(OH)_3$, the $3a_1$ state of H_2O and 2σ states of OH become even more hybridized upon further hydration and hydroxylation, respectively. Here, the magnetic moment and oxidation state for the surface iron atom approach the bulk values as 1Fe atom recovers the six-fold coordination: 1.93 |e| and 4.15 μ_B.

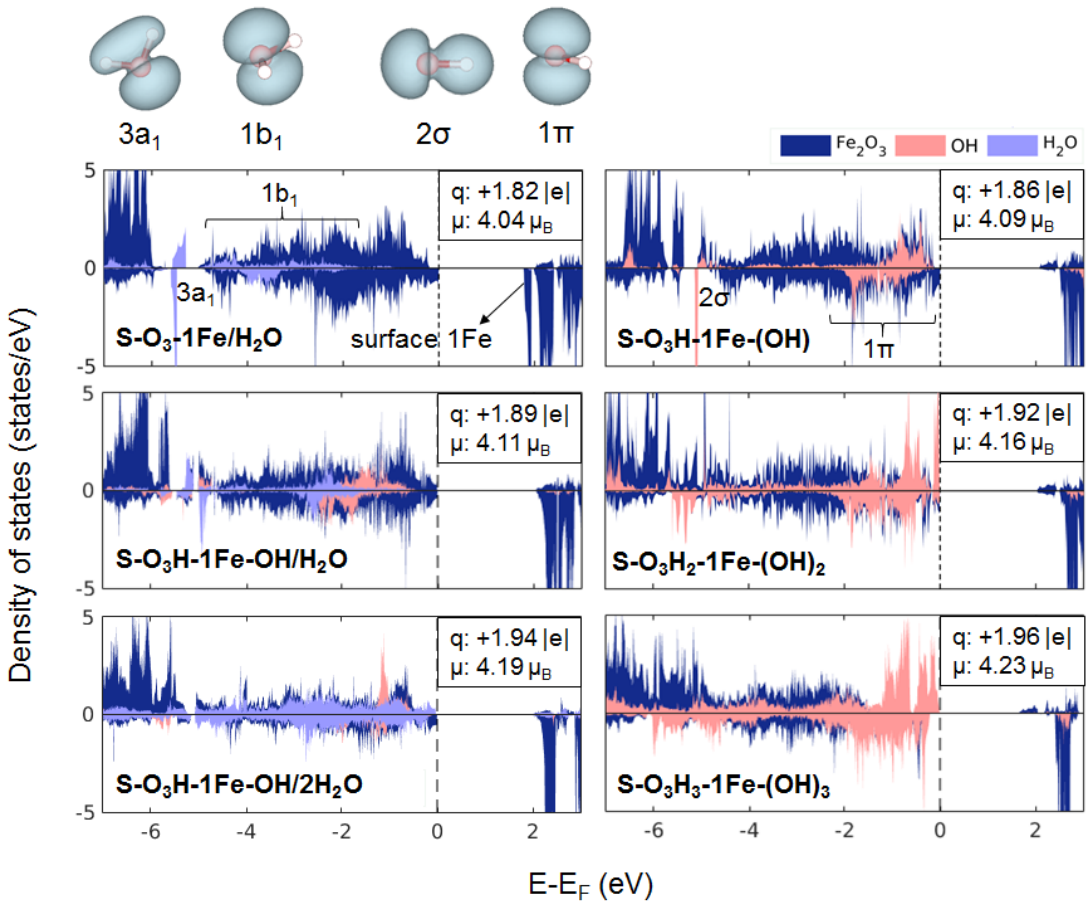

Figure 4.13 Partial density of states (DOS) derived for Fe 3d and O 2p orbitals of near-surface atoms for different hydroxyl-water configurations on the 1Fe termination. The PDOS of Fe_2O_3 colored in navy refer to the states of the surface 1Fe atom and subsurface O_3 layer while the PDOS pink and blue areas refer to adsorbed OH and H_2O, respectively. Fermi energy, defined here as the top of the valence band, is set to zero and illustrated with a dashed line. The atomic charge (q) and magnetic moment (μ) of the surface Fe ion are given in each panel. The 1Fe on the clean surface has a charge of 1.78 |e| and a μ_B value of 4.00.

4.4 Conclusions

Using Density Functional Theory PBE+*U* calculations, we investigated the Fe_3O_4 (111) surfaces and α-Fe_2O_3 (0001) surfaces to determine the thermodynamically most stable surface domains in given environmental conditions.

We have discussed the results of the DFT calculations on bulk-terminated and modified surfaces of magnetite (111) in terms of their structural, electronic and magnetic properties. The major findings are as follows:

- For the relevant limiting regimes in oxygen chemical potential, the Fe_{tet1}-terminated surface has the lowest surface energy over a wide range of oxygen chemical potentials amongst the surfaces comprised of bulk-like terminations, while Fe_{oct2} becomes more stabilized in the oxygen poor limit, which is in good agreement with experiment.

- Importantly, surfaces that contain either oxygen adatoms or cationic vacancies are calculated to be close in stability to the Fe_{tet1} surface at oxygen-rich and oxygen-poor conditions, respectively.

- These modified surfaces with adsorbates or cationic vacancies have significantly different surface geometries and electronic/magnetic structures with respect to the previously considered structures without defects. In particular, these defects have a major impact on the electron redistributions over surface layers, which lead to different spin polarization near the Fermi level and distinctive surface chemistries.

Thus, the presence of point defects at modified surfaces is expected to alter the nature of interfaces between oxide surfaces and organic layers.

For hematite in atmospheric condition with oxygen gas and water vapor present, we find that:

- The 1Fe termination, which represents the most stable clean surface, is dominantly covered by hydroxyls or/and water molecules, with the degree of hydroxylation and hydration varying with the water chemical potential. The surface structures optimized in our work provide evolutions of the O1s core level shifts and variations of the near-surface local geometries upon hydroxylation, which are fully consistent with the results from experimental measurements in humid conditions.
- Defect-containing surfaces remain higher in energy and do not appear in the equilibrium surface phase diagram; however, the transition from clean to hydroxylated surface is estimated to occur at a lower water chemical potential for surfaces with oxygen vacancies. This implies that the oxygen vacancy sites play a significant role in the water dissociation process at the early stages of water exposure.

4.5 References

[1] Sivula, K.; Le Formal, F.; Gratzel, M. *Chemsuschem* **2011**, *4*, 432.
[2] Walter, M. G.; Warren, E. L.; McKone, J. R.; Boettcher, S. W.; Mi, Q. X.; Santori, E. A.; Lewis, N. S. *Chem. Rev.* **2010**, *110*, 6446.
[3] Lad, R. J.; Henrich, V. E. *Surf. Sci.* **1988**, *193*, 81.
[4] Kresse, G.; Furthmuller, J. *Comp. Mater. Sci.* **1996**, *6*, 15.
[5] Kresse, G.; Furthmuller, J. *Phys. Rev. B* **1996**, *54*, 11169.
[6] Blochl, P. E. *Phys. Rev. B* **1994**, *50*, 17953.
[7] Anisimov, V. I.; Zaanen, J.; Andersen, O. K. *Phys. Rev. B* **1991**, *44*, 943.
[8] Perdew, J. P.; Burke, K.; Ernzerhof, M. *Phys. Rev. Lett.* **1997**, *78*, 1396.
[9] Dudarev, S. L.; Botton, G. A.; Savrasov, S. Y.; Humphreys, C. J.; Sutton, A. P. *Phys. Rev. B* **1998**, *57*, 1505.
[10] Grimme, S.; Antony, J.; Ehrlich, S.; Krieg, H. *J. Chem. Phys.* **2010**, *132*, 154104.
[11] Blochl, P. E.; Jepsen, O.; Andersen, O. K. *Phys. Rev. B* **1994**, *49*, 16223.
[12] Tang, W.; Sanville, E.; Henkelman, G. *J. Phys-Condens Mat.* **2009**, *21*, 084204.
[13] Tersoff, J.; Hamann, D. R. *Phys. Rev. B* **1985**, *31*, 805.
[14] Vanpoucke, D. E. P.; Brocks, G. *Phys. Rev. B* **2008**, *77*, 241308.
[15] Kohler, L.; Kresse, G. *Phys. Rev. B* **2004**, *70*, 165405.
[16] Janak, J. F. *Phys. Rev. B* **1978**, *18*, 7165.
[17] Slater, J. C. *Quantum theory of molecules and solids*; McGraw-Hill: New York,, 1963.
[18] Weiss, W.; Ranke, W. *Prog. Surf. Sci.* **2002**, *70*, 1.
[19] Tasker, P. W. *J. Phys. C Solid State* **1979**, *12*, 4977.
[20] Noguera, C. *J. Phys-Condens. Mat.* **2000**, *12*, R367.
[21] Lennie, A. R.; Condon, N. G.; Leibsle, F. M.; Murray, P. W.; Thornton, G.; Vaughan, D. J. *Phys. Rev. B* **1996**, *53*, 10244.
[22] Cutting, R. S.; Muryn, C. A.; Thornton, G.; Vaughan, D. J. *Geochim Cosmochim Ac.* **2006**, *70*, 3593.
[23] Zhu, L.; Yao, K. L.; Liu, Z. L. *Phys. Rev. B* **2006**, *74*, 035409.
[24] Ahdjoudj, J.; Martinsky, C.; Minot, C.; Van Hove, M. A.; Somorjai, G. A. *Surf. Sci.* **1999**, *443*, 133.
[25] Tsuda, N.; Nasu, K.; Fujimori, A.; Siratori, K. *Electronic conduction in oxides*; Springer-Verlag: Berlin ; New York, 2000.
[26] Ritter, M.; Weiss, W. *Surf. Sci.* **1999**, *432*, 81.
[27] Shaikhutdinov, S. K.; Ritter, M.; Wang, X. G.; Over, H.; Weiss, W. *Phys. Rev. B* **1999**, *60*, 11062.
[28] Paul, M.; Sing, M.; Claessen, R.; Schrupp, D.; Brabers, V. A. M. *Phys. Rev. B* **2007**, *76*, 075412.
[29] Shimizu, T. K.; Jung, J.; Kato, H. S.; Kim, Y.; Kawai, M. *Phys. Rev. B* **2010**, *81*, 235429.
[30] Grillo, M. E.; Finnis, M. W.; Ranke, W. *Phys. Rev. B* **2008**, *77*, 075407.
[31] Kiejna, A.; Ossowski, T.; Pabisiak, T. *Phys. Rev. B* **2012**, *85*, 125414.
[32] Berdunov, N.; Murphy, S.; Mariotto, G.; Shvets, I. V. *Phys. Rev. Lett.* **2004**, *93*, 057201.

[33] Sala, A.; Marchetto, H.; Qin, Z. H.; Shaikhutdinov, S.; Schmidt, T.; Freund, H. J. *Phys. Rev. B* **2012**, *86*, 155430.
[34] Nie, S.; Starodub, E.; Monti, M.; Siegel, D. A.; Vergara, L.; El Gabaly, F.; Bartelt, N. C.; de la Figuera, J.; McCarty, K. F. *J. Am. Chem. Soc.* **2013**, *135*, 10091.
[35] Campbell, C. T.; Peden, C. H. F. *Science* **2005**, *309*, 713.
[36] Rim, K. T.; Eom, D.; Chan, S. W.; Flytzani-Stephanopoulos, M.; Flynn, G. W.; Wen, X. D.; Batista, E. R. *J. Am. Chem. Soc.* **2012**, *134*, 18979.
[37] Cutting, R. S.; Muryn, C. A.; Vaughan, D. J.; Thornton, G. *Surf. Sci.* **2008**, *602*, 1155.
[38] Yu, X. H.; Huo, C. F.; Li, Y. W.; Wang, J. G.; Jiao, H. J. *Surf. Sci.* **2012**, *606*, 872.
[39] Santos-Carballal, D.; Roldan, A.; Grau-Crespo, R.; de Leeuw, N. H. *Phys. Chem. Chem. Phys.* **2014**, *16*, 21082.
[40] Govind, N.; Wang, Y. A.; da Silva, A. J. R.; Carter, E. A. *Chem. Phys. Lett.* **1998**, *295*, 129.
[41] Pople, J. A.; Headgordon, M.; Fox, D. J.; Raghavachari, K.; Curtiss, L. A. *J. Chem. Phys.* **1989**, *90*, 5622.
[42] Wang, L.; Maxisch, T.; Ceder, G. *Phys. Rev. B* **2006**, *73*, 195107.
[43] Kiejna, A.; Pabisiak, T. *J. Phys. Chem. C* **2013**, *117*, 24339.
[44] Noh, J.; Osman, O. I.; Aziz, S.; Winget, P.; Brédas, J. L. *Sci. Technol. Adv. Mat.* **2014**, *15*, 044202.
[45] Shvets, I. V.; Mariotto, G.; Jordan, K.; Berdunov, N.; Kantor, R.; Murphy, S. *Phys. Rev. B* **2004**, *70*, 155406.
[46] Rakhecha, V. C.; Murthy, N. S. S. *J. Phys. C* **1978**, *11*, 4389.
[47] Tatay, S.; Barraud, C.; Galbiati, M.; Seneor, P.; Mattana, R.; Bouzehouane, K.; Deranlot, C.; Jacquet, E.; Forment-Aliaga, A.; Jegou, P.; Fert, A.; Petroff, F. *Acs Nano* **2012**, *6*, 8753.
[48] Dedkov, Y. S.; Rudiger, U.; Guntherodt, G. *Phys Rev B* **2002**, *65*, 064417.
[49] Pratt, A.; Kurahashi, M.; Sun, X.; Gilks, D.; Yamauchi, Y. *Phys. Rev. B* **2012**, *85*, 180409(R).
[50] Shaikhutdinov, S. K.; Weiss, W. *Surf. Sci.* **1999**, *432*, L627.
[51] Dieckmann, R. *Philos. Mag. A* **1993**, *68*, 725.
[52] Lee, J.; Han, S. *Phys. Chem. Chem. Phys.* **2013**, *15*, 18906.
[53] Ketteler, G.; Weiss, W.; Ranke, W.; Schlogl, R. *Phys. Chem. Chem. Phys.* **2001**, *3*, 1114.
[54] Chambers, S. A.; Yi, S. I. *Surf. Sci.* **1999**, *439*, L785.
[55] Thevuthasan, S.; Kim, Y. J.; Yi, S. I.; Chambers, S. A.; Morais, J.; Denecke, R.; Fadley, C. S.; Liu, P.; Kendelewicz, T.; Brown, G. E. *Surf. Sci.* **1999**, *425*, 276.
[56] Bergermayer, W.; Schweiger, H.; Wimmer, E. *Phys. Rev. B* **2004**, *69*, 195409.
[57] Condon, N. G.; Murray, P. W.; Leibsle, F. M.; Thornton, G.; Lennie, A. R.; Vaughan, D. J. *Surf. Sci.* **1994**, *310*, L609.
[58] Condon, N. G.; Leibsle, F. M.; Lennie, A. R.; Murray, P. W.; Vaughan, D. J.; Thornton, G. *Phys. Rev. Lett.* **1995**, *75*, 1961.
[59] Liu, P.; Kendelewicz, T.; Brown, G. E.; Nelson, E. J.; Chambers, S. A. *Surf. Sci.* **1998**, *417*, 53.
[60] Kurtz, R. L.; Henrich, V. E. *Phys. Rev. B* **1987**, *36*, 3413.

[61] Nguyen, M. T.; Seriani, N.; Gebauer, R. *J. Chem. Phys.* **2013**, *138*, 194709.
[62] Wang, X. G.; Weiss, W.; Shaikhutdinov, S. K.; Ritter, M.; Petersen, M.; Wagner, F.; Schlogl, R.; Scheffler, M. *Phys. Rev. Lett.* **1998**, *81*, 1038.
[63] Trainor, T. P.; Chaka, A. M.; Eng, P. J.; Newville, M.; Waychunas, G. A.; Catalano, J. G.; Brown, G. E. *Surf. Sci.* **2004**, *573*, 204.
[64] Yin, S. X.; Ma, X. Y.; Ellis, D. E. *Surf. Sci.* **2007**, *601*, 2426.
[65] Tanwar, K. S.; Petitto, S. C.; Ghose, S. K.; Eng, P. J.; Trainor, T. P. *Geochim Cosmochim Ac* **2009**, *73*, 4346.
[66] Yamamoto, S.; Kendelewicz, T.; Newberg, J. T.; Ketteler, G.; Starr, D. E.; Mysak, E. R.; Andersson, K. J.; Ogasawara, H.; Bluhm, H.; Salmeron, M.; Brown, G. E.; Nilsson, A. *J Phys. Chem. C* **2010**, *114*, 2256.
[67] Catalano, J. G. *Geochim Cosmochim Ac* **2011**, *75*, 2062.
[68] Jones, F.; Rohl, A. L.; Farrow, J. B.; van Bronswijk, W. *Phys. Chem. Chem. Phys.* **2000**, *2*, 3209.
[69] Eggleston, C. M.; Stack, A. G.; Rosso, K. M.; Higgins, S. R.; Bice, A. M.; Boese, S. W.; Pribyl, R. D.; Nichols, J. J. *Geochim Cosmochim Ac* **2003**, *67*, 985.
[70] de Leeuw, N. H.; Cooper, T. G. *Geochim Cosmochim Ac* **2007**, *71*, 1655.
[71] Kerisit, S. *Geochim Cosmochim Ac* **2011**, *75*, 2043.
[72] Costa, D.; Tougerti, A.; Tielens, F.; Gervais, C.; Stievano, L.; Lambert, J. F. *Phys. Chem. Chem. Phys.* **2008**, *10*, 6360.
[73] Chase, M. W.; Davies, C. A.; Downey, J. R.; Frurip, D. J.; Mcdonald, R. A.; Syverud, A. N. *J. Phys. Chem. Ref. Data* **1985**, *14*, 927.
[74] Henderson, M. A. *Surf. Sci. Reports* **2002**, *46*, 1.
[75] Ahmed, M. H. M.; Torrelles, X.; Treacy, J. P. W.; Hussain, H.; Nicklin, C.; Wincott, P. L.; Vaughan, D. J.; Thornton, G.; Lindsay, R. *J. Phys. Chem. C* **2015**, *119*, 21426.
[76] Ogasawara, H.; Brena, B.; Nordlund, D.; Nyberg, M.; Pelmenschikov, A.; Pettersson, L. G. M.; Nilsson, A. *Phys. Rev. Lett.* **2002**, *89*, 276102.
[77] Schiros, T.; Naslund, L. A.; Andersson, K.; Gyllenpalm, J.; Karlberg, G. S.; Odelius, M.; Ogasawara, H.; Pettersson, L. G. M.; Nilsson, A. *J. Phys. Chem. C* **2007**, *111*, 15003.
[78] Knapp, M.; Crihan, D.; Seitsonen, A. P.; Lundgren, E.; Resta, A.; Andersen, J. N.; Over, H. *J. Phys. Chem. C* **2007**, *111*, 5363.
[79] Paz-Borbon, L. O.; Hellman, A.; Gronbeck, H. *J. Phys. Chem. C* **2012**, *116*, 3545.
[80] Winter, B.; Aziz, E. F.; Hergenhahn, U.; Faubel, M.; Hertel, I. V. *J. Chem. Phys.* **2007**, *126*, 124504.

CHAPTER 5. DEVELOPMENT OF CORROSION-PREVENTION ORGANIC MONOLAYERS ON IRON SURFACES

The modification of metal surfaces by self-assembled monolayers (SAMs) is a promising environment-friendly technique for corrosion protection; in a number of instances, this process simply requires the immersion of the appropriate substrate into a solution of the modifier molecules to produce a dense and stable monolayer. However, the efficiency of a given modifier has mostly been determined *a posteriori* as detailed experimental characterizations of the interfacial structures are still challenging. Thus, computational modeling of these interfaces can serve as a predictive tool and provide a useful description of the interfacial processes required to prevent corrosion of iron surfaces *via* the deposition of organic monolayers.

In this Chapter, quantum-mechanical methods and *ab initio* molecular dynamics simulations are considered to elucidate the interfacial geometric and electronic structures of iron with SAMs. The Chapter begins with a short introduction of the conventional approaches to developing organic inhibitors and their limitations (Section 5.1). The major part of this Chapter involves the chemical modification on SAMs with various binding, spacer, and terminal groups (Section 5.3). SAMs on iron oxide have been also explored in order to assess the effects of the substrate oxidation process of metallic iron prior to the SAM deposition (Section 5.4). The fundamental understanding of the SAM-Fe interface

can help molecular design and lead towards more efficient organic inhibitors for iron corrosion prevention.

5.1 Design of organic inhibitors in corrosion science

5.1.1 Conventional approach

5.1.1.1 Quantum-chemical computations in molecular design

Traditionally, the corrosion prevention performances of organic inhibitors have been both qualitatively and quantitatively investigated by experimental techniques such as weight loss assessment, electrochemical impedance spectroscopy, and electrochemical potentiodynamic polarization. Extensive research in the past suggests that the corrosion protection afforded by organic coatings results from the combined effects of transport limitation and the low electrochemical reactivity or suppression of metallic dissolution at the metal/organic interface. However, it should be noted that there is still much to understand in order elucidate the related inhibition mechanisms, due to the complexity of the interface where chemical interactions among the metal surface, inhibitors, and corroding oxidants from the environment continuously coincide. To acquire more precise descriptions of corrosion inhibition by molecular layers, computational techniques have been developed to establish the relationships between molecular structure and inhibition efficiency.[1]

Since it has generally been accepted that corrosion inhibition due to organic compounds is mainly governed by their adsorption properties on a given substrate, the conventional

theoretical approaches essentially focus on molecular design by modifying the functional groups, steric factors, aromaticity, electron density on the donor atoms, and *p*-orbital character of donating electrons of the organic inhibitor. To estimate the binding strength of organic compounds, several key quantum-chemical descriptors based on hard and soft acid and bases (HSAB) theory of chemical reactivity, such as the eigenvalues of the highest occupied (HOMO) and lowest unoccupied (LUMO) molecular orbitals, dipole moment, chemical hardness, electrophilicity index, and local reactivity, *i.e.*, Fukui indices, are theoretically evaluated, mostly for an isolated molecule.[2] For instance, one of the most frequently used quantum-chemical parameters is the HOMO-LUMO energy gap; the smaller the HOMO-LUMO energy gap of the inhibitor molecule has, then the expected higher chemical reactivity, which leads to an increase in the strength of adsorption and inhibition efficiency.[3]

However, as illustrated in Chapter 1, the electronic structure of a molecule varies with its local environment, leading to different predicted energy level alignments between isolated and non-isolated environments. Also, an adsorption geometry may prohibit wavefunction overlap between the MOs of organic inhibitors and *d* orbitals of the metal surface, which is essential to the bond formation between the two materials *via* electron transfer. Thus, it is necessary to examine the interfacial interaction between organic inhibitors and the metal surface upon molecular adsorption to obtain a comprehensive understanding of the inhibition mechanism.

5.1.1.2 Hetereocyclic compounds

The adsorption behavior of organic molecules on a metal surface is often associated with heteroatoms in the active groups, such as S, O, N, or P, as they have high basicity and electron density. In particular, attention over the past few decades has focused on non-toxic azole compounds (*e.g.* triazoles, imidazoles and thiazoles) and their derivatives.[4] Their chemical structures consist of five-membered heterocyclic compounds containing a nitrogen atom, and they often bind to the metal surface through a pyridine-like nitrogen atom, a pyrrole-like nitrogen atom, or the aromatic ring itself as the substituent can act as an active center. It has been reported that they are efficient corrosion inhibitors for metals and alloys by forming an insoluble organic film in water with cations of the metal being protected.[5,6]

Fe(001) can be fully covered by imidazole molecules (Γ=3.12×10^{14} molecules/cm^2) most likely in a face-on geometry due to strong π-*d* hybridization, as described in Figure 5.1a. The charge density difference before and after molecular adsorption ($\Delta\rho$) shows that there is a covalent bond formed between the metal surface and imidazole; the cumulative net charge transfer is ~ 0.2 e. Despite the strong binding of imidazole molecules on Fe(001), it is surprising that an O_2 molecule still can spontaneously dissociate on the metal surface with ΔE = -5.31 eV. Although this dissociation energy is lower than in the case of a bare Fe(001) (ΔE = -6.64 eV), the modified surface remains highly vulnerable to oxidation, which underlines that it is imperative to prevent strong oxidants from diffusing onto the iron surface to ensure the long-term stability of organic inhibitors. Indeed, it has been reported that an organic film based on azole compounds tends to degrade over time and possibly even delaminate after a few days due to its permeability

to oxidizing agents. Therefore, a thick film is usually required to provide a sufficient inhibition efficiency by increasing the concentration of azole-based compounds during the electrochemical deposition.[7]

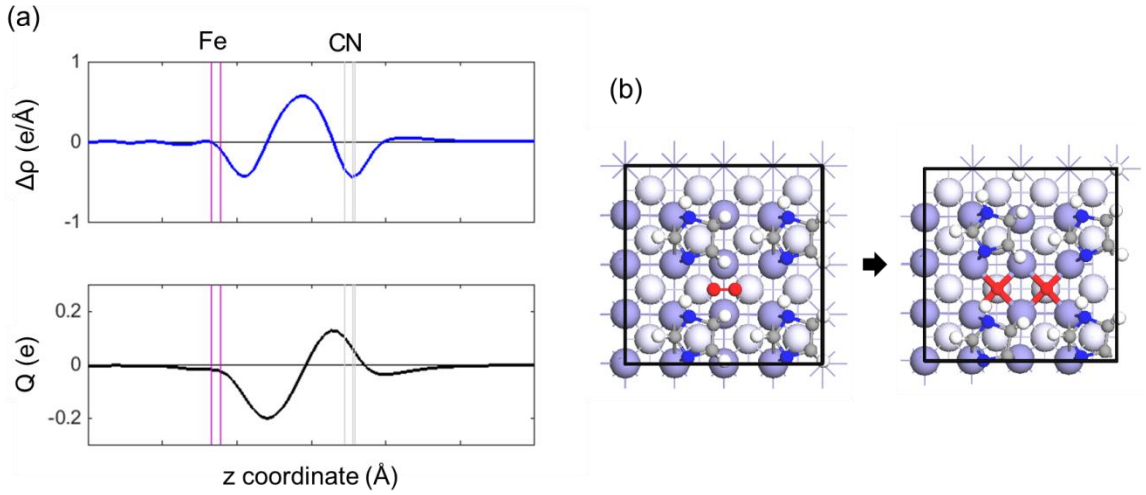

Figure 5.1 (a) Variation of the charge density (blue line) and cumulative charge difference (black line) are calculated by a plane-averaged method upon adsorption of imidazole on Fe(001) at the PBE+D3 level. The vertical lines indicate the atomic positions of surface Fe and the components in the adsorbed imidazole molecule on Fe(001). (b) Optimized geometry of imidazole/Fe(001) before (left) and after (right) O_2 dissociation.

5.1.2 Organic SAMs for corrosion prevention

Surface modification of metals by self-assembled monolayers (SAMs) is a promising, environment-friendly technique for corrosion protection. It is characterized by a spontaneous process consisting of adsorption and self-organized formation of highly

ordered molecular monolayers by immersion of an appropriate substrate into a solution of surfactant molecules. This process can lead to a dense and stable layer atop the metal surface for corrosion protection.

SAMs, in general, consist of three distinct structural moieties: binding (head) group, spacer, and terminal (tail) functional group, as illustrated in Figure 5.2. The binding group serves as a bridge between the substrate and the rest of the molecular structure. This group can directly attach to the substrate through simple physisorption, with adsorption energies on the order of 0.01-0.1 eV; however, attachment more typically occurs by chemisorption where a new ionic or covalent bond on the order of 1-10 eV forms between the surface modifier and the substrate. The spacer group often determines the physical separation between the substrate and the potentially reactive terminal group, in addition to the monolayer packing structure induced by intermolecular van der Waals (vdW) interactions. The spacer can be made flexible or rigid by the use of saturated alkyl chains or unsaturated/conjugated aryl groups, respectively. The last component of a representative monolayer is the terminal functional group that primarily determines the surface properties and chemistry after modification. The ability to tailor each part of the SAMs provides the desired control of the structure and chemical properties of the surface at the molecular level.

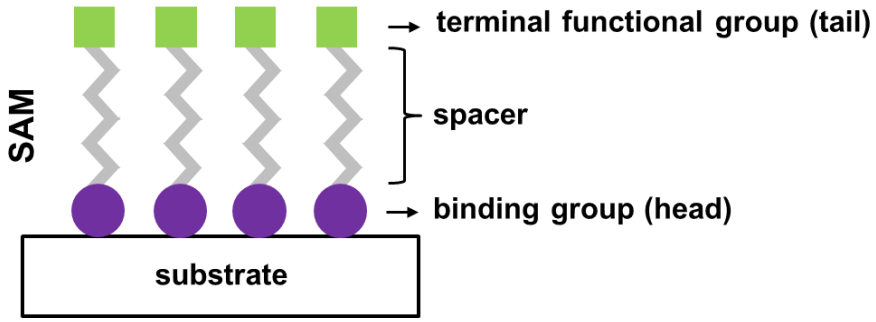

Figure 5.2 General components of a typical self-assembled monolayer (SAM) on a substrate.

In this regard, SAMs can protect the substrate from corrosive ions and molecules by (i) the binding group suppressing metal dissolution and (ii) the spacer and terminal groups building a highly compact and well-ordered monolayer with a specific chemical functionality, leading to a strong physical/chemical barrier against corrosive ions and molecules.

The first attempt at applying a SAM for corrosion protection was made by the deposition of alkanethiols (R-SH) on iron[8] and copper.[9,10] Despite good protection efficiency, the industrial application of thiol compounds is limited due to their toxicity and instability with exposure to O_2 under atmospheric conditions. Phosphonic acids (PA, R-PO$(OH)_2$) hold promise as effective corrosion protecting coatings to replace thiols since phosphonates are chelating agents that bind tightly to di- and trivalent metal ions, preventing them from forming insoluble precipitates and suppressing their catalytic properties. Generally, PA-based SAMs are found to coordinate to the metal oxide by

heterocondensation in several different binding modes on the surface in a reproducible manner, as described in Figure 5.3. The major adsorption modes depend on the type of surface atoms and the pretreatment condition. Alkylphosphonic acids have been found to exhibit corrosion-inhibiting effects on metals such as mild carbon steel, copper, and aluminum. Raman *et al.*[11] observed the formation of alkyl phosphonic acid SAMs on the native oxide surface of stainless steel. Their FT-IR and XPS measurements suggested that alkyphosphonic acids are covalently bound to the surface as phosphonates in a bidentate manner. Further investigation revealed the existence of bidentate and tridentate binding with a 98° water contact angle in the case of the iron surface.[12] Compared to carboxylic acid (CA, R-COOH)-based SAMs, one of the oldest organic compounds studied systematically,[13] PAs can be regularly and densely anchored to the Mg alloy substrate presenting higher chemical stabilities than alkanoic acid-derived SAMs in water contact angle measurements.[14] Largely, PAs have been used as mixed or anodic inhibitors.[15]

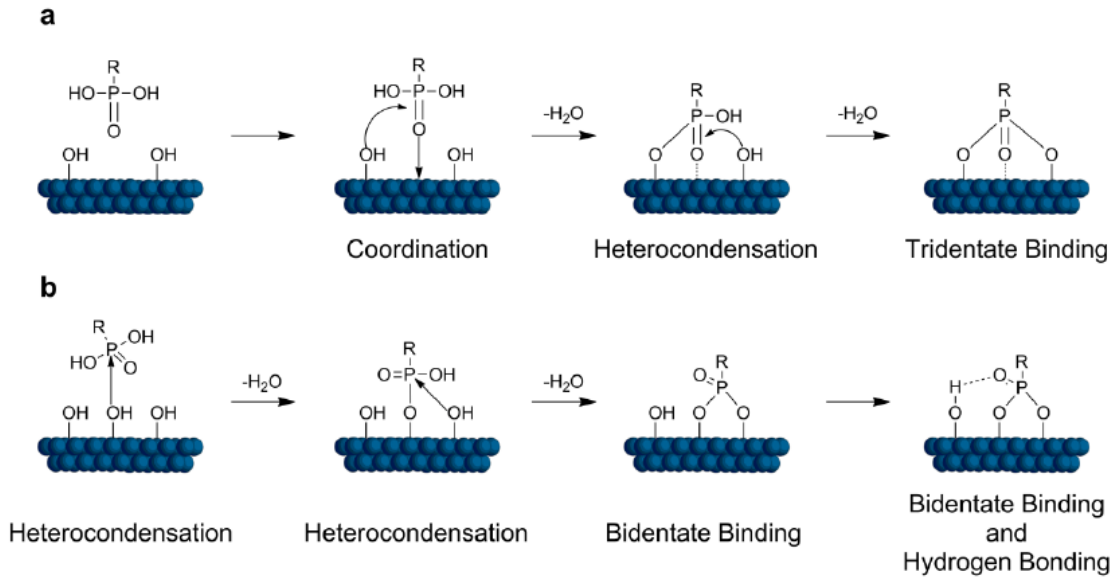

Figure 5.3 Description of a phosphonic acid binding to (a) Lewis acidic metal oxides and (b) poorly Lewis acidic metal oxides. This figure demonstrates the varieties of binding modes that are possible and outlines what type of reaction is occurring at each step. Figure adapted from Ref. 16.

Further corrosion inhibition can be achieved by modifying the spacer or the terminal group. Zamborini *et al.*[17] studied the impact of chain length and terminal functional group of n-alkanethiol SAMs on passivation of a gold surface by FTIR-ERS and STM. It has been shown that a hydrophilic SAM-modified Au surface corrodes smoothly in a layer-by-layer fashion while a methyl-terminated, hydrophobic SAM-modified surface undergoes localized corrosion, *i.e.*, pitting. Caprioli *et al.*[18] reported that aromatic thiols on copper immersed in a strongly acidic solution lead to a noticeable increase in charge-transfer resistance within the first few hours of immersion. SAMs of alkylthiols, on the contrary, are known to undergo a fast degradation in their inhibition properties when

exposed to chemically aggressive solutions. The enhanced properties of aromatic thiol monolayers are attributed to the reorganization of aromatic rings which leads to a minimization of disordered domains due to π-hydrogen interactions between the aromatic rings and water molecules. Improved protection can also be afforded by substituting functional groups onto the benzene of benzenethiol, with the degree of improvement depending on the type, position, and size of the substituents.[19] Fluorocarbon-based films, in general, are known to offer advantages over hydrocarbon coatings regarding rigidity, oleophobicity, and thermal stability.[20] Fluorinated SAMs, indeed, showed enhanced stability against ion/water penetration when biased to negative potentials by influencing the permeability, wettability, structure, and capacitance of the films.[21]

5.1.3 Research objectives

To evaluate corrosion prevention afforded by SAM deposition, we have undertaken detailed computational studies of the chemical interactions between iron/iron oxide and SAMs, using interface models based on quantum-mechanical methods and molecular dynamics simulations. The structural and chemical factors pertinent to inhibition efficiencies, such as binding energy, monolayer packing structures, and electronic structures have been investigated for parent and functionalized SAMs (Figure 5.4) adsorbed onto Fe(001). For SAMs with alkyl chains ($(CH_2)_n$-H) as the spacer, the inhibition efficiency highly depends on chain length. Experimentally, octylphosphonic acids (OPA) provide the best protection efficiency of the iron surface with a significant decrease of anodic currents among PAs of varying chain lengths (n = 6,7,8,10).[22] In more

recent work with SS316L stainless steel,[23] OPA exhibit reasonable long-term stability in acidic, neutral, and physiological solutions, as well as under dry heating, although a slight enhancement has been found any for longer chain lengths, n = 12-18. In the current discussion, we have chosen n = 8 for the hydrocarbon chain length. The PAs on γ-Fe_2O_3 (001) and α-Fe_2O_3(1-102) have been further investigated to assess the role of oxidative passivation of the iron surface before monolayer deposition. The understanding of how SAMs impact the substrate properties as a function of the chemical nature of the monolayers can provide insight into the development of efficient organic coatings to prevent iron corrosion.

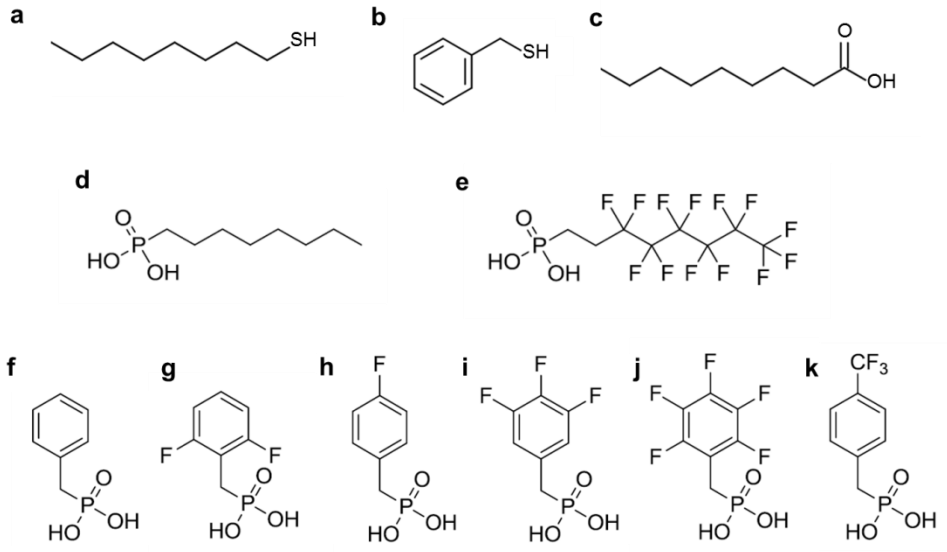

Figure 5.4 Chemical structures of the molecules investigated here: (a) Octanethiol (OT); (b) benzylthiol or benzyl mercaptan (BT); (c) nonanoic acid or pelargonic acid (NA); (d) octylphosphonic acid (OPA); (e) 3,3,4,4,5,5,6,6,7,7,8,8,8-tridecafluorooctylphosphonic acid (F_{13}OPA); (f) Benzylphosphonic acid (BPA); (g) 2,6-difluorobenzylphosphonic acid (2,6-F_2BPA); (h) 4-fluorobenzylphosphonic acid (4-FBPA); (i) 3,4,5-trifluorobenzylphosphonic acid (3,4,5-F_3BPA); (j) pentafluorobenzylphosphonic acid (PFBPA); and (k) 4-(trifluoromethyl)benzylphosphonic acid (4-CF_3BPA or pCF_3BPA).

5.2 Computational details

First-principles calculations have been performed using spin-polarized DFT as implemented in the Vienna ab initio simulation package (VASP)[24,25] with the generalized gradient approximation (GGA) exchange-correlation functional of Perdew, Burke, and Ernzerhof (PBE).[26] The ionic potentials are described by the PAW pseudopotential[27] with valence configurations of $3d^7 4s^1$ and $2s^2 2p^4$ for Fe and O atoms, respectively. The energy cutoff for a plane-wave basis set was set to 450 eV.

To build clean and hydroxylated Fe(001) surfaces, a bcc Fe unit cell was optimized with 12×12×12 Γ-centered **k**-point grids for Brillouin zone (BZ) integration. Based on the optimized bulk structure of a = 2.81 Å, a (1×1) Fe(001) slab containing five Fe layers is constructed; the topmost three layers are allowed to relax while the bottom two layers are fixed in order to maintain bulk behavior below the surface with 12×12×1 Γ-centered **k**-points grids. A vacuum region of 20-25 Å is inserted to separate the slabs in a periodic boundary condition (PBC). The Pourbaix diagram of hydroxylated Fe(001) in an aqueous solution is calculated based on a computational hydrogen electrode (CHE) model,[28] in which the relative stabilities among different surface configurations are plotted as a function of the electrode potential and the solution pH[29] in a water-based reference state.[30] The details of the procedure are illustrated in Chapter 2.

For the descriptions of maghemite and hematite, we exploited the DFT+Hubbard *U* (DFT+*U*) approach[31] to describe the intra-atomic Coulomb interaction among strongly correlated Fe 3*d* electrons. U_{eff} = 4 eV has been applied to Fe 3*d* electrons in the simplified rotationally invariant formulation of Dudarev *et al.*[32] where the on-site Coulomb parameter, *U*, and exchange parameter, *J*, are combined into a single parameter, $U_{eff} \equiv U - J$. The surface is modeled using a (1×1) unit cell of γ-Fe_2O_3 (001) and α-Fe_2O_3 (1-102) based on the optimized bulk crystal structures obtained in Chapter 3. The slabs contain ~ 20 atomic layers with a vacuum region of approximately 20 Å. During the geometry optimizations, the bottom layers were kept fixed at the bulk crystal positions while the outermost 5-6 atomic layers from the surface were allowed to relax. The ground-state bulk magnetic orderings were imposed in the slab models.

To build the interface model, SAM molecules are first optimized in an isolated box of 30 Å×30 Å×30 Å using the Γ-point. Then, the organic-inorganic interface system is constructed by building a supercell of the substrate such a way that molecules are adsorbed with a given coverage density in repeated unit cells in PBC. The **k**-point sampling for BZ integrations was downsized inversely proportionally to the increase in the unit-cell size of the interface system, as summarized in Table 5.1. The van der Waals (vdW) interactions from dynamic correlations between fluctuating charge distributions were approximated using Grimme's D3 method.[33] Geometries were optimized with a quasi-Newton or/and conjugate-gradient algorithm until the Hellmann-Feynman forces were less than 0.01 eV/Å and energy convergence was within 10^{-5} eV/atom. A Gaussian-smearing approach for the orbital occupancies with σ = 0.05 eV was used during the geometry optimizations and electronic-structure analyses of densities of electronic states (DOS). The orbital-projected densities of states (PDOS) were calculated by projecting the Kohn-Sham (KS) wave functions onto atom-centered spherical harmonic functions within each atom's Wigner-Seitz radius. The reaction energies for SAM attachment on iron and iron oxide are calculated based on the free energies that can be derived from the total energy obtained from the DFT calculations with the corrections for zero-point vibrational energy (ZPE) and entropy contributions (TS) for the adsorbates and gas (liquid) molecules. The details of these energy corrections entering the surface free energies are given in Appendix A.

Table 5.1 Surface unit-cell sizes and k-point samplings for the SAM-Fe and SAM-Fe_2O_3 systems considered in this study.

Substrate	Surface unit-cell size	k-points
Fe(001)	5.659 Å ×5.659 Å	6×6×1
	8.488 Å ×8.488Å	4×4×1
	11.317 Å × 11.317 Å	3×3×1
γ-Fe_2O_3(001)	8.378 Å × 8.378 Å	4×4×1
α-Fe_2O_3(1-102)	5.477 Å × 5.07 Å	6×6×1

Symmetry-adapted perturbation theory (SAPT) calculations of phosphonic acid-H_2O were completed at the SAPT2+/aug-cc-pvdz level (simplified throughout as SAPT2+) as implemented in the PSI4 program.[34] This level of calculation has been labeled the silver-standard by Parker *et al*. as it allows for accurate calculations of interaction energies (mean absolute error < 0.5 kcal/mol for the S22 test set) in reasonable computational times.[35]

Although DFT and SAPT are powerful techniques to understand the ground-state structural/electronic properties of the SAM-inorganic systems, their major drawbacks are the limited environmental conditions, *i.e.*, T = 0 K, p = 0 atm. To bridge the so-called "temperature/pressure gap between DFT and real-world systems, we extended our theoretical study to the level of *ab initio* molecular dynamics (MD), which is free of *ad hoc* parametrizations of force fields and computes the electronic structure from first principles to predict dynamical behaviors of SAMs at finite temperature and pressure. In this approach, vibrational and rotational motions of individual SAM moieties can be

taken into account, which is responsible to lead from a coherent packing structure to a less compact structure. Thus, in this study, we employed *ab initio* MDs for (i) obtaining the monolayer morphologies at finite temperature and (ii) assessing the O_2 diffusion kinetics with and without the presence of SAMs. To evaluate the SAM packing structures in MD runs, the initial structures were taken from the optimized geometries of SAM-Fe at the PBE level with vdW correction, then constructed into a supercell of 11.317 Å×11.317 Å, which corresponds to a (4×4×1) supercell of Fe(001) (containing 16 Fe atoms per layer). Because the Fe substrate is ferromagnetic, spin polarization (unrestricted) calculations were performed. In general, the model system was first thermally equilibrated in a canonical ensemble (NVT) for 1 ps at low temperature, 100 K, then followed by an MD production run of 3-5 ps at room temperature, in which the temperature was controlled by a Nose-Hoover thermostat.[36] During the MD simulations, all atoms are allowed to move but the cell volume and shape are kept fixed. After 4 ps of thermal equilibration of then SAM-Fe structures, the SAM geometries are taken to passivate both sides of the Fe slab (3 atomic layers), and are then equilibrated for another 1 ps in NVE. In the next step, 12 to 16 O_2 molecules are introduced into the vacuum region of the unit cell to meet the condition of $p(O_2)$ = 50 atm. Trajectories are formed by propagating the structure with the calculated Hellmann-Feynman forces with time steps of 1 fs for the integration of the equations of motion. For simulations of fluorinated SAMs, where hydrogen atoms do not have a significant impact on monolayer structure or interaction with oxygen molecules, a time step of 2 fs was used with increased hydrogen masses of 2 a.u., which allows for a larger time step for the large cell sizes. Gaussian

smearing with σ = 0.05 eV is used to broaden the one-electron levels with Γ-centered 2×2×1 **k**-point samplings.

5.3 Impact of SAM design on inhibition efficiency

To systematically investigate the impact of the molecular design of the SAMs on iron corrosion prevention, this Section is divided into three parts as we address separately the impacts of the binding group, spacer, and terminal group on inhibition efficiency. We begin with the binding groups.

5.3.1 Binding groups

5.3.1.1 Thiols on Fe (001)

Thiol adsorption onto a metal surface occurs by a two-step process, physisorption followed by chemisorption:[37]

$$(R\text{-}SH)_{sol} \rightarrow (R\text{-}SH)_{ad} \quad (5.1)$$

and then

$$(R\text{-}SH)_{ad} \rightarrow R\text{-}S\text{-}Fe + (H^{+} + e^{-}) \quad (5.2)$$

where subscripts “ad” and “sol” indicate adsorbed and in solution, respectively. Since Equation 5.2 depends on the electrode potential, the adsorption energetics and kinetics

can vary upon cathodic potentials. According to the energetics derived from PBE calculations combined with a CHE model, the chemisorption of octanethiol (OT) on Fe(001) is energetically favorable in the physically accessible potential-pH range, see Figure 5.5a. Therefore, even when the sample is repeatedly polarized to a low cathodic potential region to reduce the oxide layer and prevent oxide formation during the coating process, experimental data show that the entire surface can be covered by chemisorbed thiols.[38]

Table 5.2 summarizes the adsorption energy and structural parameters of optimized OT-Fe(001) in three different surface coverage densities. It should be noted that one of the important geometric parameters in a SAM is angle θ, defined as the tilt angle of the molecule away from the surface normal vector ($\vec{\boldsymbol{N}}$) of Fe(001), as depicted in Figure 5.5b. While the adsorption geometries do not change dramatically as a function of coverage density, a highly compact packing is thermodynamically favored. Given that the vdW correction contributes -0.22 eV among the total adsorption energy increase (-0.33 eV) as the coverage density increases from 1.39×10^{14} to 3.12×10^{14} molecules/cm^2, the dispersion from lateral interactions of alkyl chains can lead to self-assembly of thiols on the iron surface. Interestingly, the dispersion energy for a coverage of 3.12×10^{14} molecules/cm^2 is calculated to be -0.03 eV per carbon atom, which is in line with the value experimentally deduced (0.027-0.032 eV for *n*-alkanethiol on an iron electrode).[39] In such a high-coverage condition, the reaction energy for adsorption (ΔG_{ad}) of OT adsorption on Fe(001) is calculated to be -2.90 eV, which is much higher than the -1.43 eV ΔG_{ad} of imidazole at the same packing density.

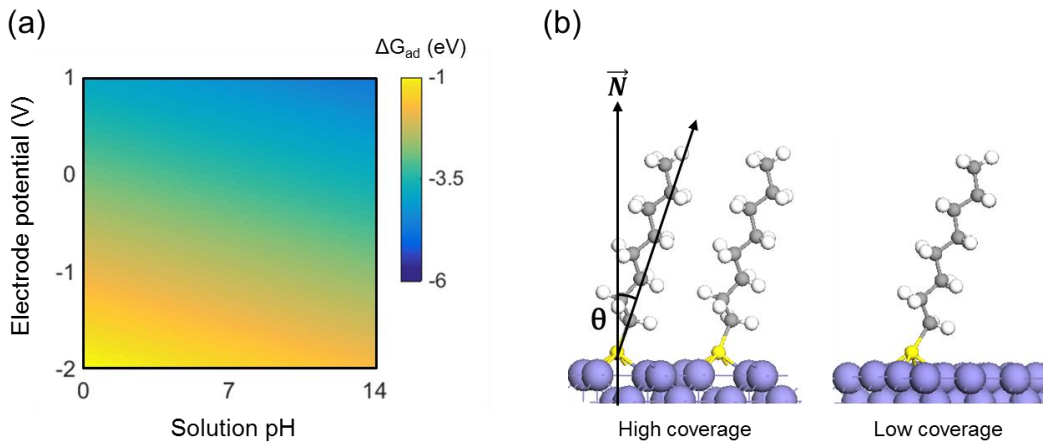

Figure 5.5 (a) Adsorption energy (ΔG_{ad}) of octanethiol on Fe(001) (Γ= 3.12×10^{14} molecules/cm^2) as a function of electrode potential (U_{SHE}) and solution pH. (b) Binding configuration of octanethiol on Fe(001) at high coverage density (Γ= 3.12×10^{14} molecules/cm^2) and low coverage density (Γ= 7.81×10^{13} molecules/cm^2). The geometric parameter, θ, is defined as the tilt angle of the molecule away from the surface normal vector ($\vec{N}$) of Fe(001).

Table 5.2 Adsorption energy (U_{SHE} = 0 V, pH = 0), tilt-away angle of octanethiol on Fe(001), average bond distance between surface Fe atom and S of thiol, and work function variation of Fe(001) upon thiol adsorption for three surface coverage densities (Γ).

Γ (mol./cm^2)	ΔG_{ad} (eV)	θ (°)	d(Fe-S) (Å)	$\Delta\Phi$ (eV)
7.81×10^{13}	-2.35	21.51	2.31	-0.43
1.39×10^{14}	-2.57	21.27	2.32	-0.65
3.12×10^{14}	-2.90	24.85	2.32	-0.98

5.3.1.2 Acids on hydroxylated Fe(001)

Despite the self-assembly process of thiols on a metal surface, it has been reported that the resulting monodentate binding typically does not withstand even simple wiping with cotton wool.[13] Thus, we extended our study to acid-based SAMs that can form stronger chemical binding with Fe(001). In the case of thiols, the adhesion layers have to be adsorbed directly on the metal; however, the situation is different for phosphonates or carboxylate that can form stable and well-ordered monolayers also on metal oxide films. As explained in Section 5.1.2, acid-based SAMs form *via* chemical interactions between the binding group of the organic molecules and the substrate surface, often a thin oxide layer that is terminated by surface-bound hydroxyls.

Typically, acid-derived SAMs such as phosphonic acid SAMs can bind on metal oxide surface in up to three different binding modes: monodentate, bidentate, and tridentate depending on the number of chemical bonds formed on the substrate. Given that the most common technique to obtain acid-based monolayers is immersion or dip coating,[13] the reaction energy of adsorption (ΔG_{ad}) is calculated assuming that the molecular attachment is induced by the heterocondensation of an acid molecule with the surface hydroxyls of the Fe substrate:

$$\Delta G_{ad} = G_{Fe-mol.} + nG_{H_2O} - (G_{Fe-(OH)_n} + G_{mol.}) \quad (5.3)$$

Here, the subscript "Fe-mol." corresponds to the optimized structure of the Fe(001) slab attached by a monolayer of phosphonic acid (PA) or carboxylic acid (CA); "H_2O", to an isolated water molecule; "Fe-$(OH)_n$", to the hydroxylated surface where *n* represents the number of hydroxyl groups per Fe(001) (2×2) surface unit cell; and "mol.", to an isolated PA (CA) molecule. We note that the reaction energy depends on *n*, which varies depending on the sample preparation conditions. In this context, the Pourbaix diagram of hydroxylated Fe(001) is first calculated to determine the most probable surface configuration prior to SAM deposition, as depicted in Figure 5.6a. There are two hydroxylated surfaces that appear as most favorable in the given electrochemical conditions. In an acidic environment, the surface atoms of Fe(001) spontaneously dissolve as ferric ions into the electrolyte at the standard hydrogen electrode potential (U_{SHE} = 0). If the electrode is polarized below ~ -0.5 V, a partially hydroxylated surface (1/2ML OH, Fe-$(OH)_2$) becomes thermodynamically favored over iron dissolution. In the case of Fe(001) in a basic solution near pH = 9-10, the Fe(001) surface can be fully covered by hydroxyls (1ML OH, Fe-$(OH)_4$) without any applied bias, while polarization at cathodic potentials leads to partial hydroxylation. In this study, we further discuss PA (CA) adsorption on these two hydroxylated surfaces.

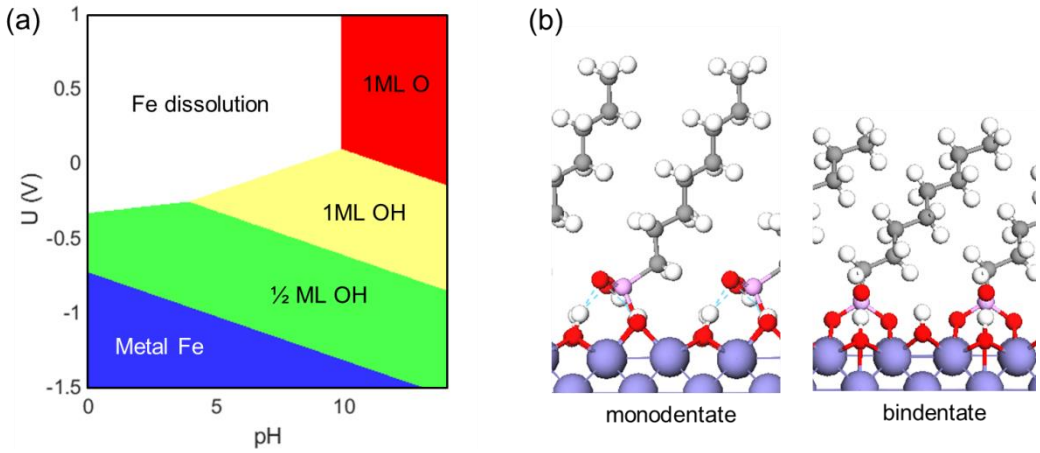

Figure 5.6 (a) Calculated Pourbaix diagram of hydroxylated Fe(001). (b) Optimized adsorption geometry of OPA on Fe(001) in two binding modes.

On the fully hydroxylated surface, phosphonic acids essentially bind to surface Fe atoms in two configurations: monodentate and bidentate, as shown in Figure 5.6b. Given that the adsorption energy in a bindentate mode is higher than a monodentate mode by 0.57 eV, it is predicted that the OPA after the first dehydration reaction preferably undergoes a second dehydration, and eventually forms two Fe-O chemical bonds at the Fe(001)/OPA interface. In this binding configuration, one hydrogen bond between a surface hydroxyl and the phosphoryl oxygen atom of PA is present along with two interface Fe-O bonds of 2.11 and 2.15 Å long, leading to a less upright geometry than for a monodentate binding configuration. The tilt angle θ is calculated to be 46.9°, which is comparable to the experimentally measured θ of OPA on other substrates: 41° ± 8° (ITO)[40], 38° (HfO_2),[41] and 47° (Ag).[41] For partially hydroxylated Fe(001), OPA favors a tridentate binding mode where PO_3 moieties are anchored on the iron surface with three chemical bonds. It

should be noted that the Fe-O bond lengths are shorter in this configuration than in the other two binding motifs, which implies that the interfacial covalent bond is the strongest for the tridentate motif.

Table 5.3 Adsorption reaction energies, optimized local geometries, and work functions for octylphosphonic acid (OPA)/Fe(001) and nonanoic acid (NA)/Fe(001) systems in various binding modes.

substrate	OPA	ΔG_{ad} (eV)	θ (°)	d(Fe-O) (Å)	Φ (eV)
Fe-$(OH)_4$	monodentate	-2.07	30.4	2.13	4.38
	bidentate	-2.64	46.9	2.11, 2.15	3.82
Fe-$(OH)_2$	monodentate	-0.92	33.4	2.08	3.31
	bidentate	-1.46	47.7	1.94, 2.01	3.34
	tridentate	-2.26	32.6	1.91, 1.96, 2.10	3.36
	NA	ΔG_{ad} (eV)	θ (°)	d(Fe-O) (Å)	Φ (eV)
Fe-$(OH)_4$	monodentate	-1.35	37.1	2.19	3.91
Fe-$(OH)_2$	monodentate	0.35	28.9	-	3.83
	bidentate	0.21	27.3	1.94, 2.03	3.22

On the other hand, for nonanoic acid (NA), the representative alkylcarboxylic acid considered in this study, the adsorption can be an endergonic process when the surface requires is hydroxylated. It should be underlined that a monodentate binding of NA on Fe-$(OH)_2$ only forms a single hydrogen bond with the surface, which implies that NA does not adsorb on the surface in a Lewis acid-base reaction through the lone-pair electrons of carbonyl oxygen atom (C=O). The only possible adsorption on fully

hydroxylated Fe(001) is in a monodentate configuration. However, the Fe-O bond distance (2.19 Å) is much longer than the bond distances calculated for PA/Fe(001).

When a molecule chemisorbed on the substrate, significant electronic redistribution occurs at the interface. To assess the interfacial charge transfer between Fe(001) and three different binding groups: thiol, PA, and CA, we calculated the plane-averaged electron density difference $\Delta\rho(z)$ upon molecular adsorption along the surface normal direction z. Figure 5.7 presents the accumulated charge (Q) across the Fe(001)-SAM interface, *i.e.*, the integration of $\Delta\rho(z)$ along the z-coordinate, which represents the amount of net charge transfer upon the formation of the interfacial chemical bonds. In all three cases, the SAM molecules bind to the surface Fe atoms *via* covalent bonds involving a large amount of electron donation from the surface Fe atoms to the binding moieties. Considering that the calculated Q values are 0.06 e, 0.15 e, and 0.25 e for OT, NA, and OPA, respectively, phosphate is seen to exhibit a stronger chemical interaction with the surface Fe atoms than the carboxylate and thiolate.

It should be pointed out that the interface dipole due to the charge transfer from surface Fe atoms to the PO_3 moiety leads to a large electrostatic potential change outside the surface ($\Delta V \sim 1.5$ eV). The cathodic reaction is concomitant with electron transfer from the iron substrate to environmental oxidizing agents, *e.g.*, oxygen or water molecules. In the presence of (locally) induced electric field at the Fe-phosphonate interface, electron donation from the iron surface becomes less favorable and can be suppressed.

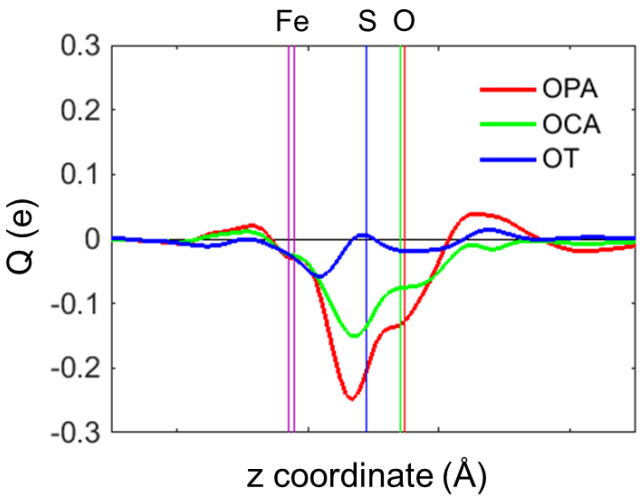

Figure 5.7 Charge density difference between the combined interface and the isolated fragments (Δρ) and accumulated charge (Q) across the interface of OPA/Fe(001) (red line), NA/Fe(001) (green line), and OT(Fe001) (blue line). Bidentate and monodentate binding mode on the fully hyroxylated surface are considered for OPA and NA, respectively. The vertical lines indicate the atomic positions of surface Fe and the components in the adsorbed binding moieties on Fe(001).

The charge transfer not only depends on the binding moiety but also the binding mode. For example, in the case of the bidentate and tridentate modes of OPA on the partially hydroxylated surface, Q is almost twice as large for the latter due to the additional covalent Fe-O bond, corresponding to a more substantial alteration in electronic redistribution. This is also confirmed by the Bader charge analysis where electron losses of 0.19 e (bidentate) and 0.36 e (tridentate) at the surface layer of Fe(001) are calculated. This is further confirmed by the calculated densities of states (DOS) of the optimized structures of the OPA-Fe(001) systems, as displayed in Figure 5.8. Interestingly, the shapes of the Fe *d* band of the surface atoms are not only modified from the clean surface

but also distinctive with respect to the binding configuration. There is more prominent deficiency of Fe *d* states near E_F for the tridentate PA, which is consistent with the larger electron transfer across the Fe-phosphonate interface.

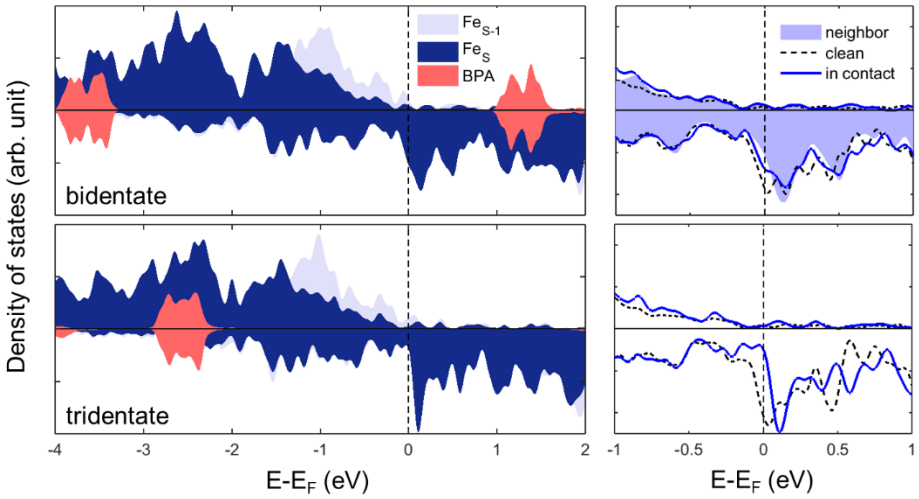

Figure 5.8 Left: Calculated densities of states (DOS) in the optimized structures of OPA in bi- and tridentate binding modes on partially hydroxylated Fe(001). Right: The modified PDOS of surface Fe atoms are compared to the clean counterpart in the range [E_F-1 eV, E_F+1 eV].

5.3.2 Spacer

5.3.2.1 Adsorption geometry

As pointed out in Section 5.1.2, the packing density of SAMs on the substrate is the key parameter to determine the corrosion inhibition efficiency of organic coatings as it can prevent the diffusion of oxidizing agents from electrolytes (or gas) to the surface, which

leads to the inhibition of the cathodic reaction. Therefore, it is imperative to confirm that tight monolayer packing is energetically favorable so that a dense SAM can be obtained, in particular when the spacer type changes from an alkyl chain to an aryl ring.

Figure 5.9a displays the calculated reaction energies of molecular adsorption for OT/Fe(001), BT/Fe(001), OPA/Fe(001), and BPA/Fe(001) at two different packing densities: high surface coverage ($\Gamma = 3.11\times10^{14}$ molecules/cm^2) and low coverage (7.81×10^{13} molecules/cm^2). When the spacer consists of a simple hydrocarbon chain, the adsorption energy is higher in a high-coverage density due to vdW interactions among neighboring alkyl chains. This is also the case for BPA whose adsorption energy (per molecule) increases by 0.11 eV in high coverage compared to low coverage. Although additional adsorption of a BPA on a site adjacent to an existing BPA on Fe(001) is electrostatically unfavorable, the dispersion energy between BPAs can render this reaction exothermic. Indeed, the calculated dispersion energy from Grimme's D3 method is larger for high coverage (-0.78 eV), than for low coverage (-0.55 eV). Thus, we can expect the formation of highly dense BPA monolayers on the iron surface. On the other hand, the adsorption of BT is less favorable in a higher packing density; 3.01 eV for $\Gamma = 3.12\times10^{14}$ molecules/cm^2 vs. 3.18 eV for $\Gamma = 7.81\times10^{13}$ molecules/cm^2. The discrepancy in adsorption energetics between BT and BPA can be ascribed to the SAM geometries in low-coverage conditions.

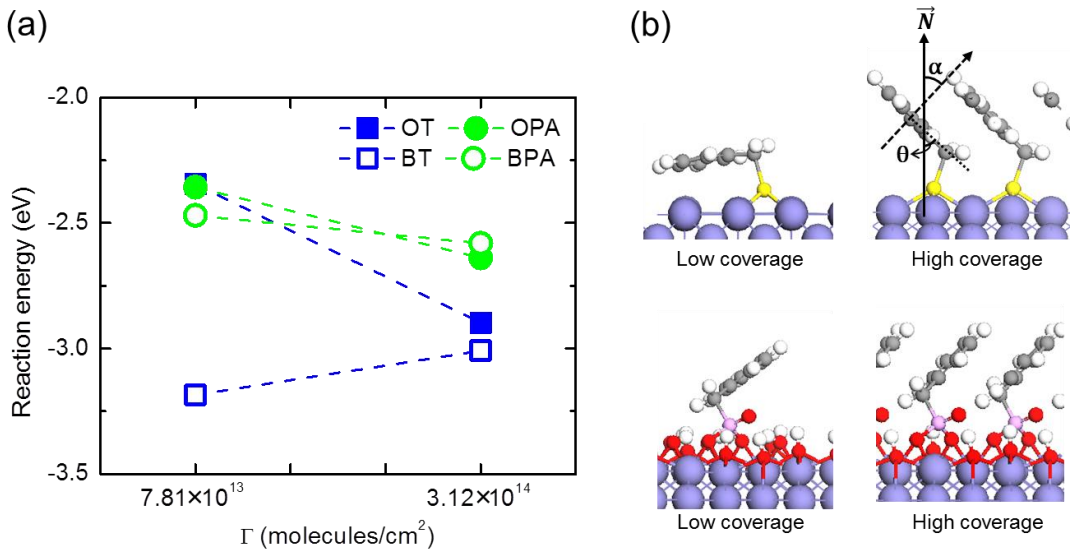

Figure 5.9 (a) Reaction energy of molecular adsorption for OT/Fe(001), BT/Fe(001), OPA/Fe(001), and BPA/Fe(001) at two different packing densities. (b) Optimized BT/Fe(001) and BPA/Fe(001) structures in high surface coverage (Γ= 3.11×10^{14} molecules/cm^2) and low coverage (7.81×10^{13} molecules/cm^2). The geometric parameters, angle α and angle θ, are illustrated in (b); α is defined as the angle between the normal vector to the benzyl ring with respect to the surface normal vector ($\vec{\boldsymbol{N}}$) while θ indicates the tilt angle of the molecular axis of the benzyl ring away from $\vec{\boldsymbol{N}}$.

To quantitatively evaluate the adsorption geometry of a SAM on the substrate, we introduce two geometric parameters, angle θ and angle α, which are measurable *via* PM-IRRAS and NEXAFS experiments. As depicted in Figure 5.9b, angle θ is defined as the tilt angle between the molecular axis of the benzyl ring away from the surface normal vector ($\vec{N}$), and α corresponds to the angle of the normal vector to the ring plane with respect to $\vec{N}$. Interestingly at low surface coverage, the tilt-away angle (θ) of BT significantly increases to 92.6° and α becomes as small as 10.3° is indicating that the

benzyl ring is lying flat on the Fe(001) surface. This substantial structural change originates from the strong interaction between the π orbitals on the benzyl ring and the 3*d* orbitals of the surface Fe atoms, which increases in the absence of any steric hindrance from neighboring BT molecules. Thus, the surface is effectively covered by the lying-down rings of BT molecules, although a large portion of the surface Fe atoms remains exposed at this coverage. BPA also shows a similar, although much smaller, tilt toward Fe(001) at high coverage, which can be attributed to the presence of surface hydroxyls that essentially prevent the π-*d* interactions.

Table 5.4 Average tilt angle of the molecular axis (θ), angle between the ring plane normal and surface normal angle (α), and optimized interface geometries for the BT/Fe(001) and BPA/Fe(001) interfaces at high-coverage and low-coverage conditions.

	BT			
Γ (mol./cm^2)	θ (°)	α (°)	d(Fe-S) (Å)	d(S-C) (Å)
3.12×10^{14}	46.8	46.1	2.32	1.95
7.81×10^{13}	92.6	10.3	2.31	1.98
	BPA			
Γ (mol./cm^2)	θ (°)	α (°)	d(Fe-O) (Å)	d(O-P) (Å)
3.12×10^{14}	54.1	46.6	2.13	1.56
7.81×10^{13}	62.1	37.1	2.17	1.56

At high coverage, BT and BPA have similar local adsorption geometries; BT is aligned more vertically on the surface (with θ = 46.8° and α = 46.1°) than BPA (θ = 54.1° and α = 46.6°). The angles obtained in this study are comparable to those calculated for BPAs on

ZnO (α = 45-47° in both bi- and tridentate modes).[42] Experimentally, it has been reported that the terphenylbiphosphonic acid monolayer is aligned on the ITO substrate with α ranging between 45-60° from NEXAFS and PM-IRRAS measurements[43] while the phenyl PAs tend to be more inclined parallel to the surface (α = 70-80°).[40,44]

5.3.2.2 Monolayer packing structure derived from ab initio MD

Although DFT provides reasonable binding geometries for SAM/Fe(001) systems, the above calculations do not take into account the dynamical behaviors of the SAMs at finite temperature, where bond vibrations and rotations of individual SAM moieties can perturb the coherent packing structure of the SAM. Thus, *ab initio* MD has been employed to investigate the dynamics of the monolayer packing structure.

Figure 5.10 presents the variations in the molecular structure of BPA adsorbed on Fe(001) in a tridentate binding mode. In Figure 5.10a, the local geometry is analyzed in terms of φ, the rotation angle of the molecular axis of a benzyl ring with respect to the lattice vector $\vec{a}$ taken as a reference, as depicted on the right-hand side of the figure. Since the initial geometry is made of a supercell of the BPA/Fe(001) optimized in DFT calculations, the molecular axes of the benzyl rings are perfectly aligned in the beginning. Starting from the same rotation angle of the molecular axis, φ ~ 250°, each moiety slowly changes the benzyl ring orientations. At t = 3 ps, the rotational angles between the two adjacent moieties (Δφ) reach 90°, implying the formation of edge-to-face configurations (herringbone-like) in two-dimensional layers.

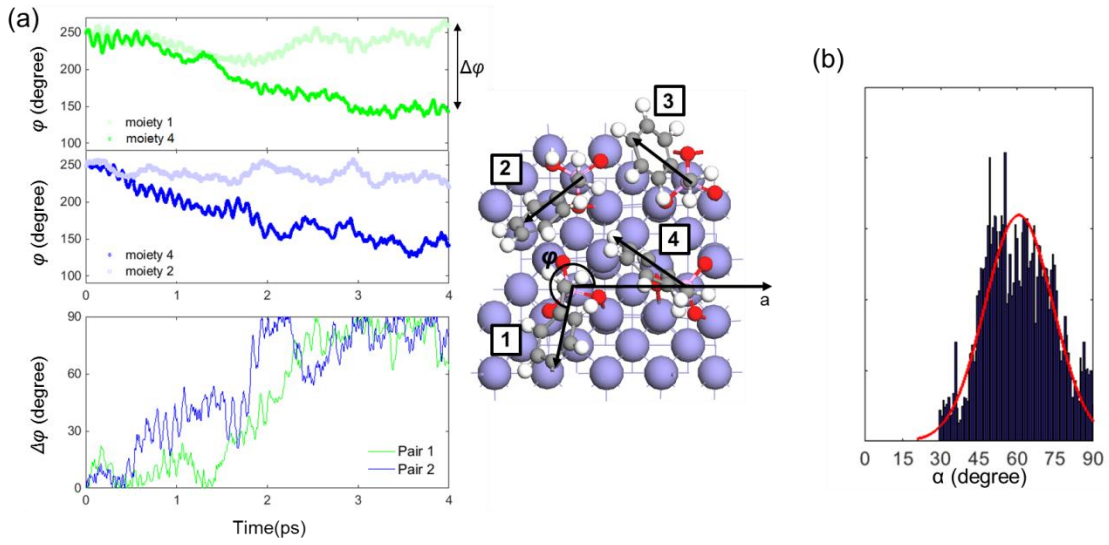

Figure 5.10 (a) Variation of φ as a function of simulation time, where φ is defined as the rotation angle of the molecular axis of a benzyl ring with respect to the lattice vector $\vec{a}$ taken as a reference. The benzyl of each BPA molecule is labeled. Two BPA benzyls are paired: Pair 1 (green line) consists of moiety 1 and 4 while benzyl 2 and 3 belong to Pair 2 (blue line). The differences in rotation angles for the benzyls in the same pair (Δφ) are given. (b) The angels (α) between the ring plane normal and the surface normal of BPAs are sampled in the MD trajectory for the last 1 ps and plotted in a distribution function (with a Gaussian fit as the red line).

The ordered packing structure of the BPA monolayer becomes more evident in Figure 5.11a, where we took the MD geometry at t = 3 ps, T= 300 K and fully optimized it at 0 K within the PBE+D3 level. Here, the rigid aryl spacer leads to an aligned packing structure on Fe(001), with an edge-to-face structure in one direction and a parallel-displaced structure in the other direction, which is similar to the herringbone structure in the (010) face of the benzene crystal (space group *Pbca*). Deviation from the perfectly aligned π-stacked morphology to the T-shaped structure can minimize electrostatic

repulsion and maximize electrostatic attraction of the quadrupoles of the benzyl rings within a monolayer, as reported for oligoacene molecular crystals.[45] On the other hand, the OPA monolayer has an amorphous-like structure (see Figure 5.11b); the alkyl chains get folded intramolecularly (see Figure 5.11b), possible due to low torsional and dihedral-angle potentials in aliphatic hydrocarbons, on the order of a few tenths of meV.[46]

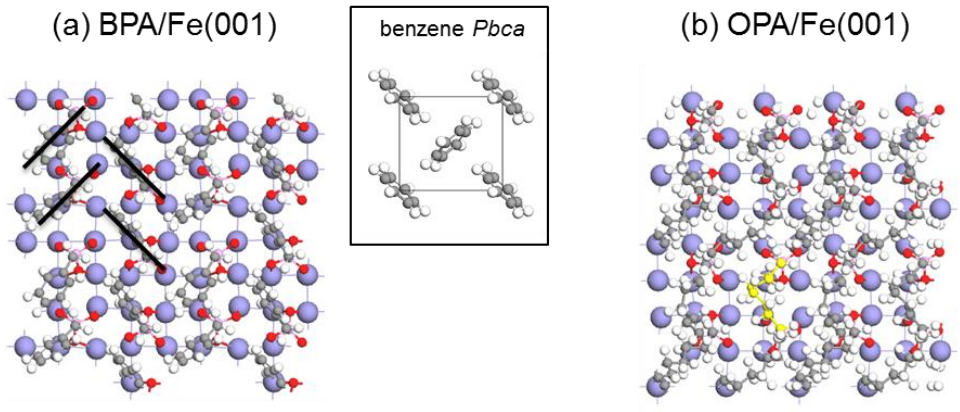

Figure 5.11 (a) BPA and (b) OPA geometries on Fe(001) taken at t = 3 ps, T = 300 k of *ab initio* MD runs and then fully relaxed at 0 K within the PBE+D3 level. The black lines (a) indicate the ring planes of BPA while one moiety of the alkyl spacer of OPA is highlighted in yellow in (b). The inset image shows (010) face of a benzene crystal (space group *Pbca*).

In the same manner, BT on Fe(001) and BPA on fully hydroxylated Fe(001), *i.e.*, BPA/Fe(001)-$(OH)_4$ are thermally equilibrated in *ab initio* MD runs. Each molecule is found to be adsorbed on the surface in a monodentate and bidentate mode, respectively.

For BT/Fe(001), $\Delta\varphi$ becomes nearly 90° within 1 ps, which is much faster than for BPA/Fe(001). However, there is a significant drop at t ~ 3 ps; Pair 2 soon recovers $\Delta\varphi$ ~

90° while the Δφ of Pair 1 starts to oscillate (see Figure 5.12a). Another geometry parameter of BT/Fe(001) that shows a noticeable difference from BPA/Fe(001) is the distribution of the angles between the ring plane normal and the surface normal (α) in the last 1 ps. While the distribution function of α in BPA/Fe(001) has a Gaussian shape (Figure 5.10b), there are two separate peaks predicted for BT/Fe(001); one of the peaks considerably deviates from the initial α values (46.1°) to much lower values < 20°, see Figure 5.12b. Since a low α indicates that the ring plane lies parallel to the substrate surface, we can expect substantial geometric distortions of BT in the course of the MD simulations. In fact, one of the BT molecules gets adsorbed on the surface through the benzyl ring plane, which is followed by bond dissociation between S and the carbon linker of the benzyl spacer. As we have seen in Section 5.3.2.1, BT prefers to lie down on the iron surface at low surface coverage. Although the simulated BT/Fe(001) interface has a high packing density of 3.12×10^{14} molecules/cm^2 here, the occasional exposure of the substrate in the MD simulations leads to Fe 3*d* orbitals being hybridized with the π orbitals of BT, which eventually destroys the monolayer packing structure.

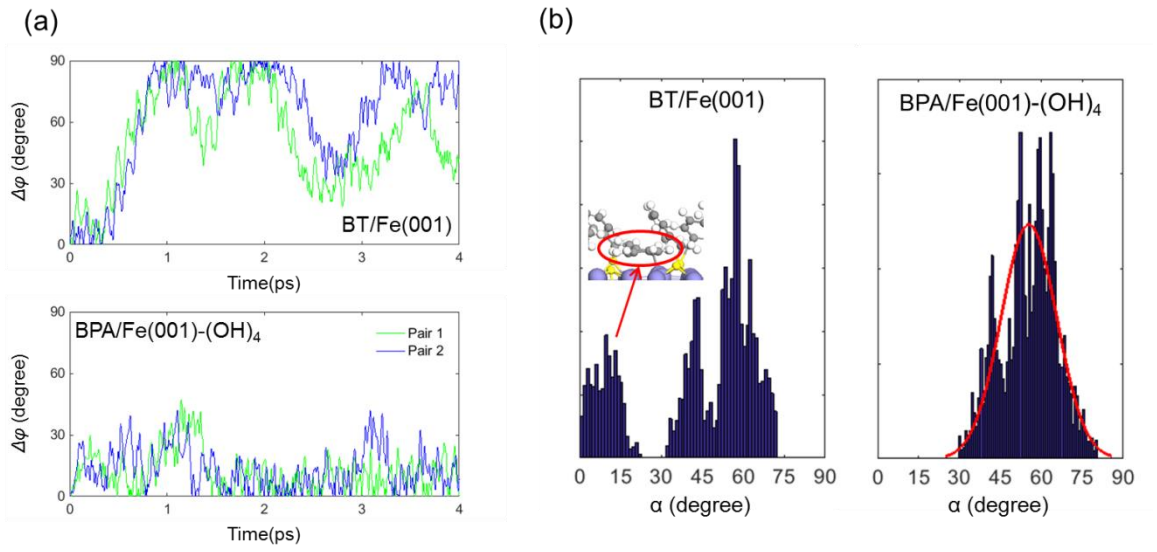

Figure 5.12 (a) Difference in the rotation angles of the molecular axes (Δφ) between the two neighboring benzyl rings in the same pair (Δφ) as a function of simulation time. (b) Angles between and the ring plane normal and surface normal (α) of BTs (BPAs), sampled in the MD trajectory for the last 1ps and plotted in a distribution function (with a Gaussian fit as the red line).

BPA on fully hydroxylated Fe(001) presents a Gaussian distribution of angles α with a peak at 55.7°, which is slightly smaller than the one for BPA/Fe(001) in a tridentate mode, 61.1°. The statistically derived α values for BPA/Fe(001) in the MD simulations are somewhat larger than the value from the static DFT calculation: 44.9° and 46.6° for a tridentate and a bidentate mode, respectively. The major difference between BPA on a fully hydroxylated surface and on a partially hydroxylated surface is that the edge-to-face structure is not observed. This can be ascribed to the presence of surface hydroxyls that may hinder the rotational motion of the benzyl rings.

5.3.2.3 O_2 diffusion kinetics

We now turn to a study of the O_2 diffusion kinetics into PA/Fe(001) with two different spacer groups on the PA, using *ab initio* MD simulations. First, we confirmed that O_2 molecules can rapidly dissociate within 1 ps on bare Fe(001). Since the iron oxidation is a highly exergonic process, the time required for O_2 dissociation is attributed to the molecular diffusion to the metal surface. For the simulations, we passivated both sides of the slab with SAMs in order to evaluate the inhibition efficiency of PA-based monolayers.

In the initial stage of oxygen exposure to the OPA monolayer, the oxygen (gas) molecules initially stay away from OPA but soon begin to penetrate into the monolayer within 1 ps, as shown in the upper panel of Figure 5.13a. As exposure time increases, the vertical penetration depth of O_2 into the SAM reaches ~ 5 Å, which corresponds to the length of 2-3 C-C bonds in an aliphatic alkyl chain. In the 2-D probability distribution of atomic positions in the octyl chains (blue) and O_2 molecules (red) taken from the entire MD runs, there is an overlapped area between blue and red, which indicates that O_2 molecules get inside of the OPA monolayer. In fact, it has been reported that there was no (or only negligible) effect of the adsorption layer on the cathodic part of the polarization curves for the alkyl PA-deposited Fe, suggesting that the protective layer is easily permeable to diffusion of oxygen.[47]

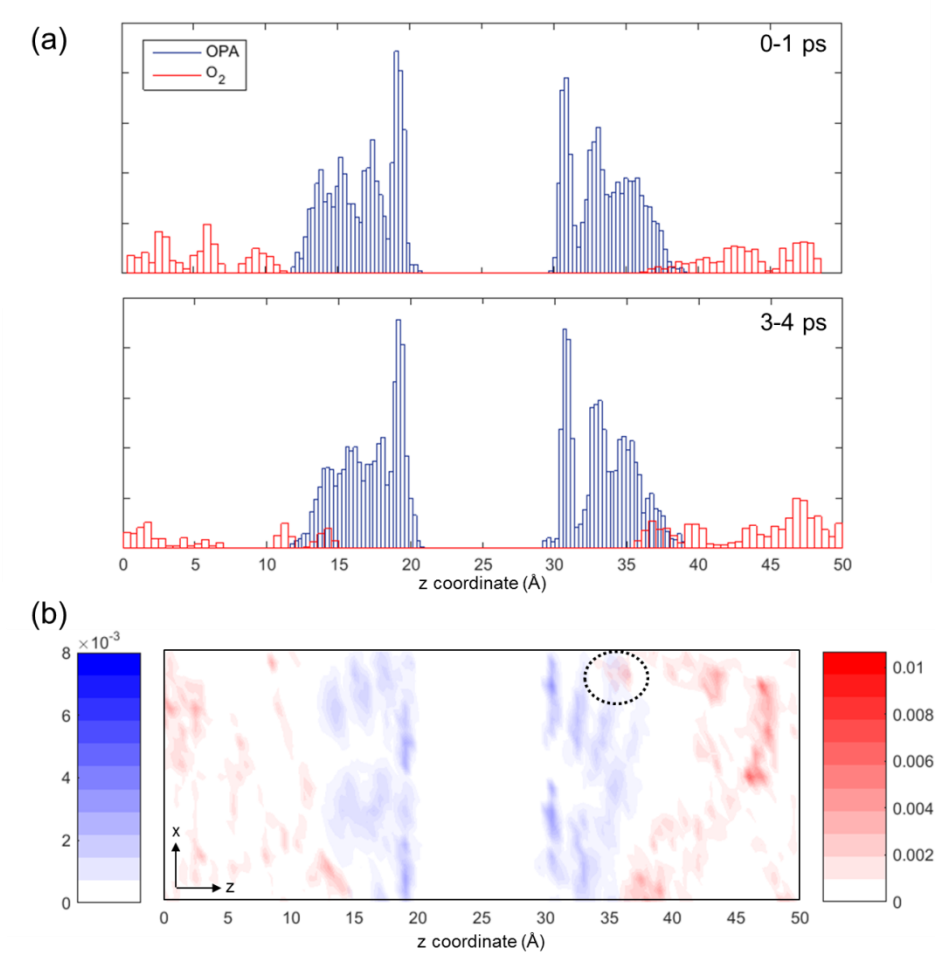

Figure 5.13 (a) Atomic positions of the octyl chains (blue) and O_2 molecules (red) sampled from OPA/Fe(001) in O_2 exposure during the time interval of 0-1 ps (upper panel) and 3-4 ps (bottom panel). The z coordinate corresponds to the surface normal direction. The empty space in z coordinate represents the Fe-phosphonate region. (b) 2-D probability distribution of the atomic positions of the octyl chains (blue) and O_2 molecules (red) averaged over 4 ps. The dotted circled region indicates the overlap between blue and red area.

In contrast, oxygen molecules are less likely to diffuse into the monolayer in the presence of a BPA-based SAM, see Figure 5.14. The vertical penetration depth of O_2 into SAM

during 3-4 ps is ~ 2 Å, with a lower probability than the one predicted for OPA/Fe(001). This can be explained by the high electrostatic energy barrier originating from the π-electron cloud in aromatic rings. As Figure 5.14b indicates, most of the oxygen gas comes near the SAM at the void sites formed in the monolayer, yet, there is no permeated region observed in the course of the simulation time we considered in this study (the MD simulation of BPA/Fe(001) has been run up to 6.5 ps). During the O_2 diffusion, the BPA packing structure tends to be distorted to accommodate the oxygen gas molecule inside the monolayer. Here, benzyl rings are slightly tilted to provide a room for oxygen to reside near BPA; however, the more rigid benzyl group requires more energy for the geometric distortions with respect to the flexible alkyl chains in OPA.

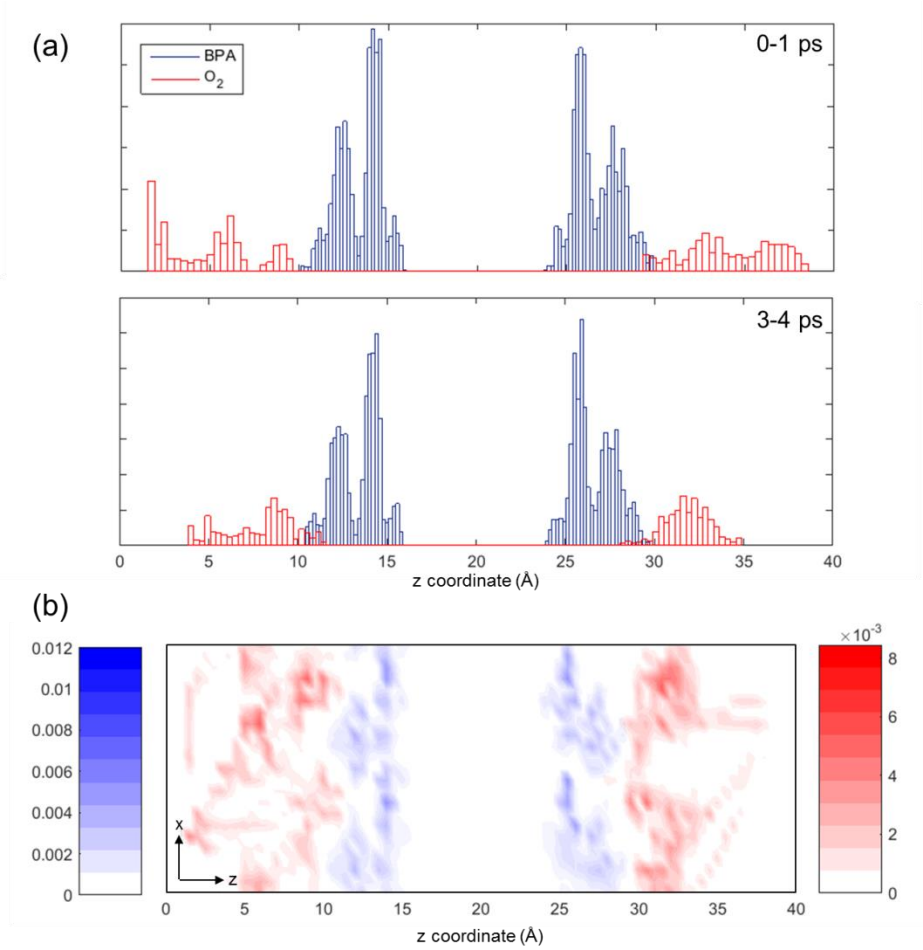

Figure 5.14 (a) Atomic positions of the benzyl rings (blue) and O_2 molecules (red) sampled from BPA/Fe(001) in O_2 exposure during the time interval of 0-1 ps (upper panel) and 3-4 ps (bottom panel). The z coordinate corresponds to the surface normal direction. The empty space in z coordinate represents the Fe-phosphate region. (b) The 2-D probability distribution of atomic positions of the benzyl rings (blue) and O_2 molecules (red) averaged over 4 ps.

5.3.3 Fluorination of terminal groups

5.3.3.1 Hydrophobicity

In the design of more efficient SAMs for corrosion prevention, the inhibition efficiency can be further enhanced by the use of molecular functionalization. In particular, fluorination on terminal/spacer group of the SAMs has been demonstrated to increase a hydrophobicity of the protective film. For example, perfluorooctyltriethoxysilane on TiO_2/Ti substrate[48] and partially fluorinated n-alkyanethiol SAMs on Au[21] show strong hydrophobic nature, prohibiting K^+, HPO_4^{2-}, H_2PO^{4-} ions, and water penetration into the SAM.

In order to obtain insight into the non-covalent interactions at play between the terminal groups of SAMs and water molecules, which is beyond the scope of conventional DFT, SAPT2+-based energy decomposition analyses have been carried out. These analyses provide understanding of the interplay among the stabilizing electrostatic, dispersion, and induction interactions and the destabilizing interactions due to electron exchange. Figure 5.15 shows the relative energetics obtained as a function of intermolecular distance between H_2O and the terminal group of PA molecules: (i) BPA; (ii) *p*CH_3BPA (4-CH_3BPA); and (iii) *p*CF_3BPA(4-CF_3BPA). Based on SAPT2+, the presence of a methyl side group at the *para* position can enhance the energy barrier against H_2O coming into proximity of *p*CH_3BPA, by ~ 1 eV compared to the parent BPA at d = 2.5 Å. Fluorination on BPA with *para*-substituted trifluoromethyl can lead to much stronger repulsion against H_2O; a water molecule has to overcome an energy barrier even at a distance of 4

Å. Considering that the longest intermolecular distance among PA molecules ranges between 7.7 - 8.0 Å at $\Gamma = 3.12\times10^{14}$ molecules/cm^2, fluorination can offer a substantial activation energy barrier for H_2O to pass through the monolayer. This suggests that fluorinated terminal groups can provide an effective hydrophobic surface, which is line with the experimental findings that a low water wettability is measured for tail groups, in the order: $CF_3 < CF_2H < CF_2 < CH_3 < CH_2$.[21]

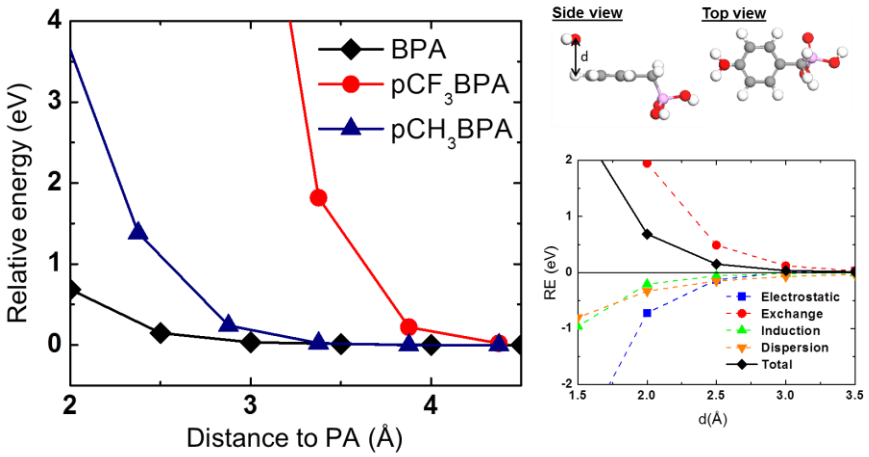

Figure 5.15 Relative energetics obtained as a function of intermolecular distance between H_2O and the terminal group of three PA molecules: BPA (black), *p*CF_3BPA(red), and *p*CH_3BPA (blue) based on SAPT2+ calculations. The energy when two molecules are separated by 5 Å is taken as a reference. The bottom-right inset image shows the interaction energy decomposition for the H_2O-BPA system.

5.3.3.2 Work function modification

Another major advantage expected from fluorinated SAMs is the effective suppression of charge transfer between the metal surface and electrolytes when the SAM acts as an electroactive layer between substrate and solution. It has been reported that the SAM can play the role of a tunneling barrier to electron transfer to a redox species in an aqueous solution, for instance, an alkanethiol on the iron electrode [39] or alkyl-coated silicon electrode.[49]

Here, we have investigated the five fluorinated aromatic PAs illustrated in Section 5.1.3. As shown in Table 5.4, the reaction energies for molecular adsorption are very similar for the fluorinated PAs, except for the ortho-substituted (2,6-F_2BPA), where adsorption is slightly less favorable than for the others, due to its steric hindrance near the surface. Also, fluorination of the aromatic ring leads to minimal changes to geometries; for instance, for the fluorinated PAs, the angle between the ring plane normal and the surface normal (α) range from 43.4° to 47.0° in the tridentate configuration (vs. 44.9° for unsubstituted BPA). On the other hand, the work function modification can vary from -1 eV to + 1 eV; the highest change is predicted for 4-CF_3BPA at ~ +1.4 eV. As mentioned above, electron transfer from the metal surface to redox molecules can occur through the SAM acting as a tunneling barrier. In this case, the interfacial electric field gradient built across the monolayer can alter the electron transfer process. A modified surface with a high work function would necessitate a high overpotential to achieve the same current density compared to the ones with a low work function, a feature advantageous to prevent interfacial electron transfer.

Table 5.5 Reaction energy of adsorption, angle between the ring plane normal and the surface normal, and work function for fluorinated BPA/Fe(001) interfaces in a tridentate mode at a coverage of $\Gamma=3.12\times10^{14}$ molecules/cm^2.

	ΔG_{ad} (eV)	α (°)	Φ (eV)
2,6-F_2BPA	-2.22	46.9	3.16
4-FBPA	-2.29	43.4	4.47
PFBPA	-2.23	47.0	4.64
3,4,5,-F_3BPA	-2.33	45.1	5.09
4-CF_3BPA	-2.36	45.1	5.22

Figure 5.16 shows the changes in work function evaluated at the DFT level as a function of the dipole moment of the modifiers along the surface normal direction. Clearly, the degree and position of fluorination of the PA modifiers affect the overall molecular dipole moment, and hence the work function. Thus, the surface work functions can be easily varied with PA modifiers by simple tuning of the functional groups bonded to the phosphonate groups, without destabilizing the surface. Similar trends have been observed for other substrates, such as ZnO[42] and ITO.[50]

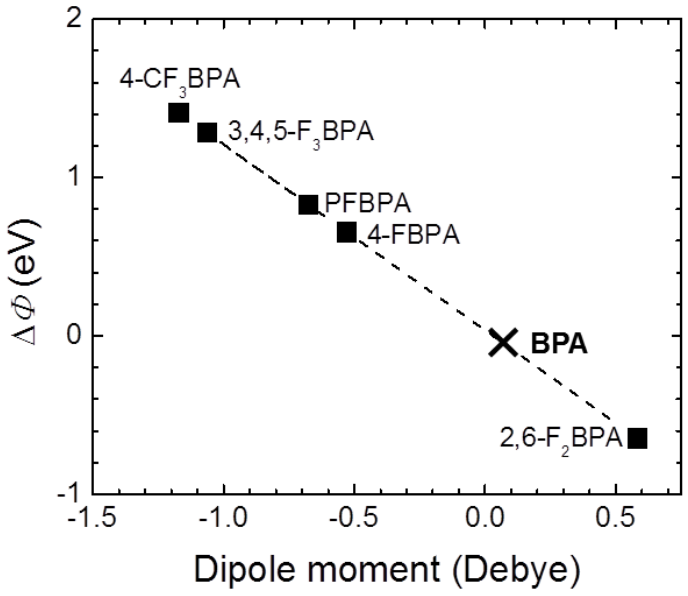

Figure 5.16 Variations in work function evaluated in DFT-PBE calculations, as a function of the component of molecular dipole moment projected along the surface normal direction.

5.3.3.3 Physical barriers against O_2 diffusion

Thus, fluorination of the terminal groups in SAMs can lead to the formation of a strong electrostatic barrier against oxygen molecules and corrosive anions such as Cl^- and SO_4^{2-}, due to the high electronegativity of the fluorine atoms. In order to understand the impact of fluorination on the prevention of O_2 diffusion, we first calculated the potential energy profile for the molecular oxygen permeating into parent and fluorinated PAs (Figure 5.17). For OPA/Fe(001), there is no energy barrier to the oxygen diffusion inside the alkyl chain layer until oxygen comes near the $PO(OH)_2$ moiety, when strong repulsion prohibits the oxygen molecules to move forward. In contrast, oxygen no longer penetrates

the SAM spontaneously in the presence of a BPA layer; the diffusion has to overcome an energy barrier of 0.20 eV. The energetic profiles for oxygen penetration are in line with the results of the *ab initio* MD simulations presented in Section 5.3.2.3. Interestingly, fluorinations of BPA and OPA lead to stronger repulsion against an oxygen molecule approaching their neighbor. Thus, the barrier for diffusion into the SAM is much higher with fluorination, which leads to slower corrosion kinetics. For example, based on the Arrhenius equation, an increase in activation energy from 0.20 eV to 0.38 eV corresponds to a reduction in the diffusion rate by three orders of magnitude.

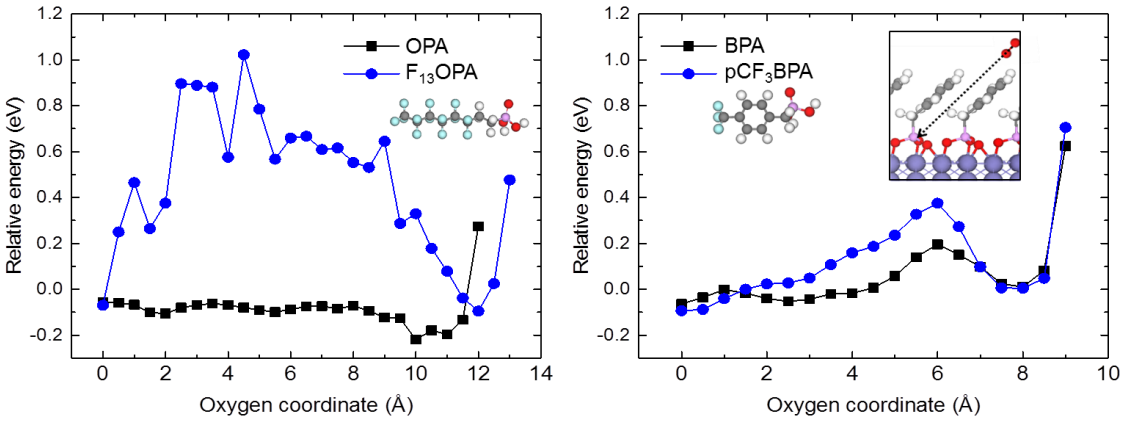

Figure 5.17 Energetic profiles for O_2 penetration into OPA and F_{13}OPA monolayers (left); and BPA and *p*CF_3BPA monolayers (right). The initial position of O_2 is 3 Å above the terminal groups of the SAMs, as shown in the inset. Parent PAs are denoted with black squares and fluorinated PAs, with blue circles.

Ab initio MD simulations of the *p*CF_3-BPA monolayer exposed to O_2 further confirm the efficacy of fluorination against oxygen diffusion. As shown in Figure 5.18, the monolayer remains completely undamaged even after 4 ps, and the oxygen trajectory suggests that O_2 molecules tend to be repelled from the terminal CF_3 group even near the vacant areas between benzyl rings. Thus, the surface protection by a *p*CF_3BPA monolayer is predicted to be superior to an OPA or BPA-based SAM that allows O_2 to diffuse inside the monolayer.

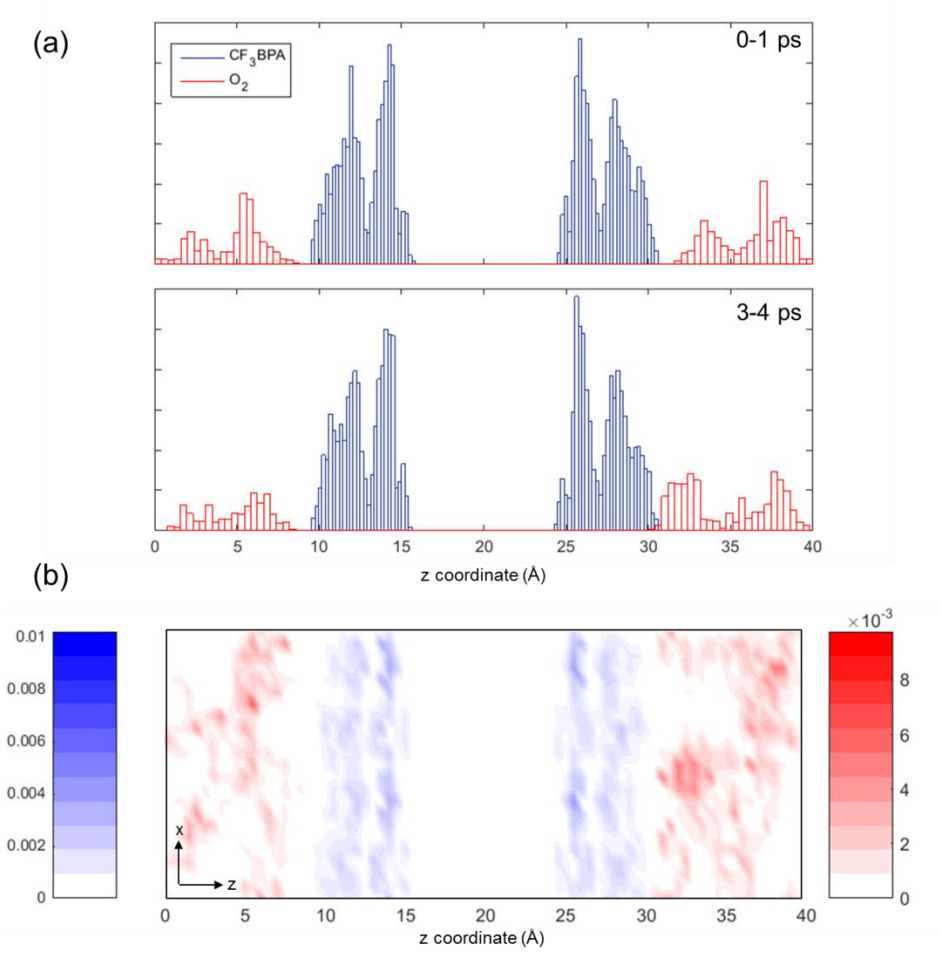

Figure 5.18 (a) Atomic positions of the *p*CF_3BPA monolayer (blue) and O_2 molecules (red) sampled during the time interval of 0-1 ps (upper panel) and 3-4 ps (bottom panel). The z coordinate corresponds to the surface normal direction. The empty space in z coordinate represents the Fe-phosphonate region. (b) The 2D probability distribution of atomic positions of the *p*CF_3BPA (blue) and O_2 molecules (red) averaged over 4 ps.

One noticeable effect of fluorination on the aliphatic chain is that it can decrease the morphological disorder of the monolayer. Figure 5.19 shows the final structure of OPA/Fe(001) F_{13}OPA/Fe(001) after 3 ps equilibration at 300K in *ab initio* MD simulations. Compared to distorted OPA chains, the F_{13}OPA molecules maintain their aligned geometry as in the initial monolayer structure. Indeed, the variation of the molecular tilt-away angles (θ) in the PA monolayer with respect to the surface normal vector is much more significant for OPA/Fe(001): θ changes progressively from 23 ° to 45° for OPA while θ only varies on average within 22-24° for F_{13}OPA moieties (black line). This can be attributed to the increase in C-C torsional potentials upon fluorination of the alkyl chain. Our MD results are consistent with earlier experiments in OPA and F_{13}OPA on ITO where the tilt angles estimated from PM-IRRAS data demonstrate that the OPA molecules are lying flatter (larger θ ~ 57°), and F_{13}OPA molecules are standing up more vertically (smaller θ ~ 26°). [40] Compared to the static DFT calculations that predict nearly the same θ for OPA and F_{13}OPA, the geometries derived from *ab initio* MD present a much better agreement with the experimental data.

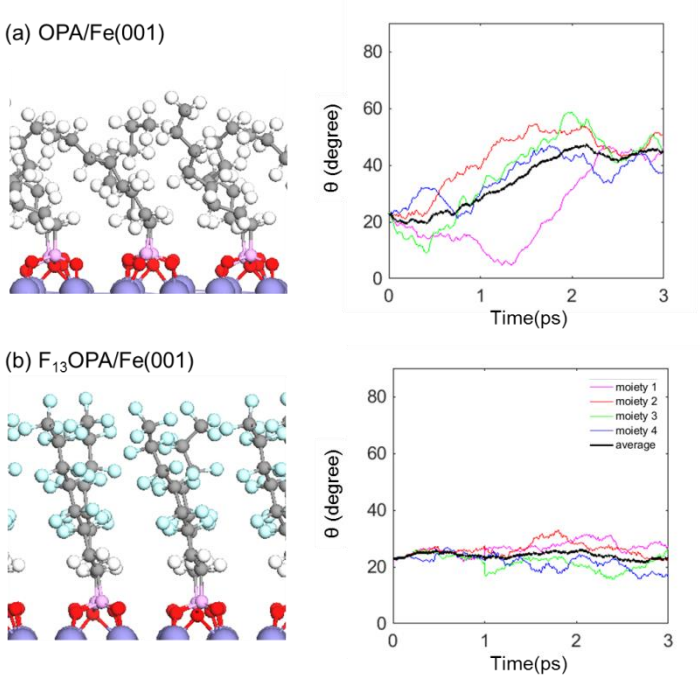

Figure 5.19 Final structure of (a) OPA/Fe(001) and (b) F_{13}OPA/Fe(001) after 3 ps equilibration at 300 K. Variation of the molecular tilt-away angles (θ) in the PA monolayer with respect to the surface normal vector as time evolves. The black solid line represents the average θ of the four PA moieties in a unit cell.

5.4 Enhancement with substrate pretreatment

Corrosion can progress in the near-surface region in parallel with the adsorption of the inhibitor molecules during the deposition, for instance, of water-soluble phosphonic acids on metal surfaces like iron, aluminum, or zinc. This prevents the formation of a densely-packed protective layer. In this regard, oxidation of the metal surface before the deposition of the organic layer can enhance the stability of the organic film. In case of iron, strong bonds can be formed between ferric/ferrous ions on the surface and oxygen atoms in PAs. A higher charge transfer resistance has been reported when OPAs are

deposited on native iron (covered with air-formed oxide)[47] or potentiostatically passivated[51] surfaces, compared to metallic iron surfaces. The authors attributed the improved blocking effect of OPAs towards metal dissolution, to the formation of more compact phosphonate layer structure on the passivated oxide film which is approximately 3 nm thick.[52]

5.4.1 PA/α-Fe_2O_3(1-102)

Although the morphology of the iron oxide surface can be determined by the passivation conditions, here, we start by considering the Fe, O-mixed surface of α-Fe_2O_3(1-102) containing surface hydroxylation. To determine the most stable surface configurations in electrochemical conditions, we have constructed the Pourbaix diagram for various bulk-truncated surfaces with different levels of hydroxylation, see Figure 5.20a. Over a wide range of (pH, U) values, O_2H_2-$(OH)_2$, where two surface-exposed Fe atoms are covered by terminal hydroxyls, $(OH)_2$, as well as two (subsurface) lattice oxygen atoms are hydroxylated, O_2H_2, become the most favorable surface phase. Therefore, we regard this hydroxylated surface as the initial substrate onto which phosphonic acids are deposited. The coverage density is assumed to be 3.6×10^{14} molecules/cm^2, which is consistent with the estimated alkyl PA coverage on passivated iron, 3×10^{14} molecules/cm^2.[52] Figure 5.20b proposes the mechanism for BPA attachment on α-Fe_2O_3(1-102); the final binding modes of the chemisorbed phosphonates can be either monodentate or bidentate, with additional hydrogen bonding of the phosphoryl oxygen of PA with surface hydroxyl groups. Both binding modes are found to be thermodynamically favored in DFT

calculations. Given that the bidentate configuration is more stable than the monodentate case by 1.10 eV, the surface is expected to be dominated by BPA in a bidentate mode in the final structure of the monolayer.

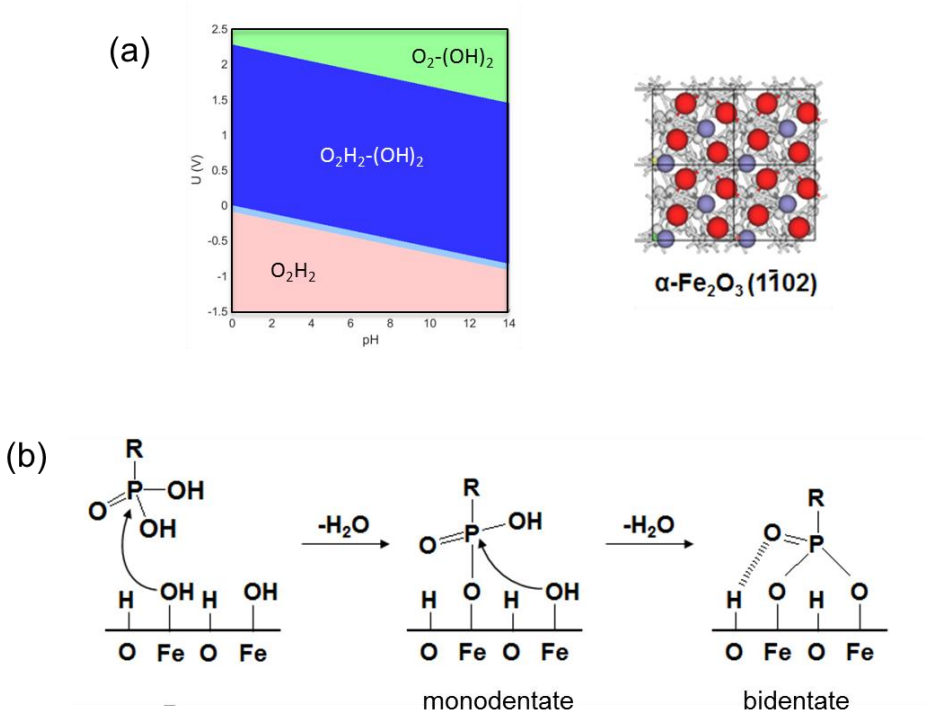

Figure 5.20 (a) PBE-derived Pourbaix diagram of α-Fe_2O_3(1-102). (b) Possible mechanisms of phosphonic acid attachment on α-Fe_2O_3(1-102). The exposed surface Fe, and O atoms of α-Fe_2O_3(1-102) are colored in blue and red, respectively.

Table 5.6 indicates that the calculated reaction energies of PAs adsorbed on hematite tend to be comparable to the ones obtained for hydroxylated Fe(001). However, the interface Fe-O bonds are much shorter: 1.89-1.95 Å on hematite vs. 2.11-2.15 Å on Fe(001) in a bidentate configuration. Therefore, the strong covalent bonds of BPAs with the oxide surface can provide more robust monolayer formation with higher chemical stability. This is consistent with experimental observations that phosphonates on stainless steel can decrease the passive current density more effectively over a longer period of time than on carbon-steel samples.[53] OPAs on the oxide surface are more likely to stand upright for the monodentate configuration in a fashion similar to BPAs on the iron surface. However, the variations in molecular tilting as a function of binding modes depend on the types of PAs: they are much more significant for OPA (~22°) than BPA (~5°).

It should be noted that the molecular tilt angle determines the intermolecular spacings within the monolayer. For example, the interchain distances of the optimized F_{13}OPA monolayer increase from 4.89-5.03 Å for θ = 28.1° (bidentate) to 5.07-5.47 Å for θ = 13.1° (monodentate). On a hematite surface, the monodentate configuration of F_{13}OPA is energetically more stable than the other PAs; thus, this binding mode is expected to appear on the oxide surface more frequently. The occurrence of this upright standing feature inside the monolayer possibly leads to a more open structure, more susceptible to the diffusion of the environmental molecules even with functionalized chains. The molecules in the *p*CF_3BPA monolayer, on the other hand, become more closely packed in one direction at a higher tilt angle (from 6.45 Å to 6.03 Å) due to the anisotropic shape of the benzyl ring, which provides less permeable barriers to electrochemically corrosive ions.

Table 5.6 Reaction energy of adsorption, tilt-away angle from the surface normal vector, and work function variation for PA/α-Fe_2O_3(1-102) systems in two different binding modes.

	ΔG_{ad} (eV)		θ (°)		$\Delta\Phi$ (eV)	
	bi	mono	bi	mono	bi	mono
BPA	-2.34	-1.24	43.7	38.3	-0.23	-0.08
pCF_3BPA	-2.42	-1.44	40.2	35.7	1.51	1.69
OPA	-2.48	-1.37	38.8	14.1	-0.77	0.16
F_{13}OPA	-2.53	-1.53	28.1	13.6	1.33	2.22

5.4.2 PA/γ-Fe_2O_3(001)

Another oxide surface we considered is maghemite (γ-Fe_2O_3). Maghemite has a spinel structure often written as $[Fe^{3+}]_A[Fe^{3+}_{5/3},V_{Fe,1/3}]_BO_4$ where the tetrahedral sites are denoted as A and the octahedral sites, as B. These octahedral sites contain a number of cationic vacancies, V_{Fe}. Therefore, maghemite can be viewed as magnetite with cationic vacancies in one sixth of the octahedral interstitial sites. This corresponds to the passive oxide film formed on iron upon electrochemical treatment.[54] Here, we focus our discussion on the (001) surface, which has a plane commensurate with Fe(001).

For OPA, bidentate adsorption is slightly more favorable than monodentate binding on fully hydroxylated γ-Fe_2O_3(001). The adsorption reaction energy of the monodentate mode is comparable to the one obtained for OPA on α-Fe_2O_3(1-102), while the bidentate configuration is less favored energetically on γ-Fe_2O_3(001) than α-Fe_2O_3(1-102). This is possibly due to the proximity of the phosphoryl oxygens of the OPAs to the lattice

oxygens of the maghemite surface. Since the molecules tilt more toward the surface with two chemical bonds formed between OPA and the oxide surface, the adsorption energy difference of OPA on γ-Fe_2O_3(001) from α-Fe_2O_3(1-102) is more prominent for the bidentate case. As discussed earlier, one of the important parameters to ensure a strong interfacial interaction is the bond distance between the surface Fe atoms and the PA oxygen atoms. On the maghemite surface, it is in the range of 1.84-1.87 Å, similar to 1.89-1.95 Å on hematite, which demonstrates that surface oxidation prior to PA deposition on iron is beneficial to the stability of the SAM-substrate interface.

Interestingly, the BPA adsorption energy is very high (-3.04 eV) compared to OPA (-1.67 eV) in the same binding configuration and surface coverage. Figure 5.21a illustrates the optimized BPA/γ-Fe_2O_3(001): the ring plane becomes vertically aligned on the oxide surface while one hydrogen atom in a benzyl ring is adjacent to the oxygen atom exposed on the surface. The electrostatic interactions between the surface anion and the positively polarized edge of a benzene ring help further stabilize BPA on γ-Fe_2O_3(001). Upon the increase in BPA coverage density, the molecules become more aligned with a much smaller tilt-away angle, which can be also seen from Figure 5.21b. The increase in the adsorption energy by 1.15 eV implies that the γ-Fe_2O_3(001) surface prefers to have a densely packed BPA monolayer. However, the coverage density does not significantly affect the interface chemical bonds; the Fe-O bond distances barely change under high-coverage conditions.

Table 5.7 Reaction energy of adsorption, tilt-away angle, the angle between the ring plane normal and the surface normal, and work function for PA/γ-Fe_2O_3(001) systems at Γ= 1.42×10^{14} molecules/cm^2 and Γ= 2.84×10^{14} molecules/cm^2 (high coverage).

	binding mode	ΔG_{ad} (eV)	θ (°)	α (°)	d(Fe-O) (Å)	Φ (eV)
OPA	monodentate	-1.51	26.8	-	2.06	5.74
	bidentate	-1.67	35.1	-	1.84, 1.87	6.31
BPA	bidentate	-3.04	72.4	79.6	1.94, 2.03	5.93
	bidentate (high coverage)	-4.19 (/2mol.)	33.8	63.5	1.95, 1.98 1.94,2.03	5.30

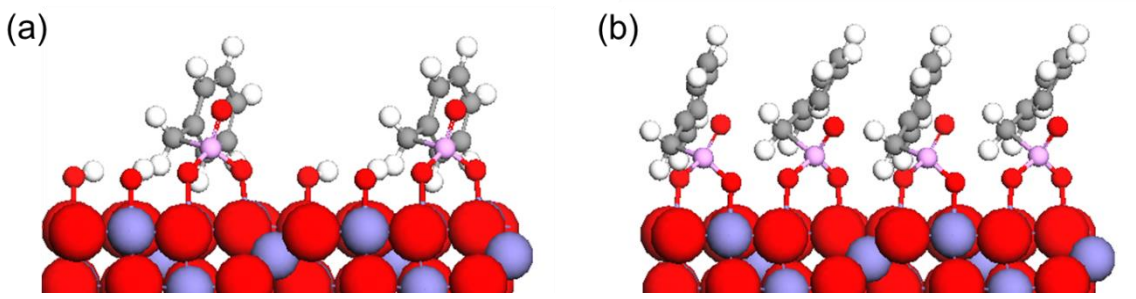

Figure 5.21 Optimized geometries of BPA/γ-Fe_2O_3(001) systems at (a) Γ= 1.42×10^{14} molecules/cm^2 and (b) Γ= 2.84×10^{14} molecules/cm^2.

5.5 Conclusions

In this Chapter, the geometric and electronic structures of iron with the interfaces of self-assembled monolayers (SAMs) have been evaluated with respect to adsorption reaction energies, packing morphologies, and modifications of the metal surface electronic structure *via* quantum-mechanical calculations and molecular dynamics (MD) simulations.

The major findings based on the DFT, SAPT2+, and *ab initio* MD results can be summarized as:

- Binding group: Among thiols, carboxylic acids, and phosphonic acids, the phosphonic acids are predicted to strongly bind to the hydroxylated Fe(001) surface in either bidentate or tridentate fashion via heterocondensation.
- Spacer: The benzyl spacer can lead to a more highly aligned monolayer than the octyl spacer, with the latter exhibiting an amorphous-like morphology in the room-temperature MD simulations. Benzyl rings can lead to a herringbone-type packing structure; however such a crystalline packing depends on the type of binding groups and substrate hydroxylation conditions.
- Fluorination of alkyl (or aryl) phosphonic acids can enhance the inhibition efficiency as it can increase the surface hydrophobicity and significantly slow down the diffusion processes of O_2 into the SAMs, compared to PAs terminated with -CH_3. Electronic-structure calculations further indicate that fluorination of the terminal group of the PA-based SAMs can shift the substrate work function

upward and reduced possible charge transfers between the metal surface and electrolytes in solution.

- PA adsorption on hydroxylated α-Fe_2O_3 and γ-Fe_2O_3 surfaces lead to stronger interfacial Fe-O bonds; thus, the oxidative passivation of an iron metal surface prior to the organic layer deposition is predicted to enhance the chemical stability of the PA-based SAM film on the substrate.

Overall, our results underline that the long-term stability of the SAM film can be achieved by: (i) a phosphonic acid-based binding group; (ii) an aryl-type spacer leading to enhanced monolayer crystallinity; (iii) fluorination of SAMs that reduces the molecular diffusion through the organic layer; and (iv) oxidative passivation of an iron metal surface prior to the organic layer deposition.

5.6 References

[1] Gece, G. *Corros. Sci.* **2008**, *50*, 2981.
[2] Obot, I. B.; Macdonald, D. D.; Gasem, Z. M. *Corros. Sci.* **2015**, *99*, 1.
[3] Obi-Egbedi, N. O.; Obot, I. B.; El-Khaiary, M. I. *J. Mol. Struct.* **2011**, *1002*, 86.
[4] Kuznetsov, Y. I. *Organic Inhibitors for Corrosion of Metals*, Springer US: New York, 1996.
[5] Subramanian, R.; Lakshminarayanan, V. *Corros. Sci.* **2002**, *44*, 535.
[6] Liu, X. F.; Huang, S. J.; Gu, H. C. *In.t J. Fatigue* **2002**, *24*, 803.
[7] Zhang, L.; He, Y.; Zhou, Y.; Yang, R.; Yang, Q.; Qing, D.; Niu, Q. *Petroleum* **2015**, *1*, 237.
[8] Volmer, M.; Stratmann, M.; Viefhaus, H. *Surf. Interface Anal.* **1990**, *16*, 278.
[9] Laibinis, P. E.; Whitesides, G. M. *J. Am. Chem. Soc.* **1992**, *114*, 9022.
[10] Yamamoto, Y.; Nishihara, H.; Aramaki, K. *J. Electrochem. Soc.* **1993**, *140*, 436.
[11] Raman, A.; Dubey, M.; Gouzman, I.; Gawalt, E. S. *Langmuir* **2006**, *22*, 6469.
[12] Raman, A.; Quinones, R.; Barriger, L.; Eastman, R.; Parsi, A.; Gawalt, E. S. *Langmuir* **2010**, *26*, 1747.
[13] Pujari, S. P.; Scheres, L.; Marcelis, A. T. M.; Zuilhof, H. *Angew. Chem. Int. Edit* **2014**, *53*, 6322.
[14] Ishizaki, T.; Okido, M.; Masuda, Y.; Saito, N.; Sakamoto, M. *Langmuir* **2011**, *27*, 6009.
[15] Guerrero, G.; Alauzun, J. G.; Granier, M.; Laurencin, D.; Mutin, P. H. *Dalton T* **2013**, *42*, 12569.
[16] Paniagua, S. A.; Giordano, A. J.; Smith, O. L.; Barlow, S.; Li, H.; Armstrong, N. R.; Pemberton, J. E.; Bredas, J. L.; Ginger, D.; Marder, S. R. *Chem. Rev.* **2016**, *116*, 7117.
[17] Zamborini, F. P.; Crooks, R. M. *Langmuir* **1998**, *14*, 3279.
[18] Caprioli, F.; Decker, F.; Marrani, A. G.; Beccari, M.; Di Castro, V. *Phys. Chem. Chem. Phys.* **2010**, *12*, 9230.
[19] Tan, Y. S.; Srinivasan, M.; Pehkonen, S. O.; Chooi, S. Y. M. *Corros. Sci.* **2006**, *48*, 840.
[20] Weinstein, R. D.; Moriarty, J.; Cushnie, E.; Colorado, R.; Lee, T. R.; Patel, M.; Alesi, W. R.; Jennings, G. K. *J. Phys. Chem. B* **2003**, *107*, 11626.
[21] Boubour, E.; Lennox, R. B. *Langmuir* **2000**, *16*, 7464.
[22] Felhosi, I.; Telegdi, J.; Palinkas, G.; Kalman, E. *Electrochim. Acta* **2002**, *47*, 2335.
[23] Kosian, M.; Smulders, M. M. J.; Zuilhof, H. *Langmuir* **2016**, *32*, 1047.
[24] Kresse, G.; Furthmuller, J. *Comp. Mater. Sci.* **1996**, *6*, 15.
[25] Kresse, G.; Furthmuller, J. *Phys. Rev. B* **1996**, *54*, 11169.
[26] Perdew, J. P.; Burke, K.; Ernzerhof, M. *Phys. Rev. Lett.* **1997**, *78*, 1396.
[27] Blochl, P. E. *Phys. Rev. B* **1994**, *50*, 17953.
[28] Peterson, A. A.; Abild-Pedersen, F.; Studt, F.; Rossmeisl, J.; Norskov, J. K. *Energ. Environ. Sci.* **2010**, *3*, 1311.
[29] Bajdich, M.; Garcia-Mota, M.; Vojvodic, A.; Norskov, J. K.; Bell, A. T. *J. Am. Chem. Soc.* **2013**, *135*, 13521.

[30] Zeng, Z. H.; Chan, M. K. Y.; Zhao, Z. J.; Kubal, J.; Fan, D. X.; Greeley, J. *J. Phys. Chem. C* **2015**, *119*, 18177.
[31] Anisimov, V. I.; Zaanen, J.; Andersen, O. K. *Phys. Rev. B* **1991**, *44*, 943.
[32] Dudarev, S. L.; Botton, G. A.; Savrasov, S. Y.; Humphreys, C. J.; Sutton, A. P. *Phys. Rev. B* **1998**, *57*, 1505.
[33] Grimme, S.; Antony, J.; Ehrlich, S.; Krieg, H. *J. Chem. Phys.* **2010**, *132*, 154104.
[34] Turney, J. M.; Simmonett, A. C.; Parrish, R. M.; Hohenstein, E. G.; Evangelista, F. A.; Fermann, J. T.; Mintz, B. J.; Burns, L. A.; Wilke, J. J.; Abrams, M. L.; Russ, N. J.; Leininger, M. L.; Janssen, C. L.; Seidl, E. T.; Allen, W. D.; Schaefer, H. F.; King, R. A.; Valeev, E. F.; Sherrill, C. D.; Crawford, T. D. *Wires Comput. Mol. Sci.* **2012**, *2*, 556.
[35] Parker, T. M.; Burns, L. A.; Parrish, R. M.; Ryno, A. G.; Sherrill, C. D. *J. Chem. Phys.* **2014**, *140*.
[36] Nose, S. *J. Chem. Phys.* **1984**, *81*, 511.
[37] Rohwerder, M.; de Weldige, K.; Stratmann, M. *J. Solid State Electr.* **1998**, *2*, 88.
[38] Rohwerder, M.; Stratmann, M. *MRS Bull.* **1999**, *24*, 43.
[39] Malkhandi, S.; Yang, B.; Manohar, A. K.; Prakash, G. K. S.; Narayanan, S. R. *J. Am. Chem. Soc.* **2013**, *135*, 347.
[40] Gliboff, M.; Li, H.; Knesting, K. M.; Giordano, A. J.; Nordlund, D.; Seidler, G. T.; Bredas, J. L.; Marder, S. R.; Ginger, D. S. *Competing Effects of Fluorination on the Orientation of Aromatic and Aliphatic Phosphonic Acid Monolayers on Indium Tin Oxide*, 2013; Vol. 117.
[41] Acton, O.; Dubey, M.; Weidner, T.; O'Malley, K. M.; Kim, T. W.; Ting, G. G.; Hutchins, D.; Baio, J. E.; Lovejoy, T. C.; Gage, A. H.; Castner, D. G.; Ma, H.; Jen, A. K. Y. *Adv. Funct. Mater.* **2011**, *21*, 1476.
[42] Wood, C.; Li, H.; Winget, P.; Bredas, J. L. *J. Phys. Chem. C* **2012**, *116*, 19125.
[43] Stockhause, S.; Neumann, P.; Kant, M.; Schülke, U.; Schrader, S. In *Host-Guest-Systems Based on Nanoporous Crystals*; Wiley-VCH Verlag GmbH & Co. KGaA: 2005, p 197.
[44] Gliboff, M.; Sang, L. Z.; Knesting, K. M.; Schalnat, M. C.; Mudalige, A.; Ratcliff, E. L.; Li, H.; Sigdel, A. K.; Giordano, A. J.; Berry, J. J.; Nordlund, D.; Seidler, G. T.; Bredas, J. L.; Marder, S. R.; Pemberton, J. E.; Ginger, D. S. *Langmuir* **2013**, *29*, 4176.
[45] Williams, J. H. *Accounts Chem. Res.* **1993**, *26*, 593.
[46] Schuler, L. D.; Daura, X.; Van Gunsteren, W. F. *J. Comput. Chem.* **2001**, *22*, 1205.
[47] Felhosi, I.; Kalman, E. *Corros. Sci.* **2005**, *47*, 695.
[48] Zhang, F.; Chen, S. G.; Dong, L. H.; Lei, Y. H.; Liu, T.; Yin, Y. S. *Appl. Surf. Sci.* **2011**, *257*, 2587.
[49] Barrelet, C. J.; Robinson, D. B.; Cheng, J.; Hunt, T. P.; Quate, C. F.; Chidsey, C. E. D. *Langmuir* **2001**, *17*, 3460.
[50] Hotchkiss, P. J.; Li, H.; Paramonov, P. B.; Paniagua, S. A.; Jones, S. C.; Armstrong, N. R.; Bredas, J. L.; Marder, S. R. *Adv. Mater.* **2009**, *21*, 4496.
[51] Paszternak, A.; Stichleutner, S.; Felhosi, I.; Keresztes, Z.; Nagy, F.; Kuzmann, E.; Vertes, A.; Homonnay, Z.; Peto, G.; Kalman, E. *Electrochim. Acta* **2007**, *53*, 337.
[52] Paszternak, A.; Felhosi, I.; Paszti, Z.; Kuzmann, E.; Vertes, A.; Kalman, E.; Nyikos, L. *Electrochim. Acta* **2010**, *55*, 804.

[53] Frank, M. A.; Meltzer, C.; Braunschweig, B.; Peukert, W.; Boccaccini, A. R.; Virtanen, S. *Appl. Surf. Sci.* **2017**, *404*, 326.
[54] Toney, M. F.; Davenport, A. J.; Oblonsky, L. J.; Ryan, M. P.; Vitus, C. M. *Phys. Rev. Lett.* **1997**, *79*, 4282.

CHAPTER 6. ELECTRONIC STRUCTURES OF ORGANIC-INORGANIC INTERFACES FOR SPINTRONICS APPLICATIONS

Hybrid organic/inorganic interfaces are ubiquitous in the realm of organic electronics, from organic solar cells to low-power-consumption organic thin-film transistors. It is well known that the device performance strongly depends on the electronic coupling between organic and inorganic materials across the interface; for instance, the efficiency of the charge injection/collection between a ferromagnetic (FM) electrode and organic molecules in organic spintronics is governed by the energy level alignment between the molecular frontier orbitals in the organic layer and the electronic bands in the FM substrate. In this regard, a fundamental understanding of interface spin chemistry in complex molecule-substrate interaction is a prerequisite to designing molecules and engineering interface spin responses in the development of next-generation functional organic spintronic devices.

In order to rationally tailor the strength of the molecule-surface interactions, we have explored hybrid organic-FM systems by varying the chemical nature of the substrate, π-conjugated organic semiconductor (OSC) molecules, and their interface geometries based

on DFT calculations. The work presented in this Chapter provides a systematic theoretical description of organic-FM interfaces and can help design an organic semiconductor-based spintronic device with optimal functionality.

.

6.1 Introduction

6.1.1 Design rules for an optimal FM/OSC hybrid interface

It is instructive first to underline the key aspects to be considered in the design of FM/OSC hybrid interfaces in order to achieve spin-polarized injection from a FM electrode to a non-magnetic (NM) OSC layer.[1-3]

In any kind of spin-injecting mechanisms *e.g.*, direct tunnelling, Fowler-Nordheim tunneling, or thermionic field emission, it is favorable to minimize the carrier injection barrier, typically defined as the energy difference between the ionization energy (IE) or electron affinity (EA) of a molecule and the Fermi level of the FM electrode, in order to maximize the transport probability. Since OSCs are typically undoped and, therefore, have hardly any free charge carriers in this equilibrium state, the carriers must be injected into the materials from contact electrodes. Given that the energy gaps of π-conjugated materials (either small molecules or polymers) generally range from 1.5 to 3.5 eV, the Schottky energy barrier scales directly with the electrode work function. Thus, low-work function metals are used to inject electrons and high-work function metals are used to inject holes in traditional organic electronic devices. In the past decades, efficient carrier injection/extraction has been achieved by tuning the energy level alignment at interfaces,

for instance, using a self-assembled monolayer,[4] electron acceptor molecules,[5] and polymer surface modifiers.[6]

Compared to organic electronics, another level of complexity should add in the field of organic spintronics, in addition to the favorable energy level alignment: the spin polarization (SP) of interface states. Since ferromagnetic electrode materials have asymmetric density of states (DOS) between spin-up and spin-down electrons, they are spin polarized at the Fermi level (E_F). On the other hand, a pristine non-magnetic OSC has no spin discrimination because it features the same spin-up/-down resistances. When an OSC is put in contact with a FM surface, hybridization between the metal valence *d* electrons and the molecular orbitals (MOs) can occur at the interface, which leads to the formation of so-called hybrid interface states (HISs). These HISs can determine the extent of spin-polarization of the injected current, which can be dramatically different, and even reversed with respect to the polarization of the electrode.[7] As HISs are generally confined at the interface between the first monolayer of OSCs and a few top layers of FM, they serve as spin filters at the hybrid interface. Since HISs have specific electronic structures, the energy level into which the charge carrier is injected (extracted) determines the spin polarization direction of the carriers taken into the bulk OSC layer. Indeed, it has been demonstrated that the dominant spin band for charge carrier injection/extraction can be altered through the introduction of an interfacial polar layer such as LiF[8] or even a switchable ferroelectric thin film.[9] Therefore, it is essential to realize strongly spin-polarized HISs in order to insure that carrier transport into the subsequent molecular layer proceeds in a spin conserving way. Thus, the fundamental understanding of interface hybridized states and energy level alignment at the OSC-FM

interface is vital for controlling the injection or extraction of a specific spin into/from the organic materials.

Lastly, the conductivity mismatch at the OSC-FM junction must be circumvented. Theoretically, the spin polarization of the current density at a non-magnetic semiconductor spacer can be derived as[10]

$$\alpha_2 = \beta \frac{\lambda_{FM}}{\sigma_{FM}} \frac{\sigma_{SC}}{x_0} \frac{2}{\left(2\frac{\sigma_{SC}\lambda_{FM}}{\sigma_{FM}x_0}+1\right)-\beta^2} \tag{6.1}$$

where β represents the spin polarization of a FM electrode; σ, the conductivity; λ, the mean-free path in the metal; and x_0, the NM spacer thickness. The maximum α_2 can be obtained in certain limiting cases, *i.e.*, $x_0 \rightarrow 0$, $\sigma_{SC}/\sigma_{FM} \rightarrow \infty$, or $\lambda_{FM} \rightarrow \infty$, which are far away from a real-world situation. Especially, when σ_{SC}/σ_{FM} is detrimental, it is referred to as the "conductivity mismatch problem". In OSCs, charge transport takes place mostly by hopping of injected carriers among localized states, which generally implies low mobility and uncertainty in carrier density. Thus, spin injection from the FM metal ($\sigma \sim 10^5$ S/cm) into normal OSCs is generally inefficient. One suggested solution is to use a tunnel barrier by adding a thin insulating layer or depletion barrier of a large Schottky barrier. This is based on a theoretical model, initially proposed by Rashba for inorganic SC[11] and later developed by Ruden for OSC as a NM spacer.[12] Here, a tunneling barrier works as a spin filter, where the conductivity mismatch problem does not apply because the transport is governed by tunneling, not diffusion. Alternatively, a large difference in the conductance of FMs and OSCs could be modulated to some extent by using more appropriate materials. For example, there are OSCs known to have a crystalline packing

structure of much higher conductivity (> 1 S/cm) than the other molecules of morphological disorder. Also, half-metallic oxide materials *e.g.*, $La_{1-x}Sr_xMnO_3$(LSMO) and magnetite (Fe_3O_4), with conductivity of a few hundred S/cm[13] can also reduce the conductivity mismatch problem by replacing a FM metal with too high conductivity compared to OSCs.

6.1.2 Research background and objectives

There have been intensive efforts made to implement an organic spin valve in the field of organic light-emitting diodes (OLEDs).[14] In OLEDs, the electroluminescence intensity depends on the spin polarization of the injected carriers, *i.e.*, whether they form singlet vs. triplet states; it is extremely beneficial if the spin direction can be controlled with external magnetic fields. In this regard, the tris(8-hydroxyquinolinato)-aluminum(III) complex, in short Alq_3, is one of the most studied OSCs in organic spintronics, as it represents a major green emitter used for OLEDs. However, it appears that a low carrier mobility of OSCs also plays a critical role in the spin scattering at the interface. Given that a conventional Alq_3 film is not easy to grow in an ordered manner, it is desirable to replace it with OSCs known to grow with crystalline morphologies on inorganic substrates, such as CuPc, rubrene, $C_{60,}$ and pentacene, in order to achieve a band-like transport upon spin injection.[15]

Over the past decades, one of the most exploited device architectures for an organic spin valve has been LSMO/Alq_3/Co with Alq_3 layers varying from a few to hundred nm thick. Despite high tunneling magnetoresistance (TMR) up to 300%,[16] the MR responses of

these prototypical devices completely disappear above 300 K, which is attributed to the low Curie temperature (T_c) of LSMO, T_c = 370 K for bulk but lower for thin films. Thus, new FM materials which magnetism sustained well above room temperature should be explored for practical operations. From this perspective, iron-based materials have attracted much attention as a very high T_c has been measured not only in Fe and Fe alloys but also in iron oxide polymorphs. In particular, magnetite has been proposed as a promising candidate in the effort to replace the LSMO electrode. This material is half-metallic and has a very high T_c (~850 K). In addition, the availability of high-quality thins film with well-defined magnetic anisotropy makes magnetite an attractive material to be used as a FM electrode for room-temperature operation. There are other transition metals whose Curie temperature is high enough, for example, with a Co T_c ~ 1400 K; however, it has been reported that Co interdiffusion into the OSC during thermal deposition often leads to the failure of the spin devices; then, a tunnel barrier, such as Al_2O_3 or LiF, is required.[15] By comparison, magnetite exhibits a less reactive nature at the surface, leading to weaker hybridization effects compared to FM metals in use. Hence, magnetite-based magnetic junction devices have been investigated with Alq_3,[17-19] rubrene,[20] C_{60}[19,21] as a nonmagnetic spacer. In particular, for a $Fe_3O_4/Al_2O_3/C_{60}$(80nm)/Co junction, Zhang *et al.*[21] have observed a MR signal up to 8%, highlighting C_{60} as a good candidate for organic spintronic devices.

In this Chapter, we investigate the electronic/magnetic properties of the interface between iron-based substrates and various OSCs. We have selected representative π-conjugated organic molecules: (i) a conventional OSC molecule that has been extensively used in organic spintronics, Alq_3 (ii) a hole transport material, pentacene and (iii) an electron

transport material, C_{60} (Figure 6.1). For the FM electrode, Fe (001) has been explored as a prototypical FM metal to understand the hybrid interface states and spin polarization of carbon-based materials with a metal contact. In addition, the half-metallic Fe_3O_4 (111) and (001) surfaces have also been examined and further compared to the metallic substrate with respect to impact on induced spin polarization on the molecules. By changing materials, substrate crystal orientation or termination, and molecular adsorption geometry, the first-principles study of the organic-FM interface systems presented in this Chapter can provide a better insight to tailor the spin transfer behavior in organic spintronics devices.

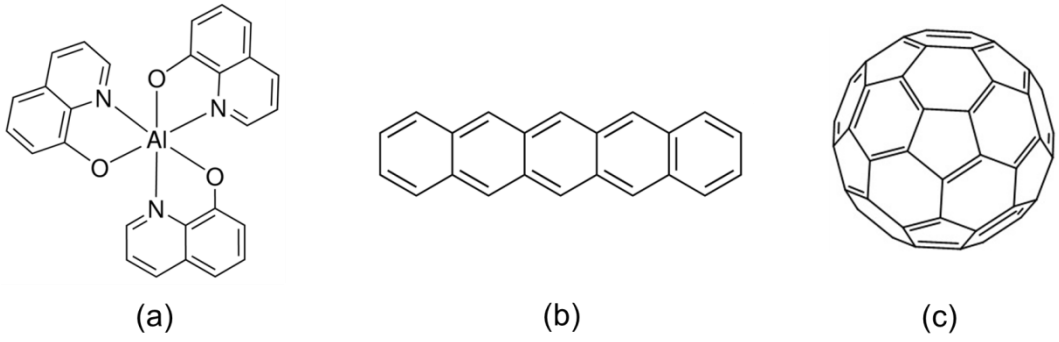

Figure 6.1 Chemical structures of (a) tris(8-hydroxyquinoline)aluminum(III) (Alq_3), (b) pentacene, and (c) C_{60}.

6.2 Computational details

First-principles calculations have been performed using spin-polarized DFT as implemented in the Vienna ab initio simulation package (VASP)[22,23] with the generalized gradient approximation (GGA) exchange-correlation functional of Perdew, Burke, and Ernzerhof (PBE).[24] The energy cutoff for a plane-wave basis set was set to 450 eV.

For magnetite, we exploited the DFT+Hubbard *U* (DFT+*U*) approach[25] to describe the intra-atomic Coulomb interaction among strongly correlated Fe 3*d* electrons. U_{eff} = 4 eV has been applied to Fe 3*d* electrons in the simplified rotationally invariant formulation of Dudarev *et al.*[26] where the on-site Coulomb parameter, *U*, and exchange parameter, *J*, are combined into a single parameter, $U_{eff} \equiv U - J$. A ferrimagnetic ordering, where the sign of the Fe_{oct} atoms are antiparallel to those on the Fe_{tet} atoms, was taken as the initial magnetic configuration and allowed to relax for all the surface models of Fe_3O_4. This approach describes the band gap and magnetic moments of magnetite with good accuracy, as described in Chapter 3. The Fe_3O_4 (111) polar surface is modeled using a symmetric slab with a (2×2) unit cell based on a primitive surface model obtained in Chapter 4. Fe_3O_4 (001) is also constructed as a (2×2) unit cell containing 12 layers of 6 repeat units. In order to maintain bulk behavior below the surface, the bottom layers were kept fixed at the bulk crystal positions while the outermost 5-6 atomic layers were allowed to relax.

To build the interface model, Alq_3, pentacene, and C_{60} molecules are first optimized in an isolated box of 30 Å×30 Å×30 Å using simply the Γ-point. Then, the organic-inorganic interface system is constructed by building a supercell of the substrate in such a way that

the adsorbed molecules in repeated unit cells stay apart from one another by at least ~ 6Å under periodic boundary conditions. Accordingly, the **k**-point sampling for Brillouin-zone integrations was downsized inversely proportionally to the increase in the unit-cell size of the interface system, as summarized in Table 6.1. The van der Waals (vdW) interactions from dynamic correlations between fluctuating charge distributions were approximated using Grimme's D3 method.[27] Geometries were optimized with a quasi-Newton or/and conjugate-gradient algorithm until the Hellmann-Feynman forces were less than 0.01 eV/Å and energy convergence within 10^{-5} eV/atom. A Gaussian-smearing approach for the orbital occupancies with σ = 0.05 eV was used during the geometry optimizations and electronic-structure analyses of densities of electronic states (DOS). The orbital-projected densities of states (PDOS) were calculated by projecting the Kohn-Sham (KS) wave functions onto atom-centered spherical harmonic functions within each atom's Wigner-Seitz radius. The magnetic moments are obtained from the integration of the spin density inside PAW spheres in a Fe atom.

Table 6.1 Unit-cell sizes and k-point samplings for various organic-inorganic systems considered in this study.

Substrate	**Adsorbate**	**Unit-cell size**	**k-points**
Fe (001)	Alq_3	14.147 Å ×14.147 Å	3×3×1
	C_{60}	11.317 Å ×11.317 Å	3×3×1
	pentacene	16.980 Å × 8.490 Å	3×5×1
Fe(001)-*p*(1×1)O	C_{60}	11.317 Å ×11.317 Å	3×3×1
Fe_3O_4 (111)	C_{60}	12.004 Å × 12.004 Å	3×3×1
Fe_3O_4 (001)	C_{60}	16.845 Å × 16.845 Å	2×2×1

6.3 Iron metal substrate

6.3.1 Surface plane of iron

In PBE calculations, the net spin magnetic moment (μ_s) per surface Fe atom is calculated to be 2.94 and 2.61 μ_B on (001) and (110), respectively, while μ_{Fe} in the bcc bulk crystal yields 2.20 μ_B (This calculated bulk magnetic moment is in excellent agreement with the value from x-ray magnetic circular dichroism (XMCD) spectra[28]). Theoretically, it is well known that the magnetic moment in the topmost layer of magnetic 3*d* transition metals tends to be enhanced with respect to the bulk magnetic moment.[29] This is commonly attributed to the reduction in coordination number and symmetry at the surface, which causes the *d* bands to narrow and increases the exchange splitting across the Fermi level.

When it comes to magnetic junction applications, such as a spin valve, the spin polarization at the Fermi level, $P(E_F)$, is a critical magnetic property to determine the characteristics of the injected spin current. Many thin-film studies have shown that the charge density on transition-metal surfaces converges rather rapidly as the film thickness increases due to the localized nature of the 3*d* electrons; hence, the overall spin polarization of the film is similar to that in the crystal in general. However, it should be pointed out that the surface spin polarization is important, particularly in the realm of organic spintronics where the molecular orbitals of the π-conjugated OSCs become strongly hybridized with the surface *d* orbitals, leading to the spin-dependent electronic structure at the interface. Given that the bulk Fe shows positive spin polarization at the Fermi level, it is interesting that both Fe(001) and (110) surfaces exhibit a negative spin

polarization, 93 % and 13 %, respectively, at the Fermi level (see Figure 6.2). This is consistent with earlier surface calculations reported in the literature.[30] The variation in $P(E_F)$ between bulk and surface Fe atoms are less pronounced for (110) than (001) since (110) retains more bulk-like character as it is the closest packed surface plane of a BCC metal.

For optimal device performance in organic spintronics, it is necessary to induce the spin polarization of molecules in a non-magnetic spacer, which requires highly spin-resolved electronic states near the Fermi level of ferromagnetic electrodes in contact. Thus, (001) is regarded as the most promising among low-index surface planes of bcc Fe metal; here, we primarily consider Fe(001) to model the interface systems involving iron substrates.

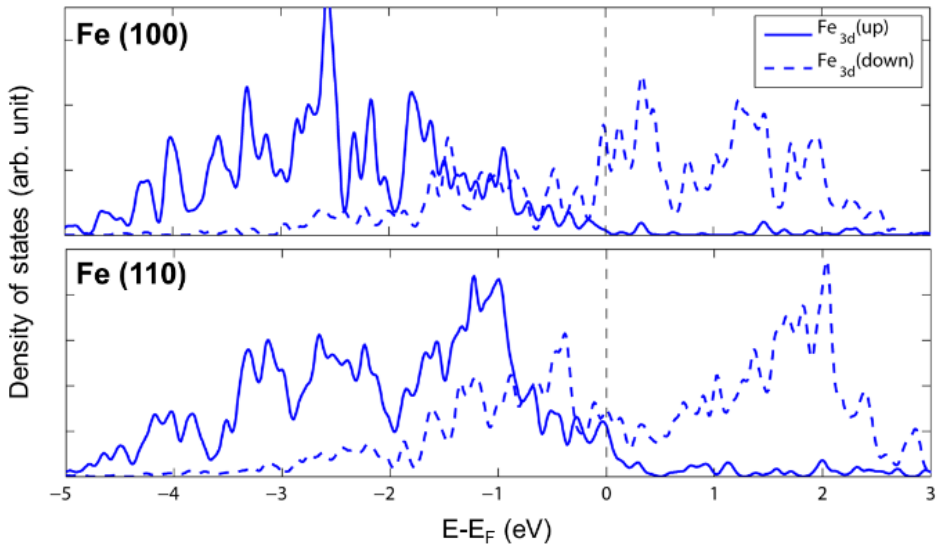

Figure 6.2 PDOS of Fe 3*d* orbitals for surface atoms on Fe(001) and Fe(110). Majority and minority spins are denoted by solid and dashed lines, respectively.

6.3.2 Molecular adsorption of organic semiconductors on Fe(001)

We have investigated the adsorption of representative OSCs: Alq_3, pentacene, and C_{60} on the Fe(001) surface; the optimized geometries are displayed in Figure 6.3. For Alq_3, two quinoline ligands adsorb on Fe(001) in a lying-down configuration while the third ligand is aligned perpendicular to the surface (see Figure 6.3a). The center of each quinoline ring is located on top of the hollow site of the surface Fe layer, which leads to strong *p-d* hybridization in the surface normal direction. This adsorption geometry of Alq_3 on Fe(001) is consistent with the one reported from angle-resolved N(1s) XPS spectra where XPS peak shifts are observed only for two quinoline ligands while the third remains at the peak position of the bulk reference.[31] Similarly, pentacene becomes strongly chemisorbed through hybridization between the Fe *d* states and the conjugated π orbitals of the molecule (Figure 6.3b). This is in good agreement with experimental findings in the initial stage of pentacene growth while the molecular plane starts to tilt from the surface with the increase in coverage.[32] In contrast to the (partially) planar molecules, the adsorption geometry of C_{60} is more difficult to define as there are six high-symmetry configurations of $C_{60,}$ which adds more complexity to identifying the most stable binding configuration at the interface. We have considered three distinctive molecular adsorption sites: (i) C_{60}(6:6), the edge shared by two hexagons (a 6:6 bond); (ii) C_{60}(h), carbon hexagon face on; and (iii) C_{60}(p), pentagon face on. The geometry optimization of C_{60}(6:6)/Fe(001) results in the interfacial configuration where a 6:6 bond is adsorbed 1.21 Å above a bridge site of Fe(001). On the other hand, the center of the carbon ring is located on top of the Fe hollow site for the C_{60}(h) and C_{60}(p) adsorption configuration

(Figure 6.3c). The lowest bond distance between a C and a surface Fe is calculated to be 1.93 Å for C_{60}(6:6), 2.00 Å for C_{60}(h), and 1.98 Å for C_{60}(p).

It should be noted that adsorption induces structural distortion of the molecules. On Fe (001), Alq_3 and pentacene somewhat bend as hydrogen atoms close to the Fe substrate tilt upwards due to the strong interactions between carbons and surface irons. A similar geometry has been observed for benzene on metal surfaces in other theoretical studies.[33-36] The distortion of pentacene to a shallow boat conformation was found to be almost negligible (<1°) here while earlier PBE calculations of pentacene/Fe(001) reported a bending of 4.2°.[36] The adsorption of C_{60} on Fe(001) in an edge configuration leads to elongation of the 6:6 bond by 0.02 Å. For the hexagon face-on geometry, the C-C bond lengths between two hexagons (6:6 bond) and between pentagon and hexagon (5:6 bond) near the interface increase by 0.05-0.08 Å and 0.3-0.5 Å, which is consistent with previous PBE calculations.[37]

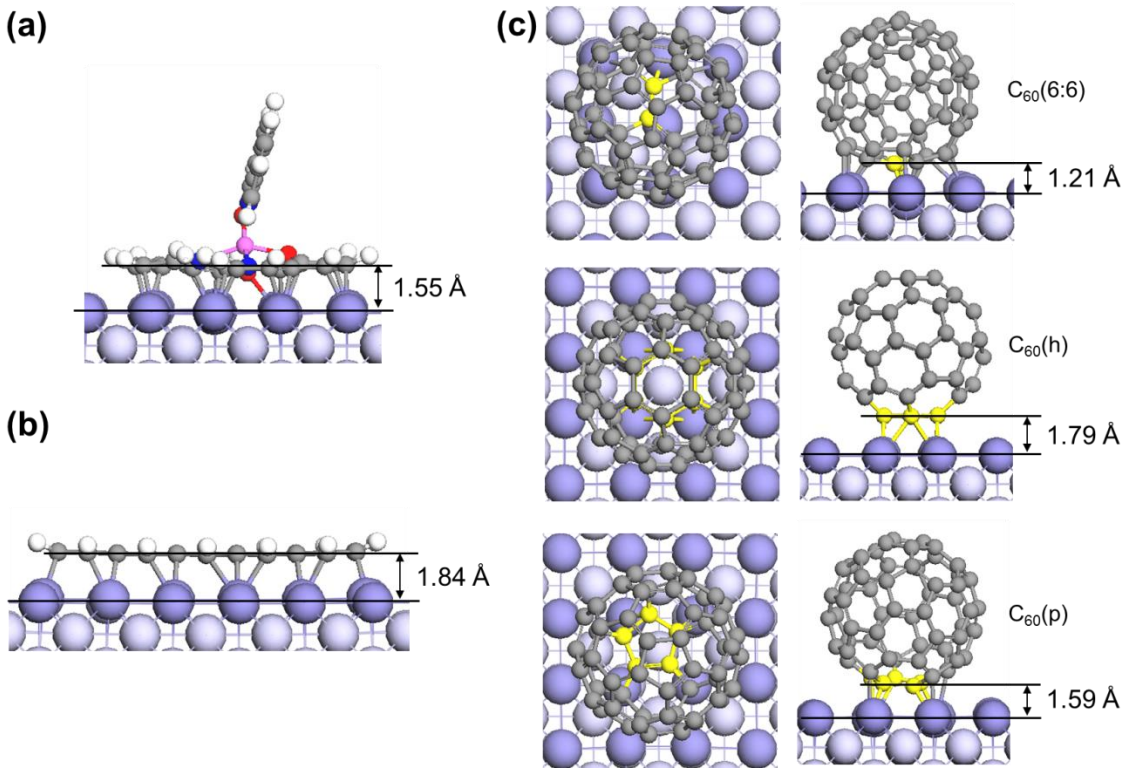

Figure 6.3 Optimized geometries of (a) Alq_3, (b) pentacene, and (c) C_{60} on three different adsorption sites on Fe(001). Molecular adsorption through a 6:6 bond, hexagon face-on, and pentagon face-on configuration are referred as C_{60}(6:6), C_{60}(p), and C_{60}(h), respectively (the C atoms in chemical bonding with the Fe substrate are colored in yellow).

We have included vdW corrections to obtain more accurate total energies for the optimized structures. Although the dispersion does not change the relative adsorption energies among the three molecules on Fe (001), the most stable interfacial geometry can be different for a given molecule. With vdW contribution, C_{60}(6:6) is predicted to be the most favorable configuration while C_{60}(h) is more favored by 0.14 eV without any correction, as a higher dispersion is expected for C_{60}(6:6) that sits on Fe surface more

adjacently. For the complexes like C_{60}/Fe (001) that show very subtle energy differences in the range of a few tenths of an eV among their adsorption configurations, the inclusion of vdW interactions is vital to understand the most favorable interfacial configuration.

Table 6.2 Calculated binding energies and shortest Fe-C bond lengths at the interface as calculated at the PBE level with vdW corrections.

	Binding energy (eV)			d_{Fe-C} (Å)
	DFT (eV)	vdW (eV)	total (eV)	
Alq_3	-2.92	-3.41	-6.32	2.03
pentacene	-3.86	-2.82	-6.68	2.07
C_{60}(6:6)	-2.38	-2.87	-5.25	1.93
C_{60}(h)	-2.52	-2.08	-4.60	2.00
C_{60} (p)	-2.10	-2.20	-4.30	1.98

The strong Fe 3*d*-C 2*p* interactions mentioned above generally accompany drastic charge redistribution over the metal-organic interface and in turn, a variation in substrate work function. As demonstrated earlier,[38,39] the work function modification upon molecular adsorption can be decomposed into three major contributing factors:

$$\Delta\emptyset_{total} = \Delta V_{ID} + \Delta V_{mol.} + \Delta V_{geo.} \quad (6.2)$$

where ΔV_{ID} is the potential energy step for a dipole formed at the interface between surface atoms and the molecules; $\Delta V_{mol.}$ indicates the potential energy step across the adsorbate molecule on the surface; and $\Delta V_{geo.}$ is the change in work function of the

substrate alone when considering the structural alterations upon adsorption with respect to the bare surface.

The interface dipole, ΔV_{ID}, can be calculated as the charge density difference before and after adsorption of OSCs on the surface by solving Poisson's equation as follows:

$$V(z) = \iint -\frac{1}{\varepsilon_0}\Delta\rho(z)\ dz \tag{6.3}$$

$$\Delta\rho(z) = \rho_{Fe-mol}(z) - [\rho_{Fe}(z) + \rho_{mol}(z)] \tag{6.4}$$

where $\Delta\rho(z)$ indicates the plane-averaged electron-density difference between the combined interface and the isolated fragments, along the surface normal direction z. The numerical calculation of ΔV_{ID} for the organic-Fe(001) systems is presented in Figure 6.4. As shown in Figure 6.4a, electronic density transfers between adsorbate and surface (~ 1e) pointing to the formation of chemical bonding at the Alq_3/Fe(001) interface. A similar charge distribution is predicted for pentacene/Fe(001) but to a higher extent, which originates from the increase in the number of interacting π-orbitals with the Fe substrate in pentacene (five aromatic rings) compared to Alq_3 (two quinoline ligands). Despite the large charge transfer at the interface, the total work function modification is rather small for Alq_3 and pentacene adsorption, *ca.* ~ 0.2 eV, due to the simultaneous electron donation in opposite directions. On the other hand, a net charge transfer of ~ 0.25 e is predicted mainly from the metal substrate to C_{60} (see cumulative charge, Q, in Figure 6.4c), which brings about a substantial rise in work function by 1 eV. The differences among the OSCs can be attributed to the high EA of C_{60} with respect to the other two systems.

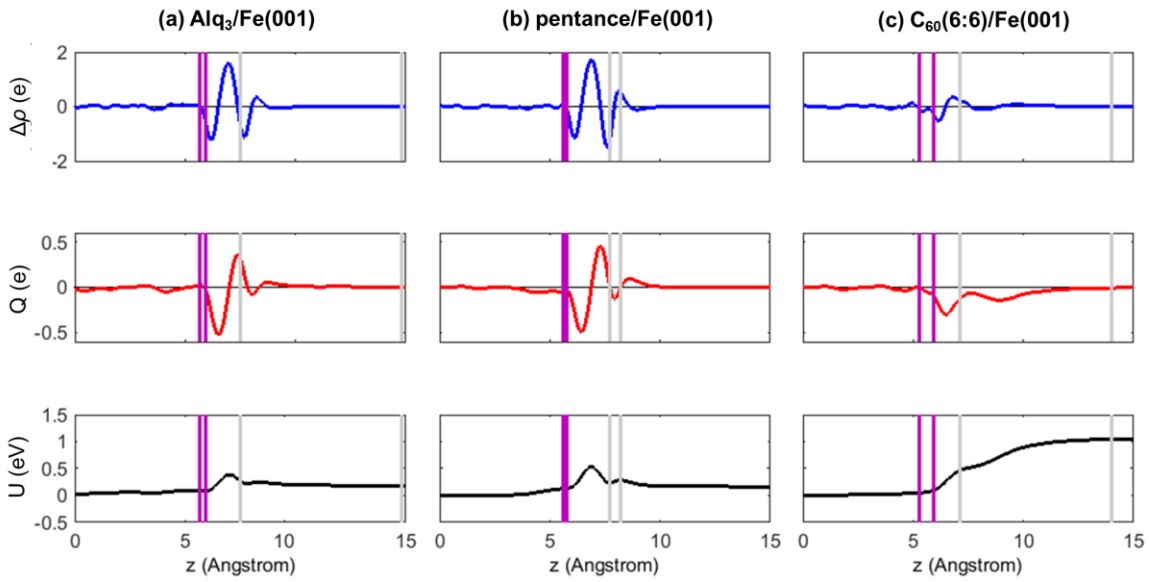

Figure 6.4 Differential charge density (ρ), accumulated charge (Q), and work function modification (U) across the interface upon BPA adsorption. The purple vertical lines indicate the maximum and minimum z-coordinate of the topmost Fe layer while the grey lines correspond to the adsorbate molecules.

Table 6.3 summarizes the calculated interfacial dipoles for three OSC/Fe(001) systems and further decomposition into the three contributing factors: ΔV_{ID}, $\Delta V_{mol.}$, and $\Delta V_{geo.}$ As discussed in Section 6.3.1, the strong Fe 3*d*-C 2*p* interaction tends to align a Alq_3 molecule on Fe(001) in a configuration where two quinolines are lying down. As a result, a high molecular dipole moment is introduced upon adsorption, leading to a remarkable potential drop across the Alq_3 layer. Combined with small bond dipoles that change Φ in the other direction, the high ΔV_{mol} results in a net decrease in work function by -0.54 eV

for Alq_3 adsorption. In earlier UPS measurements of Alq_3 on Fe,[31] the authors found a negative interface dipole and concluded it comes from a "positive charge in Alq_3 and negative charge in Fe"; however, our results point out that the origin of the lower work function comes from the static dipole moment of adsorbed Alq_3 molecules on Fe.

For pentacene adsorption, there is one experimental finding of work function decrease of the Fe substrate,[32] which is consistent with our result, -0.36 eV. Among the three components contributing to the work function modification, the main component originates from the molecular dipole moment (-0.6 eV) due to the relaxed geometry of pentacene whose hydrogen atoms points away from the iron surface upon adsorption.

In contrast, the calculated dipole moment of C_{60} itself on Fe(001) is negligible; therefore, the major contribution for work function modification for the C_{60}/Fe(001) systems is the bond dipole that does not highly depend on binding configurations. In the three interface configurations, the modified work function is in the range of 4.7-4.8 eV, which closely corresponds to the experimental value of 4.9 eV.

Table 6.3 Decomposition of the work function modification into the three components. $\Delta\Phi_{calc.}$ corresponds to the value obtained from Φ changes before and after molecular adsorption on Fe(001) for the given OSC/Fe system. The modified work function, Φ, is obtained by calculating the energy difference between the Fermi level of OSC/Fe(001) and the vacuum level.

	ΔV_{ID}	ΔV_{mol}	$\Delta V_{geo.}$	$\Delta\Phi_{total}$	$\Delta\Phi_{calc}$	Φ	Φ_{expt}
Alq_3	0.19	-0.79	-0.02	-0.62	-0.54	3.29	3.5[31]
pentacene	0.18	-0.60	0.00	-0.42	-0.36	3.47	
C_{60}(6:6)	1.02	-0.06	0.00	0.96	0.93	4.75	4.9[40]
C_{60}(h)	0.94	-0.04	0.00	0.89	0.87	4.70	
C_{60}(p)	0.99	-0.02	-0.01	0.97	0.97	4.80	

6.3.3 Electronic/magnetic structures of organic-Fe(001) interfaces

6.3.3.1 Energy level alignment

As presented in Table 6.3, an organic-FM junction has a strong interface dipole (Δ) which shifts the relative energy levels of the MOs with respect to the Fermi level. Hence, the induced interface dipoles should be taken into account to correctly describe the energy level alignment. In Figure 6.5, the schematic diagrams of energy level alignment in Alq_3, pentacene, and C_{60}(6:6) on Fe(001) are presented with the calculated interface dipoles and resulting hole/electron injection barriers (Δ_h/Δ_e).

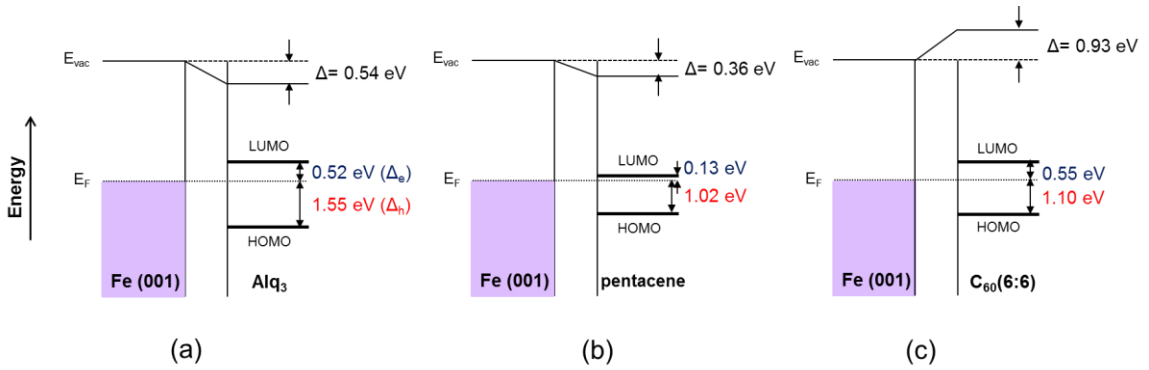

Figure 6.5 Schematic diagrams of energy level alignment in (a) Alq_3, (b) pentacene, and (c) C_{60}(6:6) on Fe(001). Δ refers to the interface dipole in Table 6.3.

For Alq_3 on Fe(001), the barrier height for holes and electrons are calculated to be 1.55 eV and 0.55 eV, respectively, which is qualitatively consistent with earlier UPS measurements that confirm that the Alq_3 LUMO is closer to the Fermi level than the HOMO. UPS spectra indicate that the Alq_3 HOMO have 2.5 eV higher binding energy than the Fermi edge, while the LUMO is then around 0.5 eV above the Fermi level considering that the band gap is about 3 eV.[31] Quantitative discrepancy stems from the theoretical limit that the Kohn-Sham eigenvalue gap is always smaller than the actual fundamental gap due to the derivative discontinuity relative to the use of a non-exact exchange-correlation functional in semi-local DFT approximations.[41] This aspect will be discussed in more detail in the Appendix B.

The LUMO level of pentacene resides far above the Fermi level before the junction contact is made; the strong interface dipole of 0.36 eV shifts the LUMO down to as close as 0.13 eV. If we were to assume a 100% spin polarization of LUMO level, pentacene

could be an optimal choice as an organic spacer in a magnetic junction as the spin injection from Fe(001) is more efficient to pentacene than Alq_3 or C_{60}.

Since the LUMO level of isolated C_{60} is lower than the Fermi level of Fe(001) as calculated with the PBE functional, our results show Fermi-level pinning for C_{60}/Fe(001) where spontaneous electron transfer from Fe to C_{60} is expected. As the interface has a finite Schottky barrier; a lower barrier height is predicted for electrons, as displayed in Figure 6.5c. Indeed, the LUMO (π^*) has been observed to play a crucial role in the hybridization with iron 3*d* surface bands, and hence determines the spin asymmetry near E_F for C_{60}[42] on Fe(001). This is also concluded from STS and PES/IPES experiments where significant broadening of the LUMO peaks is observed for C_{60} on Fe(001).[40] The hole injection barrier is calculated to be higher, 1.10 eV, which is underestimated by 0.8 eV compared to PES measurements.[40] This is, again, attributed to the shortcomings of conventional DFT approaches.

6.3.3.2 Spin polarization near the Fermi level

Combined with the predicted energy level alignment, the effect of hybridization on the Fe surface can be further analyzed using projected DOS (PDOS), as shown in Figures 6.6 and 7. Overall, strong hybridizations between Fe 3*d* states and the MOs of OSCs induce the spin-up states of the surface Fe atoms in contact with the molecules to be shifted upward, which results in a reduced spin polarization at E_F. This is supported by earlier XMCD measurements that found enhanced orbital moments of Fe upon C_{60} adsorption since the 3*d* wavefunction becomes more localized as a result of the orbital hybridization

at the interface.[43] However, the direction of $P(E_F)$ of the topmost Fe layer remains negatively spin-polarized upon molecular adsorption.

The PDOS of Alq_3 in Figure 6.6a also confirms the existence of hybridization near the Fermi level. While the main peaks related to MOs are located at the energies derived from the level alignment (Section 6.3.3.1), the hybridized interface states become extended across the Fermi level. Here, empty HISs locate exactly at the Fermi level, which is in good agreement with NEXAFS measurements that show a shoulder derived from the empty hybridized states at several hundred meV below the main peak. [31] Thus, the Alq_3-Fe interface can be regarded as an Ohmic-like contact, which enables charge injection into Alq_3 at very low bias. Extended HISs are also predicted for pentacene on Fe(001). Here, the frontier MO peaks are less discrete as all C atoms in pentacene are involved in hybridization, which leads to peak broadening.

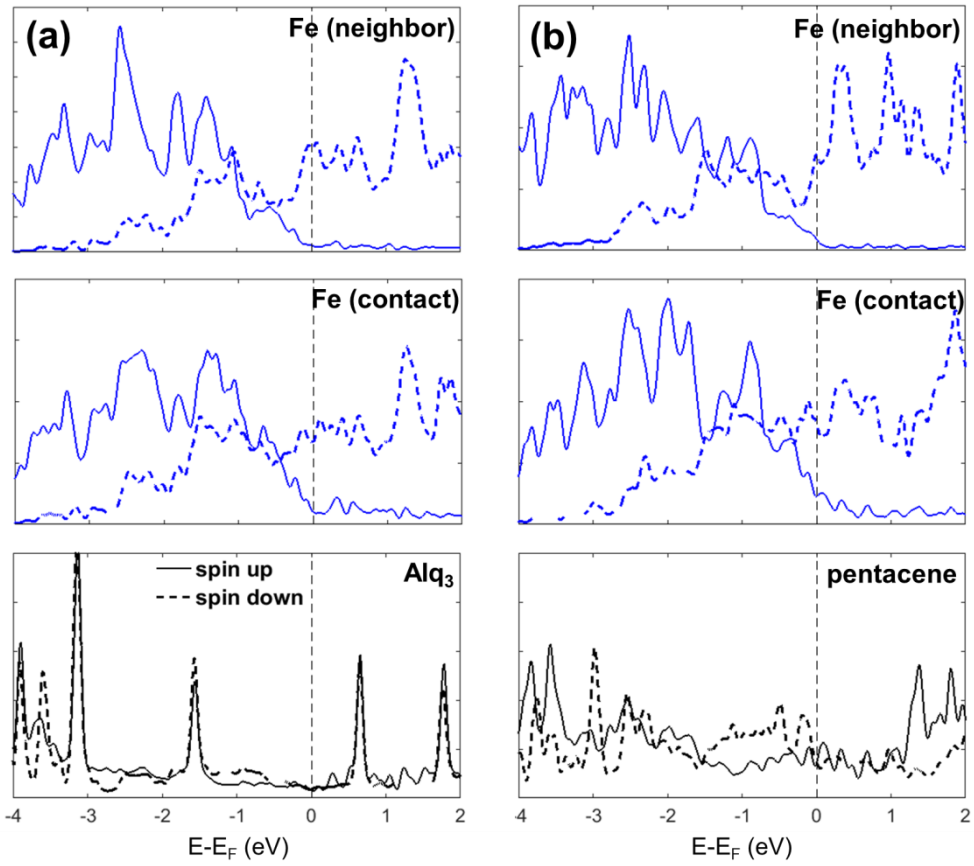

Figure 6.6 Calculated PDOS of (a) Alq_3/Fe(001) and (b) pentacene/Fe(001). Majority and minority spin are denoted by solid and dashed lines, respectively. Among surface Fe atoms, the one involved in the chemical bonding with C_{60} is denoted as Fe (contact) whereas non-interacting Fe is referred to as Fe (neighbor).

In the case of C_{60} adsorbed on Fe(001), the strongly broadened peaks around ~ 0.5 eV above E_F appear to be LUMO-derived states as predicted from the energy level alignment (see Figure 6.7). There is a noticeable reduction in Fe 3*d* states for the surface Fe atoms in contact with C_{60}(6:6) compared to C_{60} (h) and C_{60}(p). It should be noted that C_{60}(6:6) strongly binds mainly with two surface Fe atoms while the other binding configurations

involve at least four surface atoms. Given that the net charge transfer from Fe to C_{60} is more or less the same for C_{60}(6:6), C_{60} (h), and C_{60}(p) (see Section 6.3.2), higher electron deficiency is expected for Fe atoms interacting with C_{60}(6:6). Although the overall shapes of the C_{60} PDOS resemble one another, it is instructive to point out that the contact configuration of a molecule can affect the details of orbital hybridization and even the direction of spin polarization.

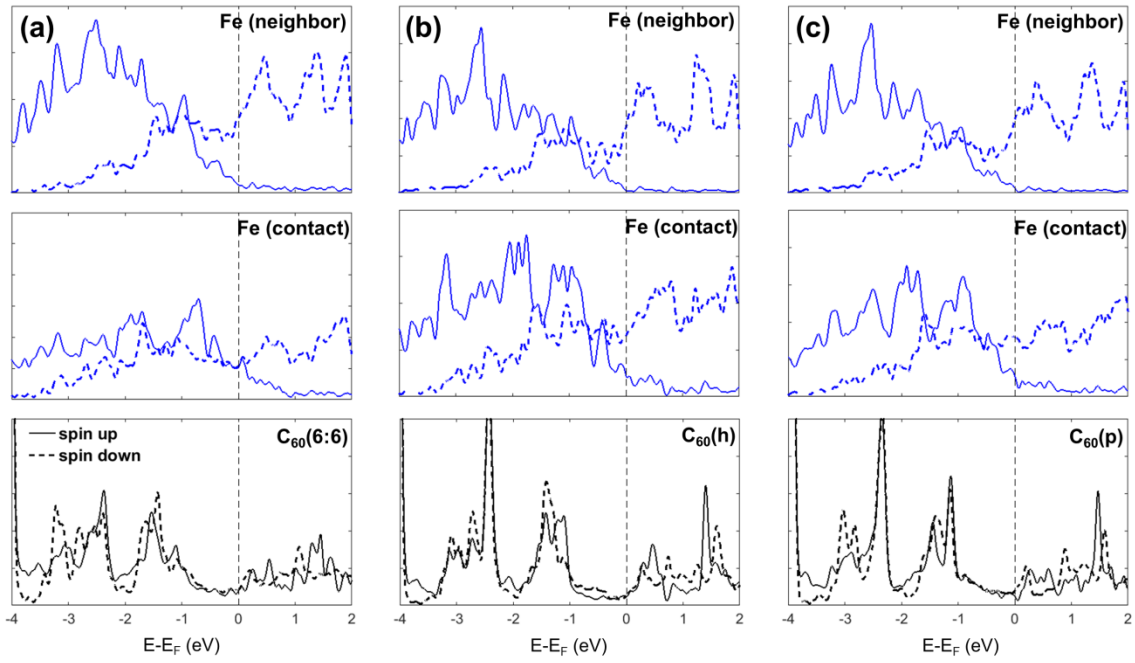

Figure 6.7 The calculated PDOS of (a) C_{60}(6:6)/Fe(001), (b) C_{60}(h)/Fe(001), and (c) C_{60}(p)/Fe(001). Majority and minority spin are denoted by solid and dashed line, respectively. Among surface Fe atoms, the one involved in the chemical bonding with C_{60} is denoted as Fe (contact) whereas non-interacting Fe is referred to as Fe (neighbor).

Our PDOS results indicate the HISs derived from three OSCs adsorbed on Fe(001) are present exactly at the Fermi level. Although an Ohmic-like contact is advantageous for electron/hole injection, it has been demonstrated that this type of contact leads to inefficient spin injection from an FM electrode to the 1st OSC layer due to the conductivity mismatch problem.[31,44] Alternatively, effective spin injection can be realized if the magnetized 1st OSC layer serves as a spin injector to the 2nd OSC layer.[45,46] Since this injection occurs from organic to organic layer, the resistance mismatch is significantly reduced, and thus there can occur coherent spin injection without dephasing.

In Figure 6.8, the spin polarization is shown as calculated from PDOS in the range of [E_F-1 eV, E_F+1 eV] using the following equation:

$$\mathrm{P(E)} = \frac{DOS_{\uparrow}(E) - DOS_{\downarrow}(E)}{DOS_{\uparrow}(E) + DOS_{\downarrow}(E)} \qquad (6.5)$$

Upon adsorption on Fe(001), an oscillatory spin polarization of Alq_3, pentacene, and C_{60} is obtained near the Fermi level. This oscillating nature of P(E) has been confirmed for pentacene on Fe(001) by spin-polarized metastable atom deexcitation spectroscopy (SPMDS) where a negative spin polarization is measured for occupied π orbitals and a positive spin polarization in the unoccupied π^* orbitals.[32] Also, XMCD measurements reveal that upon adsorption of Alq_3[31] and C_{60}[42] molecules on the ferromagnetic Fe substrate, the molecules are not only hybridized but also magnetized. Alq_3 and pentacene have mainly negative spin polarization in the occupied orbitals while a positive spin polarization appears to some extent for the unoccupied state. C_{60} is negatively spin-polarized near E_F to a smaller degree, below 20%. However, none of the presented PDOS for the OSCs shows a clear spin-discriminated peak near the Fermi level.

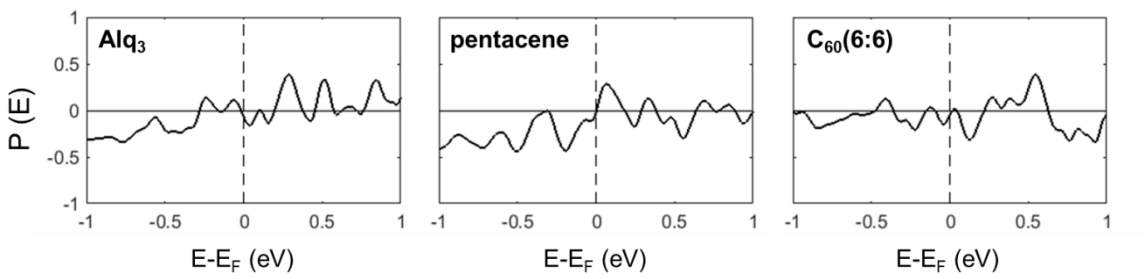

Figure 6.8 Calculated spin polarization derived from the PDOS in the range [E_F-1 eV, E_F+1 eV] for (a) Alq_3/Fe(001), (b) pentacene/Fe(001), and (c) C_{60}(6:6)/Fe(001). The vertical dotted lines indicate the Fermi level.

The spin polarization of the occupied states of the OSCs also implies that the molecules become magnetized. Indeed, this magnetization is obtained at the expense of a reduction in spin magnetic moments of the surface Fe atoms (see Table 6.4). For example, the adsorption of C_{60} on Fe (100) leads to a spin moment reduction by 4.1%, which agrees well with the experimentally derived values from XAS and XMCD, 1~2% for Fe (001)[42] and 6% for 3ML Fe/W(001)[43] substrate, respectively. It is interesting that negative spin magnetic moments are calculated for all types of molecules on iron surfaces. The (net) negative spin appearing in the molecules is in the direction opposite to the majority spin in the *d* band; this can be explained by *p-d* mixing[47] at the interface, which has been used to understand the ferromagnetism in transition metal compounds. Once a molecule spatially gets close to the surface with a negatively spin-polarized *d* band at E_F, the (originally occupied) majority spin *p* band shifts toward higher energy as a result of hybridization with the majority spin *d* band of the surface while the (originally unoccupied) minority spin *p* band makes opposite shifts to lower energy. Following the

electron transfer from the majority spin *p* states to the minority states to match the Fermi level in the system, the adsorbed molecules energetically get stabilized and become negatively magnetized.

Table 6.4 Variations in the spin magnetic moment ($\Delta\mu_s$) for the topmost layer of a Fe slab (per atom) and induced a net magnetic moment of the organic molecule. (Note that calculated $\Delta\mu_s$ for C_{60}(6:6) on Fe is has been reported in other theoretical studies to be the range of -0.21 to -0.38 μ_B.[37,43,48]) [a]The spin magnetic moment of one Fe atom on the clean surface of (100) is 2.94 μ_B.

	$\Delta\mu_s$(Fe/atom) (μ_B)[a]	$\Delta\mu_s$(mol) (μ_B)
alq_3	-0.25	-0.41
pentacene	-0.42	-0.55
C_{60}(6:6)	-0.22	-0.21
C_{60}(h)	-0.12	-0.16
C_{60}(p)	-0.12	-0.12

The relation between the two spin channels can be quantitatively described by the value of the spin polarization defined as $P = (n_\uparrow - n_\downarrow)/(n_\uparrow + n_\downarrow)$, where $n_\uparrow$ and $n_\downarrow$ stand for the spin-up and spin-down charge density. Figures 6.9-6.11 illustrate the spatial distribution of the calculated spin polarization of Alq_3, pentacene, and C_{60}(6:6) adsorbed on the Fe(001) surface for occupied [E_F−0.1 eV, E_F] and unoccupied [E_F, E_F+0.1 eV] energy intervals.

For Alq_3 on Fe(001) within the energy interval below E_F, the spin polarization at the Fe surface is negative; we find that an inversion of the spin polarization occurs at the molecular site with respect to the Fe surface, which is in line with the spin polarization derived from the PDOS in Figure 6.8a. However, the spin polarization is not uniform over the molecule; the edge sites of the benzene rings are negatively spin polarized. For an energy interval above the Fermi level, the spin polarization inversion at the core sites of quinolines is less dominant while the negative spin polarization gains intensity, which results in the total spin polarization of Alq_3 to be negative in Figure 6.8a in the [E_F, E_F+0.1 eV] range. Also in the case of pentacene, Figure 6.10 shows not a simple red or blue contrast but a mixed pattern for the spin polarization at the molecule site; however, the positive spin polarization is more prevalent. This positive spin polarization of the molecules adsorbed on FM metal can be conceptually explained by p_z-*d* Zener exchange mechanism.[49] Due to a spin-dependent hybridization at organic−ferromagnetic interfaces, the bonding states in both spin-up and spin-down channels appear at energies well below the Fermi level. On the other hand, the spin-up antibonding states are located in an energy window near the Fermi level while the spin-down states appear at higher energies above E_F when the substrate is negatively spin-polarized at E_F.[49]

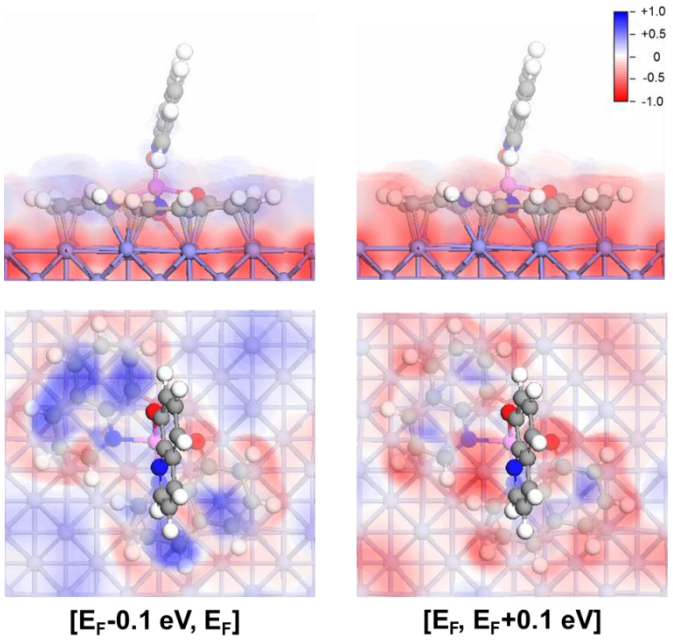

Figure 6.9 Spatial representation of spin polarization in Alq_3/Fe(001) within [E_F-0.1eV, E_F] (left) and [E_F, E_F+0.1eV] (right). The color map is given as red [blue] for negative [positive] spin polarization.

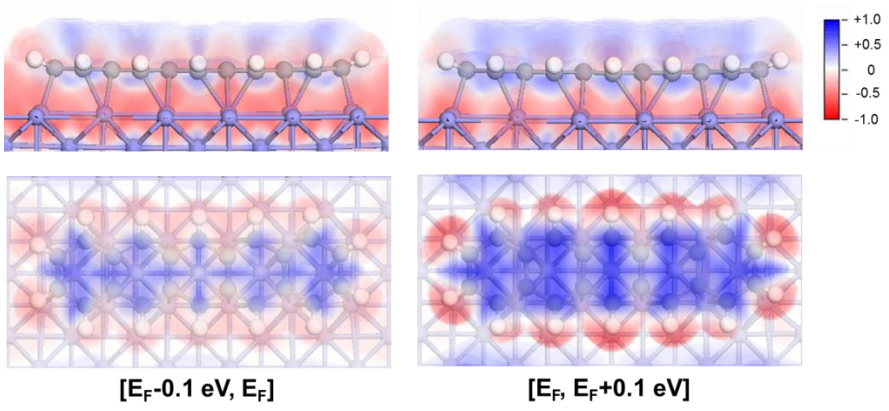

Figure 6.10 Spatial representation of spin polarization in pentacene/Fe(001) within [E_F-0.1eV, E_F] (left) and [E_F, E_F+0.1eV] (right). The color map is given as red [blue] for negative [positive] spin polarization.

For C_{60} on Fe(001), the Fe 3*d*-C 2*p* hybridization is not as strong as Alq_3 or pentacene, and also does not occur over the entire molecular site; thus, the contribution of the surface Fe *d* states is still dominant at the interface and the C_{60} SP patterns are rather featureless (see Figure 6.11). Also, the sign reversal of the spin polarization at C_{60} is not observed either below or above E_F.

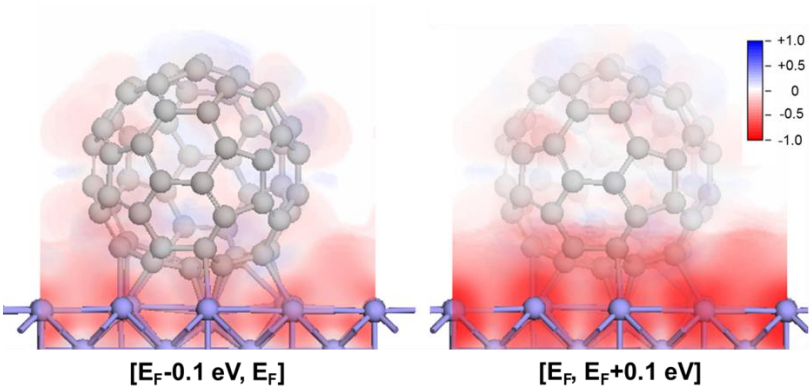

Figure 6.11 Spatial representation of spin polarization in C_{60}(6:6)/Fe(001) within [E_F-0.1eV, E_F] (left) and [E_F, E_F+0.1eV] (right). The color map is given as red [blue] for negative [positive] spin polarization.

6.3.4 Impacts of surface passivation

6.3.4.1 Fe(001)-*p*(1×1)O

As mentioned in Section 6.1, it has been reported that the insertion of a tunnel barrier, generally a thin oxide layer, can improve the conductivity mismatch at the FM-organic interface.[50] Such surface treatments can also reduce the formation of trap states at the interface, and increase the spin polarization, and prevent metal interdiffusion into the OSC during thermal deposition.[15]

One of the simplest thin oxide layers is an oxygen monolayer (ML) on Fe(001). Among various adsorption sites, an oxygen atom prefers to lie in the 4-fold hollow site of the Fe surface lattice, up to a single oxygen atom per surface unit cell, which corresponds to the Fe(001)-*p*(1×1)O structure (Figure 6.12a), previously observed in STM measurements.[51] The PBE calculations confirm the relative stability of the Fe (001)-*p*(1×1) with respect to Fe(001) above μ_O ~ 2.9 eV, as presented in Figure 6.12b. Indeed, the well-ordered Fe(001)-*p*(1×1) can appear by exposing a clean Fe(001) substrate to pure O_2 (~10^{-7} mbar) at 770 K, followed by heating at 970 K.[40] A single oxygen monolayer on Fe(001) leads to a large charge transfer from the surface Fe atoms to the adsorbed O atoms, which accompanies leads to a work function increase by 0.6 eV. The oxidation strongly modifies the electronic structure of the Fe surface; the 3*d* bands become more localized as shown in Figure 6.12c.

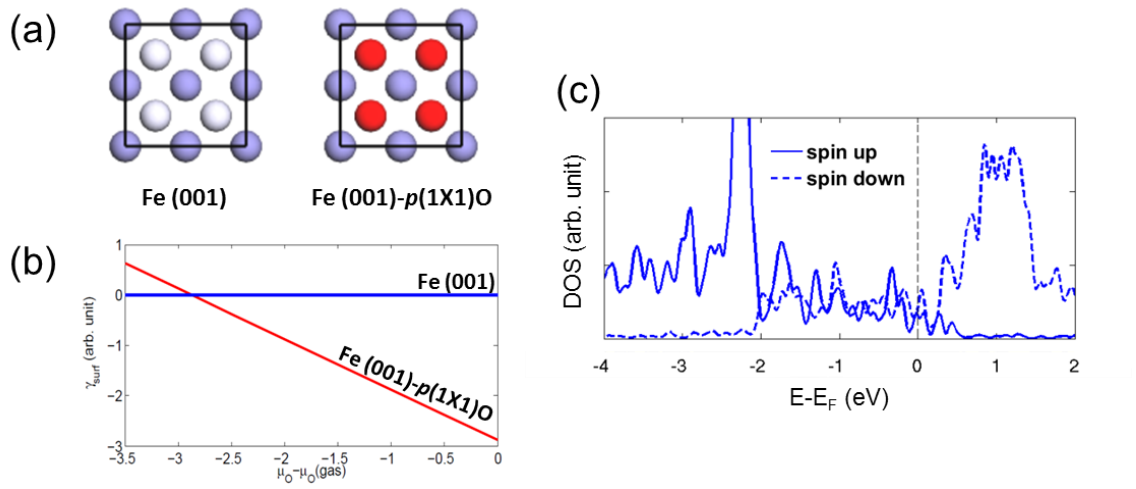

Figure 6.12 (a) Top view of Fe(001) and Fe(001) covered by an O monolayer at hollow sites, *i.e.*, Fe(001)-*p*(1×1)O. (b) Relative stability of Fe(001)-*p*(1×1)O with respect to clean Fe (001) in a physically accessible range of oxygen chemical potential. (c) PDOS of Fe 3*d* orbitals for subsurface Fe atoms on Fe(001)-*p*(1×1)O.

6.3.4.2 Geometric and electronic structure of C_{60}/Fe(001)-*p*(1×1)O

Table 6.5 summarizes the binding energies calculated for C_{60} on Fe(001)-*p*(1×1)O for three different adsorption sites. In contrast to the strong chemisorption of C_{60} on Fe(001), the C_{60} molecules physisorbs on the O-passivated surface and dispersion plays a major role in the molecular adsorption. In this case, the binding energies are similar for C_{60}(6:6), C_{60}(h), and C_{60}(p), which implies no preferential adsorption configuration. The weak coupling between C_{60} and Fe(001)-*p*(1×1)O is further supported by the small bond dipole energies < 0.1 eV, and the presence of discrete MOs of C_{60} as shown in Figure 6.13a. The calculated work function is 4.5-4.6 eV, which is in very good agreement with the experimental value, 4.4 eV.[40] In STM measurements of C_{60}/Fe(001) and C_{60}/Fe(001)-

p(1×1)O, Picone *et al.* observed different adsorption morphologies of the C_{60} molecules on the two substrates.[40] On the metal surface, single molecules are randomly distributed while large C_{60} islands form on the passivated surface. This variation in C_{60} adsorption patterns is consistent with the different coupling strengths calculated between molecules and the substrate. On Fe(001), strong organic-metal interactions render the C_{60} molecules immobile upon adsorption; on the other hand, the weak coupling of C_{60} to the oxygen-passivated surface leads to high C_{60} diffusivity, enabling the clustering of C_{60} in islands due to molecular dispersion interactions. This complete decoupling of C_{60} from the Fe(001)-*p*(1×1)O could be advantageous to increase the local degree of order of C_{60} layer, possibly arranging as a closely packed (111) face,[40] leading to faster spin transport within the non-magnetic C_{60} spacer upon spin injection.

Table 6.5 Binding energies of C_{60} on Fe(001)-*p*(1×1)O calculated at the PBE level with vdW corrections and the decomposition of the work function modification into the three components.

	Binding energy (eV)			Work function modification (eV)					
	DFT	vdW	total	ΔV_{ID}	ΔV_{mol}	$\Delta V_{geo.}$	$\Delta\Phi_{total}$	$\Delta\Phi_{calc}$	Φ
C_{60}(6:6)	0.10	-1.48	-1.38	0.11	0.00	-0.02	0.09	0.08	4.52
C_{60}(h)	0.17	-1.47	-1.30	0.13	0.00	-0.01	0.12	0.14	4.58
C_{60}(p)	0.17	-1.49	-1.33	0.16	0.00	0.00	0.16	0.17	4.61

In Figure 6.13b, the hole injection barrier is calculated to be 1.43 eV, which highly underestimates the value seen in PES measurements, 2.6 eV. Also, the calculated electron

injection barrier of 0.22 eV is far below the IPES estimated value of 0.8 eV. As illustrated in Section 6.3.3.1, DFT can give a reasonable prediction of the hole/electron injection barriers only in a qualitative manner, *e.g.*, their relative heights; however, the absolute values are mostly underestimated. It should be noted that the errors are more significant for Fe(001)-*p*(1×1)O where the surface passivation results in the missing of the polarization effect from the metallic substrate on the adsorbates, which always contributes to decrease EA and increase IP. Since DFT methods cannot capture this many-body effect, the lack of metal polarization generally cancels out to some extent the underestimation of the molecular fundamental gap. Therefore, we adopted techniques going beyond DFT: DFT+Σ^{axc} and G_0W_0(PBE), in order to correct the fundamental gap and improve the description of the energy level alignment, as presented in Table 6.6. Since this issue is beyond the scope of this Chapter, the detailed methodological procedure to introduce these corrections is set aside in an Appendix B.

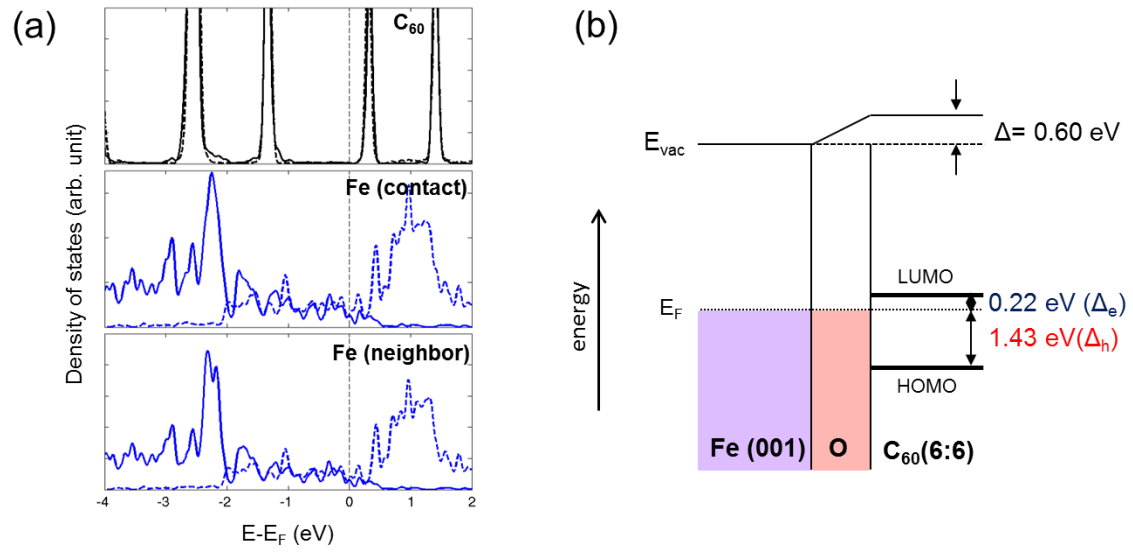

Figure 6.13 (a) Calculated PDOS of C_{60}(6:6)/Fe(001)-*p*(1×1)O. Majority and minority spin are denoted by solid and dashed lines, respectively. Among surface Fe atoms, the one involved in the chemical bonding with C_{60} is denoted as Fe (contact) whereas non-interacting Fe is referred to as Fe (neighbor). (b) Schematic diagram of energy level alignment for C_{60}(6:6) on Fe(001)-*p*(1×1)O. Δ refers to the Φ increase with respect to Fe(001).

Table 6.6 Calculated interface dipole (Δ), hole injection barrier (Δ_h), electron injection barrier (Δ_e) for C_{60}(6:6) on Fe(001)-*p*(1×1)O as calculated at the DFT, DFT+Σ^{axc}, and G_0W_0(PBE) levels. Details of the correction schemes are provided in the Appendix B. Experimental values are taken from Ref. 40.

	Δ	Δ_h	Δ_e
DFT	1.65 eV	1.43 eV	0.22 eV
DFT+Σ	3.56 eV	2.29 eV	1.27 eV
G_0W_0(PBE)	2.82 eV	2.17 eV	0.55 eV
Expt.	3.2 eV	2.6 eV	0.8 eV

6.4 C_{60}/Magnetite (Fe_3O_4)

6.4.1 Material selection procedure

6.4.1.1 Surface plane and termination

In magnetite, a characteristic dichroic signature has been observed in XAS and XMCD for samples with [100] and the [111] orientations and thickness around one unit cell, however with a lower spin magnetic moment than the bulk value.[52] At a thickness of 2 unit cells, the spin magnetic moment is nearly recovered, and exhibits a ferrimagnetic behavior; this points to the potential usage of Fe_3O_4(111) and Fe_3O_4(001) in spin electronic devices down to (sub)nanoscale thickness.

As illustrated in Chapter 4, the magnetite crystal contains layers of either only iron cations or oxygen anions along the [111] direction with the stacking sequence: O_1-Fe_{oct1}-O_2-Fe_{tet2}-Fe_{oct2}-$Fe_{tet1.}$ Among the six bulk-truncated structures, we have chosen the Fe_{tet1}- and Fe_{oct2}-terminated surfaces for further evaluation of molecular adsorption as they are predicted to be the two most stable terminations often observed in experiments.[53,54]

In the [001] direction, Fe_3O_4 is composed of alternating layers containing two Fe_{tet} cations (A termination) and a plane comprising eight O^{2-} anions and four Fe_{oct} cations (B termination). Among the two bulk terminations, the B layer is preferred to be exposed on the surface with a $(\sqrt{2}\times\sqrt{2})R45°$ reconstruction resulting from a lattice distortion coupled to subsurface charge order. Thus, the B termination is often referred as a distorted bulk truncation (DBT) in the literature.[55]

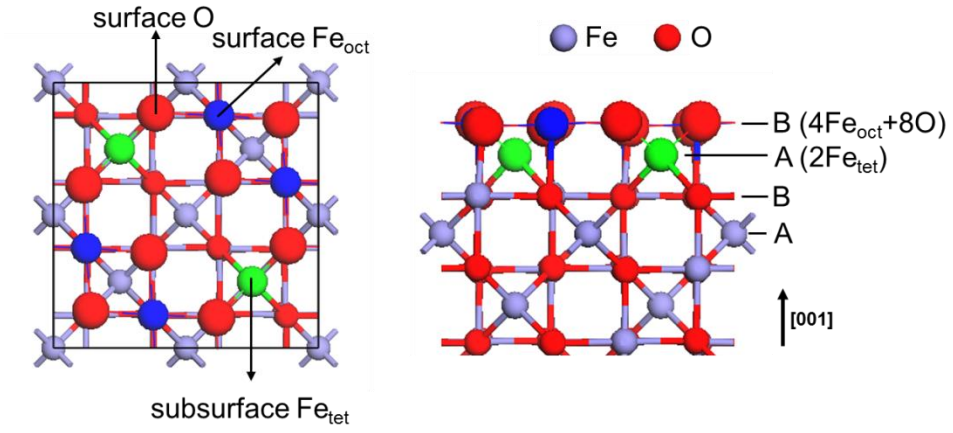

Figure 6.14 Top view (left) and side view (right) of $Fe_3O_4(001)$-$(\sqrt{2}\times\sqrt{2})R45°$, *i.e.*, the B termination. Surface Fe_{oct} atoms and subsurface Fe_{tet} atoms are highlighted in blue and green, respectively, and oxygen atoms in red.

Here, we consider two modified surfaces: a surface cation vacancy (SCV) model and a hydrogen-passivated $Fe_3O_4(001)$ surface, as shown in Figure 6.15. The surface cation vacancy (SCV) model was developed in the course of a study of cobalt adsorption on $Fe_3O_4(001)$. Initially, Co adsorbs as an adatom on the magnetite surface but gradually incorporates within the surface lattice, particularly in the subsurface layers.[55] In the SCV model, the surface Fe_{oct}-O layer remains stoichiometric but is distorted by a rearrangement of the cations in the subsurface layers. Specifically, an additional interstitial Fe_{tet} atom in the second layer replaces two Fe_{oct} atoms from the third layer. Recently, the SCV model with a $(\sqrt{2}\times\sqrt{2})R45°$ reconstruction has been confirmed in LEED experiments together with DFT+*U* calculations that predict the SCV structure to

be thermodynamically more stable than the bulk-truncated surface over the accessible range of oxygen chemical potentials in UHV.[56] While the SCV model is based on intrinsic defects, the 8H-passivated $Fe_3O_4(001)$ surface can be regarded as a chemical pretreatment to manipulate the substrate electronic properties by surface engineering. Experimentally, recovery of the surface half-metallic character was observed for $Fe_3O_4(001)$ annealed at H_2 partial pressure of 10^{-6} mbar.[57] In such conditions, an H_2 is dissociated with a sticking probability ~ 1 and adsorbed on O, forming surface hydroxyls over the B termination. Fe 2*p* core levels are shifted toward lower binding energy in XPS spectra, suggesting the transition from Fe^{3+} to Fe^{2+}. Concomitantly, the H adsorption increases the DOS near E_F and this H-induced DOS shows a spin polarization > 50%.

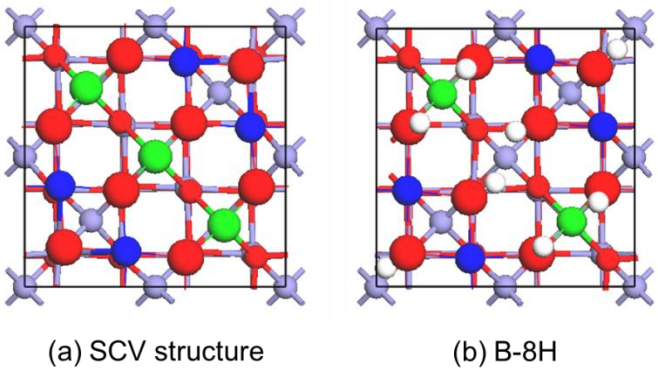

Figure 6.15 Unit cell of (a) a subsurface cation vacancy (SCV) structure and (b) a hydrogen-passivated B termination. Surface Fe_{oct} atoms and subsurface Fe_{tet} atoms are highlighted in blue and green, respectively, and oxygen atoms in red. Hydrogen atoms are in white.

6.4.1.2 Selection of organic semiconductors

The molecular orientation on the substrate plays an important role in determining not only the interface electronic structure but also the subsequent growth pattern of organic films in organic-inorganic hybrid systems.[58] In general, FM metals prefer to have the 1st organic layer deposited on the surface lying flat, particularly with π-conjugated molecules, due to surface stabilization induced by strong *p-d* hybridization. Thus, even a molecule with a large HOMO-LUMO gap, *e.g.*, benzene, can show a broad resonance originating from the hybridization with a dispersive 3*d* band[1] of iron near E_F, leading to an Ohmic-like junction upon metal contact. However, the situation is different for oxide surfaces that typically have high surface stability. On an oxide, only the cation sites can strongly interact with the molecules; therefore, the adsorption geometries can be more diverse. In Figure 6.16, the PDOS are presented for two molecular orientations of benzene on Fe_{tet1}-terminated $Fe_3O_4(111)$: parallel and perpendicular to the surface plane. The adsorption on $Fe_3O_4(111)$ induces rather discrete bonding and antibonding molecule-surface electronic states, and no hybrid interface states are found at E_F (Figure 6.16a). For parallel adsorption, HOMO and HOMO-1 hybridize with surface *d* states of Fe_{tet1} atoms in the region of -1.5 to -3 eV below E_F. On the other hand, the MOs of benzene in a standing configuration (Figure 6.16b) are nearly unperturbed compared to the flat-lying geometry. Also, the adsorption energy is merely ~ 50 meV, indicative of physisorption. Thus, the interface electronic structures are very similar to a linear combination of

[1] Although the d band of metal iron is much sharper than s or p orbitals, it is more dispersive than t_{2g} states of magnetite.

benzene and Fe_{tet1}-terminated magnetite, except that the Fe_{tet1} states slightly shift to higher energy. The main message from this PDOS comparison is that when π-conjugated molecules stand upright on the oxide surface, HISs do not appear; hence, the MOs show no spin polarization.

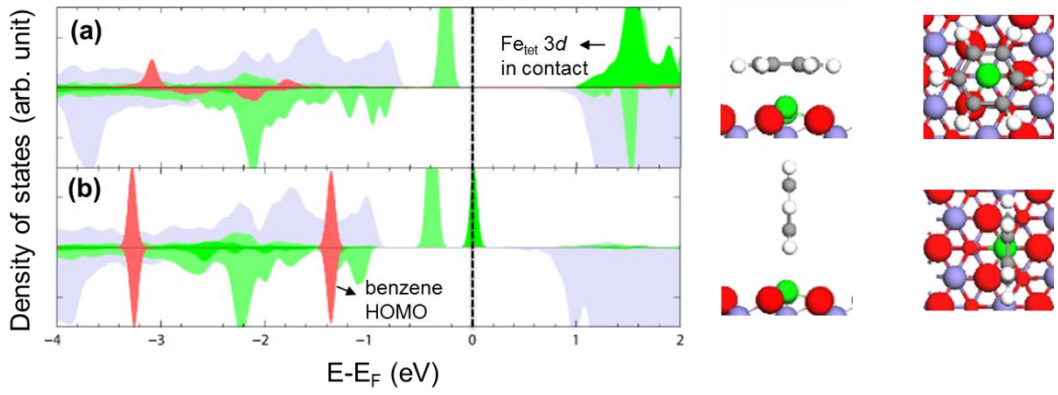

Figure 6.16 (Left) PDOS of benzene/Fe_{tet1}-terminated Fe_3O_4(111) in two different molecular orientations: (a) parallel and (b) perpendicular to the surface. The surface Fe_{tet1} atoms are colored in green; a more saturated color is used to indicate the surface atom on which a benzene molecule adsorbs. Light blue corresponds to Fe_{oct} atoms in the 3rd layer. The molecule-derived orbitals are colored in red. (Right) Optimized interface structure within the top three layers (Fe_{tet1}-O_1-Fe_{oct1}). Green, red, and purple represents $Fe_{tet1,}$ O_1, and Fe_{oct1} atoms, respectively.

As the surface coverage of π-conjugated molecules gets higher on the oxide, the dispersion between neighboring molecules becomes stronger, and eventually overcomes

the weak coupling with the substrate. It possibly leads the molecules to cluster in a standing configuration. NEXAFS measurements indicate that pentacene has a tilt angle of ~22° on top of LSMO (angle between the molecular axis and the substrate surface normal) with no evidence for charge transfer from XAS and UPS measurements.[59] Therefore, the major bottleneck in designing an efficient OSC-FM oxide interface is to find molecules that can have a flat-lying adsorption on the oxide surface. In this context, C_{60} is a promising candidate as its isotropic structure ensures overlap between its π-electron levels and the surface Fe 3*d* states, regardless of binding configuration. Thus, we now focus on C_{60} as a non-magnetic spacer for Fe_3O_4.

6.4.2 $C_{60}/Fe_3O_4(111)$

Based on our previous study, the DOS have distinctive features depending on the surface termination of $Fe_3O_4(111)$, which are directly reflected in the surface spin polarization. As presented in the inset of Figure 6.17, the Fe_{tet1} termination shows a positive spin polarization below and negative above the Fermi level, while the termination with octahedral Fe atoms (Fe_{oct2}) presents a negative $P(E)$ in the vicinity of the Fermi level.

After geometric relaxation, we find the center of the hexagon face of C_{60} placed above one surface Fe atom, both for Fe_{tet1}- and Fe_{oct2}-terminated $Fe_3O_4(111)$. Upon C_{60} adsorption, interface *p-d* hybridization leads to spin-discriminated molecular orbitals of C_{60}. We should note that the surface states play a pivotal role in determining the spin polarization direction of the adsorbed molecule near the Fermi level. For Fe_{tet1} termination, the LUMO hybridizes mostly with positively polarized surface states; thus,

the tails of the hybridized peak in the spin majority channel appear at E_F (Figure 6.17a). In contrast, on the Fe_{oct2} termination that has negatively spin-polarized surface states, the spin-resolved hybrid interface states appear in the spin minority channel at E_F (Figure 6.17b). By comparison to the metal-organic interface, the spin polarization of hybrid states could be essentially 100%. In particular, in the case of C_{60}/Fe_{oct2}, an appreciable negative spin polarization right below E_F can be obtained. Figure 6.18 illustrates the spatial distribution of spin polarization in the vicinity of E_F. Strikingly, the spin polarization of the hybridized state extends all over the molecule, which implies a significant enhancement of the spin transport from the interface (1^{st}) C_{60} layer to the bulk C_{60}. Furthermore, the direction of spin polarization is consistently negative at any part of C_{60}, confirming that the interface C_{60} layer can be used as an efficient spin injector. Considering that there is no evident spin-split peak near the Fermi level in the case of OSC/Fe(001), see Section 6.3, this is a fascinating feature specific to organic-FM oxide interfaces. However, our theoretical evaluation of relative surface stabilities suggests that the Fe_{oct2} termination becomes favorable over Fe_{tet1} only under very reducing conditions, nominally less than 10^{-20} mbar O_2 at a typical annealing temperature (assuming a stoichiometric sample). This is consistent with the fact that experimentally only a small fraction of the surface exhibits the Fe_{oct2} termination.[60] Thus, the thermal deposition of C_{60} on a Fe_{oct2}-terminated $Fe_3O_4(111)$ is actually not a likely event.

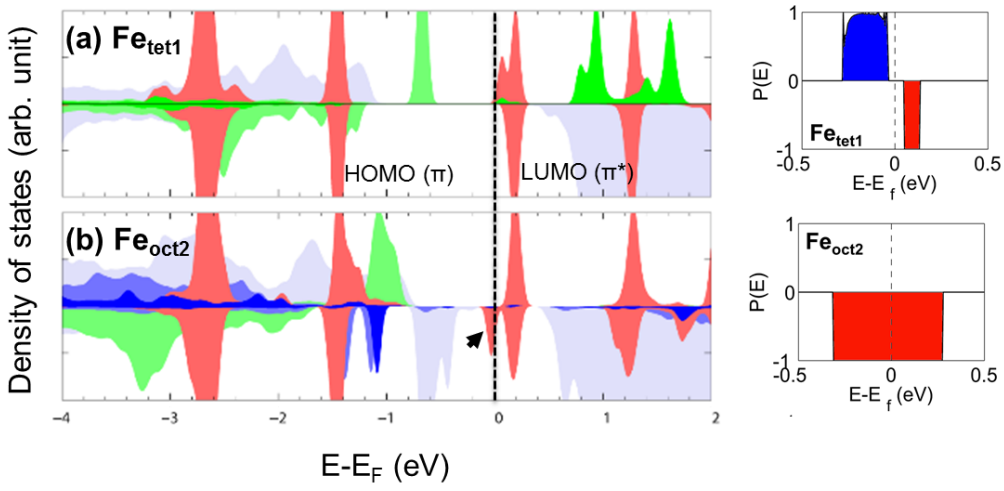

Figure 6.17 PDOS of (a) C_{60}/Fe_{tet1}-terminated Fe_3O_4(111) and (b) C_{60}/Fe_{oct2}-terminated Fe_3O_4(111). After geometry optimization, the center of the hexagon face of C_{60} appears above one surface Fe atom. The surface Fe_{tet} and Fe_{oct} atoms are colored in a green and blue, respectively; a more saturated color is used to indicate the surface atom on which C_{60} (red area) directly adsorb. The light blue area corresponds to Fe_{oct} atoms in subsurface layer. Inset images represent spin polarization as a function of energy, P(E), calculated for the Fe_{tet1} and Fe_{oct2} terminations of Fe_3O_4(111) in the range [E_F -0.5 eV, E_F +0.5 eV]

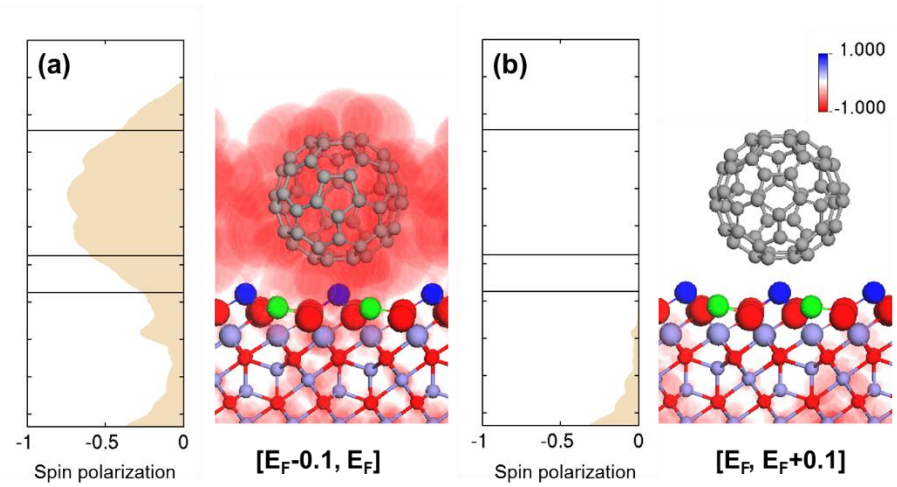

Figure 6.18 Spatial representation of spin polarization in C_{60}/Fe_{oct2} within a finite energy interval of (a) [E_F-0.1eV, E_F] and (b) [E_F, E_F+0.1eV]. The color map is given as red [blue] for negative [positive] spin polarization. The graph on the left side indicates the plane-averaged spin polarization at the given z-coordinate.

6.4.3 $C_{60}/Fe_3O_4(001)$

6.4.3.1 Perfect B termination

As explained in Section 6.4.1.1, the most favorable bulk termination of $Fe_3O_4(001)$ contains four Fe_{oct} atoms exposed on the surface. Thus, the B termination allows the π electron levels of C_{60} to interact with the half-metallic t_{2g} states of Fe_3O_4, which overcomes the problem we previously discussed regarding $Fe_3O_4(111)$.

In the initial geometry, one 6:6 edge site of C_{60} is lying on top of two Fe_{oct} atoms, which corresponds to the most favorable interface configuration found for C_{60} on Fe(001), *i.e.*, C_{60}(6:6)/Fe(001). After geometry optimization, the Fe_{oct} atoms at the surface B layer tend

to be compressed by 0.06-0.15 Å upon C_{60} adsorption. C_{60} remains located 2.42 Å above surface Fe_{oct} atoms and the shortest Fe-C distance is calculated to be 2.57 Å. Given that the calculated vertical distance and the shortest bond length of Fe-C_{60} are 1.21 Å and 1.93 Å, respectively, in C_{60}(6:6)/Fe(001), C_{60} has much weaker interaction with Fe_3O_4(001) than the metal substrate. While this optimized geometry is indicative of physisorption, the interface electronic structures suggest chemical interactions between C_{60} and Fe_3O_4(001).

In Figure 6.19, the PDOS of Fe_3O_4(001) is displayed before and after adsorption of C_{60} on the surface. Interestingly, the Fe 3*d*-C 2*p* hybridized peak appears exactly at the Fermi level (marked with an arrow in Figure 6.19b). This is consistent with C *K*-edge XAS spectra that point to electronic interactions between C_{60} π (π*) and Fe_3O_4 3*d* states.[61] To qualitatively examine this interface state, we plotted the spatial distribution of spin polarization near the Fermi level based on the spin density calculated at the PBE+*U* level. As for C_{60}/Fe_{oct2}-terminated Fe_3O_4(111), a negative spin polarization of the hybridized state entirely dominates over the whole molecular site. Considering the energy level alignment, electron injection is more favorable than hole injection with barriers of 0.4 eV and 1.3 eV, respectively. This is in good agreement with the experimental measurements that show an electron injection barrier of 0.6 eV and hole injection barrier of 1.7 eV.[62]

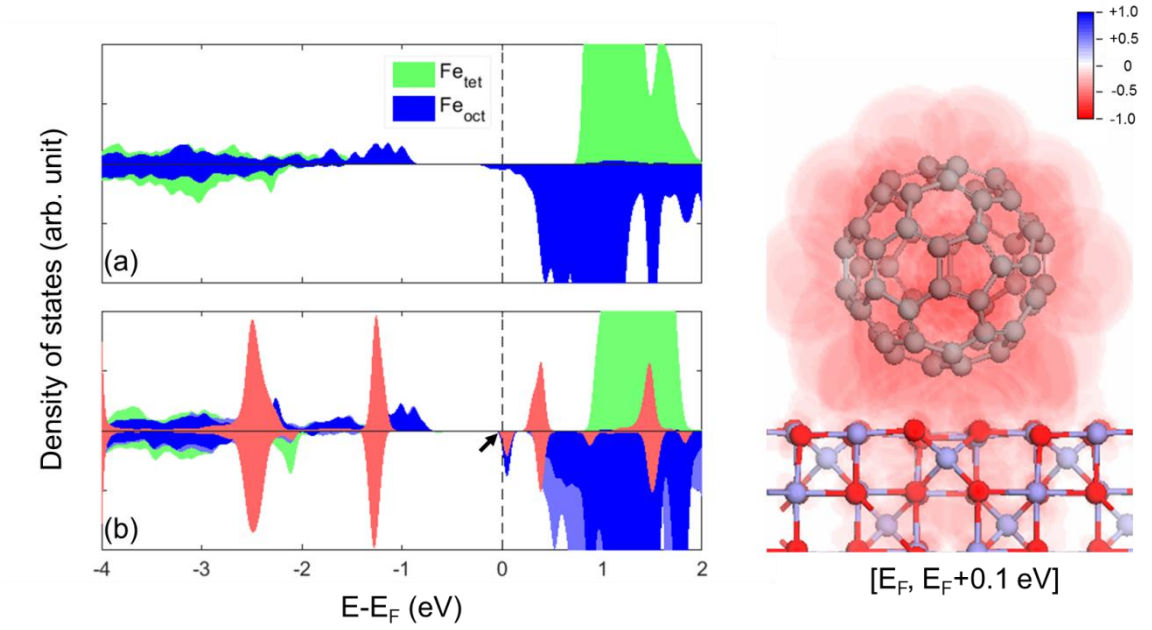

Figure 6.19 PDOS of (a) a clean B-terminated Fe_3O_4(001) and (b) with C_{60} adsorption. Here, the 6:6 bond of C_{60} is located above two surface Fe_{oct} atoms. The surface Fe_{oct} atoms are colored in blue (states/atom); a more saturated color is used to indicate the surface atom (states/atom) on which C_{60} (red area, 1/6*states/molecule) directly adsorbs. The subsurface Fe_{tet} is colored in green. The inset represents the spatial representation of spin polarization in C_{60}/Fe_3O_4(001) in the range [E_F, E_F+0.1eV], as indicated in (b). The color map is given as red [blue] for negative [positive] spin polarization.

The interface hybridization effect leads to a charge transfer between C_{60} and Fe_3O_4: the electron donation from C_{60} to Fe_3O_4(001) is calculated to be 0.17 e based on Bader charge analysis. This charge transfer further induces the magnetization of C_{60} with a net magnetic moment of 0.06 μ_B. In recent synchrotron-based PES experiments, Wong *et al.* found a relative increase in Fe_{oct}^{2+} concentration in epitaxial Fe_3O_4(001) upon C_{60} adsorption, primarily caused by filling of the spin-down t_{2g} band with electrons donated

by C_{60}. If charge transfer dominantly occurs between C_{60} and surface Fe_{oct} atoms in contact, these must gain the same amount of charge as the adsorbed C_{60} loses. However, the calculated atomic charges suggest that only a negligible change in magnetic moment is predicted for surface Fe_{oct} atoms facing C_{60} on top, which appears contradictory. Our DFT results suggest that the reduction may occur in the neighboring Fe_{oct} atoms which are exposed on surface but not directly bind to the adsorbate. The calculated net charge increase of the surface B layer is +0.15 e, which implies that the non-interacting Fe_{oct} atoms on the surface play a pivotal role in accepting electron from C_{60}. The reduction of Fe_{oct} upon molecular adsorption has been seen experimentally for other organic molecules, for example, benzene.[63] It should be pointed out that the electron gain of the surface layer is slightly lower than the amount of electrons donated by C_{60}; the remainder of the charge leads to reduction of subsurface layers even including Fe_{tet}^{3+}. This corresponds to one of the major findings in Ref. 62 where the authors found non-negligible peak attenuation for Fe_{tet}^{3+} in resonant PES spectra upon C_{60} adsorption. However, we cannot confirm their physical model of charge rebalancing by electron transfer from the t_2 band of Fe_{tet}^{3+} to the t_{2g} band of Fe_{oct}^{2+}. The Fe-C bond dipole combined with the charge redistribution within the substrate leads to a small decrease in work function of Fe_3O_4 (001) by 0.15 eV.

6.4.3.2 Impacts of surface modification

In the proposed SCV structure, two Fe_{oct} cations (S-2) are replaced by one Fe_{tet} interstitial (S-1) in subsurface layers. Such subsurface reorganization distorts the surface layer, and

the resulting interlayer relaxation at the surface region is more pronounced compared to B-terminated Fe_3O_4(001) (see Table 6.7). The structural distortion also brings about modifications of the electronic structure. As shown in Figure 6.20a, the spin-down *d* band of the surface Fe_{oct} is shifted above E_F, leaving the surface states at the bottom of the unoccupied band, consisting of t_{2g} states. However, the calculated atomic charges and spin magnetic moments within the topmost three layers indicate that the surface chemistry does not change dramatically with introducing of cation vacancy (see Table 6.8).

Table 6.7 Surface relaxations in the topmost three layers given as a percentage (Δ_{ij}) of the bulk interlayer distances between two adjacent surface planes (i) and (j) projected onto the c axis for three surface models.

	B	SCV	8H
Δ_{12}	-20.22	-26.03	9.70
Δ_{23}	15.04	7.05	9.48
Δ_{34}	9.28	5.84	-9.75

Table 6.8 Atomic charge and magnetization (per atom) of the Fe cations in the top three layers for three surface models. The calculated values for the equivalent atoms in cubic Fe_3O_4 are given for the sake of comparison. A and B represent a tetrahedral and octahedral site, respectively.

	Bader charge (e)			Spin magnetic moment (μ_B)		
	B	SCV	8H	B	SCV	8H
S (B)	6.18	6.13	6.51	4.17	4.15	3.71
S-1 (A)	6.12	6.14	6.54	-4.09	-4.09	-3.64
S-2 (B)	6.13	6.11	6.36	4.18	4.18	3.89
bulk	6.36(B), 6.14(A)			3.97(B), -4.08(A)		

As we have learned from previous studies on $C_{60}/Fe_3O_4(111)$, the energy level and density of the oxide surface states are the key factors that determine the nature of the hybridized interface states upon molecular adsorption. This is confirmed once again from the PDOS of C_{60} on the SCV structure where a small negative spin-polarized HIS appears near E_F. In contrast to C_{60} on the unmodified surface for which HIS is located right at E_F, the hybridized state on SCV appears at the tail of the spin-down t_{2g} band, suggesting the interface to have resistive spin-filtering, which would require an external bias for carrier injection. Despite the fact that C_{60} is fairly distant from the substrate (2.65 Å), there occurs a charge transfer of 0.18 e from C_{60} to the electrode, which is consistent with the decreased in work function by 0.17 eV.

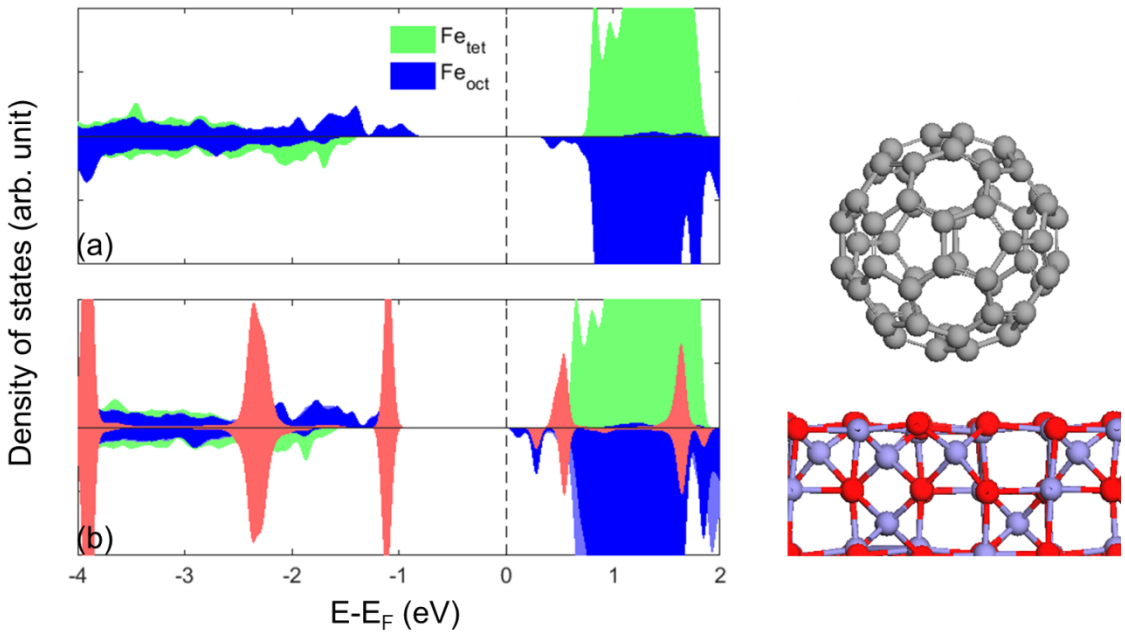

Figure 6.20 PDOS of (a) a subsurface cation vacancy (SCV) structure of Fe_3O_4(001) and (b) the same surface upon C_{60} adsorption. The surface Fe_{oct} atoms are colored in blue (states/atom); a more saturated color is used to indicate the surface atom (states/atom) on which C_{60} (red area, 1/6*states/molecule) directly adsorbs. The subsurface Fe_{tet} is colored in green (states/atom).

To construct H-passivated Fe_3O_4(001), a single H atom was placed on atop position at each of the surface O atoms. After geometric relaxation, some of the hydrogen atoms are slightly tilted while the others are strongly displaced laterally from their initial positions in order to have surface hydroxyls nearly parallel to the surface, forming a complex hydrogen bond network with the neighboring surface O atoms. The recovery of a perfect coordination of surface O atoms leads to the elongation of Fe_{oct}-O bonds by up to 0.2 Å,

which leads to even longer bonds than for the Fe_{oct}-O bond length in the bulk. On this H-saturated surface, Fe_{oct} atoms are strongly reduced and convert completely to Fe^{2+}, which is in line with the PDOS of Figure 6.21a that shows a strong Fe 3*d* peak below E_F. It should be noted that this reduction is not limited to the Fe atoms in octahedral sites but also the ones in subsurface tetrahedral sites (see Table 6.8). The origin of this electron-rich surface is the electron donation coming from the adsorbed H to the surface O atoms and then to Fe cations. This mechanism was initially proposed by Parkinson *et al.*[57] and confirmed in the recent work by Hiura and coworkers using XPS and STM/STS.[64]

Interestingly, the direction of electron transfer is now reversed from what is seen on clean Fe_3O_4(001); electron donation from the substrate to C_{60} is expected. This is not unexpected given that the calculated work function of 8H-passivated Fe_3O_4(001) is as low as 2.91 eV. In this condition, even a full integer charge transfer may occur from the Fermi level of the substrate to the unoccupied levels of C_{60}. However, the broadened LUMO peak of C_{60} is positioned at E_F, which implies hybridization-induced charge transfer. Accordingly, the work function significantly increases by 1.26 eV, which conflicts with the case of C_{60} adsorption on a clean surface. In addition, the molecule becomes negatively magnetized, which is the opposite of the results for C_{60} on the other surfaces studied in this work.

Due to the populating of surface Fe 3*d* states between -1 to -2 eV, more dispersive MOs with spin discrimination are obtained for C_{60} on 8H-passivated Fe_3O_4(001), as displayed in Figure 6.21b. Spin polarization of HISs at E_F is antiparallel to the polarization of a magnetite electrode (negative), which is not favorable for efficient injection.

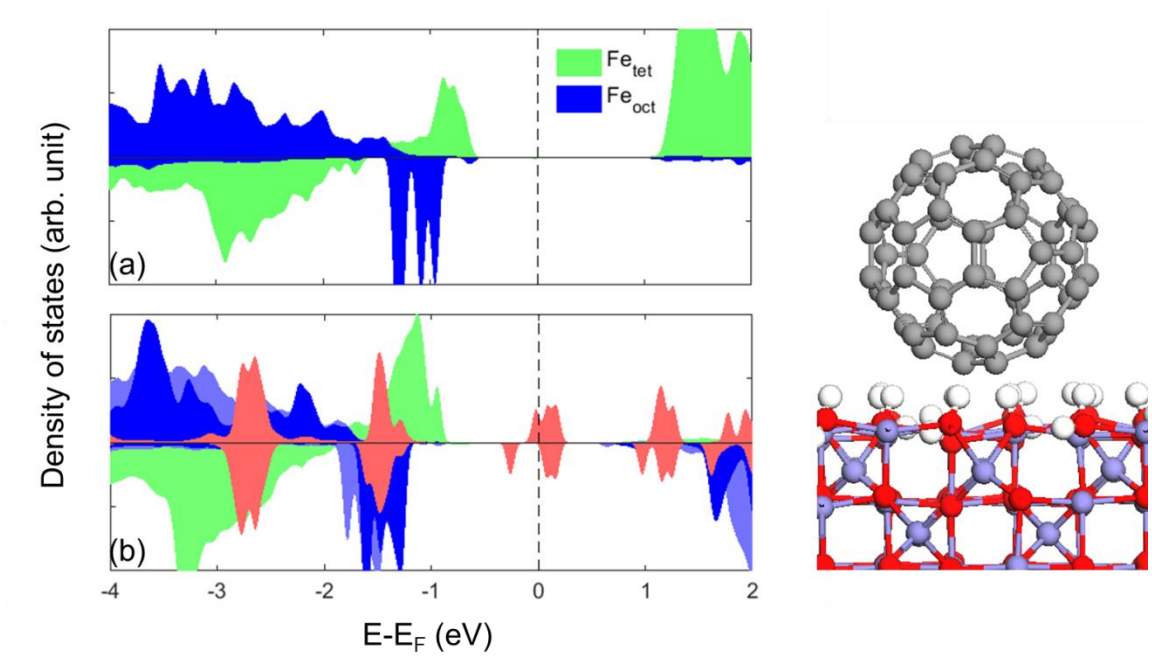

Figure 6.21 PDOS of (a) 8H-passivated Fe_3O_4(001) and (b) with C_{60} adsorption on it. The surface Fe_{oct} atoms are colored in blue (states/atom); a more saturated color is used to indicate the surface atom (states/atom) on which C_{60} (red area, 1/6*states/molecule) directly adsorbs. The subsurface Fe_{tet} is colored in green (states/atom).

Table 6.9 Average change in atomic charge and magnetization (per atom) in C_{60} and the surface Fe_{oct} in contact with the molecule. All the values listed represent the changes from the values for the equivalent surface without C_{60} adsorption.

	C_{60}		Surface Fe_{oct} in contact	
	ΔQ (e)	$\Delta\mu_S$ (μ_B)	ΔQ (e)	$\Delta\mu_S$ (μ_B)
B	-0.17	0.06	-0.02	-0.01
SCV	-0.18	0.05	0.00	-0.01
8H	1.33	-0.05	-0.05	-0.01

6.5 Conclusions

In this Chapter, a comprehensive first-principles study based on DFT has been presented to investigate the distinctive interface electronic/magnetic properties of organic-ferromagnetic junctions.

We first started with conventional organic-ferromagnetic metal systems: Alq_3, pentacene, and C_{60} in contact with Fe(001). Strong interface π-d hybridization leads to chemisorption of the adsorbate molecules on the metal surface, accompanied by significant charge redistribution at the interface. The energy level alignment including the effect of interface dipoles suggests that all three molecules have lower injection barrier for electrons. Despite the strong coupling between OSCs and Fe(001), the adsorbed molecules show highly dispersive hybridized interface states near E_F with low spin discrimination. C_{60} on Fe(001)-p(1×1)O has been also explored to understand the interaction between OSC and FM in the presence of a tunnel barrier. Even a single monolayer of oxygen can completely decouple the adsorbate from the substrate; molecular adsorption in this condition can be characterized as physisorption. Here, there is no magnetization or spin polarization for C_{60} in the interfacial layer.

Then, we assessed the potential utilization of magnetite as a ferromagnetic electrode by investigating the interface electronic structures in $C_{60}/Fe_3O_4(111)$ and $C_{60}/Fe_3O_4(001)$. We found that the proximity of the molecular orbital and surface state energies is a major issue that plays a critical role in determining the spin polarization direction of the adsorbed molecule near the Fermi level. The calculations predict that an appreciable negative spin polarization can be achieved only in specific systems, such as C_{60} on Fe_{oct2}-

terminated Fe_3O_4(111) or ($\sqrt{2}\times\sqrt{2}$)*R*45°- B-terminated Fe_3O_4(001). The subsurface cation vacancy introduced in Fe_3O_4(001) does not have any major impact on electron transfer between C_{60} and magnetite; however, hybridized states derived from the modified electronic structures of the substrate lead to a resistive spin-filtering character of the interfacial layer. The reduced Fe_{oct} atoms resulting from H adsorption do not introduce spin-coherent hybridized states to the bulk polarization near the Fermi level.

6.6 References

[1] Lach, S.; Altenhof, A.; Tarafder, K.; Schmitt, F.; Ali, M. E.; Vogel, M.; Sauther, J.; Oppeneer, P. M.; Ziegler, C. *Adv. Func. Mater.* **2012**, *22*, 989.

[2] Atodiresei, N.; Raman, K. V. *MRS Bull.* **2014**, *39*, 596.

[3] Shi, S. W.; Sun, Z. Y.; Bedoya-Pinto, A.; Graziosi, P.; Li, X.; Liu, X. J.; Hueso, L.; Dediu, V. A.; Luo, Y.; Fahlman, M. *Adv. Func. Mater.* **2014**, *24*, 4812.

[4] Chen, W.; Huang, C.; Gao, X. Y.; Wang, L.; Zhen, C. G.; Qi, D. C.; Chen, S.; Zhang, H. L.; Loh, K. P.; Chen, Z. K.; Wee, A. T. S. *J. Phys. Chem. B* **2006**, *110*, 26075.

[5] Duhm, S.; Glowatzki, H.; Rabe, J. P.; Koch, N.; Johnson, R. L. *App.l Phys. Lett.* **2006**, *88*, 326.

[6] Zhou, Y. H.; Fuentes-Hernandez, C.; Shim, J.; Meyer, J.; Giordano, A. J.; Li, H.; Winget, P.; Papadopoulos, T.; Cheun, H.; Kim, J.; Fenoll, M.; Dindar, A.; Haske, W.; Najafabadi, E.; Khan, T. M.; Sojoudi, H.; Barlow, S.; Graham, S.; Bredas, J. L.; Marder, S. R.; Kahn, A.; Kippelen, B. *Science* **2012**, *336*, 327.

[7] Galbiati, M.; Tatay, S.; Barraud, C.; Dediu, A. V.; Petroff, F.; Mattana, R.; Seneor, P. *MRS Bull.* **2014**, *39*, 602.

[8] Schulz, L.; Nuccio, L.; Willis, M.; Desai, P.; Shakya, P.; Kreouzis, T.; Malik, V. K.; Bernhard, C.; Pratt, F. L.; Morley, N. A.; Suter, A.; Nieuwenhuys, G. J.; Prokscha, T.; Morenzoni, E.; Gillin, W. P.; Drew, A. J. *Nature Mater.* **2011**, *10*, 252.

[9] Sun, D. L.; Fang, M.; Xu, X. S.; Jiang, L.; Guo, H. W.; Wang, Y. M.; Yang, W. T.; Yin, L. F.; Snijders, P. C.; Ward, T. Z.; Gai, Z.; Zhang, X. G.; Lee, H. N.; Shen, J. *Nature Commun.* **2014**, *5*, 4396.

[10] Schmidt, G.; Ferrand, D.; Molenkamp, L. W.; Filip, A. T.; van Wees, B. J. *Phys. Rev. B* **2000**, *62*, R4790.

[11] Rashba, E. I. *Phys. Rev. B* **2000**, *62*, R16267.

[12] Ruden, P. P.; Smith, D. L. *Journal of Applied Physics* **2004**, *95*, 4898.

[13] Tannhauser, D. S. *J. Phys. Chem. Solids* **1962**, *23*, 25.

[14] Nguyen, T. D.; Ehrenfreund, E.; Vardeny, Z. V. *Science* **2012**, *337*, 204.

[15] Vardeny, Z. V. *Organic spintronics*; CRC Press/Taylor & Francis: Boca Raton, 2010.

[16] Barraud, C.; Seneor, P.; Mattana, R.; Fusil, S.; Bouzehouane, K.; Deranlot, C.; Graziosi, P.; Hueso, L.; Bergenti, I.; Dediu, V.; Petroff, F.; Fert, A. *Nature Phys.* **2010**, *6*, 615.

[17] Dey, P.; Rawat, R.; Potdar, S. R.; Choudhary, R. J.; Banerjee, A. *J. Appl. Phys.* **2014**, *115*.

[18] Pratt, A.; Dunne, L.; Sun, X.; Kurahashi, M.; Yamauchi, Y. *J. Appl. Phys.* **2012**, *111*.

[19] Zhang, X. M.; Mizukami, S.; Ma, Q. L.; Kubota, T.; Oogane, M.; Naganuma, H.; Ando, Y.; Miyazaki, T. *J. Appl. Phys.* **2014**, *115*.

[20] Zhang, X. M.; Ma, Q. L.; Suzuki, K.; Sugihara, A.; Qin, G. W.; Miyazaki, T.; Mizukami, S. *Acs Appl. Mater. Inter.* **2015**, *7*, 4685.

[21] Zhang, X. M.; Mizukami, S.; Kubota, T.; Ma, Q. L.; Oogane, M.; Naganuma, H.; Ando, Y.; Miyazaki, T. *Nature Commun.* **2013**, *4*.

[22] Kresse, G.; Furthmuller, J. *Comp. Mater. Sci.* **1996**, *6*, 15.

[23] Kresse, G.; Furthmuller, J. *Phys. Rev. B* **1996**, *54*, 11169.

[24] Perdew, J. P.; Burke, K.; Ernzerhof, M. *Phys. Rev. Lett.* **1997**, *78*, 1396.
[25] Anisimov, V. I.; Zaanen, J.; Andersen, O. K. *Phys. Rev. B* **1991**, *44*, 943.
[26] Dudarev, S. L.; Botton, G. A.; Savrasov, S. Y.; Humphreys, C. J.; Sutton, A. P. *Phys. Rev. B* **1998**, *57*, 1505.
[27] Grimme, S.; Antony, J.; Ehrlich, S.; Krieg, H. *J. Chem. Phys.* **2010**, *132*.
[28] Iota, V.; Klepeis, J. H. P.; Yoo, C. S.; Lang, J.; Haskel, D.; Srajer, G. *Appl. Phys. Lett.* **2007**, *90*.
[29] Alden, M.; Mirbt, S.; Skriver, H. L.; Rosengaard, N. M.; Johansson, B. *Phys. Rev. B* **1992**, *46*, 6303.
[30] Ohnishi, S.; Freeman, A. J.; Weinert, M. *Phys. Rev. B* **1983**, *28*, 6741.
[31] Zhan, Y. Q.; Holmstrom, E.; Lizarraga, R.; Eriksson, O.; Liu, X. J.; Li, F. H.; Carlegrim, E.; Stafstrom, S.; Fahlman, M. *Adv. Mater.* **2010**, *22*, 1626.
[32] Suzuki, T.; Kurahashi, M.; Ju, X.; Yamauchi, Y. *Surf. Sci.* **2004**, *549*, 97.
[33] Sun, X.; Suzuki, T.; Kurahashi, M.; Zhang, J. W.; Yamauchi, Y. *J. Appl. Phys.* **2007**, *101*, 09G526.
[34] Chen, W. K.; Cao, M. J.; Liu, S. H.; Xu, Y.; Li, Y.; Li, J. Q. *Acta Physico-Chimica Sinica* **2005**, *21*, 903.
[35] Chen, W. K.; Cao, M. J.; Liu, S. H.; Lu, C. H.; Xu, Y.; Li, J. Q. *Chem. Phys. Lett.* **2006**, *417*, 414.
[36] Sun, X.; Suzuki, T.; Yamauchi, Y.; Kurahashi, M.; Wang, Z. P.; Entani, S. *Surf. Sci.* **2008**, *602*, 1191.
[37] Cakir, D.; Otalvaro, D. M.; Brocks, G. *Phys. Rev. B* **2014**, *90*, 245404.
[38] Wood, C.; Li, H.; Winget, P.; Bredas, J. L. *J. Phys. Chem. C* **2012**, *116*, 19125.
[39] Li, H.; Ratcliff, E. L.; Sigdel, A. K.; Giordano, A. J.; Marder, S. R.; Berry, J. J.; Bredas, J. L. *Adv. Func. Mater.* **2014**, *24*, 3593.
[40] Picone, A.; Giannotti, D.; Riva, M.; Calloni, A.; Bussetti, G.; Berti, G.; Duo, L.; Ciccacci, F.; Finazzi, M.; Brambilla, A. *Acs Appl. Mater. Inter.* **2016**, *8*, 26418.
[41] Perdew, J. P.; Parr, R. G.; Levy, M.; Balduz, J. L. *Phys. Rev. Lett.* **1982**, *49*, 1691.
[42] Tran, T. L. A.; Wong, P. K. J.; de Jong, M. P.; van der Wiel, W. G.; Zhan, Y. Q.; Fahlman, M. *Appl. Phys. Lett.* **2011**, *98*, 222505.
[43] Tran, T. L. A.; Cakir, D.; Wong, P. K. J.; Preobrajenski, A. B.; Brocks, G.; van der Wiel, W. G.; de Jong, M. P. *Acs Appl. Mater. Inter.* **2013**, *5*, 837.
[44] Zutic, I.; Fabian, J.; Das Sarma, S. *Rev. Mod. Phys.* **2004**, *76*, 323.
[45] Raman, K. V.; Kamerbeek, A. M.; Mukherjee, A.; Atodiresei, N.; Sen, T. K.; Lazic, P.; Caciuc, V.; Michel, R.; Stalke, D.; Mandal, S. K.; Blugel, S.; Munzenberg, M.; Moodera, J. S. *Nature* **2013**, *493*, 509.
[46] Raman, K. V. *Appl. Phys. Rev.* **2014**, *1*, 031101.
[47] Kanamori, J.; Terakura, K. *J. Phys. Soc. Japan* **2001**, *70*, 1433.
[48] Li, D. Z.; Barreteau, C.; Kawahara, S. L.; Lagoute, J.; Chacon, C.; Girard, Y.; Rousset, S.; Repain, V.; Smogunov, A. *Phys. Rev. B* **2016**, *93*, 085425.
[49] Lazic, P.; Caciuc, V.; Atodiresei, N.; Callsen, M.; Blugel, S. *J Phys.-Condens. Mat.* **2014**, *26*, 263001.
[50] Galbiati, M. Molecular Spintronics: From Organic Semiconductors to Self-Assembled Monolayers; Springer Theses-Reco, 2016.

[51] Donati, F.; Sessi, P.; Achilli, S.; Bassi, A. L.; Passoni, M.; Casari, C. S.; Bottani, C. E.; Brambilla, A.; Picone, A.; Finazzi, M.; Duo, L.; Trioni, M. I.; Ciccacci, F. *Phys. Rev. B* **2009**, *79*, 195430.
[52] Gomes, G. F. M.; Bueno, T. E. P.; Parreiras, D. E.; Abreu, G. J. P.; de Siervo, A.; Cezar, J. C.; Pfannes, H. D.; Paniago, R. *Phys. Rev. B* **2014**, *90*, 134422.
[53] Lennie, A. R.; Condon, N. G.; Leibsle, F. M.; Murray, P. W.; Thornton, G.; Vaughan, D. J. *Phys. Rev. B* **1996**, *53*, 10244.
[54] Cutting, R. S.; Muryn, C. A.; Thornton, G.; Vaughan, D. J. *Geochim Cosmochim Ac* **2006**, *70*, 3593.
[55] Parkinson, G. S. *Surf. Sci. Reports* **2016**, *71*, 272.
[56] Bliem, R.; McDermott, E.; Ferstl, P.; Setvin, M.; Gamba, O.; Pavelec, J.; Schneider, M. A.; Schmid, M.; Diebold, U.; Blaha, P.; Hammer, L.; Parkinson, G. S. *Science* **2014**, *346*, 1215.
[57] Parkinson, G. S.; Mulakaluri, N.; Losovyj, Y.; Jacobson, P.; Pentcheva, R.; Diebold, U. *Phys. Rev. B* **2010**, *82*, 125413.
[58] Duhm, S.; Heimel, G.; Salzmann, I.; Glowatzki, H.; Johnson, R. L.; Vollmer, A.; Rabe, J. P.; Koch, N. *Nature Mater.* **2008**, *7*, 326.
[59] Li, F. H.; Graziosi, P.; Tang, Q.; Zhan, Y. Q.; Liu, X. J.; Dediu, V.; Fahlman, M. *Phys. Rev. B* **2010**, *81*.
[60] Shimizu, T. K.; Jung, J.; Kato, H. S.; Kim, Y.; Kawai, M. *Phys. Rev. B* **2010**, *81*, 235429.
[61] Wong, P. K. J.; Zhang, W.; Wang, K.; van der Laan, G.; Xu, Y. B.; van der Wiel, W. G.; de Jong, M. P. *J. Mater. Chem. C* **2013**, *1*, 1197.
[62] Wong, P. K. J.; Zhang, W.; van der Laan, G.; de Jong, M. P. *Org. Electron.* **2016**, *29*, 39.
[63] Pratt, A.; Kurahashi, M.; Sun, X.; Yamauchi, Y. *J. Phys. D Appl. Phys.* **2011**, *44*, 064010.
[64] Hiura, S.; Ikeuchi, A.; Shirini, S.; Subagyo, A.; Sueoka, K. *Phys. Rev. B* **2015**, *91*, 205411.

CHAPTER 7. CONCLUSIONS AND OUTLOOK

7.1 Conclusions

Much attention is given to corrosion phenomena of iron and iron alloys as corrosion-related structural failures have led to serious environmental incidents and cause tremendous economic losses. Over the past decades, hazardous biological and environmental effects from chromium-based coatings have called for their replacement with eco-friendly corrosion inhibitors. In this Thesis, we have explored self-assembled monolayers (SAMs) as a promising organic inhibitor to protect iron from oxidation. Our computational/theoretical approaches have provided quantitative structure-property descriptions of the interfacial processes to elucidate the inhibition mechanisms and assess the inhibition efficiencies for series of molecular modifiers with various chemical functionalities. Since iron oxides themselves can be of practical importance in the field of organic spintronics, we have also investigated the distinct electronic and magnetic properties of the interfaces between iron oxide-based substrates and representative π-conjugated molecules in the context of development of efficient magnetic junctions.

Largely, this Thesis has focused on the theoretical characterization of the surface and interface chemistry of iron and iron oxides when modified by an organic layer. Materials

containing an organic-inorganic heterojunction have been examined not only individually (Chapters 3 and 4) but also collectively (Chapters 5 and 6).

Starting from thorough computational studies on bulk iron and iron oxides with different oxidation states, we first established an optimal level of calculations that could be applied to more complex systems, such as a modified surface, at a reasonable computation cost. The work presented in Chapter 3 points out that a Hubbard U correction or partial inclusion of HF exact exchange (E_{xx}) in hybrid functionals can alleviate the failure of conventional DFT calculations in describing the strongly correlated nature of iron oxides. It is important to carefully choose the U_{eff} or E_{xx} parameters by tuning them to reproduce the experimentally obtained physical values. We showed that either DFT+ U with U_{eff} = 4 eV or HSE06 with E_{xx} = 15% is a reasonable choice for iron oxides. Among many-body quasi-particle (QP) techniques that do not require any empirical input, scQPGW_0 based on PBE-derived Kohn-Sham wavefunctions is found to describe well the electronic structures of iron oxides, both quantitatively and qualitatively.

The surface structure calculations of Chapter 4, when combined with thermochemistry, can be used to determine the equilibrium surface configurations of iron oxides as a function of the partial pressures of oxygen and water, temperature, solution pH, and electrode potential. A given set of these conditions represent the thermodynamic variables during oxide thin-film growth via thermal oxidation and electrochemical passivation. The results of this Chapter demonstrate that defect formation and/or molecular adsorption can be introduced on specific surface domains at certain preparation/experimental conditions, and play a critical role in surface chemistry and electronic structures.

Overall, the ability to predict the details of surface configurations of iron oxides is an interesting scientific endeavor in its own right, but when put in the context of their industrial application as magnetic electrodes or catalysts, the significance of surface characterization of oxides is even more critical. For example, a single oxygen adatom on magnetite, $Fe_3O_4(111)$, which is theoretically predicted to appear in oxygen-rich conditions, can in fact lead to noise effects detrimental to spin-coherent injection from a half-metallic magnetite electrode to an organic spacer; this in turn can explain the experimentally reported underperformance of magnetite-based spintronic devices.

The largest portion of this Thesis has been devoted to the theoretical description of organic-inorganic interfaces for two separate applications: The development of self-assembled monolayers as a corrosion-prevention technique to protect the iron surface (Chapter 5); and the investigation of the hybrid interface electronic states and spin polarization in the case of an organic semiconductor (OSC)-based spintronic device consisting of an iron-based ferromagnetic (FM) electrode (Chapter 6).

Even though SAMs have been used as organic inhibitors against metal corrosion over the past few decades, a fundamental understanding of their prevention mechanisms and the development guidelines for molecular design of organic inhibitors of high efficiency have been missing to date. In this regard, the work of Chapter 5, where we provided a study combining quantum-mechanical calculations and molecular dynamics simulations of SAM/Fe interface structures, can be a useful reference to appreciate the structure-property relationships of organic monolayers serving as corrosion inhibitors.

By carefully examining each component of SAMs, we found successful conditions to produce long-term stability of the protecting organic monolayer on the iron surface. Our findings underline that phosphonic acid-based SAMs can bind to the hydroxylated iron surface much more strongly than thiol- or carboxylic acid-based SAMs. PA-based SAMs were calculated to bind to the surface in a bidentate or tridentate fashion exothermically via heterocondensation; the adsorption can be facilitated when a hydroxylated oxide substrate is used, leading to a considerable increase in binding strength. Thus, the oxide passivation of the iron metal surface before organic layer deposition is predicted to be advantageous, which is in good agreement with experiment. However, the packing morphology of SAMs with an alkyl-type spacer is not dense enough to prohibit the diffusion of small gas molecules into the monolayer even at high surface coverage (Γ=3.12×10^{14} molecules/cm^2).

Interestingly, the problem can be resolved either by replacing the conventionally used aliphatic chain by an aryl group or by fluorination of the alkyl spacer. Both approaches lead to a more aligned monolayer-packing structure with fluorination introducing in addition a strong electrostatic barrier against major oxidizing agents. To the best of our knowledge, this is the first time that a theoretical study demonstrates the application of a chemically modified SAM to protect the iron surface from corrosion.

In Chapter 6, we turned our focus to a completely different topic, albeit one that still involves organic-inorganic interfaces where iron and iron oxides are used as a substrate. As the organic spacer between two magnetic electrodes shows new spintronic functionalities that are unavailable with conventional inorganic materials, there has been

a need for a comprehensive study of the distinct interface electronic/magnetic properties of organic-ferromagnetic junctions.

Based on the bulk/surface calculations of iron and iron oxides in Chapter 3 and Chapter 4, we extended our attention to hybrid heterojunctions, in order to understand the spin polarization physics occurring at the organic/inorganic interface in iron-based organic magnetic junctions. Here, the actual interfaces were computationally modeled with molecules being adsorbed on ferro-(or ferri-)magnetic electrodes. To ascertain the condition where device efficiency could be maximized, we examined the interface systems by varying the crystal orientation or termination of the electrode (Fe, Fe_3O_4), the nature of the π-conjugated molecules (Alq_3, C_{60}, and pentacene), and the adsorption geometries on a given electrode. Although Fe_3O_4 is a half-metallic oxide with a high Curie temperature that can potentially replace conventional FM electrodes for room-temperature operation, this material has been less studied so far, particularly in the field of organic spintronics. Therefore, our systematic first-principles study of OSC-Fe_3O_4 interfaces was intended to assess whether or not magnetite can be employed to design an organic semiconductor-based spintronic device with optimal functionality.

The results of Chapter 6 demonstrated that the interface electronic structures of OSC-FM oxide are markedly different from those of OSC-FM metal interfaces. For the latter, π-conjugated OSC molecules show a broad resonance originating from the hybridization with the Fe dispersive 3*d* band near E_F, leading to an Ohmic-like junction upon metal contact. Due to the significant molecular orbital broadening, the hybrid interface states only exhibit minor spin discrimination. On the other hand, an appreciable negative spin polarization at E_F can be achieved in specific OSC-FM oxide systems, such as C_{60} on

Fe_{oct2}-terminated $Fe_3O_4(111)$ or $(\sqrt{2}\times\sqrt{2})R45°$- B-terminated $Fe_3O_4(001)$. This Chapter has afforded insight that that the surface electronic states of the electrode play a pivotal role in determining the spin polarization direction of the adsorbed molecule near the Fermi level.

In summary, our design rules for efficient OSC-FM metal/oxide magnetic junctions point to: (i) OSCs with a high carrier mobility; low spin-orbit coupling/hyperfine interaction; flat-lying adsorption; and a low injection barrier from the electrode; and (ii) FM electrodes with high "surface" density of states and spin polarization at the Fermi level; high T_C; and chemical stability with the organic layer.

Overall, this Thesis sought to examine how the surface and interface chemistry of iron and iron oxide can be modified by the presence of organic materials. Throughout this Thesis, we have theoretically demonstrated that the hybrid-interface electronic structures can greatly vary not only upon the choice of materials but also the substrate surface configurations, particularly of oxides; this, in turn, highlights the importance of surface engineering prior to molecular deposition. In conclusion, the fundamental understanding of adsorbate-substrate interactions at the interface we have provided is expected to offer useful guidelines to molecular design or substrate preparation procedure for targeted applications.

7.2 Future direction

The results of Chapter 5 imply that we can further examine these systems in terms of effects of chain lengths and other functionalization such as tethering, given that each part and function of SAMs can be modulated independently like a molecular building unit.

One interesting (and initially unexpected) expansion of the work of Chapter 5 could be the in-depth study of the monolayer morphology with *ab initio* MD simulations, especially for the ones including an aryl-type spacer. As discussed in Section 5.3.2, some particular conditions, *e.g.*, biphenyl-phosphonic acid on partially hydroxylated Fe(001), can lead to a nearly crystalline packing structure of the monolayer. Given that the electronic coupling of π-conjugated molecules highly depends on the packing structure, and the molecular orientation during the deposition is susceptible to the morphology of the organic film,[1] the possibility to align the SAM monolayer in an ordered manner could prove to be very useful in organic electronic devices, such as organic field-effect transistors where SAMs can be used as a dielectric layer placed between the OSC and electrode.[2]

In Chapter 6, we have mainly explored C_{60} as a non-magnetic organic spacer due to its isotropic shape, which ensures wavefunction overlap between its π orbitals and the oxide surface *d* states. However, C_{60} is known to display a high spin-orbit coupling compared to other molecules. Therefore, molecules that can lie flat even on the oxide surface can be potential candidates for future considerations, *e.g.*, metal phthalocyanine complexes. Since these complexes are chemically tunable as a function of derivatization and can be

grown in a crystalline state (electron mobility ~ 1 cm^2/Vs),[3] they appear as promising organic spacers that can further aid in the development of an efficient organic magnetic junction.

Based on the work of Chapters 5 and 6, we can envision SAM/Fe_3O_4 interfaces for magnetic tunnel junctions as the modularity of the SAMs can also be advantageous in the spintronic field. Interest in using SAMs in molecular spintronic devices has rapidly increased over the last few years. For instance, alkylphosphonic acids (C_nP) can be successfully grafted on LSMO[5] and further processed as LSMO/C_nP/Co MTJs fabricated via a nanoindentation lithography technique, see Figure 7.1.[6] By accurately choosing and combining the properties of each component of a SAM, it will become possible to customize the interface metal/molecule hybridization. For example, it has been proposed that a selection of the orbitals involved in the tunnel current could be achieved by choosing the binding group: thiols would select *s* bands, while –CN groups would select *d* bands.[4]

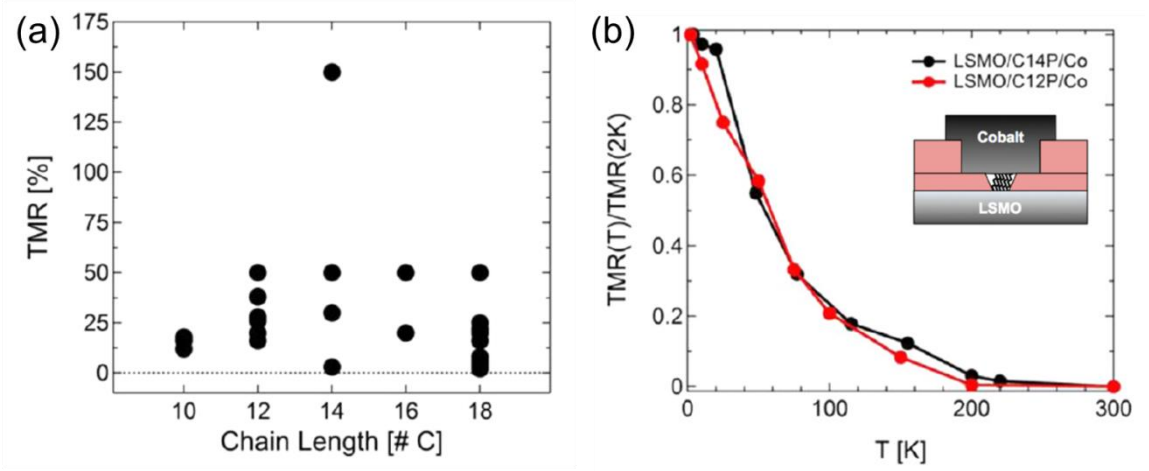

Figure 7.1 (a) TMR values recorded at 10 mV and low temperature for every working contact as a function of the molecular chain length in LSMO/C_nP/Co MTJs. (b) Temperature dependence of TMR measured at 10 mV for the C_{12}P and C_{14}P contacts. Reprinted with permission from Ref. 6, copyright 2016 by IOP Publishing.

While our computational studies have led to an improved understanding of organic-inorganic interfaces, in particular those involving transition metals and metal oxides as a substrate, there remain several methodological aspects that need to be further developed to describe accurately these complex heterojunctions.

Even though our work in Chapter 6 provided a reasonable quantitative description of OSC/FM interface electronic structures, the study remains incomplete since the accurate prediction of the energy level alignments at the interface is beyond the scope of standard DFT calculations. As discussed in Appendix B, there are several affordable techniques to improve the accuracy, such as G_0W_0 calculations and DFT+Σ^{axc}. However, these two methods also have their own limitations, related to extremely high computational cost

and non-self-consistency, respectively. Therefore, other computational techniques with a proper self-interaction correction should be explored to describe more extensive organic-inorganic systems. The alternatives can include the constrained local-spin-density approach[8] and a local-orbital formulation with a scissor operator in such a way that self-consistency is implemented on the orbital occupation numbers.[9]

One of the biggest merits that *ab initio* MD simulations based on DFT can provide is that they do not require any *ad hoc* parametrizations of force fields. Indeed, as the system involves more diverse chemical species, for example, in the case of Fe/SAM/O_2 as seen in Chapter 5, it is not a trivial task to build an accurate force field to take into account all the possible arrangements of molecules and their intermolecular interactions in a dynamical picture. However, *ab initio* MD is restricted to small unit-cell sizes and very short time scales (< 1 ns) compared to classical MD (< 1 μs), as the electronic structure has to be computed to solve the equation of motion; therefore, a single-shot DFT calculation has to occur at each time step for the projection of the next coordinates. Computationally reasonable time scales for *ab initio* MD are too short to describe chemical reactions such as a phase transition or detachment of atoms, which proceeds at a speed of about one atomic layer per minute. To extend the simulation times at least beyond a nanosecond regime, methods such as reactive force fields (ReaxFF) and charge-optimized many-body (COMB) potentials have been developed to combine the speed and scaling characteristics of classical MD with the bond-breaking/forming ability of quantum mechanics. However, our preliminary studies with ReaxFF have shown that the final geometries are often force-field dependent, which casts doubt on the optimized final structures of the systems. Also, the construction of accurate potentials is a tedious task

and can result in several months of ‘‘laborious iterative fitting’’.[10] One of the alternative approaches for large-scale simulations to describe chemical reactions in complex systems could be the *neural-network potential energy surface (NN PES)* methodology, as this biology-inspired algorithm can provide an accurate tool for the representation of arbitrary functions. Simply put, this scheme includes calculations to optimize the parameters of the NN in order to reproduce the input data by building a continuous and differentiable representation of the PES (usually at the DFT level) in a ‘‘training’’ process. Once trained, the arbitrary atomic coordinates are given to the NN, and the potential energy where forces can be calculated analytically is obtained.[11] This approach has been demonstrated to be applicable to a wide range of systems: small molecules, condensed systems, and even molecules on surfaces.[12] Therefore, in addition to an understanding of chemical reactions, it can be utilized as a powerful predictive tool to find the molecular adsorption geometry on substrates, which is essential to determine the interface electronic structures, as underlined throughout this Thesis.

7.3 References

[1] Duhm, S.; Heimel, G.; Salzmann, I.; Glowatzki, H.; Johnson, R. L.; Vollmer, A.; Rabe, J. P.; Koch, N. *Nature Mater.* **2008**, *7*, 326.

[2] Casalini, S.; Bortolotti, C. A.; Leonardi, F.; Biscarini, F. *Chem. Soc. Rev.* **2017**, *46*, 40.

[3] Jiang, H.; Ye, J.; Hu, P.; Wei, F. X.; Du, K. Z.; Wang, N.; Ba, T.; Feng, S. L.; Kloc, C. *Sci. Rep.* **2014**, *4*.

[4] Chen, J.; Calvet, L. C.; Reed, M. A.; Carr, D. W.; Grubisha, D. S.; Bennett, D. W. *Chem. Phys. Lett.* **1999**, *313*, 741.

[5] Tatay, S.; Barraud, C.; Galbiati, M.; Seneor, P.; Mattana, R.; Bouzehouane, K.; Deranlot, C.; Jacquet, E.; Forment-Aliaga, A.; Jegou, P.; Fert, A.; Petroff, F. *ACS Nano* **2012**, *6*, 8753.

[6] Tatay, S.; Galbiati, M.; Delprat, S.; Barraud, C.; Bouzehouane, K.; Collin, S.; Deranlot, C.; Jacquet, E.; Seneor, P.; Mattana, R.; Petroff, F. *J. Phys.-Condens. Mat.* **2016**, *28*.

[7] Jones, C. F.; Reeve, R. A.; Rigg, R.; Segall, R. L.; Smart, R. S.; Turner, P. S. *J. Chem. Soc. Farad. T 1* **1984**, *80*, 2609.

[8] Souza, A. M.; Rungger, I.; Pemmaraju, C. D.; Schwingenschlogl, U.; Sanvito, S. *Phys. Rev. B* **2013**, *88*.

[9] Rangan, S.; Ruggieri, C.; Bartynski, R.; Martinez, J. I.; Flores, F.; Ortega, J. *J. Phys. Chem. C* **2016**, *120*, 4430.

[10] Behler, J. *Chem. Model Appl. Theo.* **2010**, *7*, 1.

[11] Behler, J.; Parrinello, M. *Phys. Rev. Lett.* **2007**, *98*.

[12] Behler, J. *Phys. Chem. Chem. Phys.* **2011**, *13*, 17930.

APPENDIX A. SURFACE GIBBS FREE ENERGY IN DFT CALCULATIONS

This Appendix presents the complementary computational details for the surface energy calculations using first-principles thermodynamics which is discussed in Chapter 2. Here, we take hematite as a representative example of iron oxides.

A.1 Assumptions taken for the surface energy calculations

For the sake of simplicity, we assume that there is a thermal equilibrium between surface and bulk, with the latter serving as a reservoir of Fe atoms; the following relationship can be satisfied:

$$2\mu_{Fe}(T,p) + 3\mu_O\left(T,p_{O_2}\right) = g^{bulk}_{Fe_2O_3}(T,p) \qquad \text{(A. 1)}$$

Hereafter, lower-case g is used to denote the Gibbs free energy per formula unit.

The two gas species are considered not to be involved in any gas-phase reactions and the oxygen chemical potential is taken to equilibrate between the two reservoirs, which follows the work by Sun *et al.* [1] and Fronzi *et al.*[2]:

$$\mu_{H_2O}\left(T,p_{H_2O}\right) - 2\mu_H\left(T,p_{H_2O}\right) = \frac{1}{2}\mu_{O_2}\left(T,p_{O_2}\right) \qquad \text{(A. 2)}$$

With these assumptions applied to Equation 2.28 in Chapter 2, we obtain:

$$\gamma(T, p_{O_2}, p_{H_2O}) = \frac{1}{2A}\left[G_{slab} - \frac{1}{2}N_{Fe}g_{bulk}^{Fe_2O_3} - \left(\frac{1}{2}N_O - \frac{3}{4}N_{Fe} - \frac{1}{4}N_H\right)\mu_{O_2}(T, p_{O_2}) - \frac{1}{2}N_H\mu_{H_2O}(T, p_{H_2O})\right] \quad (A.3)$$

where G_{slab} denotes the free energy of the symmetric slab with two equivalent surfaces of area A; $g_{bulk}^{Fe_2O_3}$, the free energy of a bulk hematite per formula unit; and N_{Fe}, N_{O}, and N_{H}, the number of atoms of each element in the total system. The surface energy (γ) is expressed as a linear function of the chemical potentials of the two gas reservoirs, μ_{O_2} and μ_{H_2O}, which are determined by the temperature and partial pressures of each component.

A.2 Zero-point vibrational energy (ZPE) and entropy contribution (TS) corrections

Table A.1 presents the ZPE corrections for the isolated molecules and adsorbed species based on Equation A.4 that is the calculated vibrational frequencies from the Hessian matrix constructed by finite displacements of an atom by 0.015 Å:

$$U_0 = E_{elec} + \sum_{i}^{modes} \frac{1}{2}h\omega_i \quad (A.4)$$

Here, we regard the non-stoichiometric components of the surface atoms for a given hematite slab as adsorbates whose energy is to be corrected for zero-point vibration.

Table A.1 Calculated zero-point energy energies for isolated gas molecules and adsorbed reactive species on the hydroxylated/hydrated 1Fe-terminated α-Fe_2O_3 (0001) surface. The values obtained here are in good agreement with the ones obtained in previous studies on various oxides. The ranges of ZPE values for the adsorbed species come from the different surface states.

	This work	Liao[3]	Hellman[4]	Valdés(TiO_2)[5]	Bajdich(CoOOH)[6]
H_2	0.27	0.27	0.33	0.27	0.35
O_2	0.10	0.10	0.10	0.10	
H_2O	0.57	0.57	0.58	0.56	0.57
*O	0.07-0.08	0.04	0.06-0.09	0.05	0.06
*OH	0.35-0.40	0.37	0.33-0.39	0.35	0.37
*OOH	0.45-0.47	0.48	0.44-0.45	0.41	0.44
*OH_2	0.67-0.70	0.67		0.70	

The standard molar entropy (S) of a gas molecule in the initial state is calculated from the experimental value in NIST-JANAF table. These values comprehensively include molecular motions (translations, rotations, and vibrations) before adsorption on the surface. Only the vibrational contribution to the total entropy is considered for the adsorbates using Equation A.5:

$$S_{vib} = k_B \sum_{i}^{modes} \left[\frac{h\omega_i}{k_B T(e^{h\omega_i/k_B T} - 1)} - \ln(1 - e^{-h\omega_i/k_B T}) \right] \quad (A.5)$$

A.3 Thermodynamically accessible ranges for oxygen gas and water vapor

The molar Gibbs energy, *i.e.*, the chemical potential of an ideal gas, varies with its partial pressure (p) and temperature (T):

$$\mu_O(T,p) = \mu_O(T,p^\circ) + 1/2 k_B T \ln\left(\frac{p_{O_2}}{p^\circ}\right) \qquad \text{(A. 6)}$$

where p° is the pressure in the reference state and k_B, the Boltzmann constant. As experimental conditions have a considerable impact on the oxygen chemical potential, it is necessary to evaluate the surface energies for various surface terminations as a function of the chemical potential of oxygen to determine the surface stability in the given environment. It is useful to restrict the range of oxygen chemical potentials by considering the relevant limiting conditions.

The oxygen-rich limit can be defined as the chemical state in which molecular oxygen starts to condense on the surface. By assuming that such condensed oxygen is in equilibrium with gas-phase oxygen, the upper limit of the oxygen chemical potential is conventionally approximated as:

$$\mu_O(0\ K, p^\circ) = \frac{1}{2} E_{O_2}^{DFT} \qquad \text{(A. 7)}$$

where $E_{O_2}^{DFT}$ is the DFT calculated energy of an O_2 molecule. Here, in order to avoid the over-binding issue of O_2 in DFT, we chose to calculate the energetics of molecular oxygen using the experimental formation enthalpies of water as suggested by Zeng *et al.*:[8]

$$\frac{1}{2}E_{O_2} = E_{H_2O}^{DFT} - E_{H_2}^{DFT} - \Delta H_f^0 - \Delta ZPE = \mu_O(0\ K, p^\circ) \qquad (A.8)$$

with the standard formation enthalpy ΔH_f^0 = -2.476 eV at 0 K (taken from the NIST-JANAF table) and $\Delta ZPE = ZPE(H_2O) - ZPE(H_2) - \frac{1}{2}ZPE(O_2)$ = 2.510 eV.

At the oxygen-poor limit, iron oxide begins to decompose and form metallic iron. Thus, a reasonable minimum μ_O corresponds to the condition where Fe crystallizes and oxygen (and hydrogen) separates toward the surface according to the equilibrium of bulk hematite, that is:

$$\mu_O - \mu_O(0\ K, p^\circ) = \frac{1}{3}\Delta_f H^\circ_{Fe_2O_3} \qquad (A.9)$$

where $\Delta_f H^\circ_{Fe_2O_3}$ is the standard formation enthalpy taken from the NIST-JANAF table.

Similarly, the chemical potential of water vapor depends on temperature and pressure according to:

$$\mu_{H_2O}(T,p) = \mu_{H_2O}(T,p^\circ) + k_B T \ln\left(\frac{p_{H_2O}}{p^\circ}\right) \qquad (A.10)$$

From the JANAF table, $\mu_{H_2O}(T,p^\circ)$ is calculated as a function of temperature, as shown in Table A.2. To assure that water in the gas phase is thermodynamically most favorable in any condition, the maximum value of μ_{H_2O} is set to the saturated water vapor pressure (p_v) taken from the water phase diagram[9] at each temperature. The lower limit is set to the lowest possible chemical potential, -2.65 eV, at the experimental critical temperature, T_c= 647 K in UHV condition, *i.e.* 10^{-9} mbar; the upper limit corresponds to -0.51 eV, the

highest chemical potential of water in the vapor phase based on the saturation point, *i.e.* $\mu_{H_2O}(g) = \mu_{H_2O}(l)$ at 200 K, 3.32×10^{-6} bar**.**

Table A.2 Temperature dependence of the chemical potential of molecular water and oxygen, $\mu_{H_2O}(T, p^\circ)$ and $\mu_O(T, p^\circ)$ at the standard pressure, p°=1 bar. $\mu_{H_2O}(T, p_v)$ at each temperature is calculated at the saturated vapor pressure, taken from the water phase diagram.

T (K)	$\mu_{H_2O}(T, p^\circ)$ (eV)	p_v (bar)	$\mu_{H_2O}(T, p_v)$ (eV)	$\mu_O(T, p^\circ)$ (eV)
200	-0.30	3.32×10^{-6}	-0.51	-0.17
300	-0.48	0.0354	-0.57	-0.27
400	-0.69	2.46	-0.66	-0.38
500	-0.90	26.8	-0.76	-0.50
600	-1.11	134	-0.87	-0.61

A.4 References

[1] Sun, Q.; Reuter, K.; Scheffler, M. *Phys. Rev. B* **2003**, *67*.

[2] Fronzi, M.; Piccinin, S.; Delley, B.; Traversa, E.; Stampfl, C. *Phys. Chem. Chem. Phys.* **2009**, *11*, 9188.

[3] Liao, P. L.; Keith, J. A.; Carter, E. A. *J. Am. Chem. Soc.* **2012**, *134*, 13296.

[4] Hellman, A.; Pala, R. G. S. *J. Phys. Chem. C* **2011**, *115*, 12901.

[5] Valdes, A.; Qu, Z. W.; Kroes, G. J.; Rossmeisl, J.; Norskov, J. K. *J. Phys. Chem. C* **2008**, *112*, 9872.

[6] Bajdich, M.; Garcia-Mota, M.; Vojvodic, A.; Norskov, J. K.; Bell, A. T. *J. Am. Chem. Soc.* **2013**, *135*, 13521.

[7] Chase, M. W.; Davies, C. A.; Downey, J. R.; Frurip, D. J.; Mcdonald, R. A.; Syverud, A. N. *J. Phys. Chem. Ref Data* **1985**, *14*, 927.

[8] Zeng, Z. H.; Chan, M. K. Y.; Zhao, Z. J.; Kubal, J.; Fan, D. X.; Greeley, J. *J. Phys. Chem. C* **2015**, *119*, 18177.

[9] Hardy, B. In *Proceedings of the Third International Symposium on Humidity and Moisture* Teddington, London, England, 1998, p 214.

APPENDIX B. DESCRIPTION OF THE ENERGY LEVEL ALIGNMENT AT ORGANIC-INORGANIC INTERFACE WITH THE *GW* APPROXIMATION

Most calculations on organic/inorganic interfaces have been carried out to date at the level of conventional density functional theory (DFT) or semi-empirical one-particle Hamiltonians, which cannot correctly describe the excited states.[1] Thus, such calculations often fail to provide accurate excited-state properties, such as the polarization response of a molecule near a metal or metal oxide surface, even though conventional DFT can then adequately capture the chemical interactions leading to rearrangements of electron density at the interface. One of the resulting problems involves an inaccurate prediction of energy level alignment at the organic-inorganic interfaces, as discussed in Section 6.3. In this Appendix, we demonstrate how the *GW* approximation (GWA)[1] can provide major improvement, taking C_{60}/Fe(001)-*p*(1×1)O as a benchmark heterogamous interface. Given its complexity and high computational cost, we limit our discussion here to the G_0W_0 scheme that corresponds to the first-order perturbative correction of the Kohn-Sham (KS) eigenvalues by the self-energy, $\Sigma = iGW$; here G is the Green's function and W is the screening. The scheme relies on the assumption that the KS wave functions are a good zeroth-order approximation for the true quasiparticle wave functions; therefore, the difference between the self-energy and the DFT exchange-correlation potential can be treated as a small perturbation. For comparison, we also

present the results from the hybrid functionals: PBE0 and HSE06 that contain a fraction of exact Hartree-Fock exchange (E_{xx}). An alternative approach also considered in this Appendix is the so-called "DFT+Σ^{axc}" scheme, which basically consists of: (i) a correction of orbital energies obtained for the gas-phase molecules; and (ii) the inclusion of renormalization effects described in an image-potential manner. The details of these methodologies are given in Chapter 2.

B.1. Fundamental gap correction using hybrid functionals

As described in Section 6.3.4, the hole injection barrier at C_{60}/Fe(001)-*p*(1×1)O interface is calculated to be 1.4 eV, strongly underestimates the PES measured the value of 2.6 eV. Also, the calculated electron injection barrier of 0.3 eV is far below IPES data, 0.8 eV. In general, there are two major components to cause this error: (i) underestimation of the molecular fundamental gap arising from too lower ionization energy (IE) and too higher ionization energy (IE); and (ii) neglect of the polarization effect from the surrounding medium, *i.e.*, energy level normalization.

In the case of point (i), it is known that the exact total energy as a function of fractional particle number is a series of discontinuous straight lines whose vortexes are located at integer occupations.[2,3] Since the semi-local LDA and GGA exchange-correlation (XC) potentials are continuous in the density and its gradient, these potentials fail to exhibit the correct "derivative discontinuity" condition, which explains the discrepancies between the KS eigenvalues and the IE and EA values. Since Hartree-Fock (HF) behaves in the way opposite to DFT, balancing DFT and HF adequately can lead to a much better

satisfaction of thethe linearity condition, where we can essentially approximate $-\varepsilon_{HOMO}^{KS}[-\varepsilon_{LUMO}^{KS}]$ to IE [EA].[4] In this context, many hybrid functionals have been developed to improve the theoretical prediction of a fundamental gap.

So far, one of the best solutions to deal with this problem in an organic system is to utilize range-separated hybrid functionals (RSH). Here, the Coulomb interaction is divided into long-range (LR) and short-range (SR) contributions using the error function. Exchange in the LR term is treated Hartree-Fock-like to correctly describe the asymptotic region of the XC potential; the SR term is treated in the GGA to mimic short-range static correlation effects that are essential for chemical bonding.[5] The fraction of exact exchange included in the RSH exchange potential as a function of interelectronic distance is illustrated in Figure A1. The long-range correction has solved a wide variety of problems of earlier Kohn–Sham calculations. The most remarkable problems that have been resolved with the long-range correction include electronic excitation spectra, optical response properties, and orbital energies.[6]

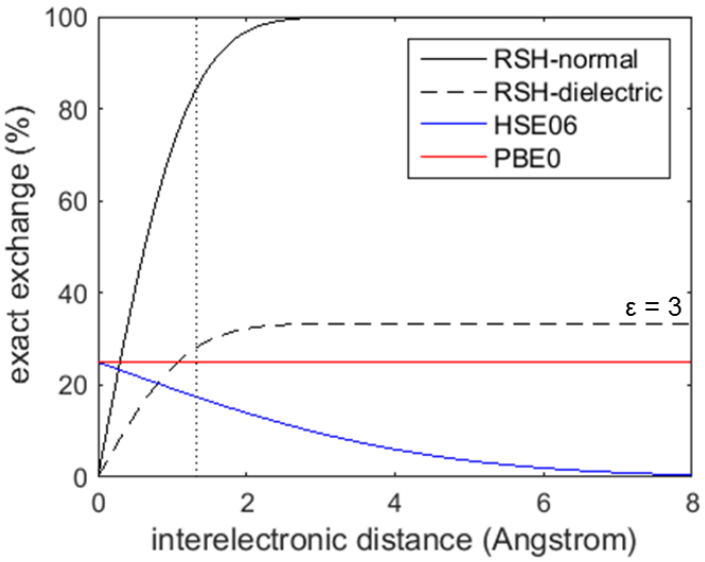

Figure B.1 Percentage of exact exchange included in the exchange potential as a function of interelectronic distance for a range-separated hybrid functional (LC-ωPBE, ω=0.40 $Bohr^{-1}$), RSH corrected with a dielectric constant (LC-ωPBE, ω=0.40 $Bohr^{-1}$, $\alpha+\beta=1/\epsilon$), and the HSE06 (α=0.25, ω=0.207$Å^{-1}$) and PBE0 (α=0.25) functionals. α, β, and ω are tuning parameters (see Chapter 2).

On the other hand, in the field of solid-state physics, PBE0[7] and HSE06[8] have been frequently adopted. The PBE0 hybrid functional intends to physically enhance the PBE-GGA XC functional by replacing 25% of the PBE exchange functional with the non-local Fock exchange integral. It has been shown that PBE0 provides a better electronic and geometric description of inorganic materials than PBE; however, slowly decaying LR component of the Fock exchange in periodic solids is associated with a large computational cost, especially for metallic systems that require dense Brillouin zone sampling.[9] In this context, HSE06, the short-range corrected version of PBE0, was

developed; here, the PBE exchange functional is mixed with the Fock exchange integral only for the SR part (see the blue line in Figure B.1). As illustrated above, it has been confirmed that the absence of LR exchange results in an incorrect asymptotic potential, which vanishes exponentially instead of as 1/r. However, in the case of solids such as oxide semiconductors, the SR correction alone in HSE06 can yield a reasonable HOMO–LUMO gap close to the experimental band gap.[10]

Figure B.2 shows IE and EA for isolated C_{60} calculated with various hybrid functionals. Among all functionals studied, one of the RSH-type functionals, LC-ω^*PBE (with optimally tuned ω^*) stands out as the only one leading to a correct description of the 1/r potential, therefore, provides a very accurate estimation of EA and IE of C_{60} in the gas phase. On the other hand, PBE0 and HSE with a fraction of E_{xx}, α= 0.15-0.25 with the range separation at ω=0.2-0.3Å^{-1} cannot open up the gap as much as LC- ω^*PBE due to the absence of long-range correction.

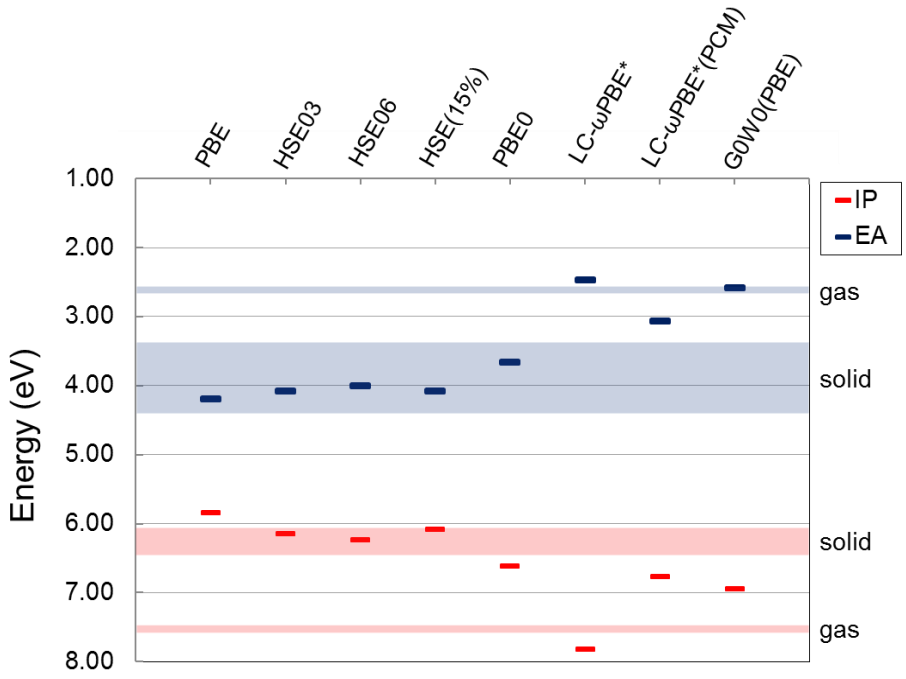

Figure B.2 IP and EA of an isolated C_{60} molecule derived from the eigenvalues calculated from various functionals and G_0W_0. LC-ω*PBE(PCM) indicates the LC-ω*PBE where ω* is tuned in a polarizable continuum model (PCM). G_0W_0(PBE) represents the G_0W_0 taking the initial guess of QP energies and wave function from PBE calculations. The horizontal shaded areas show the experimental values (windows) for IE and EA for C_{60} in the gas phase and solid state.

We should note that a more general asymptotic potential should be 1/(εr), where ε is the static dielectric constant, which suggests that LR Fock exchange is screened when environmental effects are present. One solution is to incorporate the dielectric response into RSH by substituting E_{xx}^{LR} with $\frac{1}{\epsilon}E_{xx}^{LR}+\left(1-\frac{1}{\epsilon}\right)E_{GGAx}^{LR}$. This treatment was demonstrated to reproduce well the band gap of molecular crystals by successfully taking into account of electronic polarization.[11] Also, our results that the polarizable continuum model (PCM)-tuned LC-ω*PBE can give reasonable values for C_{60} in the solid state, is in line with previous work.[11,12] One of interesting points is that the PBE0 and HSE

functionals can predict IE and EA values close to those taken for solid C_{60}. This can be attributed to the fraction of HF exchange in these functionals: 0.15-0.25 is fortuitously close to $1/\epsilon$ of C_{60} in the solid state (~ 0.2). In this context, if the coverage density of adsorbed molecules is high enough on the substrate to have a dielectric constant of ~4-5, it could be expected that HSE and PBE0 functionals could be used effectively to describe the energy levels of the adsorbates. Indeed, as displayed in Figure B.3, we obtain interfacial electronic level alignment in quantitative agreement with experiment when hybrid functionals, particularly PBE0, are employed for C_{60}/Fe(001)-*p*(1×1)O. PBE0 downshifts the HOMO by 0.7 eV and upshifts the LUMO by 0.6 eV with respect to PBE, which leads to Δ_h = 2.0 eV and Δ_e = 0.9 eV. Experimentally, the C_{60} molecules cluster into islands, building up the (111) face of a FCC C_{60} crystal with the [IE-EA] transport gap measured to be 3.2 eV from PES/IPES and STS experiments. [13]

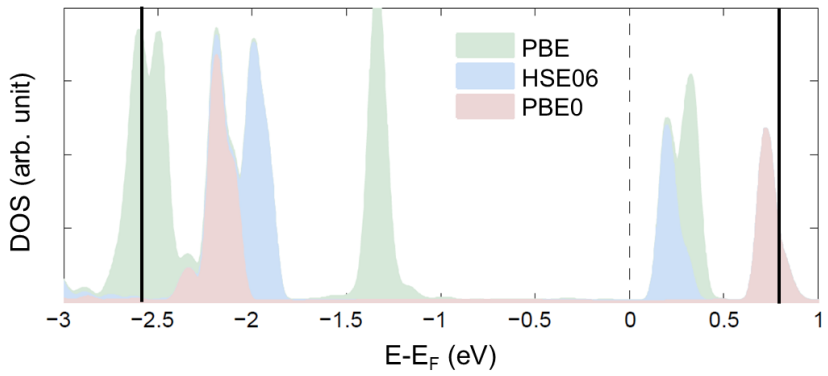

Figure B.3 C_{60}-projected density of states (DOS) with PBE, HSE06, and PBE0 for the C_{60}/Fe(001)-*p*(1×1)O interface. The Fermi level is set to zero. Two vertical black solid lines indicate experimental IE(left)/EA(right) energies taken from UPS/IPES measurements. [13]

B.2. Limits of hybrid functionals

Still, there are physical phenomena at the interface that cannot be well treated with DFT-based hybrid functionals. The energy level alignments of molecular junctions taken from PES/IPSE experiments correspond to charge excitation; therefore, the molecular levels at the interfaces should be theoretically treated as quasiparticle energy levels. In this instance, dielectric screening in the Hartree term is essential to introduce correlations into the many-body eigenstates, including the response of the other electrons to extra electron/hole.[14] However, the eigenvalues of the KS Hamiltonian correspond to "one-electron" energies for the N-particle ground state for which orbital relaxation in N±1-particle cases is neglected;[15] therefore, a quantitative agreement with experimental IE or EA values cannot be expected even with a hypothetical "exact" exchange-correlation functional.[16] In particular, screening effects are not negligible when a molecule is adsorbed on the substrate due to the presence of neighboring molecules in addition to the substrate.

Another problem is the incorrect description of "free-electron-like" systems in hybrid functionals. Figure B.4 displays the calculated DOS of a Fe(001) slab at the PBE0 and HSE06 levels. Although it has been reported that some inert metal electrodes, *e.g.*, gold, can be described fair well by hybrid functionals (or better than with PBE),[17] for metal with highly populated states at E_F, even gap states can be introduced in metallic electronic structures as the addition of non-local exchange leads to spurious electron localization and large splitting between orbital energies. Unlike molecules, these features

areit is detrimental in the cased of metals since hybrid functionals do not reflect dynamical correlation effects that generally decrease the bandwidth.[18] As a result, the DOS becomes highly extended over a wide range of energy with much lower intensity.

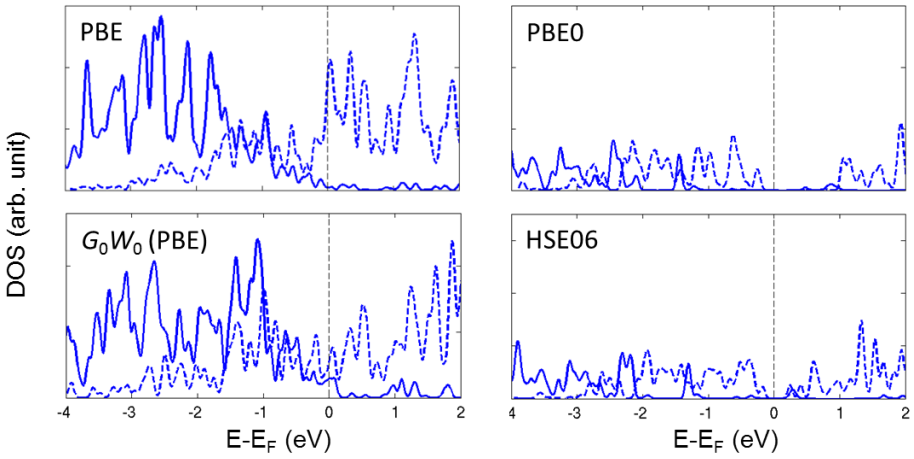

Figure B.4 Electronic density of states of Fe (001) computed using the PBE, PBE0, HSE06, and G_0W_0(PBE) method. A solid line represents the spin-up electrons while a dashed line corresponds to the spin-down electrons.

B.3. The DFT+Σ^{axc} approach

One technique that is able to correct the fundamental gap of the adsorbed molecule while using the electronic structure of the metal from DFT is the "DFT+Σ^{axc}" approach proposed by Egger *et al.* [19], which corresponds to a single-shot non-self-consistent correction combining two steps.

The first step of DFT+Σ^{axc} is to correct the orbital energies for the gas-phase molecules using range-separated functionals. Since orbital energies depend not only on the level of calculation but also on the type of basis sets, it is important to set the reference point correctly. If the calculation for the organic-metal junction is based on plane-wave (PW) basis sets, the reference orbital energy of the gas-phase molecule should be the KS eigenvalue described in the PW basis set, not the one in an atomic orbital (AO) basis set. Therefore, the corrected orbital energy (ε_i') from the first step can be expressed as follows:

$$\varepsilon_i' = \varepsilon_i^{PBE/PW} + [\varepsilon_i^{RSH/AO} - \varepsilon_i^{PBE/AO}] \qquad \text{(B.1)}$$

where $\varepsilon_i^{PBE/PW}$, $\varepsilon_i^{PBE/AO}$, and $\varepsilon_i^{RSH/AO}$ represent the orbital energies calculated in PBE with a PW basis set, PBE with AO basis set, and RSH with AO basis set.

In the second step, the impact on energy level alignment of renormalization due to screening from the environment can be treated with a classical model of image-charge effect. The exact XC-hole above a polarizable medium far away from a metallic surface must decay in an image-potential manner:[20]

$$V = \frac{(1-\epsilon)/(1+\epsilon)}{4(d-z_0)} \qquad \text{(B. 2)}$$

where d is the coordinated perpendicular to the surface and z_0 is the image-plane position. For a metal surface with $\epsilon = \infty$, the potential can be further simplified as $V = -\frac{1}{4(d-z_0)}$. According to ref. 19, z_0 can be derived by finding the common tangent point of the XC-potential with the classical image potential, as shown in Figure B.5.

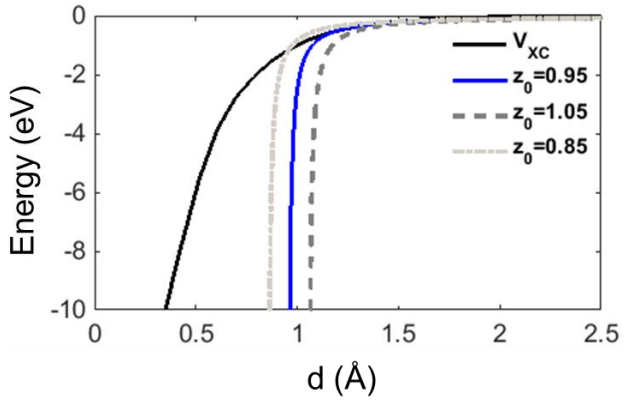

Figure B.5 Plane-averaged XC potential taken from PBE calculations of Fe(001) for the Fe(001) surface (black solid line). The origin of the x-axis is set to the geometric edge of the slab. Curves from a classical image-charge model with image-plane values, z_0, of 0.95 (blue solid line), 1.05 (dark grey dashed line), and 0.85 Å (light grey dotted line) are presented.

We note that, in many accounts, the adsorbed molecule is also surrounded by neighboring molecules (which can be either on the surface or in the bulk of the organic layer); therefore, their polarization should be taken into account. As demonstrated above, it can be incorporated in the procedure of the fundamental gap correction by using the PCM-tuned RSH results for $\varepsilon_i^{RSH/AO}$.

Therefore, the final correction can be given as:

$$\varepsilon_i^{DFT+\Sigma^{axc}} = \varepsilon_i^{PBE/PW} + [\varepsilon_i^{RSH/AO} - \varepsilon_i^{PBE/AO}] \pm \frac{1}{4(d - z_0)} \qquad \text{(B. 3)}$$

where ε_i is the calculated *i*th electronic state, *d* is the molecule-substrate distance, and z_0 is the image-plane position. The image potential term is positive for the occupied orbitals and negative for the unoccupied orbitals. For C_{60}/Fe(001)-*p*(1×1)O, the overall correction is -0.86 eV for HOMO and +1.05 eV for LUMO, leading to 2.3 eV for Δ_h and 1.3 eV for Δ_e (see Table B.1). Here, the surface polarization has a small impact (~ 0.1 eV) compared to the fundamental gap correction as the molecule is adsorbed relatively far above (*d* = 2.5 Å) the surface.

Table B.1 Calculated interface dipole (Δ), hole injection barrier (Δ_h), and electron injection barrier (Δ_e) for C_{60}(6:6) on Fe(001)-*p*(1×1)O at the DFT, PBE0, HSE06, DFT+Σ^{axc}, and G_0W_0(PBE) levels. The values are taken from the peak positions for the MOs in PDOS with respect to the vacuum level. Experimental values are taken from Ref. 13.

	Δ	**Δ_h**	**Δ_e**
DFT	1.65 eV	1.35 eV	0.30 eV
PBE0	2.92 eV	2.03 eV	0.89 eV
HSE06	2.19 eV	1.99 eV	0.20 eV
DFT+Σ	3.56 eV	2.29 eV	1.27 eV
G_0W_0(PBE)	2.82 eV	2.17 eV	0.55 eV
Expt.	3.2 eV	2.6 eV	0.8 eV

B.4 GW approximation

Although the "DFT+Σ^{axc}" approach can correctly predict and explain the level alignment taking place at the interfaces, this method can be only applied to the case of weak coupling, *i.e.*, physisorption, as it is inherently non-self-consistent. Thus, other techniques need to be found for the case of chemisorption.

A major problem to describe the heterogeneous organic-inorganic junction with DFT or hybrid functionals is that the reliability of a functional is limited to one system, and not applicable as well to the other. One of the main advantages of GWA involves its versatility among different classes of materials including molecules, organic crystals, and inorganic semiconductors. At the G_0W_0 level, the technique can give a reasonable energy gap for C_{60} (Figure B.2), at the same time, properly reproduce the metallic (and ferromagnetic) character of Fe(001) (Figure B.4) due to the inclusion of dynamic screening. Here, we employ the G_0W_0 scheme with the initial guess of QP energies and wave function from PBE calculations, *i.e.*, G_0W_0(PBE) to calculate the electronic structure at the C_{60}/Fe(001)-p(1×1)O interface, as presented in Figure B.6. As predicted from the remarkable improvement of IE and EA estimations for an isolated C_{60}, G_0W_0(PBE) can provide a sensible prediction for the QP energies of the adsorbed molecular resonance, 2.2 eV for HOMO, and 0.8 eV for LUMO, which are close to the experimental values: 2.6 eV and 0.8 eV, respectively. The discrepancies with the measurements can be further reduced by refinements within the *GW* framework; however, this is beyond the scope of the current study.

Our study confirms that GWA can be expanded to evaluate the QP level alignment for organic molecules adsorbed on metal or metal oxide surfaces, regardless of the nature of their adsorption. This methodology can thus unravel the physical and chemical features of complex heterogeneous system aby accurately dealing with many-body effects.

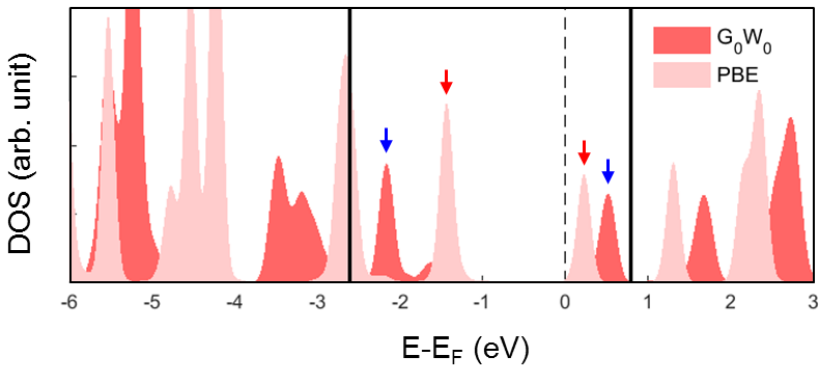

Figure B.6 C_{60}-projected density of states (DOS) with at the PBE and G_0W_0(PBE) levels for C_{60}/Fe(001)-p(1×1)O. The Fermi level is set to zero. Two vertical black solid lines indicate experimental HOMO(left)/LUMO(right) level taken from UPS/IPES measurements.[13]

B.5 References

[1] Hedin, L. *Phys. Rev.* **1965**, *139*, A796.
[2] Perdew, J. P.; Parr, R. G.; Levy, M.; Balduz, J. L. *Phys. Rev. Lett.* **1982**, *49*, 1691.
[3] Kummel, S.; Kronik, L. *Rev. Mod. Phys.* **2008**, *80*, 3.
[4] Cohen, A. J.; Mori-Sanchez, P.; Yang, W. T. *Chem. Rev.* **2012**, *112*, 289.
[5] Korzdorfer, T.; Bredas, J. L. *Accounts Chem. Res.* **2014**, *47*, 3284.
[6] Tsuneda, T. *Density Functional Theory in Quantum Chemistry*; Springer Japan, 2014; Vol. 1.
[7] Adamo, C.; Barone, V. *J. Chem. Phys.* **1999**, *110*, 6158.
[8] Heyd, J.; Scuseria, G. E.; Ernzerhof, M. *J. Chem. Phys.* **2006**, *124*.
[9] Heyd, J.; Scuseria, G. E.; Ernzerhof, M. *J. Chem. Phys.* **2003**, *118*, 8207.
[10] Marsman, M.; Paier, J.; Stroppa, A.; Kresse, G. *J. Phys.-Condens. Mat.* **2008**, *20*, 064201.
[11] Refaely-Abramson, S.; Sharifzadeh, S.; Jain, M.; Baer, R.; Neaton, J. B.; Kronik, L. *Phys. Rev. B* **2013**, *88*, 081204.
[12] Sun, H. T.; Ryno, S.; Zhong, C.; Ravva, M. K.; Sun, Z. R.; Korzdorfer, T.; Bredas, J. L. *J. Chem. Theory Comput.* **2016**, *12*, 2906.
[13] Picone, A.; Giannotti, D.; Riva, M.; Calloni, A.; Bussetti, G.; Berti, G.; Duo, L.; Ciccacci, F.; Finazzi, M.; Brambilla, A. *Acs Appl. Mater. Inter.* **2016**, *8*, 26418.
[14] Garcia-Lastra, J. M.; Rostgaard, C.; Rubio, A.; Thygesen, K. S. *Phys. Rev. B* **2009**, *80*.
[15] Chong, D. P.; Gritsenko, O. V.; Baerends, E. J. *J. Chem. Phys.* **2002**, *116*, 1760.
[16] Tamblyn, I.; Darancet, P.; Quek, S. Y.; Bonev, S. A.; Neaton, J. B. *Phys. Rev. B* **2011**, *84*, 201402.
[17] Biller, A.; Tamblyn, I.; Neaton, J. B.; Kronik, L. *J. Chem. Phys.* **2011**, *135*.
[18] Northrup, J. E.; Hybertsen, M. S.; Louie, S. G. *Phys. Rev. Lett.* **1987**, *59*, 819.
[19] Egger, D. A.; Liu, Z. F.; Neaton, J. B.; Kronik, L. *Nano Lett.* **2015**, *15*, 2448.
[20] Almbladh, C. O.; Vonbarth, U. *Phys. Rev. B* **1985**, *31*, 3231.